

O. Celik, S. Sritharan

**An Evaluation of Seismic Design Guidelines
Proposed for Precast Concrete Hybrid Frame Systems**

**ISU-ERI-Ames Report ERI-04425
Submitted to the Precast/Prestressed Concrete
Manufacturers Association of California**

JANUARY 2004

Final

REPORT

IOWA STATE UNIVERSITY
OF SCIENCE AND TECHNOLOGY

**Department of Civil, Construction
and Environmental Engineering**

**An Evaluation of Seismic Design Guidelines
Proposed for Precast Concrete Hybrid Frame Systems**

by

**Onur Celik
Graduate Research Assistant**

**Sri Sritharan
Assistant Professor**

ISU-ERI-Ames Report ERI-04425

**A Final Report to the Precast/Prestressed Concrete
Manufacturers Association of California**

**Department of Civil, Construction and Environmental Engineering
Iowa State University
Ames, IA 50011**

January 2004

ABSTRACT

The development of hybrid frame systems has enabled application of precast concrete in seismic regions. In addition to the benefits of the precast concrete technology, the hybrid frame systems offer additional benefits during seismic response. Using experimental data from two component tests and one building test, this report examines the validity of the design guidelines proposed for hybrid frame systems by (1) Stanton and Nakaki as part of the PRESSS (PREcast Seismic Structural Systems) program (2002) and (2) ACI (American Concrete Institute) Innovation Task Group (2003). By establishing analysis methods based on the proposed design steps and assumptions, and comparing the analysis results with the experimental results, the adequacy of the proposed guidelines is examined. The accuracy of the *Monolithic Beam Analogy* (MBA) concept in predicting the response of hybrid frame connections is also investigated as part of this study. Based on the comparisons between the experimental and various analytical results, recommendations are made to improve the design of precast hybrid frame connections.

ACKNOWLEDGEMENTS

The research presented in this report was made possible by funding from the Precast/Prestressed Concrete Manufacturers Association of California (PCMAC), which is gratefully acknowledged. The authors also thank Gerry Cheok and Sivakkolundu Vernu for their assistance with interpretation of the NIST test data and MBA analysis of the hybrid connections, respectively.

Conclusions, opinions and recommendations expressed in this report are those of the authors alone, and should not be construed as being endorsed by the financial sponsor.

TABLE OF CONTENTS

LIST OF FIGURES	viii
LIST OF TABLES	xvi
LIST OF SYMBOLS	xviii
CHAPTER 1. INTRODUCTION	1
1.1 General	1
1.1.1 Benefits of Precast Concrete	2
1.1.2 Precast Concrete Applications in Seismic Regions	3
1.1.3 Non-Emulative Connections	6
1.1.4 Hybrid Connection	12
1.2 Scope of Study	14
1.3 Report Layout	15
1.4 References	16

CHAPTER 2. LITERATURE REVIEW	19
2.1 Introduction	19
2.2 Experimental Studies	20
2.2.1 NIST Tests	20
2.2.2 The PRESSS Research Program	29
2.3 Analytical Studies	35
2.3.1 Englekirk (1989)	35
2.3.2 Priestley and Tao (1993)	37
2.3.3 El-Sheikh, Sause, Pessiki, and Lu (1999)	39
2.3.4 Pampanin, Priestley, and Sritharan (2001)	42
2.3.5 Vernu, Sritharan and Vernu	51
2.4 Design Methods	54
2.4.1 Cheok, Stone, and Nakaki (1996)	53
2.4.2 PRESSS Design Guidelines (2002)	62
2.4.3 ACI T1.2-03 Document (2003)	78
2.5 References	80

CHAPTER 3. FORMULATION OF VARIOUS ANALYSIS

PROCEDURES	83
3.1 Introduction	83

3.2	PRESSS Guidelines	85
3.2.1	PRESSS Analysis Procedure	85
3.2.2	Modified PRESSS Analysis Procedure	96
3.3	ACI T1.2-03 Analysis Procedure	110
3.4	Monolithic Beam Analogy (MBA)	111
3.5	Summary of Experimental Data	122
3.5.1	Specimens M-P-Z4 and O-P-Z4	123
3.5.2	Hybrid Frame in the PRESSS Building	129
3.6	References	137

CHAPTER 4. PRECAST HYBRID FRAME SYSTEMS:

VALIDATION OF SEISMIC DESIGN GUIDELINES

AND RECOMMENDATIONS

4.1	Abstract	141
4.2	Introduction	142
4.3	Research Significance	145
4.4	Analysis Procedures	146
4.4.1	PRESSS Analysis Procedure	146
4.4.2	Modified PRESSS Analysis Procedure	153
4.5	ACI T1.2-03 Analysis Procedure	161
4.6	Monolithic Beam Analogy (MBA)	162

4.7	Comparison with Experimental Results	167
4.7.1	Connection Level Validation	167
4.7.2	System Level Validation	186
4.8	Conclusions	191
4.9	Recommendations	194
4.10	References	196
4.11	Acknowledgements	198
APPENDICES		199
A.	PRESSS ANALYSIS PROCEDURE	199
B.	MODIFIED PRESSS ANALYSIS PROCEDURE	205
C.	MODIFIED PRESSS DESIGN PROCEDURE	211

LIST OF FIGURES

Figure

1.1	A view of a collapsed precast parking structure in the 1994 Northridge earthquake [1.3]	4
1.2	A partial collapse of structure due to inadequate connection details between precast floors and walls in the 1988 Armenian earthquake [1.3]	5
1.3	A summary of connection types used in precast concrete frames	7
1.4	A view of 39-story, 420-ft high, Paramount apartment building in San Francisco, California [1.15]	8
1.5	The pretensioned frame connection details used in the PRESSSS test building (Sritharan et al., [1.16])	9
1.6	The TCY-gap frame connection details used in the PRESSSS test building (Sritharan et al., [1.16])	10
1.7	The TCY frame connection details used in the PRESSSS test building (Sritharan et al., [1.16])	11
1.8	Details of a precast hybrid frame connection	13

2.1	Details of the Phase IV-B NIST hybrid frame tests conducted by Cheok et al. [2.7]	24
2.2	Force-displacement hysteresis responses observed for hybrid frames tested in Phase IV-B of the NIST test program [2.9]	26
2.3	The measured total prestressing force during testing of Specimen M-P-Z4 [2.8]	28
2.4	A view of the PRESSSS test building [2.14]	29
2.5	The floor plan of the PRESSSS test building in the lower three stories [2.13]	30
2.6	The floor plan of the PRESSSS test building in the upper two stories [2.13]	31
2.7	The 5% damped acceleration response spectra representing different intensities of ground motions (EQ-I, EQ-II and EQ-IV correspond to 33%, 50%, and 150% of the design-level earthquake, EQ-III) [2.14] .	32
2.8	Rotation of beams experienced in the hybrid frame of the PRESSSS building during the seismic test [2.14]	33
2.9	Conditions of hybrid connections at the interior column of the PRESSSS building	34
2.10	Curvature-displacement relations proposed for a cantilever beam [2.15]	36
2.11	Displacement components of a beam-column subassembly [2.15]	37

2.12	Trilinear idealization to characterize the response of a precast frame assembly connected with unbonded prestressing	38
2.13	A fiber model representation of an unbonded post-tensioned precast concrete frame [2.16]	39
2.14	A spring model representation of an unbonded post-tensioned precast concrete frame [2.16]	40
2.15	Measured and predicted responses of Specimen G-P-Z4 with unbonded prestressed connection [2.16]	41
2.16	Moment-rotation envelopes predicted by the fiber model and trilinear idealization for an unbonded post-tensioned connection [2.16]	42
2.17	The concept of the monolithic beam analogy, where $\Delta_{precast}$ is assumed to be equal to $\Delta_{monolithic}$	43
2.18	A hybrid frame when subjected to an interface rotation of θ	46
2.19	Identifying elastic and plastic strain components for the mild steel reinforcement	48
2.20	A flowchart summarizing the steps based on MBA to determine the moment-rotation behavior of a hybrid frame connection	50
2.21	A comparison of MBA analysis results with experimental data presented in Reference [2.19]	53
2.22	Various displacements and corresponding forces at interface rotation of θ at the hybrid connection [2.3]	59

2.23	A hybrid frame system at the design limit state	71
2.24	A flowchart representation of the PRESSSS guidelines for designing hybrid frame connections	77
3.1	Dimensions of the beam section used in the hybrid frame analysis ...	86
3.2	Forces acting on a precast concrete hybrid beam	92
3.3	A flowchart summarizing the analysis procedure based on the PRESSSS design guidelines	93
3.4	An assumed relationship between the over-strength factor and interface rotation for the tension mild steel reinforcement	98
3.5	The neutral axis depth as a function of interface rotation for the PRESSSS first floor connection reported by Vernu [3.3]	100
3.6	Neutral axis depth comparisons for the NIST test Specimen M-P-Z4	102
3.7	The neutral axis depth used for computing steel areas in the PRESSSS guidelines with that calculated iteratively using the guidelines for computing moment resistance and that determined using Eq. 3.21 as part of the modified PRESSSS analysis procedure at two percent interface rotation	103
3.8	The theoretical stress-strain curve for Grade 270 prestressing strands proposed by Mattock [3.11]	104
3.9	Stress profiles at the critical section caused by (a) prestressing force, (b) lateral decompression force F_{decomp} , (c) superposition of (a) and (b)	107

3.10	A flowchart summarizing the modified PRESSSS analysis procedure .	109
3.11	An idealization for the response of an equivalent monolithic beam ...	113
3.12	Deflection components at the end of a hybrid beam	114
3.13	The data points required to define the stress-strain curve given by Eq. 3.39	118
3.14	A flowchart summarizing the analysis based on the MBA concept ...	121
3.15	The post-tensioning tendon stress distribution assumed along the beam length for the NIST test units	124
3.16	Beam moment resistance as a function of interface rotation for M-P-Z4	127
3.17	Beam moment resistance as a function of interface rotation for O-P-Z4	127
3.18	Total prestressing force as a function of story drift for Specimen M-P-Z4	128
3.19	Total prestressing force as a function of story drift for Specimen O-P-Z4	129
3.20	Variables defining the dimensions of the beam and grout pad as well as the connection details for the precast hybrid frame in the PRESSSS test building	130
3.21	Stress-strain behavior of the mild steel reinforcement used in the PRESSSS hybrid frame	132
3.22	Measured response of the hybrid frame in the PRESSSS test building .	134

3.23	The neutral axis depth as a function of the interface rotation obtained at the first floor level for the hybrid frame of the PRESS building ...	135
3.24	Post-tensioning tendon elongation as a function of column drift in the PRESS test building	136
4.1	Typical hybrid frame connection details	144
4.2	A flowchart summarizing the analysis procedure based on the PRESS design guidelines	147
4.3	Forces acting on a precast concrete hybrid beam	151
4.4	A flowchart summarizing the modified PRESS analysis procedure .	154
4.5	An assumed relationship between the over-strength factor and interface rotation for the tension mild steel reinforcement	156
4.6	The neutral axis depth as a function of the interface rotation reported for the PRESS first floor hybrid connection by Vernu [4.2]	158
4.7	Comparison of neutral axis depths calculated from the PRESS guidelines [4.5] and the modified PRESS procedure for the NIST test Specimen M-P-Z4	159
4.8	A theoretical stress-strain curve proposed for Grade 270 prestressing strands by Mattock [4.12]	160
4.9	A flowchart describing the MBA analysis procedure [4.14]	163
4.10	The concept of the Monolithic Beam Analogy ($\Delta_{precast} = \Delta_{monolithic}$) ...	164
4.11	Details of the frame tests conducted in Phase VI-B by Stone et al. [4.3]	169

4.12	Lateral cyclic load sequence used for testing NIST Specimens [4.1] ..	170
4.13	Response of NIST Specimen M-P-Z4	172
4.14	Response of NIST Specimen O-P-Z4	173
4.15	Suggested trilinear idealization to improve the neutral axis depth representation in the modified PRESSSS analysis procedure	174
4.16	Comparison of the assumed interface rotations with the calculated interface rotations for Specimen M-P-Z4	176
4.17	An illustration showing displacement transducers mounted to the face of the column at first floor of the hybrid frame in the PRESSSS test building	177
4.18	The neutral axis depth variation in the hybrid frame connection at the first floor of the PRESSSS test building	178
4.19	Prestressing tendon elongation vs. column drift at the first floor of the PRESSSS test building	180
4.20	The total prestressing force as a function of column drift for Specimen M-P-Z4	181
4.21	The Total prestressing force as a function of column drift for Specimen O-P-Z4	182
4.22	Stress-strain response of the tension mild steel reinforcement used in the first floor of the PRESSSS building	183
4.23	Details of the five-story hybrid frame	187
4.24	Finite element model of the frame [4.2]	188

4.25	Comparison of hybrid connection behavior obtained by the modified PRESSS analysis procedure and analytical model using RUAUMOKO	189
4.26	Comparison of the base moment resistance of the hybrid building as a function of lateral displacement at the third floor	190
4.27	Comparison of the base shear resistance of the hybrid building as a function of lateral displacement at the third floor	191

LIST OF TABLES

Table

2.1	Description of the specimens used in Phases I, II, and III of the NIST test program [2.7]	21
2.2	Description of the precast specimens used in Phase IV of the NIST test program [2.8]	22
2.3	Key results reported for the hybrid frames tested in Phase IV-B of the NIST test program [2.8]	27
2.4	Geometric and material parameters used in the design procedure proposed by Cheek et al. [2.3]	57
2.5	Suggested strains and reinforcement over-strength factors for ASTM 706 bars [2.4]	65
3.1	Comparison of moment contributions and measured residual interface rotations (θ_{res}) after the frame is subjected to about 2% drift	122
3.2	Measured properties of Specimens M-P-Z4 and O-P-Z4	125
3.3	Parameters describing the hybrid frame in the PRESSSS test building .	131

4.1	Suggested reinforcement over-strength factors for ASTM 706 bars by Stanton and Nakaki [4.5]	149
4.2	Comparison of assumed and calculated interface rotations for Specimen M-P-Z4. (Similar comparisons were also observed for O-P-Z4)	176
4.3	Re-centering check as suggested by the PRESSSS guidelines at the design and maximum system states	184
4.4	Comparisons of the plastic hinge length and concrete compressive strain suggested by the PRESSSS guidelines with those used in the MBA analysis at the design system state	185
4.5	Hybrid connection details used for the building frame in Figure 4.23	188

LIST OF SYMBOLS

a	depth of equivalent rectangular compression stress block
a_{des}	depth of equivalent rectangular compression stress block at the design limit state
a_0	depth of equivalent rectangular compression stress block at zero drift
A_{pt}	area of prestressing tendon
A_s	area of tension or compression mild steel reinforcement in the beam
b	beam width
b_g	width of grout pad at the beam-column interface
c	neutral axis depth
ch	depth of chamfer
d	depth to tension mild steel reinforcement from the extreme compression fiber
d'	distance from compression mild steel reinforcement to the extreme compression fiber
d_b	diameter of mild steel reinforcement

d_g	depth to tension mild steel reinforcement from the extreme compression fiber in grout pad
d'_g	distance from compression mild steel reinforcement to the extreme compression fiber in grout pad
d_{pt}	diameter of prestressing tendon bundle
E_c	elastic modulus of concrete
E_p	elastic modulus of prestressing steel
E_s	elastic modulus of mild steel reinforcement
E_{sec}	secant modulus of concrete at f'_{cc}
f'_c	concrete compression strength
f'_{cc}	confined concrete strength
f'_g	interface grout strength
f_l	maximum lateral confining pressure
f'_l	effective lateral confinement pressure
f_{pi}	initial (jacking) stress in prestressing tendon, after losses
f_{pt}	stress in prestressing tendon
$f_{pt,des}$	stress in prestressing tendon at the design limit state
f_{py}	yield strength of prestressing tendon
f_{p0}	stress in prestressing tendon, after losses, at zero drift
f_{sc}	stress in compression mild steel reinforcement

$f_{sc,des}$	stress in compression mild steel reinforcement at the design limit state
f_{se}	effective stress in prestressing tendon
f_{st}	stress in tension mild steel reinforcement
$f_{st,des}$	stress in tension mild steel reinforcement at the design limit state
f_{su}	ultimate tensile strength of mild steel reinforcement
f_{sy}	yield strength of mild steel reinforcement
f_x	stress corresponds to ε_c on the strain hardening portion of mild steel stress-strain curve
F_c	resultant concrete compression force at beam-column interface
$F_{c,des}$	resultant concrete compression force at beam-column interface at the design limit state
$F_{c,0}$	resultant concrete compression force at beam-column interface at zero drift
F_{decomp}	decompression force
F_{pi}	force in tendon due to initial prestressing
F_{pt}	force in prestressing tendon
$F_{pt,des}$	force in prestressing tendon at the design limit state
$F_{pt,0}$	force in prestressing tendon at zero drift
F_{sc}	force in compression mild steel reinforcement
$F_{sc,des}$	force in compression mild steel reinforcement at the design limit state

$F_{sc,0}$	force in compression mild steel reinforcement at zero drift
F_{st}	force in tension mild steel reinforcement
$F_{st,des}$	force in tension mild steel reinforcement at the design limit state
$F_{st,0}$	force in tension mild steel reinforcement at zero drift
h	beam height
h_g	height of grout pad at the beam-column interface
I	moment of inertia of beam section based on gross section properties
k_p	plastic hinge length factor
K_e	confinement effectiveness coefficient
l	beam length
l_d	development length of debonded mild steel reinforcement
l_p	plastic hinge length
l_{pu}	unbonded length of prestressing tendon
l_{sp}	strain penetration length
l_{su}	debonded length of mild steel reinforcement at the connection interface
M	moment resistance in previous step of the iteration procedure
M_{cap}	moment capacity of connection
$M_{cap,des}$	moment capacity of connection at the design limit state
M_D	moment due to dead load
M_{decomp}	moment resistance at the decompression point

M_E	moment due to earthquake load
M_{exp}	measured peak strength
M_L	moment due to live load
M_n	nominal moment capacity
M_{pr}	probable moment capacity
M_{pred}	predicted strength
M_{pt}	resisting moment provided by prestressing tendon
$M_{pt,des}$	resisting moment provided by prestressing tendon at the design limit state
$M_{pt,0}$	resisting moment provided by prestressing tendon at zero drift
M_{sc}	resisting moment provided by compression mild steel reinforcement
$M_{sc,des}$	resisting moment provided by compression mild steel reinforcement at the design limit state
$M_{sc,0}$	resisting moment provided by compression mild steel reinforcement at zero drift
M_{st}	resisting moment provided by tension mild steel reinforcement
$M_{st,des}$	resisting moment provided by tension mild steel reinforcement at the design limit state
$M_{st,0}$	resisting moment provided by tension mild steel reinforcement at zero drift
M_y	yield moment defined using tension reinforcement of ε_{sy}

n	number of jointed beam-column connection interfaces in precast frame at a floor level
s	distance from the pin to the nearest member
V_D	shear demand at connection interface due to dead load
V_L	shear demand at connection interface due to live load
α	distance from resultant concrete compression force to the extreme compression fiber divided by h_g
α_b	coefficient quantifying growth length in debonded length of mild steel reinforcement
α_{des}	distance from resultant concrete compression force to the extreme compression fiber divided by h_g at the design limit state
β_1	ratio of equivalent stress block depth to neutral axis depth
δ_b	displacement component associated with beam flexibility
δ_c	displacement component associated with column flexibility
δ_p	displacement component associated with plastic rotation of beam
$\Delta_{elastic}$	beam end displacement due to elastic curvature
Δ'_e	beam end displacement in monolithic frame due to elastic deformation
Δ_e^*	beam end displacement in hybrid frame due to elastic curvature
Δf_{pt}	stress change in prestressing tendon between zero interface rotation and design interface rotation

$\Delta_{monolithic}$	beam end displacement of monolithic frame
$\Delta_{plastic}$	beam end displacement due to plastic curvature over the plastic hinge length
$\Delta_{precast}$	beam end displacement in the precast frame
Δ_{pt}	elongation in prestressing tendon
Δ_{sp}	elongation in mild steel reinforcement expected due to strain penetration
Δ_{st}	elongation in tension mild steel reinforcement due to interface rotation θ
Δ_{system}	ultimate displacement of a beam-column subassembly
Δ_u	total member displacement corresponding to ultimate loading
Δ_{θ}	beam end displacement of precast frame due to interface rotation θ
ε_c	compression strain in the concrete extreme fiber
ε_{cc}	strain corresponding to f'_{cc}
ε_{co}	strain corresponding to f'_c
$\varepsilon_{elastic}$	elastic strain in mild steel reinforcement
ε_i	strain in beam due to initial prestressing
ε_{pi}	axial strain in prestressing tendon due to initial prestressing
$\varepsilon_{plastic}$	plastic strain in mild steel reinforcement
ε_{pt}	strain in prestressing tendon
ε_{sc}	strain in compression mild steel reinforcement

ε_{sh}	strain in mild steel reinforcement at the onset of strain hardening
ε_{st}	strain in tension mild steel reinforcement
$\varepsilon_{st,max}$	maximum permissible strain in mild steel reinforcement under cyclic loading
ε_{su}	ultimate strain of mild steel reinforcement
ε_{sy}	yield strain of mild steel reinforcement
ε_x	arbitrary strain on strain hardening portion of the mild steel stress-strain curve
σ_i	axial stress in beam due to initial prestressing
ζ	distance from compression mild steel reinforcement to extreme compression fiber divided by h_g
η	neutral axis depth divided by h_g
η_{des}	neutral axis depth divided by h_g at the design limit state
θ	interface rotation at the precast beam-column connection
θ_{cal}	calculated interface rotation from strain
γ_{decomp}	beam end rotation at the decompression point
θ_{des}	beam-column interface rotation at the design limit state
θ_{drift}	column inter-story drift
θ_{max}	beam-column interface rotation at the maximum credible limit state
θ_p	rotation due to plastic curvature

θ_{res}	residual beam-column interface rotation
$\theta_{ultimate}$	beam-column interface rotation at the maximum credible system state
θ_y	interface rotation at beam-column connection at the first yield limit state
λ_{sc}	over-strength factor for compression mild steel reinforcement
$\lambda_{sc,des}$	over-strength factor for compression mild steel reinforcement at the design limit state
λ_{st}	over-strength factor for tension mild steel reinforcement
$\lambda_{st,des}$	over-strength factor for tension mild steel reinforcement at the design limit state
μ	coefficient of friction
ϕ	flexural strength reduction factor
ϕ_e, Φ_E	elastic curvature
ϕ_p	plastic curvature
ϕ_u, Φ_u	ultimate curvature
ϕ_y	yield curvature

CHAPTER 1

INTRODUCTION

1.1 General

Precast concrete frames have several advantages, including high quality, efficient use of materials, reduced construction time, and cost efficiency. In addition to these benefits, precast concrete allows architects and engineers to perform more innovative designs than traditional cast-in-place concrete design. Despite these benefits and unique properties of precast concrete, application of precast concrete systems has been limited in the high seismic regions of the United States [1.1]. In this chapter, benefits of precast concrete structures are discussed in detail, together with the limitations imposed by design codes and a summary of performance of precast buildings in past earthquakes. A brief discussion on non-emulative precast connections including the hybrid frame connection is also presented.

1.1.1 Benefits of Precast Concrete

Concrete is a brittle material, which exhibits high compressive strength and low tensile strength. As a result, flexural cracks develop in concrete members at the early stages of loading as tensile stresses exceed the tensile strength of concrete. By prestressing the concrete, development of undesirable flexural cracking in structures may be delayed or avoided under service conditions. Together with the precast technology, precast, prestressed concrete systems offer the following benefits over the cast-in-place concrete systems.

- **High quality:** Precast concrete products are factory made under a controlled environment, and thus they exhibit higher quality and more uniform properties than cast-in-place counterparts. Curing conditions such as temperature and humidity are typically controlled, and the dependency on craftsmanship is somewhat reduced under factory environment. Monitoring and inspection of construction are efficiently performed in precast plants, which also enhance the quality of concrete products [1.2].
- **Efficient use of materials:** In precast concrete elements, high strength concrete and steel are used which lead to smaller concrete sections. Thus, a significant reduction to the concrete volume is achieved, which in turn reduces the transportation costs. The utilization of high strength materials provides a longer life cycle for the structures [1.3].
- **Reduced construction time:** Use of prefabricated concrete members reduces the construction time of structures in comparison to the cast-in-place concrete

construction. Furthermore, the construction using precast components requires a significantly reduced amount of formwork and temporary supports in the field. Time is not wasted due to bad weather conditions or for curing of concrete. All of these factors will contribute to speedy construction of structures when using precast concrete technology [1.2].

- **Cost efficiency:** As a result of factory production and faster erection time, precast technology reduces both the construction and labor costs. Moreover, forms can be used several times for casting similar member types at precast plants, which also leads to reduction in the construction costs [1.4].

Precast concrete technology also offers the following less obvious benefits over cast-in-place concrete [1.5]:

- As a result of the high quality products, precast systems are more durable, thus reducing maintenance cost.
- The factory production enables incorporation of high quality architectural finishes.
- Fewer workers are employed at the construction site, reducing the number of work related illnesses and injuries.

1.1.2 Precast Concrete Applications in Seismic Regions

Poor performances of precast structures in past earthquakes have given designers, architects, and contractors a misconception that precast concrete is not a desirable construction technology in seismic regions. Although precast concrete has many advantages, this real-

world experience, together with the lack of approved design guidelines, has resulted in limited use of precast concrete structures in high seismic regions of the United States. In a recent study, Vernu [1.3] conducted a detailed literature survey on the performance of precast concrete buildings in past earthquakes. This author concluded that poor performance of most precast structures in past earthquakes was either due to the lack of sufficient number of lateral load resisting systems or a result of using poor connection details between precast elements that contributed to brittle structural behavior (see examples in Figures 1.1 and 1.2). This conclusion was supported by the observed damage to precast structures in several earthquakes around the world, including the 1977 Romanian Earthquake, the 1985 Mexico City Earthquake, the 1988 Armenian Earthquake, the 1994 Northridge Earthquake, and the 1995 Kobe Earthquake [1.3, 1.6].



Figure 1.1 A view of a collapsed precast parking structure in the 1994 Northridge earthquake [1.3].



Figure 1.2 A partial collapse of structure due to inadequate connection details between precast floors and walls in the 1988 Armenian earthquake [1.3].

Design codes in the United States such as UBC 1997 (*Uniform Building Code*) [1.7] and IBC 2000 (*International Building Code*) [1.8] as well as the ACI (*American Concrete Institute*) Standard [1.9] do not include adequate provisions for the design of precast structures in high seismic zones. However, they permit design of precast structures in these seismic zones through two means. The first approach requires the design of precast structures to emulate behavior of comparable monolithic concrete structures in terms of strength and toughness. The second approach permits alternative designs, but requires experimental and analytical evidence verifying satisfactory behavior of the precast systems under simulated seismic loading [1.1, 1.10, 1.11]. Ambiguous code requirements combined with the lack of

confidence introduced by poor seismic performance of precast buildings in past earthquakes have led designers to limit concrete design largely to cast-in-place systems in high seismic regions.

1.1.3 Non-Emulative Connections

The types of connections between precast concrete elements in moment-resisting frames may be classified into two main categories: emulative connections and non-emulative connections [1.12]. A classification of connections used in precast concrete frames is given in Figure 1.3, which reflects the two precast connection types permitted by the design codes. The emulation concept promotes the first recommended code approach while the non-emulative connections fall under the alternative design method for precast systems. When compared with the emulative connections, the non-emulative connections offer several advantages: (1) by concentrating flexural cracking at the precast connection interfaces, damage to the beam ends is avoided at large story drifts, (2) residual displacements are controlled by including unbonded prestressing in the connection design, and (3) principal tensile stresses due to prestressing are reduced in the beam-to-column joints, thus reducing the potential for joint damage. Researchers have also studied other suitable alternative connections for precast concrete. These connections, which are not included in Figure 1.3, are not viewed superior to the jointed non-emulative connections listed in Figure 1.3. More details about these alternative connections may be found in Reference [1.3].

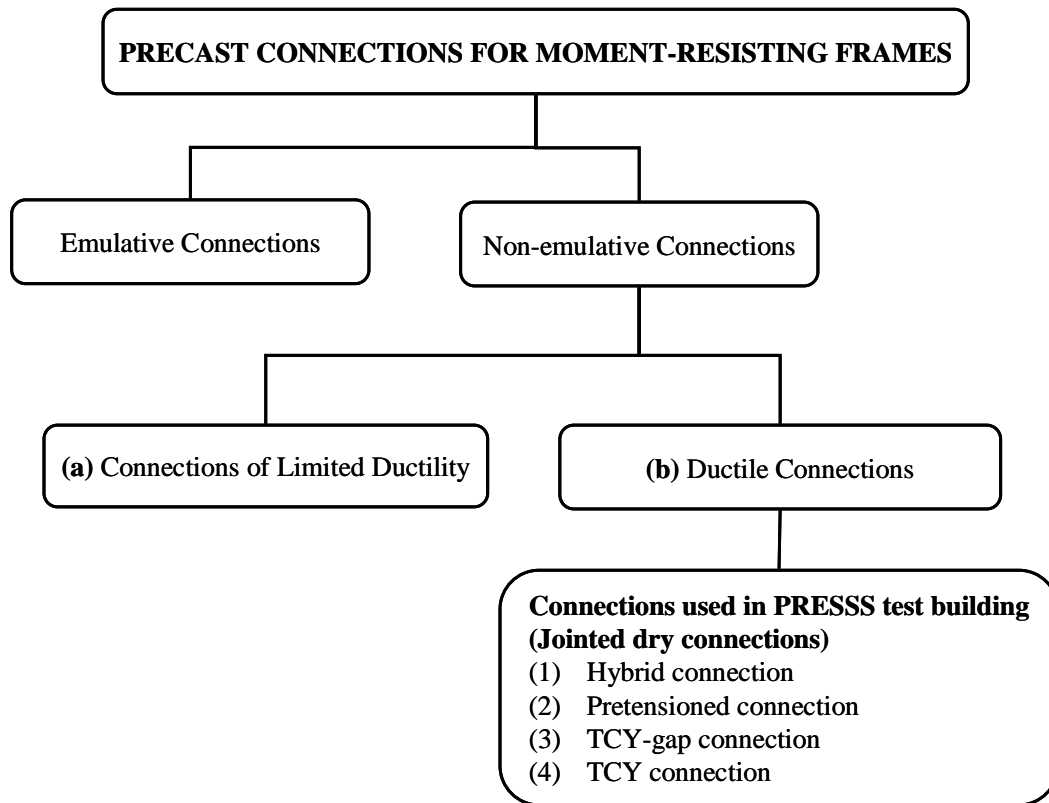


Figure 1.3 A summary of connection types used in precast concrete frames.

In non-emulative type connections, the connections are designed to be weaker than the adjoining precast members, forcing inelastic actions in the connections. The non-emulative connections may be designed as limited ductility connections or ductile connections. Welded or bolted reinforcing bars are typically used for establishing connections of limited ductility. On the other hand, mild steel reinforcement and/or unbonded prestressing are commonly used in ductile non-emulative type jointed connections. The prestressing steel is typically designed to remain elastic under design level earthquake response, providing re-centering capability for the system when the lateral load is removed [1.13]. Four types of ductile jointed connections were investigated as part of the PRESSS (*PREcast Seismic Structural*

Systems) building test [1.14], which are: hybrid, pretensioned, TCY-gap (*TCY denotes tension-compression yielding*), and TCY connections. The hybrid connection is the focus of research presented in this report. Hybrid frames, described in detail in Section 1.1.4, have been implemented in several buildings including the tallest concrete structure in Seismic Zone 4 of the United States (Figure 1.4).



Figure 1.4 A view of 39-story, 420-ft high, Paramount apartment building in San Francisco, California [1.15].

The pretensioned connection uses single-story high precast columns and continuous multi-bay pretensioned beams (Figure 1.5). The continuous beams are threaded over column reinforcing bars extending from the top of the precast columns. In addition to grouting them in the beams, the column longitudinal bars extended through the beams are spliced in the bottom region of the columns placed on the top of the beams. The beams have pretensioned strands, which are typically bonded in the external stubs of the beams, but debonded over the beam lengths between column faces. By designing the beam to column connections stronger than the beam end moment resistance at the column faces, inelastic actions are developed at the beam ends, providing nonlinear elastic response for the system with very low energy dissipation [1.16].

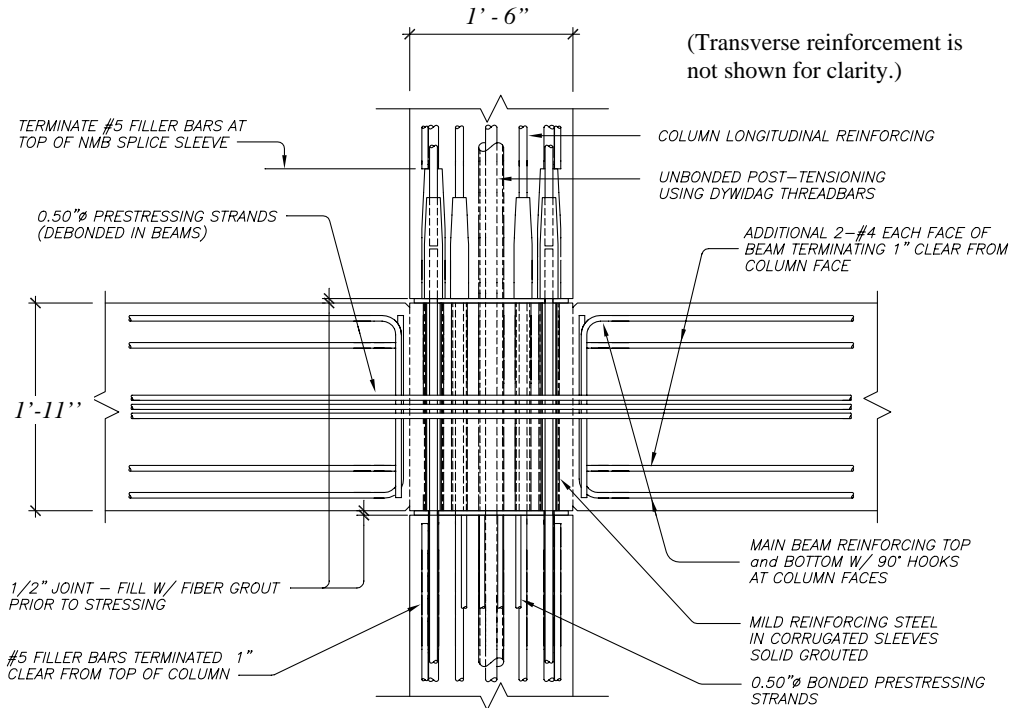


Figure 1.5 The pretensioned frame connection details used in the PRESSS test building (Sritharan et al., [1.16]).

In the TCY-gap connection, a small gap is left between the column and beam, except in the bottom region of the beam where a full contact between the precast members is ensured through a grout pad as shown in Figure 1.6. This gap is designed to avoid frame elongation despite the inelastic actions in the connections. Unbonded post-tensioning bars are placed at the bottom of the beam while mild steel reinforcing bars are placed at the top of the beam to provide moment resistance at the beam-to-column interface. The gap prevents damage to the beam ends and assures that the compression and tension force transfer at the top of the beam occurs only through the mild steel reinforcement. Although no elongation is expected with this type of connection, some residual displacements and hysteretic damping are expected for the frames due to the inelastic actions expected in the mild steel reinforcement [1.16].

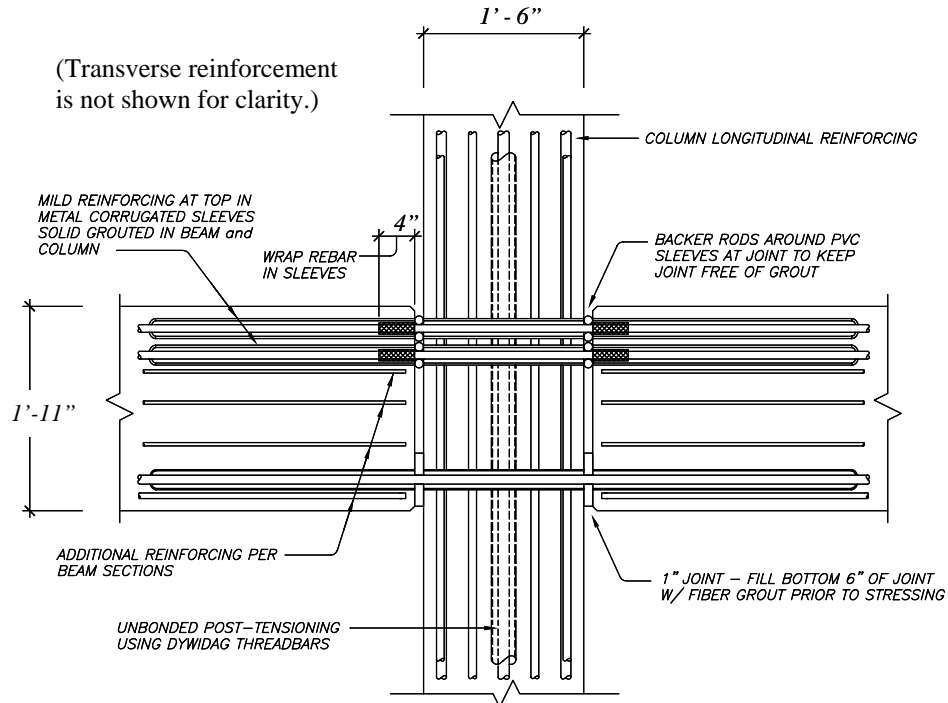


Figure 1.6 The TCY-gap frame connection details used in the PRESSS test building (Sritharan et al., [1.16]).

Another non-emulative frame connection used in the PRESSS test building was the TCY connection. The TCY frame connection closely emulates the cast-in-place concrete frame connection using the jointed concept by utilizing mild steel reinforcing bars at the top and bottom of the beams as illustrated in Figure 1.7. As with the hybrid connection and TCY-gap connection, the mild steel reinforcement is debonded over a small distance in order to reduce the accumulation of inelastic strains in the critical region. In comparison to the TCY-gap connection, significantly high energy dissipation and residual displacements are expected for frames with the TCY connection [1.16].

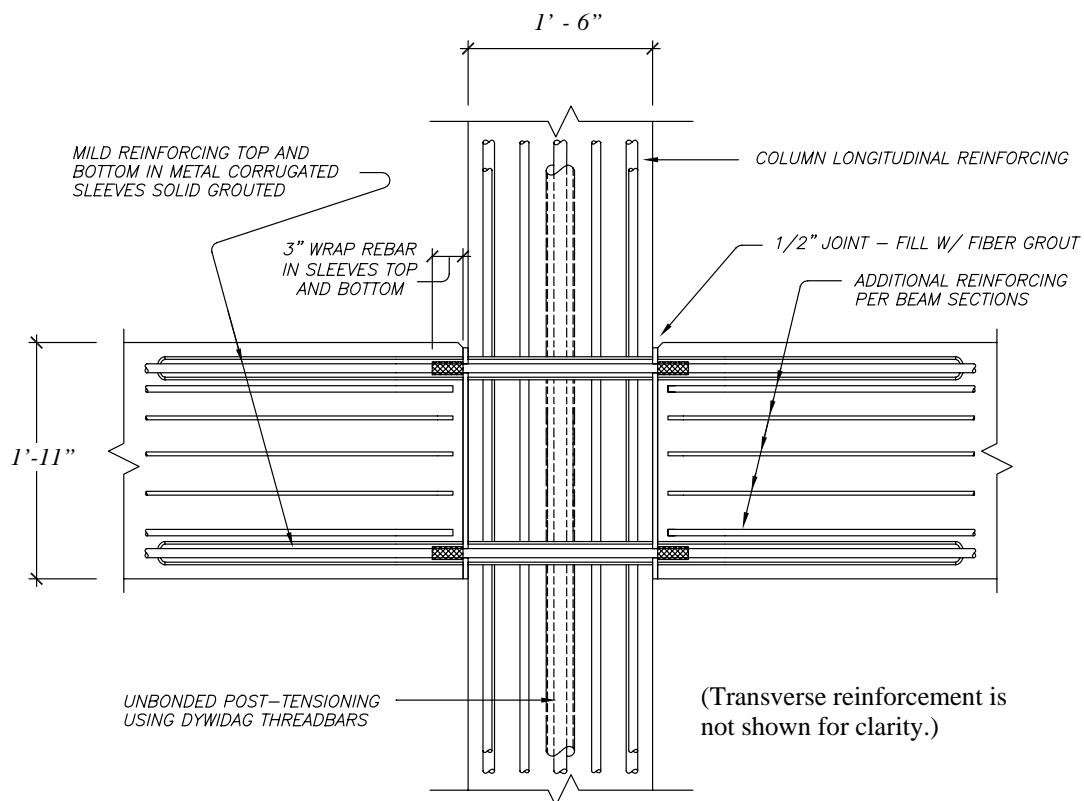


Figure 1.7 The TCY frame connection details used in the PRESSS test building (Sritharan et al., [1.16]).

1.1.4 Hybrid Connection

Precast single bay beams are typically connected to multi-story high precast columns to form hybrid frame systems with connections between the precast elements relying on unbonded prestressing and mild steel reinforcement. Unbonded post-tensioning steel is located at the mid-height and the mild steel reinforcing bars are located at the top and bottom of the beam section as shown in Figure 1.8. Prior to applying the prestressing force, the gap between the column face and the beam end is filled with fiber reinforced grout to ensure continuity between the precast members. The post-tensioning steel is designed to remain elastic when the hybrid frame is subjected to design level earthquakes, which is one reason why the post-tensioning steel is located at the mid-height of the beam. It is noted that yielding of the post-tensioning steel will reduce the initial prestressing force and elastic stiffness, which can lead to strength degradation. When subjected to reverse cyclic loading, mild steel reinforcing bars, located at the top and bottom of the beam, are expected to provide energy dissipation by yielding of tension and compression in the beam end regions. The mild steel bars are debonded over a short length on either side of the column to avoid premature fracture resulting from low cycle fatigue at small to medium drifts. A friction mechanism is relied upon for shear transfer from the beam to the column in the hybrid and other jointed connections that utilize prestressing.

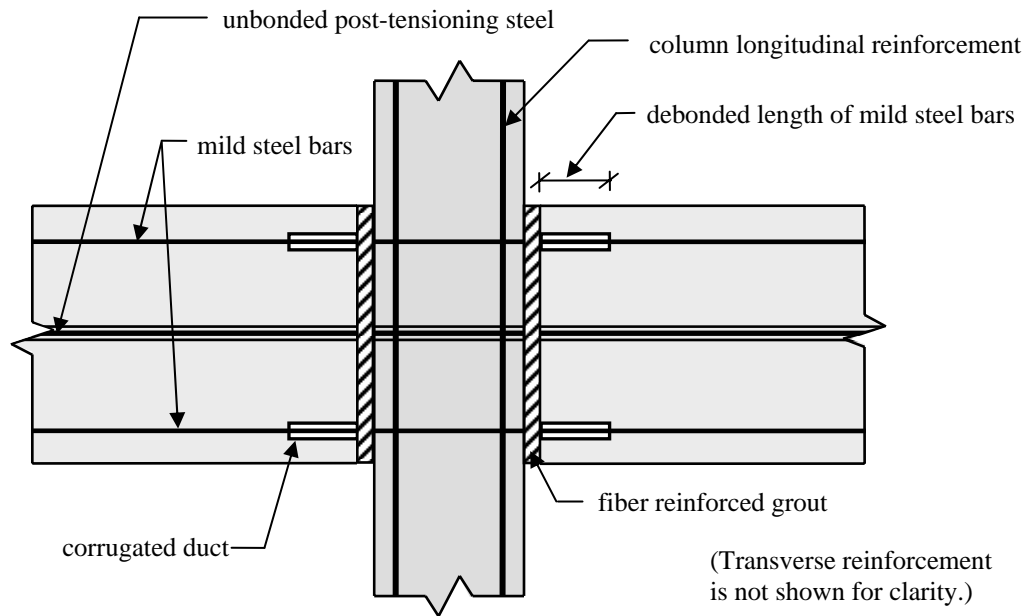


Figure 1.8 Details of a precast hybrid frame connection.

As a result of the elastic behavior, the post-tensioning steel provides a restoring force for the hybrid frame even when the mild steel reinforcement develops inelastic strains due to an earthquake loading. This restoring force helps to minimize the residual displacements of the frame when the lateral load is removed. This re-centering potential of the hybrid frame systems depends on the amounts of post-tensioning steel and mild steel reinforcement, debonded length of the mild steel reinforcement, and the initial prestressing force [1.3].

1.2 Scope of Study

The hybrid frame concept has been developed over the past decade, starting with the component tests at the *National Institute of Standards and Technology* (NIST, [1.1]) through to the system level test in the PRESSSS test building [1.14, 1.16]. At various stages of this development, guidelines for designing hybrid frame systems have been published [1.17, 1.18, 1.19]. Unlike the monolithic frame connections, a section level analysis cannot be easily performed at the hybrid connection because of the strain incompatibility resulting from the use of unbonded prestressing and mild steel reinforcement. Consequently, the published guidelines have ignored the concrete confinement effects and used the equivalent stress block concept to determine the neutral axis depth in the design calculations. Furthermore, the stresses in the tension and compression mild steel reinforcing bars are approximated to predetermined values. These approximations help to overcome the strain incompatibility issue introduced by the debonded steel at the critical section.

Using the experimental results from two NIST tests and the PRESSSS building test, the aim of the study presented in this report is to validate the design guidelines of hybrid frame connections proposed by (1) Stanton and Nakaki [1.18] as part of the PRESSSS program and (2) ACI Innovation Task Group in the ACI T1.2-03 document [1.19]. By establishing analysis methods based on the proposed design steps and assumptions, the accuracy of the guidelines are examined by comparing the analysis results with experimental data.

Also investigated as part of the study is the accuracy of the *Monolithic Beam Analogy* (MBA) concept in predicting the response of the hybrid frame connections. Based on the comparison between experimental data and the different analysis results, recommendations to improve the design of the hybrid frame connections are made.

1.3 Report Layout

The research outlined in the previous section is presented in four chapters including the introduction to the non-emulative precast connections and the hybrid frame in this chapter. A summary of literature on hybrid frame systems is given in Chapter 2, which focuses on three areas of research: experimental studies, analytical studies, and design methods. Analysis methods for hybrid connections based on the PRESSS guidelines [1.18], ACI T1.2-03 document [1.19], and MBA [1.3] are presented in Chapter 3 together with a modified PRESSS analysis procedure and a summary of the experimental studies that are used in the validation process. The validation of the design guidelines is presented in Chapter 4 by comparing the results from the various analysis procedures with the experimental data. Since a paper format is followed for this chapter, a summary of materials presented in the previous chapters, conclusions drawn from the study, and recommendations to improve the design of the hybrid frame connections are also included in Chapter 4. Various Mathcad programs developed as part of the study are presented in Appendices A – C.

1.4 References

- [1.1] Stone, W. C., Cheok, G. S., and Stanton, J. F., “Performance of Hybrid Moment-Resisting Precast Beam-Column Concrete Connections Subjected to Cyclic Loading,” *ACI Structural Journal*, Vol. 92, No. 2, 1995, pp. 229-249.
- [1.2] Park, R., “A Perspective on the Seismic Design of Precast Concrete Structures in New Zealand,” *PCI Journal*, Vol. 40, No. 3, 1995, pp. 40-59.
- [1.3] Vernu, S., “Connection and structural level analysis of precast hybrid frame systems,” *Master Thesis, Iowa State University, Ames, Iowa, 2003.*
- [1.4] Priestley, M. J. N., “Overview of PRESSS Research Program,” *PCI Journal*, Vol. 36, No. 4, 1991, pp. 50-57.
- [1.5] Seismic Design of the International Federation for Structural Concrete (*fib*), “State-of-the-Art Report on The Seismic Design of Precast Concrete Building Structures,” *Draft Report of Task Group 7.3 of Commission 7, (In Press).*
- [1.6] Fintel, M., “Performance of Buildings With Shear Walls in Earthquakes of the Last Thirty Years,” *PCI Journal*, Vol. 40, No. 3, 1995, pp. 62-80.
- [1.7] International Conference of Building Officials, *Uniform Building Code*, Whittier, CA, 1977.
- [1.8] International Code Council, *International Building Code*, Virginia, 2000.
- [1.9] American Concrete Institute, *Building Code Requirements for Structural Concrete (ACI 318-02) and Commentary (ACI 318R-02)*, Michigan, 2002.

- [1.10] Cleland, N. M., Gosh, S. K., “Untopped Precast Concrete Diaphragms in High Seismic Applications,” *PCI Journal*, November-December, 2002, pp. 94-99.
- [1.11] Gosh, S. K., “Seismic Design Provisions in U.S. Codes and Standards: A Look Back and Ahead,” *PCI Journal*, Vol. 47, No. 1, 2002, pp. 94-99.
- [1.12] Park, R., “The fib state-of-the-art report on the seismic design of precast concrete building structures,” *In Proceeding of the 2003 Pacific Conference on Earthquake Engineering*, Paper No. 011, 2003.
- [1.13] Sritharan, S., Vernu, S., “Analysis and Design of Precast Hybrid Frames,” *In Proceeding of the 2003 Pacific Conference on Earthquake Engineering*, Paper No. 024, 2003.
- [1.14] Priestley, M. J. N., Sritharan, S., Conley, J. R., Pampanin, S., “Preliminary Results and Conclusions From the PRESSS Five-Story Precast Concrete Test Building,” *PCI Journal*, Vol. 44, No. 6, 1999, pp. 42-67.
- [1.15] Englekirk, R. E., “Design-Construction of The Paramount – A 39-Story Precast Concrete Apartment Building,” *PCI Journal*, July-August, 2002, pp. 56-69.
- [1.16] Sritharan, S., Pampanin, S., Conley, J. R., “Design Verification, Instrumentation, & Test Procedures,” *PRESSS-3: The Five-Story Precast Test Building*, Vol. 3-3, Iowa State University, ISU-ERI-Ames Report ERI-03325, 2002.
- [1.17] Cheok, G. S., Stone, W. C., Nakaki, S. D., “Simplified Design Procedure for Hybrid Precast Concrete Connections,” National Institute of Standards and Technology, *SCTR 5765*, 1996.

- [1.18] Stanton, J. F. and Nakaki, S. D., “Design Guidelines For Precast Concrete Seismic Structural Systems,” *PRESSS Report No. 01/03-09, UW Report No. SM 02-02*, The University of Washington and The Nakaki Bashaw Group, Inc., 2002.
- [1.19] ACI Innovative Task Group 1 and Collaborators, *Special Hybrid Moment Frames Composed of Discretely Jointed Precast and Post-Tensioned Concrete Members (ACI T1.2-03) and Commentary (T1.2R-03)*, Michigan, 2003.

CHAPTER 2

LITERATURE REVIEW

2.1 Introduction

In this chapter, an overview of past research on non-emulative precast frame connections that utilized both prestressing steel and mild steel reinforcing bars is given. The literature review, which primarily focuses on the hybrid frame connections, is divided into three parts: experimental studies, analytical studies, and design methods. In the section on experimental studies, a four-phase experimental investigation conducted at NIST and the five-story precast concrete building test performed in the final phase of the PRESSSS research program are summarized. In the section on analytical studies, several methods proposed for analyzing precast frames with ductile jointed connections are discussed. The monolithic beam analogy (MBA) method proposed by Pampanin et al. [2.1] and further investigated by Vernu [2.2] are also described in detail. Finally, the section on design methods, guidelines proposed for designing hybrid frame connections by NIST researchers [2.3], Stanton and Nakaki [2.4], and the ACI Innovative Task Group [2.5] are presented.

2.2 Experimental Studies

2.2.1 NIST Tests

An extensive series of experiments were performed at NIST to investigate the behavior of precast concrete beam-to-column connections under reversed cycling loading. Four phases of tests using several one-third-scale beam-to-column subassemblages were conducted from 1991 through to 1995 by a group of researchers [2.6, 2.7, 2.8, 2.9]. The connection details were gradually improved from one series to the next series of tests, eventually leading to the development of the hybrid frame concept. The primary outcome of this research program was the establishment of the first set of guidelines for designing hybrid frame connections suitable for high seismic regions.

The first three phases of the experiments, conducted from 1991 to 1993, concentrated on precast, prestressed frame connections made from bonded prestressing steel, both alone and in combination with some mild steel reinforcement. The specimens tested during Phases I, II and III are summarized in Table 2.1, which were labeled by three alphabets followed by a numeral. The middle alphabet is either M or P corresponding to monolithic or precast concrete, and the last two letters are either Z2 or Z4 representing seismic zones 2 and 4, respectively. For example, A-M-Z2 means monolithic type A designed for seismic zone 2.

The viability of using only post-tensioning steel in precast connections was tested in Phase I. Although these connections were as strong and as ductile as comparable monolithic

connections, their energy dissipation capabilities were reported to be unsatisfactory for high seismic regions. To improve this deficiency, six precast concrete frame specimens in Phase II and two specimens in Phase III were designed and tested, exploring different ways of incorporating energy dissipation in precast frame systems.

Table 2.1 Description of the specimens used in Phases I, II, and III of the NIST test program [2.7].

Test phase	Specimens	Seismic zone	Type	Post-tensioning steel	
				Type	Bond condition
I	A-M-Z2 & B-M-Z2	2	Monolithic	–	–
I	A-M-Z4 & B-M-Z4	4	Monolithic	–	–
I	A-P-Z4 & B-P-Z4	4	Precast	Bar	Fully grouted
II	A-P-Z2 & B-P-Z2	2	Precast	Strand	Fully grouted
II	C-P-Z4 & D-P-Z4	4	Precast	Bar	Fully grouted
II	E-P-Z4 & F-P-Z4	4	Precast	Strand	Fully grouted
III	G-P-Z4 & H-P-Z4	4	Precast	Strand	Partially grouted

In addition to changing the location of the bonded post-tensioning steel, the use of prestressing strands instead of prestressing bars was investigated as a measure of increasing the energy dissipation of the frames in Phase II. It was observed that the use of prestressing strands located close to the beam centroid led to an increase in the energy dissipation characteristics of the frames. However, inelastic strains were developed in the prestressing steel upon unloading after the hybrid frame was subjected to high column drifts. As a result, the prestressing force at the critical section was reduced significantly, causing strength

degradation. To alleviate the strength degradation problem, partially unbonded prestressing strands were used in the Phase III specimens; the benefits of using unbonded prestressing in frames have been discussed by Priestley and Tao [2.10]. However, more crushing of the beam end regions and less energy dissipation were observed for Phase III specimens than for the Phase II specimens with fully bonded strands. The results of tests conducted in Phases I, II, and III are reported in detail by Cheok and Lew [2.6, 2.7]. Based on these results, the concept for the hybrid frame connection was developed and tested in Phase IV from 1993 to 1994. A summary of Phase IV specimens are given in Table 2.2.

Table 2.2 Description of the precast specimens used in Phase IV of the NIST test program [2.8].

Test phase	Specimens	Post-tensioning steel		Mild steel	
		Type	Bond condition	Type	Bond condition
IV-A	I-P-Z4 & K-P-Z4	Strand	Fully grouted	Grade 60 steel	Fully grouted
IV-A	J-P-Z4	Bar	Unbonded	Grade 60 steel	Fully grouted
IV-A	L-P-Z4A	Strand	Unbonded	Grade 60 steel	–
IV-A	L-P-Z4B	Bar	Unbonded	Grade 60 steel	–
IV-A	L-P-Z4C	Strand	Unbonded	Grade 60 steel	Unbonded
IV-B	M-P-Z4	Strand	Partially grouted	Grade 60 steel	Partially grouted
IV-B	N-P-Z4	Strand	Partially grouted	304 Stainless steel	Partially grouted
IV-B	O-P-Z4	Strand	Partially grouted	Grade 60 steel	Partially grouted
IV-B	P-P-Z4	Strand	Partially grouted	304 Stainless steel	Fully grouted

The Phase IV experiments were conducted in two sub-phases, namely A and B. In Phase IV-A, six frame tests were conducted with the main variables being the location, type, bond condition, and the amounts of the post-tensioning steel and mild steel reinforcement.

The conclusions of the Phase IV-A tests are:

- The combined use of post-tensioning steel and mild steel reinforcement provided a desirable frame connection between precast beams and columns. The mild steel reinforcement contributed to energy dissipation while the post-tensioning steel provided the restoring force during the seismic response and assisted with the transfer of shear forces at the precast connection.
- Instead of prestressing bars, prestressing strands should be used for the post-tensioning because strands have a high yield strain limit and can remain elastic when they experience large elongations.
- Unbonded post-tensioning strands located at the mid-height of the beam section were found to be the best prestressing detail.
- Debonding the mild steel reinforcement over a short distance on either side of the column was considered appropriate to avoid premature bar fracture.

A total of four one-third-scale hybrid frame systems, designated as M-P-Z4, N-P-Z4, O-P-Z4, and P-P-Z4, were tested in Phase IV-B. The basic details of the specimens are shown in Figure 2.1; the amount and type of passive steel reinforcement were varied between the specimens. Three, Grade 270, 1/2-inch diameter unbonded prestressing tendons were used at the mid-height of the beam section in all specimens. The frame connection in Specimens O-P-Z4 and M-P-Z4 included two No. 3 and three No. 3 Grade 60 mild steel

reinforcing bars at the top and bottom of the beam section, respectively. Two 0.36-inch and three 0.36-inch diameter, 304 stainless steel bars were used instead of the Grade 60 steel in Specimens N-P-Z4 and P-P-Z4, respectively. The mild steel reinforcing bars were debonded in the beam over one-inch distance from each face of the column as recommended from Phase IV-A observations. However, stainless steel reinforcement in Specimen P-P-Z4 was fully bonded due to the observed bond failure in Specimen N-P-Z4 in which the stainless steel bars were debonded over a distance of one-inch.

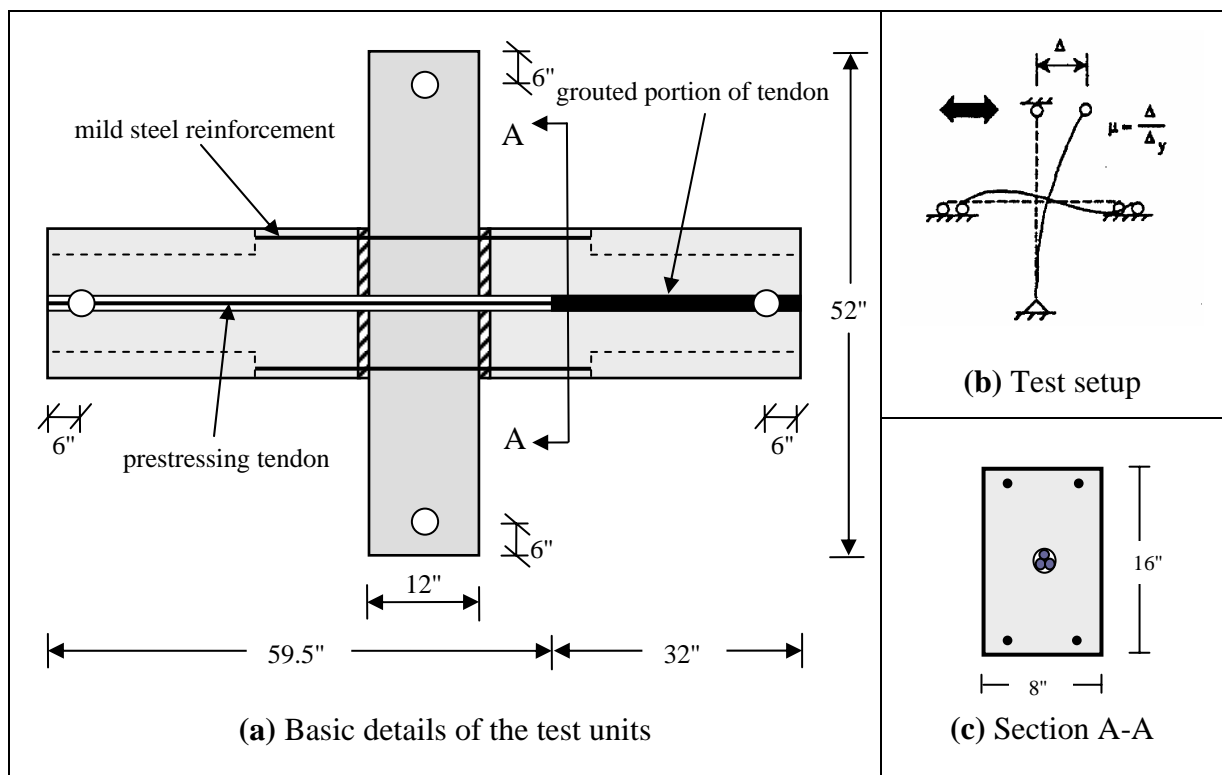


Figure 2.1 Details of the Phase IV-B NIST hybrid frame tests conducted by Cheek et al. [2.7].

The force-displacement hysteresis responses of the Phase IV-B test units observed under cyclic loading are shown in the Figure 2.2, with a summary of key results in Table 2.3. An observation, which was made at small drifts as well as at large drifts of up to 3.0–3.5 percent, was that flexural cracks were generally concentrated at the member ends. Also observed in some specimens was that they exhibited small or no residual displacements upon removal of the lateral seismic load. These unique observations were a consequence of the presence of a significant amount of restoring force in the frame provided by the unbonded prestressing.

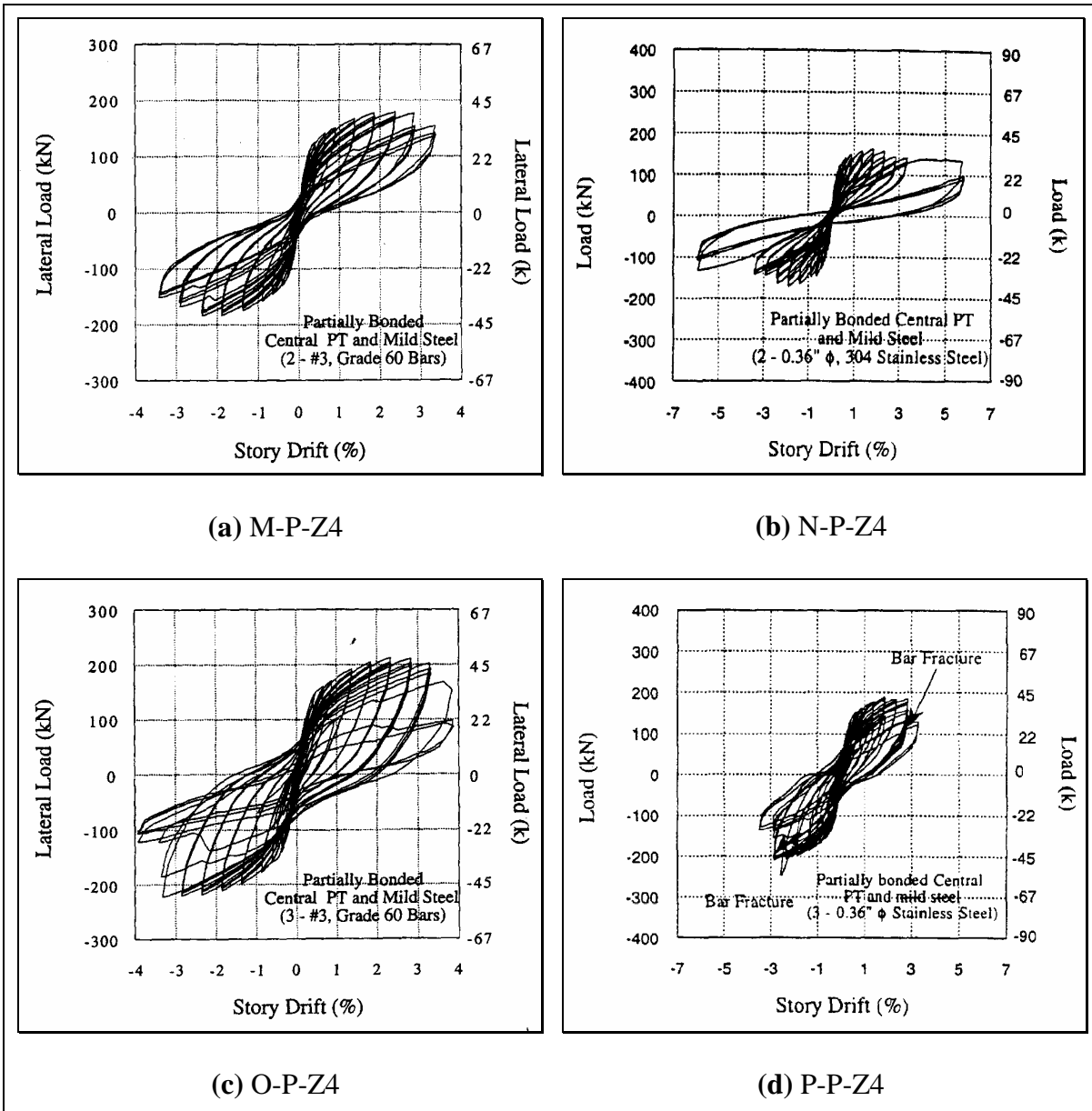


Figure 2.2 Force-displacement hysteresis responses observed for hybrid frames tested in Phase IV-B of the NIST test program [2.9].

Table 2.3 Key results reported for the hybrid frames tested in Phase IV-B of the NIST test program [2.8].

Specimen	Failure drift (percent)	Peak load drift (percent)	M_{exp} (kip-in)	M_{pred} (kip-in)	Number of cycles	Failure mode
M-P-Z4	3.4	3.4	1054	966	42	Bar fracture
N-P-Z4	2.9	5.9	1028	1028	38	Debonding
O-P-Z4	3.4	3.9	1231	1116	43	Bar fracture
P-P-Z4	2.9	3.4	1134	1098	57	Bar fracture

M_{exp} = measured peak strength, M_{pred} = predicted strength

By comparing the response of the hybrid frames with several equivalent conventional cast-in-place frame tests reported by Stone et al. [2.8] and Stanton et al. [2.9], the following conclusions were drawn:

- The specimens with hybrid connections investigated in Phase IV-B exhibited either equal or better performance than the cast-in-place concrete frames.
- The post-tensioning steel in hybrid frames remained elastic during the tests and thus it did not contribute to strength degradation of the specimens. As illustrated by Figure 2.3, the initial prestressing force applied to the test unit was generally maintained when the lateral displacement was brought back to zero. Failure of the specimens resulted due to fracture of the passive steel reinforcement at the top and/or bottom of the beam, except in N-P-Z4 in which debonding of these bars caused strength degradation (see Table 2.3).
- Hybrid frame systems were capable of withstanding very large drifts (e.g., ± 6 percent) while maintaining more than 55 percent of the lateral strength.

- Up to 1.5 percent drift, the hybrid frame dissipated more hysteretic energy than the conventional concrete frames. Beyond this drift, the energy dissipation capacity of the hybrid frames gradually dropped to 75 percent of equivalent monolithic concrete frames.
- Unlike the monolithic concrete frames, the level of damage in hybrid frames was negligible and no visible cracks in precast members were observed upon removal of the lateral load from the specimens.

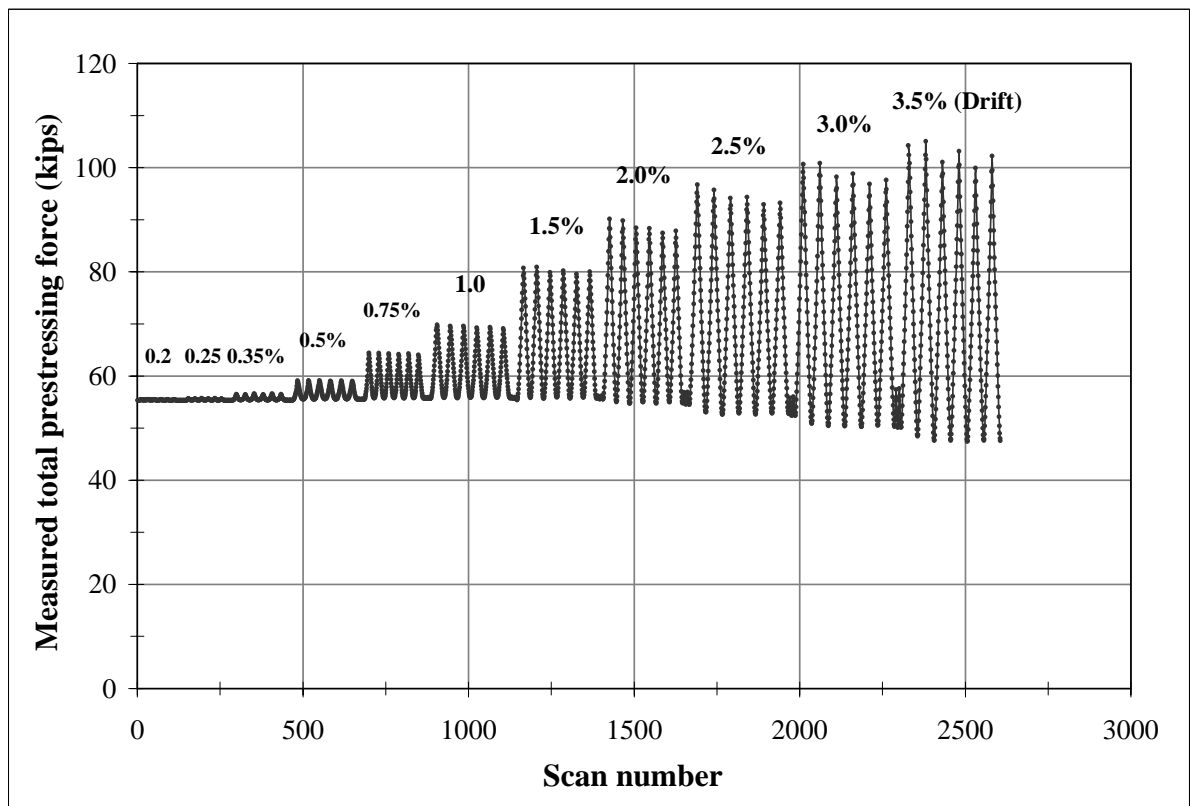


Figure 2.3 The measured total prestressing force during testing of Specimen M-P-Z4 [2.8].

2.2.2 The PRESSS Research Program [2.11, 2.12, 2.13, 2.14]

The primary objectives of the PRESSS program were (1) to develop new materials, concepts, and technologies for precast concrete construction in different seismic zones, and (2) to develop comprehensive and rational design recommendations needed for a broader acceptance of precast concrete construction in different seismic zones. In Phase III of the PRESSS research program, a five-story, 60 percent scale precast concrete test building consisted of jointed connections, (Figure 2.4) was designed and tested under simulated seismic loading at the University of California, San Diego (UCSD).



Figure 2.4 A view of the PRESSS test building [2.14].

With 2 bays by 2 bays in plan view, the test building utilized two seismic frames with four different types of jointed moment resisting frames in one direction and a jointed structural wall system in the orthogonal direction. As detailed in Figures 2.5 and 2.6, the hybrid and TCY-gap connections were used in the lower three stories of the two seismic frames, while pretensioned and TCY connections were adopted in the upper two stories.

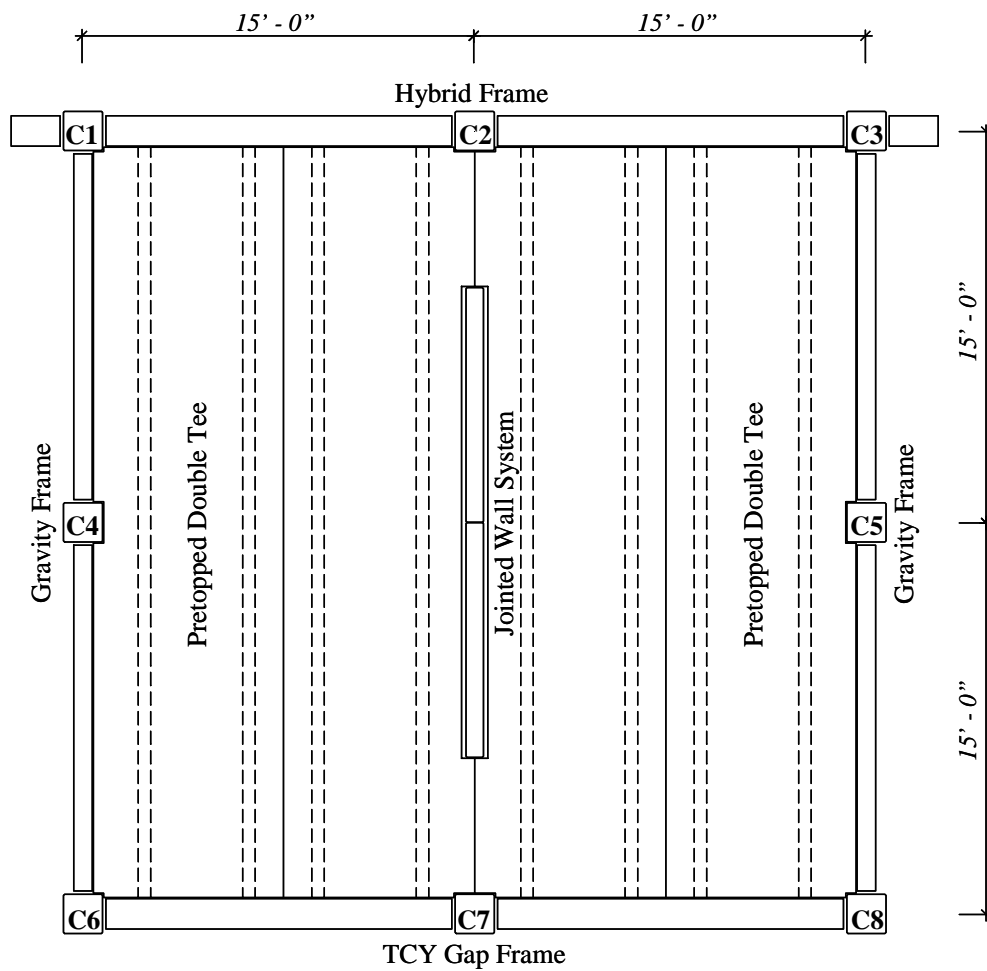


Figure 2.5 The floor plan of the PRESSS test building in the lower three stories [2.13].

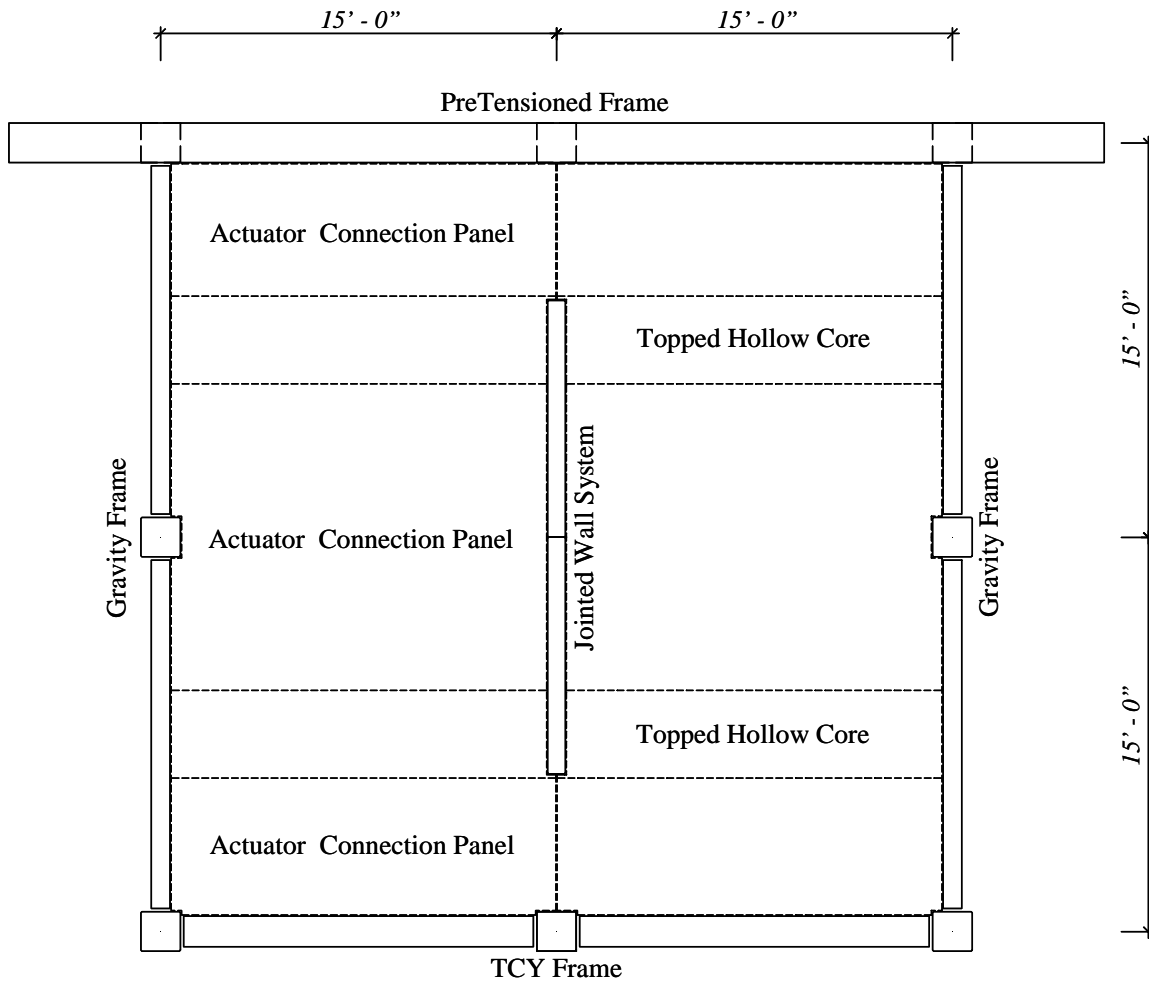


Figure 2.6 The floor plan of the PRESSS test building in the upper two stories [2.13].

The design of the test building was mainly based on the precast connection concepts established in the previous two phases of the PRESSS program, and the development of the hybrid frame system in the NIST research program. The test building was subjected to a series of simulated seismic loading, including pseudo-dynamic tests with input motions matching different earthquake spectra shown in Figure 2.7. Through simulated testing, the PRESSS researchers aimed to demonstrate the applicability of precast concrete structures with jointed connections in regions of high seismicity.

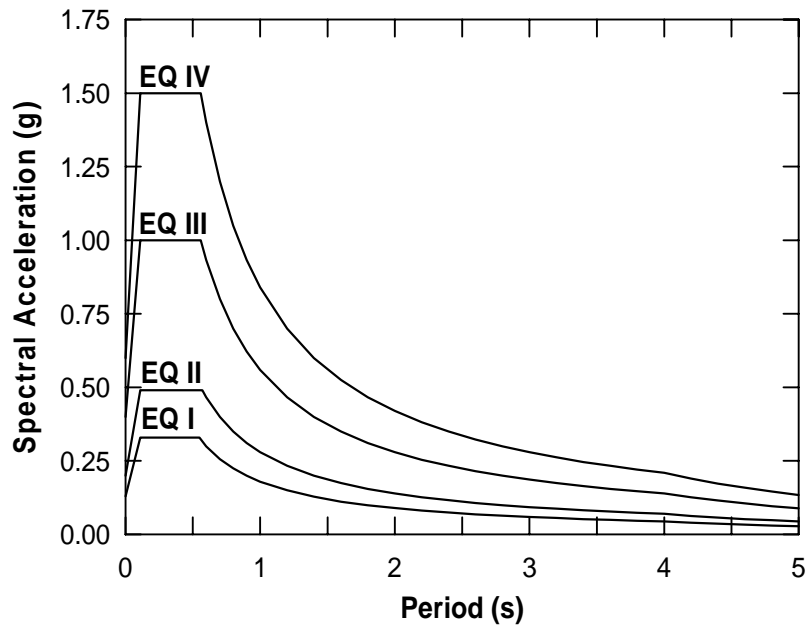


Figure 2.7 The 5% damped acceleration response spectra representing different intensities of ground motions (EQ-I, EQ-II and EQ-IV correspond to 33%, 50%, and 150% of the design-level earthquake, EQ-III) [2.14].

Based on the test observations from the PRESSS building, Priestley et al. [2.14] concluded that (1) the structural response of the frame systems under different levels of seismic actions was satisfactory, (2) the damage to seismic frames was noticeably less than that expected in equivalent monolithic reinforced concrete frames, and (3) the performance of the hybrid frame was extremely good up to an interstory drift of about 4 percent with damage limited to minor spalling of cover concrete. Test observations reported on the behavior of hybrid frame may be summarized as follows:

- During testing to 33 and 50 percent design-level earthquakes, low levels of damage were observed in the beam-to-column connections, as expected.

- At the design-level earthquake, the beams of the hybrid frames rotated inward about the longitudinal axis as shown in Figure 2.8. This torsional rotation was a result of transferring the weight of the double-tee floor to the end of the beam. Further rotations of the beams in the remainder of the test was prevented by welding the steel angles located at the bottom end of the webs in the double-tees to the steel angles attached to the inside face of the beams. This detail consisted of steel angles was used to transfer vertical loads from the floor to the beams in seismic frames.

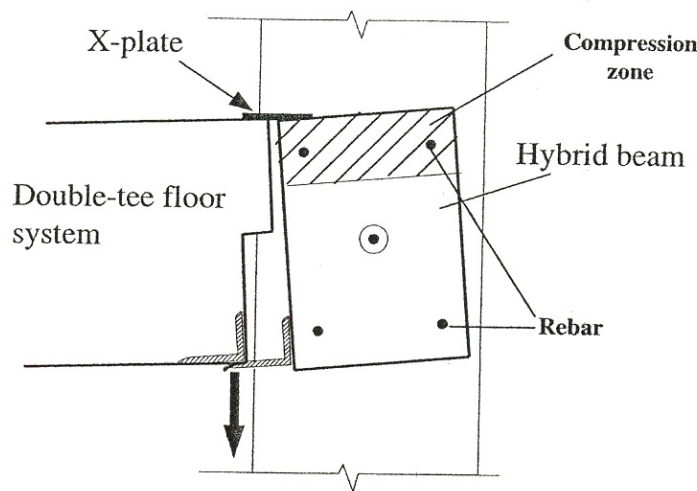


Figure 2.8 Rotation of beams experienced in the hybrid frame of the PRESSS building during the seismic test [2.14].

- Under the design-level seismic action, the hybrid frame displayed negligible damage except the torsional rotation noted above (see Figure 2.9a). There was no significant cracking in the beam-to-column joints, with the largest crack opening limited to 0.005 inches.

- Figure 2.9b shows the condition of a hybrid connection subjected to drift levels of more than twice the design drift of 2% , which appears to be extremely good. Only minor damage to the beam cover concrete, and some crushing of the fiber grout pads placed between the precast beams and column were noted. The width of shear cracks in the beam-to-column joints at large drifts did not significantly increase beyond that cracks observed for the design-level seismic testing.

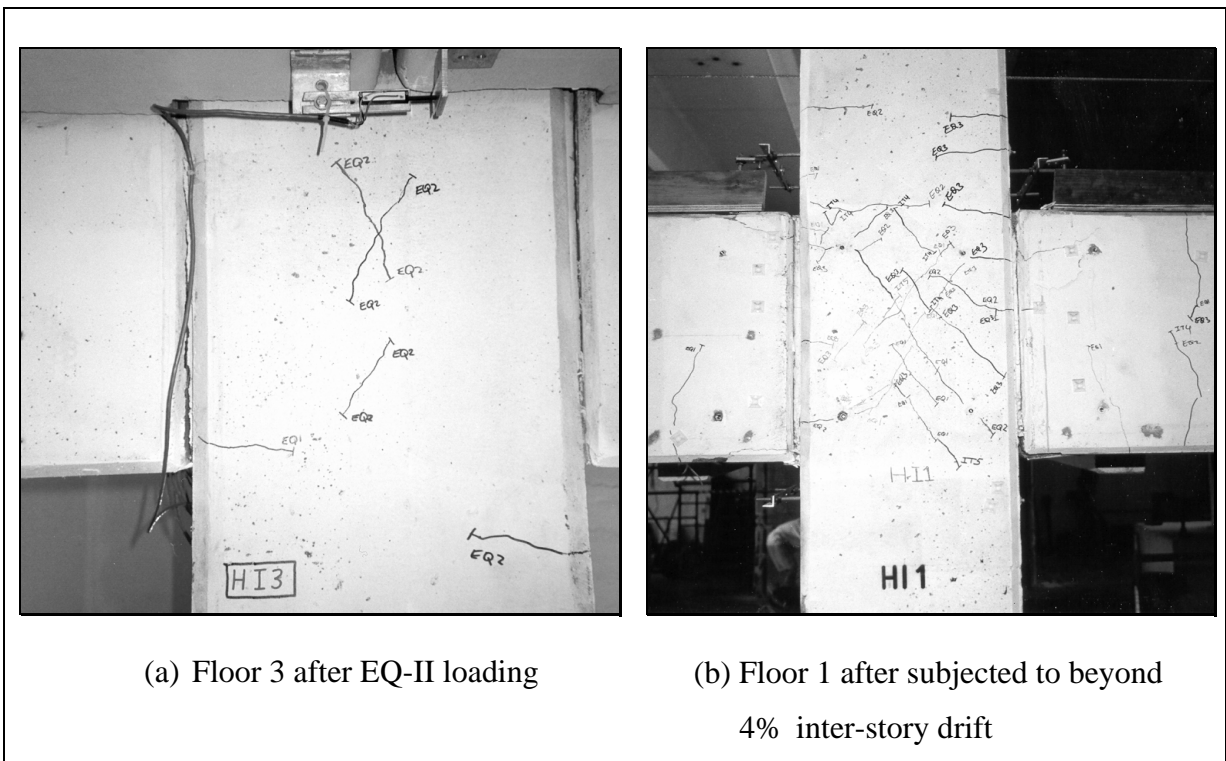


Figure 2.9 Conditions of hybrid connections at the interior column of the PRESS building.

2.3 Analytical Studies

2.3.1 Englekirk (1989)

Englekirk [2.15] proposed an analytical procedure to investigate the behavior of ductile frames constructed with precast concrete. In this procedure, the component ductility and system ductility concepts were introduced to rapidly assess the suitability of different assembly procedures for ductile precast frames and to compare their responses with similar cast-in-place concrete frames.

In the component ductility concept (see Figure 2.10), the total member displacement corresponding to the ultimate loading (Δ_u) is calculated from the elastic and plastic curvature components using:

$$\Delta_u = \Phi_u \cdot l_p \cdot \left(l - \frac{l_p}{2} \right) + \Phi_E \cdot \frac{l^2}{3} \quad (2.1)$$

where Φ_u is the plastic curvature, Φ_E is the elastic curvature, l_p is the plastic hinge length, and l is the beam length as defined in Figure 2.10.

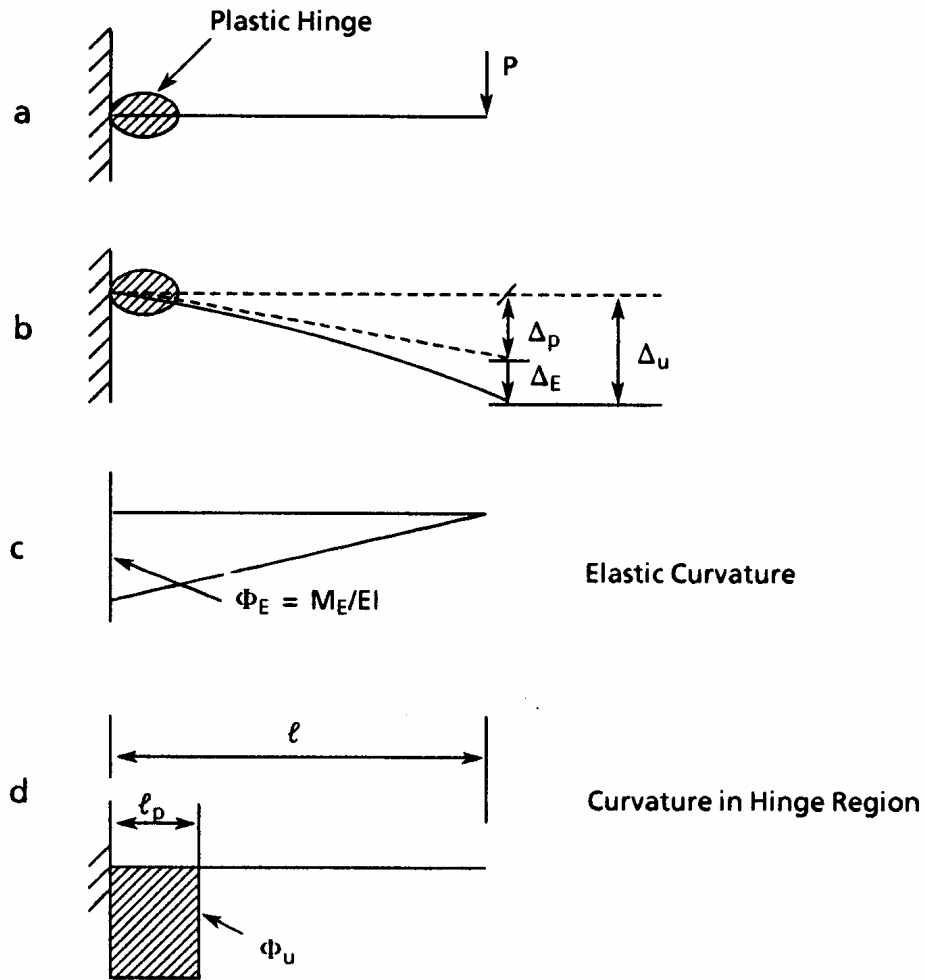


Figure 2.10 Curvature-displacement relations proposed for a cantilever beam [2.15].

Relying on the displacements defined at the component level at the ultimate limit state, the system ductility concept identifies three components for a beam-column subassembly. These components include displacements due to the column flexure, beam flexure, and plastic rotation of the beam as detailed in Figure 2.11. Hence, the total end displacement of the beam-column subassembly can be expressed as follows:

$$\Delta_{system} = \delta_c + \delta_b + \delta_p \quad (2.2)$$

where Δ_{system} = ultimate displacement of a subassembly,

δ_c = displacement component associated with column flexibility,

δ_b = displacement component associated with beam flexibility,

δ_p = displacement component associated with plastic rotation of the beam.

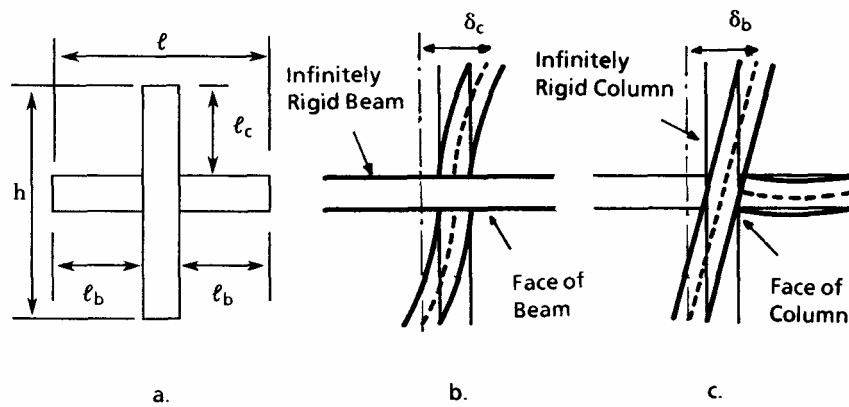


Figure 2.11 Displacement components of a beam-column subassembly [2.15].

2.3.2 Priestley and Tao (1993)

Priestley and Tao [2.10] proposed a simplified analytical method for precast frames with ductile connections. This procedure was developed for precast beam-column connections with partially debonded tendons and no mild steel reinforcement. In this method, the force-displacement response envelope was idealized by using three critical points as illustrated in Figure 2.12.

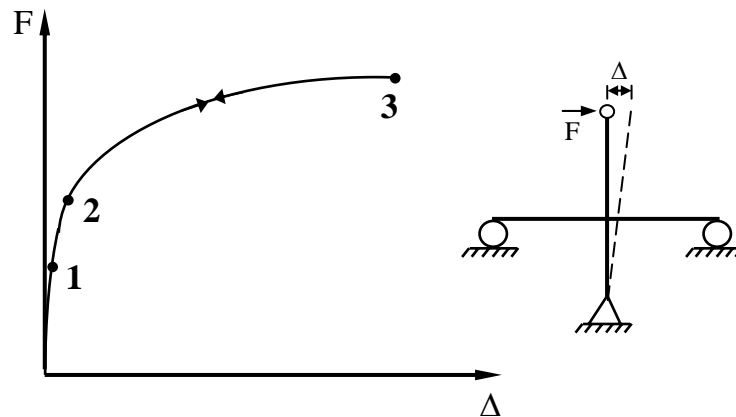


Figure 2.12 Trilinear idealization to characterize the response of a precast frame assembly connected with unbonded prestressing.

The authors provided the following descriptions for these critical points:

Point 1

This point corresponds to the beginning of flexural cracks in the beam when concrete at the extreme fiber reaches zero stress.

Point 2

This point defines the end of the elastic range. Beyond this point, the force-displacement relationship cannot be estimated accurately due to the lack of strain incompatibility between the concrete and steel.

Point 3

It is assumed that the concrete strain reaches the ultimate value as the prestressing tendons reach the yield strain. The error resulting from this assumption is expected to be small. The concrete compression stress distribution is represented with an equivalent stress block to define this critical point in Figure 2.12.

2.3.3 El-Sheikh, Sause, Pessiki, and Lu (1999)

The behavior of unbonded post-tensioned precast concrete frames was investigated by El-Sheikh et al. [2.16] using finite element models. Two types of models were developed to predict the behavior of beam-column subassemblages: the Fiber Model (FM) and the Spring Model (SM). In the fiber model, the behavior of concrete in the beam-column interface was modeled using fiber elements. As shown in Figure 2.13, truss elements were used to model the unbonded post-tensioning reinforcement, whereas zero-length springs defined the shear deformations of the joint panel zone. The portions of the beams and columns within the joint panel zone were represented with rigid links and rigid end zones, respectively.

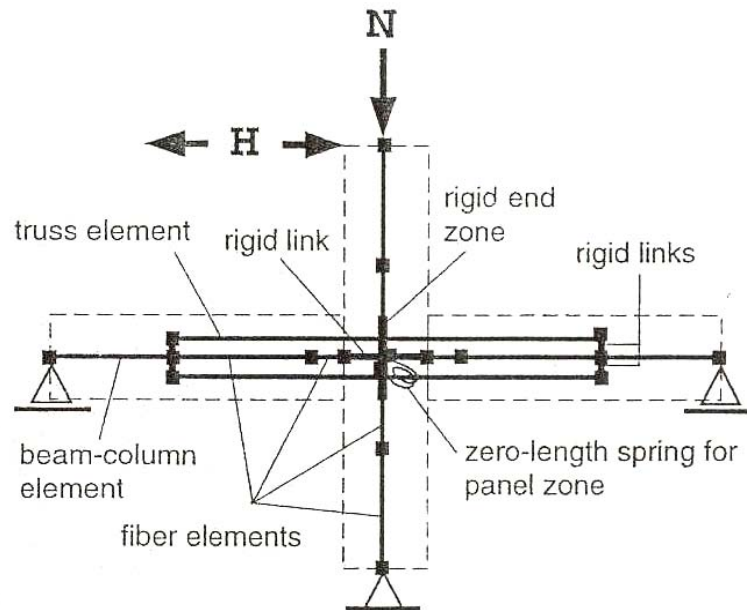


Figure 2.13 A fiber model representation of an unbonded post-tensioned precast concrete frame [2.16].

In the spring model, zero-length rotational springs were used to model the nonlinear behavior of beam-column connections instead of fiber and truss elements. Similar to FM, the joint panel was modeled with rotational springs and rigid links, while the beam and columns were modeled with beam-column elements as illustrated in Figure 2.14.

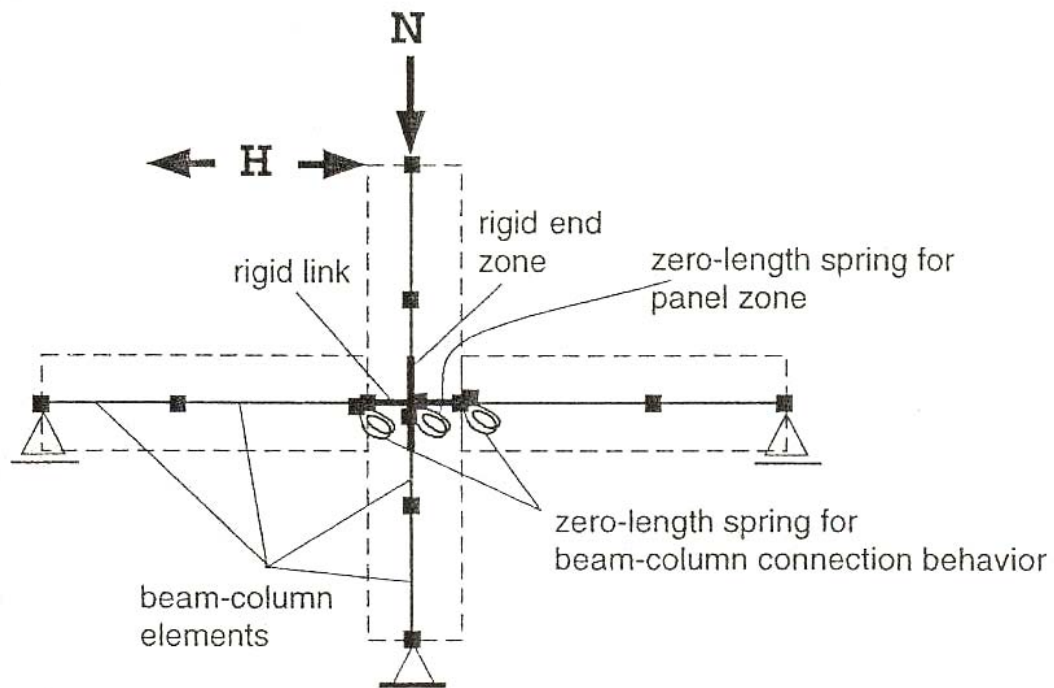


Figure 2.14 A spring model representation of an unbonded post-tensioned precast concrete frame [2.16].

The accuracy of the proposed models was examined using the NIST test data obtained from Specimen G-P-Z4 (see Section 2.2.1), and the simplified analytical method proposed by Priestley and Tao [2.10] (see Section 2.3.2). As shown in Figure 2.15, both the fiber and spring models satisfactorily captured the lateral load-displacement hysteresis response of

Specimen G-P-Z4. However, the hysteresis loops obtained from analytical models appeared to be narrower than the test results, indicating that the energy dissipation was somewhat underestimated by both the fiber and spring models. As shown in Figure 2.16, the moment-rotation behavior of the unbonded post-tensioned frame predicted by the fiber model was found to satisfactorily compare with the trilinear idealization suggested by Priestley and Tao [2.10].

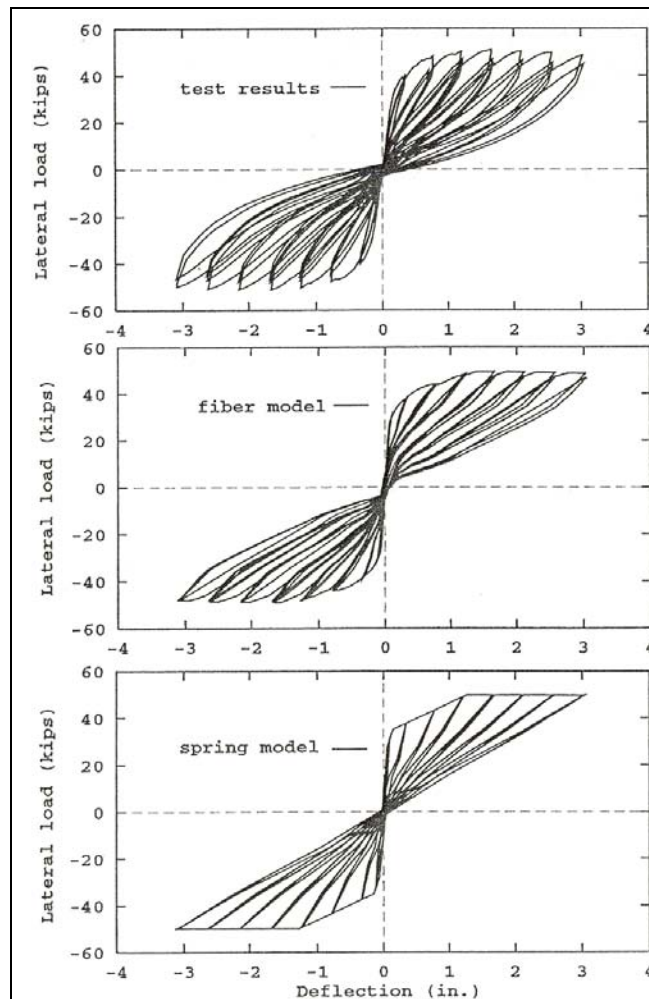


Figure 2.15 Measured and predicted responses of Specimen G-P-Z4 with unbonded prestressed connection [2.16].

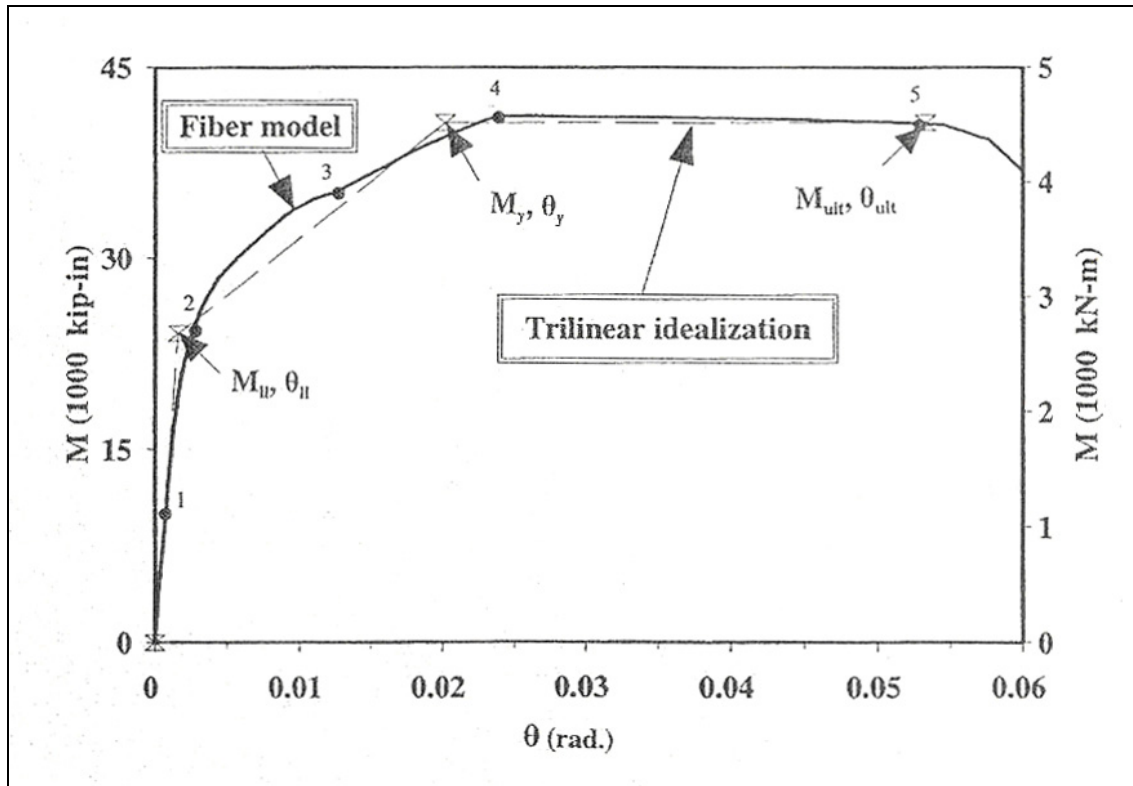


Figure 2.16 Moment-rotation envelopes predicted by the fiber model and trilinear idealization for an unbonded post-tensioned connection [2.16].

2.3.4 Pampanin, Priestley, and Sritharan (2001)

The classical section analysis method that utilizes strain compatibility to obtain stress distribution at the section level can not be applied to jointed precast systems. In these systems, strain compatibility between steel reinforcement and concrete does not exist because the steel reinforcement is unbonded at the critical section. Referred to as the *Monolithic Beam Analogy* (MBA), Pampanin et al. [2.1] proposed an alternative method to analyze precast systems with jointed connections having unbonded reinforcement. Accordingly, an additional condition at the section level is introduced by equating the end displacement of the

precast beam ($\Delta_{precast}$) that undergoes a large deformation with that of a monolithically connected beam ($\Delta_{monolithic}$), as illustrated in Figure 2.17. This analysis method has been validated using overall hybrid frame response obtained from the NIST test program and the PRESSS building test (see Section 2.2).

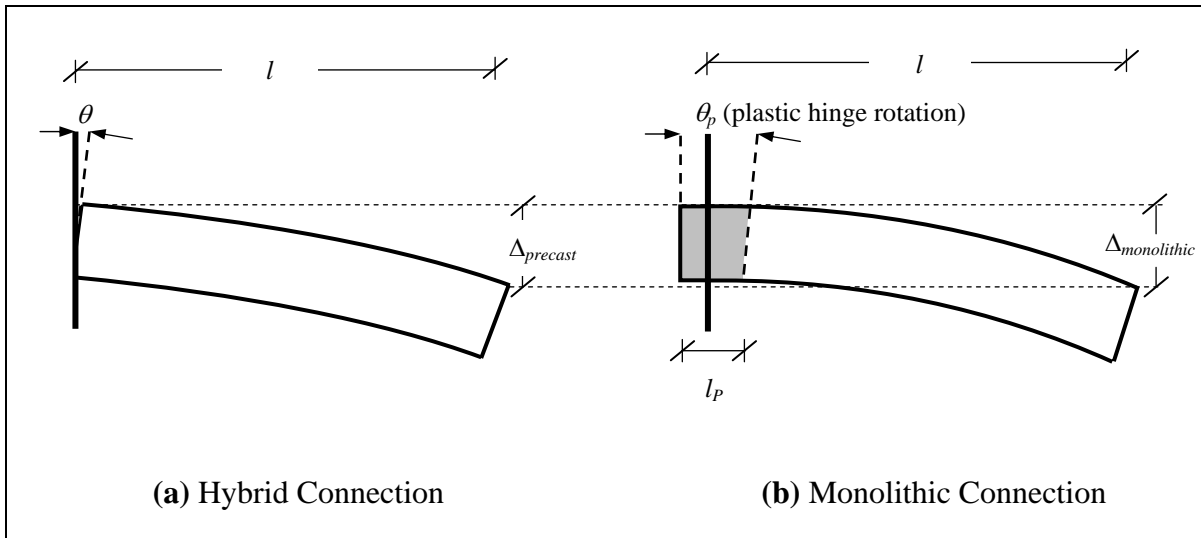


Figure 2.17 The concept of the monolithic beam analogy, where $\Delta_{precast}$ is assumed to be equal to $\Delta_{monolithic}$.

The steps involved in establishing the moment-rotation curve using MBA are as follows:

Step 1: Equate beam end displacements

Assuming identical dimensions for both the precast and monolithic beams in Figure 2.17, the beam end displacements are equated.

$$\Delta_{precast} = \Delta_{monolithic} \quad (2.3)$$

$$\text{i.e., } \Delta_{elastic} + \Delta_{\theta} = \Delta_{elastic} + \Delta_{plastic} \quad (2.4)$$

where $\Delta_{elastic}$ = beam end displacement due to elastic curvature along the member,

Δ_{θ} = beam end displacement of the precast frame due to interface rotation θ , and

$\Delta_{plastic}$ = beam end displacement of the monolithic frame due to plastic curvature over the plastic hinge length, l_p .

From Eq. 2.4,

$$\Delta_{\theta} = \Delta_{plastic} \quad (2.5)$$

$$\theta \cdot l = \Delta_{plastic} \quad (2.6)$$

where θ is the concentrated rotation at the beam-column interface.

Step 2: Define plastic displacement of the monolithic beam

Using the ultimate and yield curvatures (ϕ_u and ϕ_y), the plastic displacement component of the monolithic beam is defined as suggested by Paulay and Priestley [2.17].

$$\Delta_{plastic} = \theta_p \cdot \left(l - \frac{l_p}{2} \right) \quad (2.7)$$

where $\theta_p = (\phi_u - \phi_y) \cdot l_p$, and

θ_p = plastic hinge rotation.

Assuming $l - \frac{l_p}{2} \approx l$, Eq. 2.7 is simplified as follows:

$$\Delta_{plastic} = (\phi_u - \phi_y) \cdot l_p \cdot l \quad (2.8)$$

Substituting Eq. 2.8 in Eq. 2.6 and recognizing that $\phi_u = \frac{\varepsilon_c}{c}$,

$$\varepsilon_c = \left(\frac{\theta}{l_p} + \phi_y \right) \cdot c \quad (2.9)$$

where ε_c is the compression strain in the extreme fiber of concrete, and c is the neutral axis depth.

Step 3: Determine neutral axis depth

The neutral axis depth is determined iteratively using the force equilibrium condition at the critical section where the precast connection is established. For an assumed neutral axis depth, the procedure described below is followed to quantify strains in the post tensioning tendon (ε_{pt}) and tension mild steel reinforcement (ε_{st}), from which the stresses and forces are readily established.

(a) Strain in Post-tensioning Tendon

Using the frame geometry corresponding to an interface rotation of θ as shown in Figure 2.18, the elongation in the post-tensioning tendon (Δ_{pt}) can be expressed as

$$\Delta_{pt} = \left(\frac{h}{2} - c \right) \cdot \theta \quad (2.10)$$

where h is the height of the beam. The strain in the post-tensioning tendon corresponding to elongation Δ_{pt} is determined from

$$\varepsilon_{pt} = \frac{n \cdot \Delta_{pt}}{l_{pu}} \quad (2.11)$$

where n is the number of jointed beam-to-column interface connections in the precast frame at a given floor level, and l_{pu} is the unbonded length of the post-tensioning tendon.

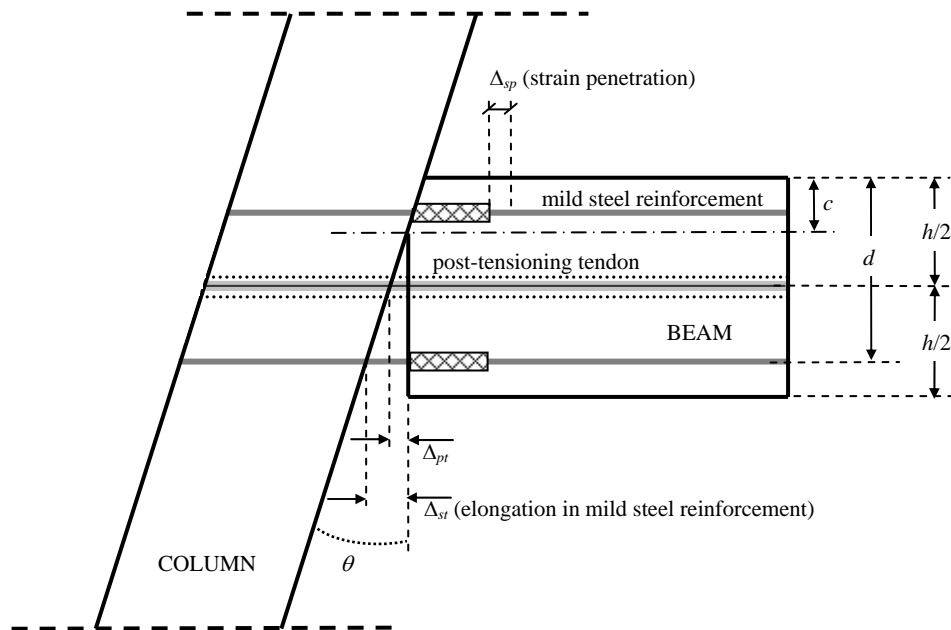


Figure 2.18 A hybrid frame when subjected to an interface rotation of θ .

By substituting for Δ_{pt} in Eq. 2.11 from Eq. 2.10,

$$\varepsilon_{pt} = \frac{n \cdot \left(\frac{h}{2} - c \right) \cdot \theta}{l_{pu}} \quad (2.12)$$

(b) Strain in Tension Mild Steel Reinforcement

From geometry (see Figure 2.18):

$$\Delta_{st} = (d - c) \cdot \theta \quad (2.13)$$

$$\varepsilon_{st} = \frac{\Delta_{st} - 2 \cdot \Delta_{sp}}{l_{su}} \quad (2.14)$$

where Δ_{st} is the elongation in the tension mild steel reinforcement corresponding to interface rotation θ , d is the depth to the tension mild steel reinforcement from the extreme compression fiber, l_{su} is the debonded length of the mild steel reinforcement at the connection interface, and Δ_{sp} is the elongation in the mild steel reinforcement expected due to strain penetration into the beam and column. The value for Δ_{sp} is determined by incorporating the effects due to elastic and plastic strains, as suggested by Sritharan [2.18]:

$$\Delta_{sp} = \frac{2}{3} \cdot l_{sp} \cdot \varepsilon_{elastic} + l_{sp} \cdot \varepsilon_{plastic} \quad (2.15)$$

where $\varepsilon_{elastic}$ is the elastic strain in the mild steel reinforcement, $\varepsilon_{plastic}$ is the plastic strain in the mild steel reinforcement (see Figure 2.19), l_{sp} is the strain penetration length and is taken

as $0.15 \cdot f_{sy} \cdot d_b$ with f_{sy} and d_b defining the yield strength and the diameter of the mild steel reinforcing bar.

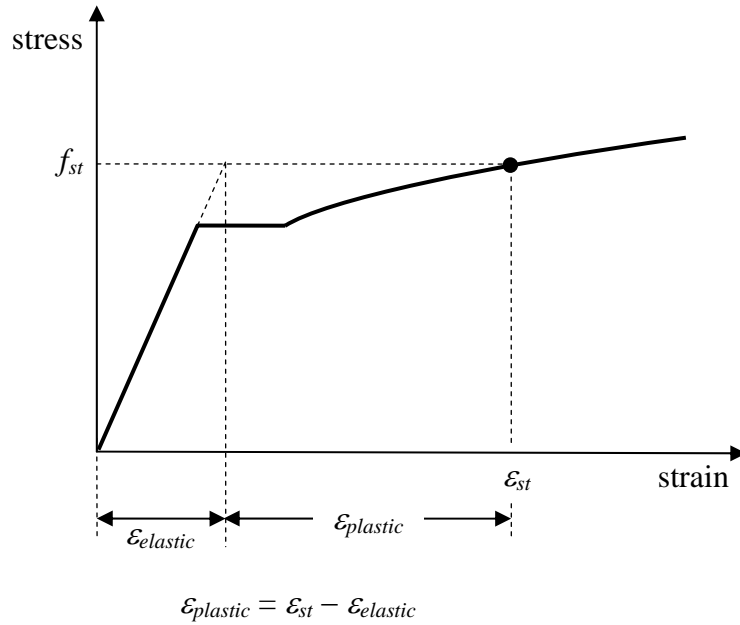


Figure 2.19 Identifying elastic and plastic strain components for the mild steel reinforcement.

Combining Eqs. 2.13 to 2.15 yields:

$$\epsilon_{st} = \frac{\Delta_{st} + \frac{2}{3} \cdot l_{sp} \cdot \frac{f_{st}}{E_s}}{l_{pu} + 2 \cdot l_{sp}} \quad (2.16)$$

where f_{st} is the stress in the tension mild steel reinforcement, and E_s is the elastic modulus of the mild steel.

Step 4: Determine resultant concrete compression force

Representing the concrete stress distribution using a confined concrete model, the resultant concrete compression force is determined and compared against that determined from the equilibrium condition as shown in Eq. 2.17.

$$F_c = F_{pt} + F_{st} - F_{sc} \quad (2.17)$$

where F_c is the resultant concrete compression force at the beam-column interface, F_{pt} is the post-tensioning force determined from both the initial prestressing force and ε_{pt} estimated from Eq. 2.12, F_{st} is the mild steel tension force corresponding to ε_{st} (see Eq. 2.16), and F_{sc} is the mild steel compression force. Given the debonded condition of the mild steel reinforcement, no details were provided as to how F_{sc} should be estimated.

Steps 3 and 4 are repeated by revising the neutral axis depth until the two computed compression forces converge. Using the resultant forces and their locations, the moment resistance of the connection at selected θ is determined at the end of this step.

Step 5: Develop continuous moment-rotation response envelope

By repeating Steps 1 to 4 for different interface rotations, a continuous moment-rotation response envelope may be developed to describe the connection behavior.

The steps described above for the MBA analysis may be summarized using a flowchart given in Figure 2.20.

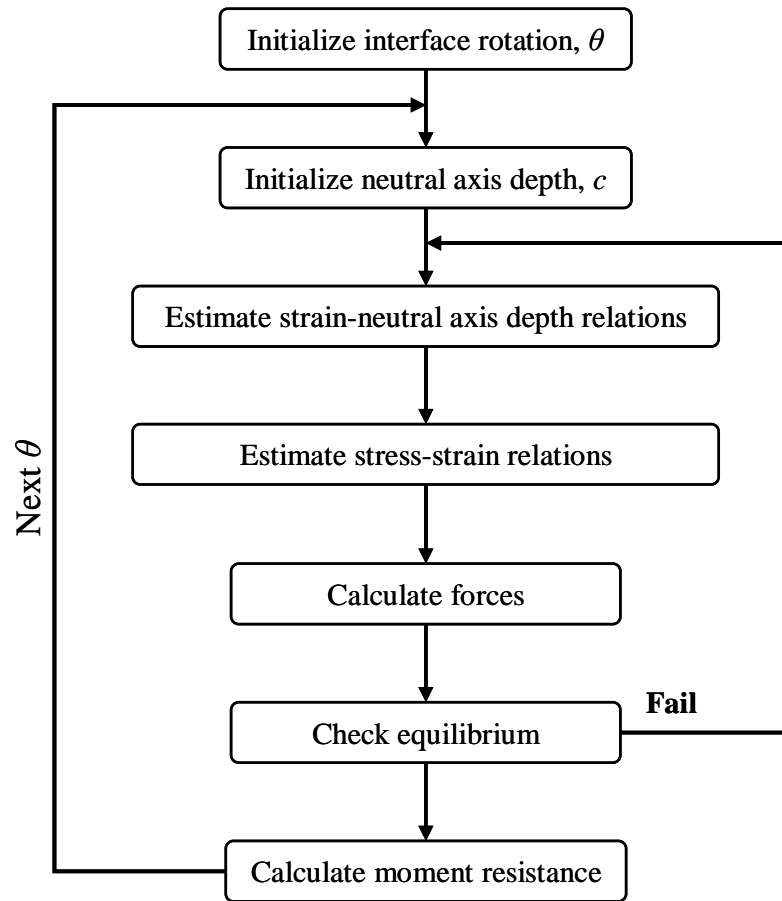


Figure 2.20 A flowchart summarizing the steps based on MBA to determine the moment-rotation behavior of a hybrid frame connection.

The robustness of the MBA concept was demonstrated by comparing the measured beam end moment vs. column drift behavior of two NIST tests (namely M-P-Z4 and O-P-Z4 from Phase IV-B) with the predicted response envelopes. A good correlation was generally seen. The application of MBA to jointed frame systems was further demonstrated using the

PRESSS test building. By using a 2D frame model and representing the behavior of all jointed frame connections with the results obtained from MBA analyses, researchers showed that the observed behavior of the PRESSS building could be satisfactorily reproduced using the MBA concept [2.1].

2.3.5 Vernu, Sritharan and Vernu [2.2, 2.19]

In this study, the monolithic beam analogy concept, presented above (Pampanin et al., [2.1]), was applied to hybrid precast frames with some modifications and results were compared with available experimental data. In the application process, the authors made a modification to the strain penetration term, expressed the stress-strain behavior of the post-tensioning steel with the Mattock's model [2.20], and provided an expression to compute the strain in the compression mild steel so that the corresponding force contribution could be estimated. Accordingly, for a given interface rotation θ , the following equations were suggested at the connection interface for estimating the strains in the compression mild steel reinforcement (ε_{sc}), tension mild steel reinforcement, post-tensioning tendon, and extreme concrete compression fiber, respectively:

$$\varepsilon_{st} = \frac{(d - c) \cdot \theta + \frac{2}{3} \cdot l_{sp} \frac{f_{st}}{E_s}}{l_{su} + 2 \cdot l_{sp}} \quad (2.18)$$

$$\varepsilon_{pt} = \frac{\left(\frac{h}{2} - c\right) \cdot \theta}{l_{pu}} + \varepsilon_{pi} \quad (2.19)$$

$$\varepsilon_c = \left[\theta + \phi_e \cdot \left(l_p - \frac{4}{3} \cdot l_{sp} \right) \right] \cdot \frac{c}{l_p} \quad (2.20)$$

$$\varepsilon_{sc} = \frac{1}{2} \cdot \left[\frac{(c - d')}{c} \cdot \varepsilon_c + \varepsilon_{sy} \cdot \frac{M}{M_y} \right] \quad (2.21)$$

where ε_{pi} is the strain in the post-tensioning tendon due to initial prestressing, ϕ_e is the elastic curvature, d' is the distance from the compression mild steel reinforcement to the extreme compression fiber, ε_{sy} is the yield strain of the mild steel reinforcement, M is the moment resistance in the previous step of iteration procedure, and M_y is the yield moment defined when the tension reinforcement reaches ε_{sy} .

Using the strain equations and appropriate stress-strain material models (described in Step 2 of Section 3.4), the stresses in the steel and concrete are obtained for an assumed neutral axis depth as discussed in Section 2.3.4. Using a trial and error procedure, the neutral axis depth satisfying the equilibrium condition is found for a given interface rotation. More details of the analysis using Eqs. 2.18 to 2.21 may be found in Section 3.4. A visual computer tool to perform the analysis method was developed by Vernu [2.2], which was used in the research study described in this report. As shown in Figure 2.21, this analysis tool satisfactorily predicted the test results obtained from Specimens M-P-Z4 and O-P-Z4 and the PRESSS test building, which included the beam moment vs. column drift behavior, and change in post-tensioning force and neutral axis depth as a function of interface rotation.

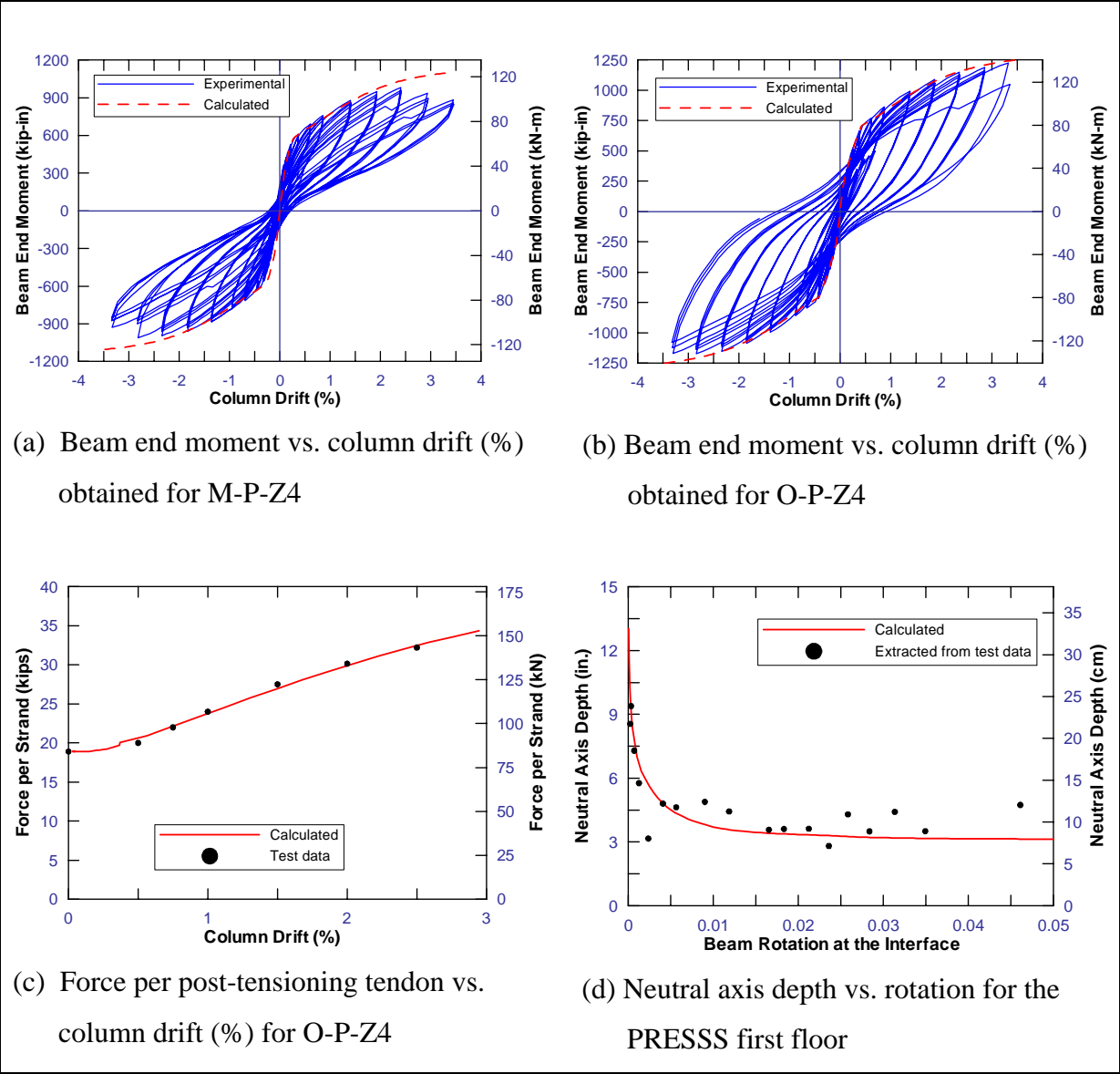


Figure 2.21 A comparison of MBA analysis results with experimental data presented in Reference [2.19].

2.4 Design Methods

2.4.1 Cheok, Stone, and Nakaki (1996)

In this report, a design procedure for hybrid precast concrete connections is presented by defining two different moment capacities: “the probable moment capacity” and “the nominal moment capacity”. A trial and error procedure that hinges on the design concept and assumptions presented below is used to perform the hybrid connection design. This design procedure was developed in compliance with the test results obtained from a limited number of hybrid frame tests conducted at NIST, which was summarized in Section 2.2.1. The authors cautioned the application of this design procedure outside the range of the experimental variables studied.

Design Concept

- A ductile connection is generated at the beam-column interface. Thus, inelastic actions develop at the connection while precast concrete members are protected from any significant damage.
- The post-tensioning reinforcement is used to provide a reliable clamping at the beam-column interface, which also creates a friction mechanism to transfer the beam shear resulting from gravity and seismic loads to the columns.
- The post-tensioning steel is designed to remain elastic up to the required maximum drift.

- An adequate confinement is provided at the beam end regions to avoid crushing and spalling of concrete.
- The mild steel reinforcement provided at the precast connection contributes to the flexural moment resistance while providing the energy dissipation capability for the system.
- Failure of the connection is designed to be due to fracture of the mild steel reinforcement after the system has reached the required maximum drift.

Assumptions

- The equivalent rectangular (Whitney) stress block assumption is used to define the concrete compression force at the connection interface, which helps to overcome the strain incompatibility problem at this critical section.
- The contribution of the compression mild steel reinforcement to the moment resistance of the connection is neglected.
- Mild steel reinforcing bars are effectively debonded over a distance of $l_{su} + 5.5 \cdot d_b$, which includes the intentional unbonded length of l_{su} and a growth length in debonded length of $2.75 \cdot d_b$ on either side of l_{su} . The debonding of the mild steel bars over a short distance is required to prevent them from premature fracture due to low cycle fatigue.

The description of the design is given by presenting a procedure for determining the probable moment capacity for a hybrid connection. Using this procedure, the definition for the nominal moment capacity of the connection is also given.

(a) Probable Moment Capacity

The design procedure is intended to ensure that the hybrid connection will accommodate the necessary story drift demands while retaining at least 80 percent of its maximum moment capacity. The steps involved in the calculation of the probable moment capacity are described below assuming that the geometric and material parameters including the steel areas as defined in Table 2.4 are known.

Table 2.4 Geometric and material parameters used in the design procedure proposed by Cheok et al. [2.3].

Geometric Properties	
Beam section details	h = beam height
	b = beam width
	d = effective beam depth to the tension reinforcement
Reinforcing steel	A_{pt} = area of the post-tensioning tendon
	A_s = area of the tension mild steel reinforcement in one face of beam
	d_b = diameter of the mild steel reinforcement
Unbonded lengths	l_{su} = debonded length of the mild steel reinforcement
	l_{pu} = unbonded length of the post-tensioning tendon
Material Properties	
Strengths	f'_c = concrete compression strength
	f_{sy} = yield strength of the mild steel reinforcement
	f_{su} = ultimate tensile strength of the mild steel reinforcement
Steel strains	ϵ_{pi} = strain in the post-tensioning tendon due to initial prestressing
	ϵ_{su} = ultimate strain of the mild steel reinforcement

STEP 1: Calculate tension force in the mild steel reinforcement

The area of the mild steel reinforcement is estimated using Eq. 2.22, ensuring that the connection will have sufficient passive steel to resist shear resulting from gravity loads.

$$A_s \geq \frac{V_D + V_L}{f_{sy}} \quad (2.22)$$

where V_D and V_L are the shear demands at the connection interface due to dead load and live

load, respectively. To define the probable moment capacity, the tension mild steel reinforcement is assumed to have reached its ultimate strength. Therefore, the tension force in the mild steel is calculated from:

$$F_{st} = A_s \cdot f_{su} \quad (2.23)$$

STEP 2: Calculate force in the post-tensioning tendon corresponding to the probable moment capacity

Elongation of the mild steel reinforcement and elongation, strain, and stress in the post-tensioning tendon are determined consecutively to obtain the post-tensioning force corresponding to the probable moment capacity. From geometry (see Figure 2.22), the elongation of the mild steel reinforcement is calculated by assuming a uniform strain over the effective debonded length of the mild steel reinforcement. Hence,

$$\Delta_{st} = \varepsilon_{su} \cdot (l_{su} + 5.5 \cdot d_b) \quad (2.24)$$

Using the mild steel bar elongation estimated from Eq. 2.24, the elongation of the post-tensioning tendon is calculated from Eq. 2.25 utilizing an assumed neutral axis depth (c).

$$\Delta_{pt} = \left(\frac{\frac{h}{2} - c}{d - c} \right) \cdot \Delta_{st} \quad (2.25)$$

Hence, the strain in the post-tensioning tendon is calculated as

$$\varepsilon_{pt} = \frac{\Delta_{pt}}{l_{pu}} + \varepsilon_{pi} \quad (2.26)$$

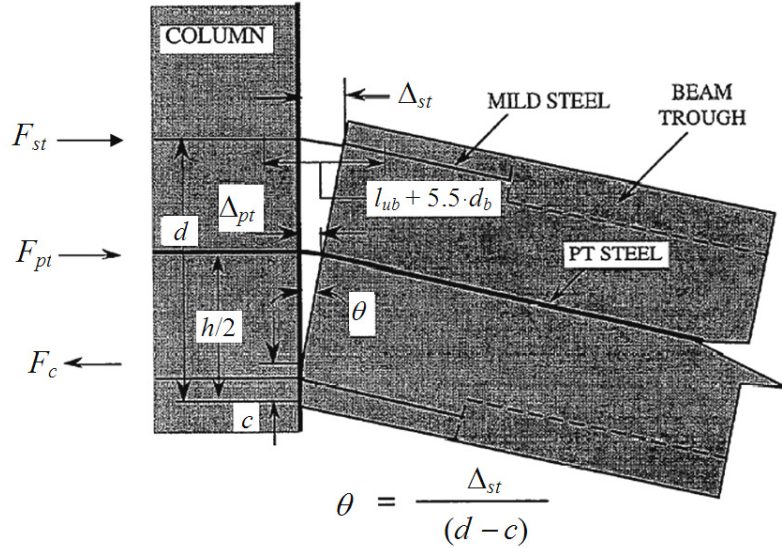


Figure 2.22 Various displacements and corresponding forces at interface rotation of θ at the hybrid connection [2.3].

Using the analytical stress-strain curve proposed by Mattock [2.20] for Grade 270 prestressing steel, the stress in the post-tensioning tendon (f_{pt}) is determined. If $f_{pt} > 0.9 \cdot f_{pu}$, the following suggestions are given to reduce the stress in the post-tensioning tendon [2.3]:

- increase the unbonded length of the post-tensioning tendon,
- increase the amount of the post-tensioning tendon, or
- decrease the amount of the mild steel reinforcement.

After the necessary steps are repeated to finalize ε_{pt} from Eq. 2.26 and the corresponding stress, the post-tensioning force is obtained by multiplying the prestressing stress with the post-tensioned tendon area. Thus,

$$F_{pt} = A_{pt} \cdot f_{pt} \quad (2.27)$$

STEP 3: Determine neutral axis depth

Using the equilibrium condition and an equivalent rectangular stress block to represent the compressive stress distribution, the neutral axis depth is estimated from the following equation:

$$F_c = F_{st} + F_{pt} \quad (2.28)$$

$$c = \frac{F_c}{0.85 \cdot f'_c \cdot b \cdot \beta_1} \quad (2.29)$$

where β_1 is the ratio of the equivalent stress block to the neutral axis depth. The neutral axis depth calculated from Eq. 2.29 is compared with that assumed in Step 2. Steps 2 and 3 are repeated until the assumed neutral axis depth converges to that calculated from Eq. 2.29.

STEP 4: Calculate probable moment capacity

The probable moment capacity (M_{pr}) of the section is obtained by summing the moments contributed by the post-tensioning tendon (M_{pt}) and mild steel reinforcement (M_{st}). By taking moments about the resultant concrete compression force,

$$M_{pt} = F_{pt} \cdot \left(\frac{h}{2} - \frac{\beta_1 \cdot c}{2} \right) \quad (2.30)$$

$$M_{st} = F_{st} \cdot \left(d - \frac{\beta_1 \cdot c}{2} \right) \quad (2.31)$$

$$M_{pr} = M_{pt} + M_{st} \quad (2.32)$$

STEP 5: Check restoring capability of the connection

As the final step, the moment contribution of the post-tensioning tendon is compared against the moment contribution of the tension mild steel reinforcement to see if the frame will re-center after a seismic event. To account for this feature in the design, it is suggested that M_{pt} must be greater than $0.5 \cdot M_{pr}$. If $M_{pt} < 0.5 \cdot M_{pr}$, either A_{pt} must be increased or A_s must be decreased, and the design steps are repeated starting from Step 1.

(b) Nominal Moment Capacity

In order to calculate the nominal moment capacity of the section, the following modifications are introduced to the procedure outlined above for determining the probable moment capacity.

- It is assumed that the tension stress in the mild steel reinforcement is equal to the yield strength, which modifies Eq. 2.23 to

$$F_{st} = A_s \cdot f_{sy} \quad (2.33)$$

- The strain in the mild steel reinforcement is taken as the strain at the onset of hardening (ε_{sh}). The following value is suggested for Grade 60 reinforcing steel:

$$\varepsilon_{sh} = 0.01 \quad (2.34)$$

- Growth in the debonded length of the mild steel reinforcement is assumed to be zero. Therefore, the total debonded length of the mild steel is set equal to the intentional debonded length. Hence, Eq. 2.24 is replaced with Eq. 2.35.

$$\Delta_{st} = \varepsilon_{sh} \cdot l_{su} \quad (2.35)$$

Approximating the nominal moment capacity to 70 percent of the probable moment capacity is also suggested to be adequate. The nominal moment capacity (M_n) is required to satisfy the following strength requirements:

$$\phi \cdot M_n \geq 1.4 \cdot M_D + 1.7 \cdot M_L \quad (2.36)$$

$$\phi \cdot M_n \geq 1.4 \cdot (M_D + M_L + M_E) \quad (2.37)$$

$$\phi \cdot M_n \geq 0.9 \cdot M_D \pm 1.4 \cdot M_E \quad (2.38)$$

where ϕ = flexural strength reduction factor, M_D = moment due to dead load,
 M_L = moment due to live load, and M_E = moment due to earthquake load.

2.4.2 PRESSS Design Guidelines (2002)

The PRESSS guidelines proposed by Stanton and Nakaki [2.4] provide design procedures for five different jointed precast concrete structural systems, which were included in the PRESSS test building. This building was designed with two different seismic frames based on four types of beam-column connections in one direction and a jointed wall system in the orthogonal direction. More details of the test building and a summary of the experimental observations are described in Section 2.2.2.

The guidelines were published at the end of the PRESSSS program, but experimental validations of the proposed design procedures have not been conducted. For all the systems, the guidelines use an iterative procedure to determine the neutral axis depth that satisfies the force equilibrium condition at the critical section. The guidelines proposed for unbonded frame systems with damping are intended for the design of hybrid frame systems. More details of the hybrid frame connection design are presented below while the subsequent chapters provide a validation of this design procedure. Recommendations to improve the design of the hybrid frame systems described in the PRESSSS guidelines are also included.

Design Assumptions

The design assumptions considered in the PRESSSS guidelines suggested for the unbonded frame systems with damping are as follows:

- The overall dimensions of the frame members are known and the beams are of a constant cross section.
- The design forces and drifts are known. Interface rotations are obtained from the drift ratio using the geometry of the system.
- The post-tensioning tendons are totally unbonded over the entire length of the frame and anchored at the exterior faces of the end columns.
- The post-tensioning tendons are located at the mid-height of the beam section, which remain elastic until the frame reached the required design drift. Yielding of the tendons is assumed to begin at the design drift.
- The mild steel reinforcement is unbonded over a short distance at the beam-column interface.

- An equal amount of mild steel reinforcement is used at the top and bottom of the beam.
- Fiber reinforced grout pads are used at the interface between the precast concrete columns and beams. The use of fiber is expected to prevent grout degradation when the frame connection is subjected to reverse cyclic loading.

Design Procedure

STEP 1: Establish material properties

The following material properties are established in this step: the beam concrete strength (f'_c), the interface grout strength (f'_g), a suitable value for corresponding β_1 , the yield strength (f_{py}) and modulus of elasticity (E_p) of the prestressing steel, the yield strength of the mild steel reinforcement (f_{sy}), over-strength factors for tension and compression reinforcement at the design limit state ($\lambda_{st,des}$ and $\lambda_{sc,des}$), and the maximum permissible strain in the mild steel reinforcement under cyclic loading ($\varepsilon_{st,max}$). The over-strength factors for the reinforcement were suggested at three limit states of the system and are reproduced in Table 2.5.

Table 2.5 Suggested strains and reinforcement over-strength factors for ASTM 706 bars [2.4].

Suggested System State	Strain ($\varepsilon_{st,max}$)	over-strength factor of tension reinforcement (λ_{st})	over-strength factor of compression reinforcement (λ_{sc})
First yield	0.002	1.0	1.0
Design	0.04	1.35	1.0
Maximum credible	0.08	1.5	1.0

The drift at the maximum credible state was suggested to be the extreme drift required in the acceptable criteria defined in documents such as ACI ITG 1.1 [2.21]. The drift at the yield state was not specified. However, as described below, the design procedure only requires the design drift, which is dictated by the code requirements.

STEP 2: Obtain design loads and drifts

Using the displacement-based design (DBD) or the force-based design (FBD), design loads are obtained. The corresponding overturning moment and design drift are then established. In this report, a design drift of two percent is assumed consistent with the allowable interstory drift in UBC 1997 [2.22].

STEP 3: Estimate beam section dimensions

By considering the shear forces in the beam-column joints and the elongation of the post-tensioning tendons at the design drift, the beam section should be appropriately dimensioned.

Deeper beams reduce shear demands in the joints, but they induce higher stress changes in the tendons due to an increase in the elongation.

Using the criterion given in Section 21.3.1.2 of ACI 318-99 [2.23] as the basis, the effective height of the beam (h_g) is taken as

$$h_g \leq \frac{l}{3} \quad (2.39)$$

It is also suggested that the beam width (b_g) should be selected to satisfy the criterion in Section 21.3.1.3 of ACI 318-99 [2.23]. Accordingly,

$$b_g \leq 0.3 \cdot h_g \quad (2.40)$$

STEP 4: Establish various constants

Calculate the stress change in the post-tensioning tendon between zero interface rotation and design interface rotation (Δf_{pt}) if the beam is rocked about its corner,

$$\Delta f_{pt} = 0.5 \cdot E_p \cdot \theta_{des} \cdot \frac{h_g}{l_{pu}} \quad (2.41)$$

where θ_{des} is the interface rotation at the design limit state.

STEP 5: Estimate moments resisted by the post-tensioning tendons and mild steel reinforcement

Both the post-tensioning tendons and mild steel reinforcement provide moment resistance at the connection interface. The mild steel reinforcement also enables the frame to dissipate energy during an earthquake loading while the post-tensioning tendons provide an elastic restoring force that helps re-centering the frame at the end of an earthquake loading. Although the exact proportion of moments required for re-centering depends on the design interface rotation, beam span/depth ratio, allowable jacking stress, and yield strength of the tendons, the following moment distribution is suggested in the design procedure to maintain the re-centering capability of the frame.

$$M_{pt,des} \approx 0.55 \cdot M_{cap,des} \quad (2.42)$$

$$M_{st,des} = M_{cap,des} - M_{pt,des} \quad (2.43)$$

where $M_{pt,des}$ is the moment resistance provided by the post-tensioning tendons at the design drift, $M_{st,des}$ is the corresponding moment resisted by the tension mild steel reinforcement, and $M_{cap,des}$ is the moment capacity of the connection at the design drift.

STEP 6: Calculate area of the post-tensioning tendons

As noted previously, the post-tensioning tendons are assumed to yield at the design limit state. Consequently, the required area of the post-tensioning tendons is calculated from Eq. 2.44, which is based on the assumption that the location of the resultant concrete

compression force in the beam is at $0.05 \cdot h_g$ from the extreme compression fiber, giving a lever arm of $0.45 \cdot h_g$.

$$A_{pt} = \frac{M_{pt,des}}{(0.45 \cdot h_g) \cdot f_{py}} \quad (2.44)$$

STEP 7: Calculate area of the mild steel reinforcement

Using the assumption used in Step 6 for the location of the resultant compression force in the beam, the area of the mild steel reinforcement is obtained from Eq. 2.45.

$$A_s = \frac{M_{st,des}}{(0.95 - \zeta) \cdot h_g \cdot \lambda_{st,des} \cdot f_{sy}} \quad (2.45)$$

where ζ is the distance from the compression mild steel reinforcement to the extreme compression fiber divided by h_g . In accordance with Table 2.5, $\lambda_{st,des}$ is taken as 1.35.

STEP 8: Estimate neutral axis depth

The neutral axis location in the beam at the connection interface is obtained from Eq. 2.46, which is again consistent with the assumption used for the location of the resultant compression force in Steps 6 and 7. This initial guess for the neutral axis location is corrected by an iterative design procedure as discussed further in Step 13.

$$\eta_{des} = \frac{0.1}{\beta_1} \quad (2.46)$$

where η_{des} is the neutral axis depth divided by h_g .

STEP 9: Calculate stress in the tension mild steel reinforcement

The strain in the tension mild steel reinforcement exceeds the yield strain and is given by

$\varepsilon_{st,max}$ (see Table 2.5). The corresponding stress ($f_{st,des}$) is

$$f_{st,des} = \lambda_{st,des} \cdot f_{sy} \quad (2.47)$$

STEP 10: Calculate stress in the compression mild steel reinforcement

The strain in the compression mild steel reinforcement is smaller than that of the tension mild steel reinforcement because the presence of the concrete and grout prevents development of large compressive strains. However, the stress cannot be related directly to the instantaneous strain due to the presence of significant inelastic tension strain accumulation expected from the previous inelastic cycles. Hence, the corresponding stress in the compression mild steel reinforcement ($f_{sc,des}$) is taken as

$$f_{sc,des} = \lambda_{sc,des} \cdot f_{sy} \quad (2.48)$$

$\lambda_{sc,des}$ is taken as 1.0 in accordance with Table 2.5.

STEP 11: Calculate elongation and current stress in the post-tensioning tendons at θ_{des}

Using the system geometry (see Figure 2.23a), the elongation in the post-tensioning tendon is found in terms of the interface rotation at the design drift and neutral axis depth obtained in Step 8.

$$\Delta_{pt} = \theta_{des} \cdot h_g \cdot (0.5 - \eta_{des}) \quad (2.49)$$

The corresponding stress change in the post-tensioning tendon is:

$$\Delta f_{pt} = \frac{\Delta_{pt}}{l_{pu}} \cdot E_p \quad (2.50)$$

The stress in the post-tensioning tendons ($f_{pt,des}$) is obtained by considering two criteria. First, the stress in the tendons must not exceed the yield stress to satisfy the design requirement. Second, the stress in the tendon, after losses, at zero drift (f_{p0}) must not exceed f_{pi} to prevent strength degradation, where $f_{p0} = f_{py} - \Delta f_{pt}$ and f_{pi} is the initial (jacking) stress in the post-tensioning tendon, after losses. These two criteria can be satisfied by taking $f_{pt,des}$ as the greater of the values given by Eqs. 2.51 and 2.52.

$$f_{pt,des} = f_{py} \quad (2.51)$$

$$f_{pt,des} = f_{pi} + \Delta f_{pt} \quad (2.52)$$

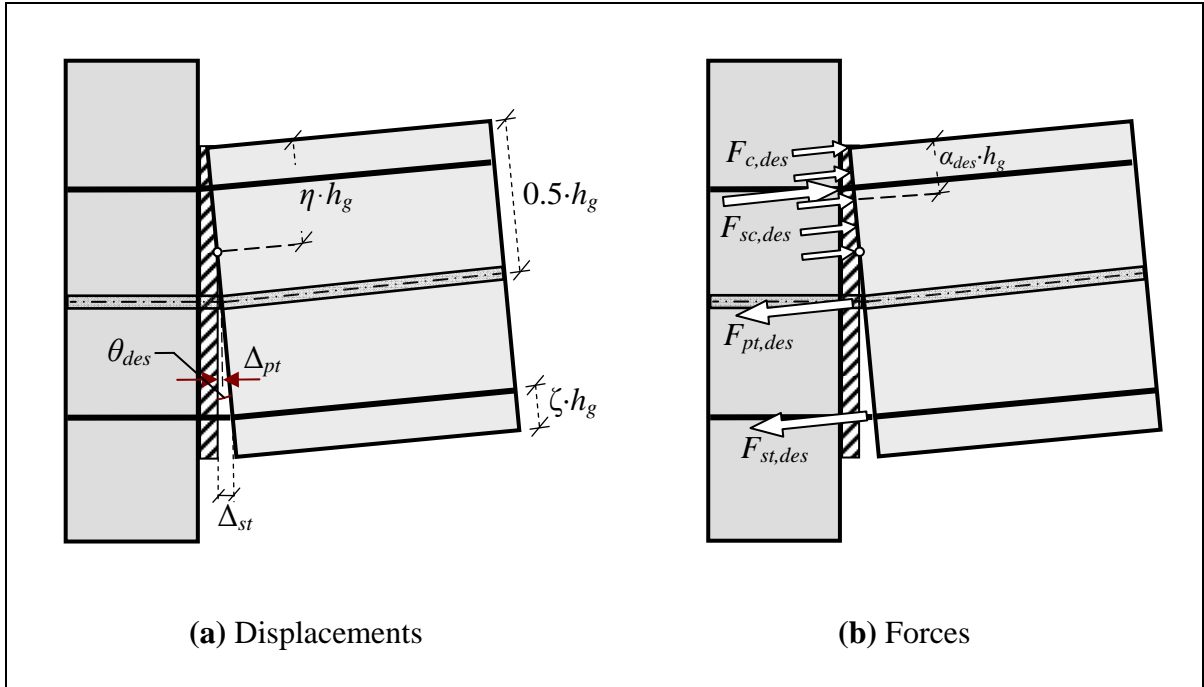


Figure 2.23 A hybrid frame system at the design limit state.

STEP 12: Calculate resultant concrete compression force at θ_{des}

The forces in the post-tensioning tendons ($F_{pt,des}$), and the tension and compression mild steel reinforcement ($F_{st,des}$ and $F_{sc,des}$) are:

$$F_{pt,des} = A_{pt} \cdot f_{pt,des} \quad (2.53)$$

$$F_{st,des} = A_s \cdot f_{st,des} \quad (2.54)$$

$$F_{sc,des} = A_s \cdot f_{sc,des} \quad (2.55)$$

The resultant concrete compression force ($F_{c,des}$) at the beam-column interface can be found using the section equilibrium condition. Hence,

$$F_{c,des} = F_{pt,des} + F_{st,des} - F_{sc,des} \quad (2.56)$$

STEP 13: Calculate locations of the resultant concrete compression force and the neutral axis depth

Using the Whitney equivalent rectangular stress concept, the depth of the rectangular stress block (a_{des}) is determined from Eq. 2.57.

$$a_{des} = \frac{F_{c,des}}{0.85 \cdot f'_g \cdot b_g} \quad (2.57)$$

Therefore, the neutral axis depth is $\eta_{des} \cdot h_g$, where

$$\eta_{des} = \frac{a_{des}}{\beta_1 \cdot h_g} \quad (2.58)$$

The procedure described from Step 8 to Step 13 is repeated until the estimated and calculated neutral axis depth values converge.

STEP 14: Calculate moment resistance of the connection

Since the forces at the connection interface, their locations, and the neutral axis depth are known from Steps 12 and 13, the moment strength of the section is calculated by taking the moments of the forces about the resultant concrete compression force (see Figure 2.23b). The moment strengths provided by the post-tensioning tendons, and the tension and compression mild steel reinforcement at the design drift are defined using Eqs. 2.59 to 2.61.

$$M_{pt,des} = F_{pt,des} \cdot (0.5 - \alpha_{des}) \cdot h_g \quad (2.59)$$

$$M_{st,des} = F_{st,des} \cdot (1 - \alpha_{des} - \zeta) \cdot h_g \quad (2.60)$$

$$M_{sc,des} = F_{sc,des} \cdot (\alpha_{des} - \zeta) \cdot h_g \quad (2.61)$$

where α_{des} is the distance from the resultant concrete compression force to the extreme concrete compression fiber divided by h_g at the design drift, and $M_{sc,des}$ is the moment provided by the compression mild steel reinforcement. The total moment strength of the hybrid frame connection is

$$M_{cap,des} = M_{pt,des} + M_{st,des} + M_{sc,des} \quad (2.62)$$

The moment strength from Eq. 2.62 must be greater than the moment demand at the design limit state. If this condition is not satisfied, the reinforcement quantities must be increased and the iteration process must be repeated starting from Step 6. However, a guidance for increasing the quantities of the two reinforcement types to satisfy the design requirement was not provided.

STEP 15: Check restoring properties of the beam

To ensure that there is no residual displacement in the frame after an earthquake loading, both the top and bottom mild steel reinforcement provided in the beam are assumed to be in compression at zero drift due to cyclic nature of the loading. Therefore, the stresses in both the tension and compression steel are calculated using an over-strength factor of 1.0

consistent with Table 2.5. Following the procedure from Step 12 to Step 14, the stresses, forces, and moments in all components of the beam section are calculated as follows:

$$F_{pt,0} = A_{pt} \cdot f_{p0} \quad (2.63)$$

$$F_{st,0} = A_s \cdot \lambda_{sc,des} \cdot f_{sy} \quad (2.64)$$

$$F_{sc,0} = A_s \cdot \lambda_{sc,des} \cdot f_{sy} \quad (2.65)$$

$$F_{c,0} = F_{pt,0} - F_{st,0} - F_{sc,0} \quad (2.66)$$

where $F_{pt,0}$ is the force in the post-tensioning tendon at zero drift, $F_{st,0}$ and $F_{sc,0}$ are the forces in the tension and compression mild steel reinforcement at zero drift, respectively, and $F_{c,0}$ is the resultant concrete compression force at the beam-column interface at zero drift. The depth of the Whitney equivalent rectangular stress block (a_0) is:

$$a_0 = \frac{F_{c,0}}{0.85 \cdot f'_g \cdot b_g} \quad (2.67)$$

The resisting moments provided by the post-tensioning tendon ($M_{pt,0}$), and the tension and compression mild steel reinforcement ($M_{st,0}$ and $M_{sc,0}$) about the resultant concrete compression force at zero drift are:

$$M_{pt,0} = F_{pt,0} \cdot (0.5 - \alpha_0) \cdot h_g \quad (2.68)$$

$$M_{st,0} = F_{st,0} \cdot (1 - \alpha_0 - \zeta) \cdot h_g \quad (2.69)$$

$$M_{sc,0} = F_{sc,0} \cdot (\alpha_0 - \zeta) \cdot h_g \quad (2.70)$$

At zero drift, the moment provided by the prestressing is required to be greater than the sum of the moments provided by the forces in the tension and compression mild steel reinforcement. Hence, it is required that

$$M_{pt,0} \geq M_{st,0} + M_{sc,0} \quad (2.71)$$

If the condition in Eq. 2.71 is not satisfied, $\frac{M_{pt,des}}{M_{cap,des}}$ ratio must be increased in Step 5 and the hybrid connection is re-designed to provide the system with an adequate restoring force.

STEP 16: Calculate elongation and unbonded length of the mild steel reinforcement

The strain in the mild steel reinforcement must be smaller than the maximum usable strain at the design drift, which is 0.04 for ASTM 706 bars according to Table 2.5. From system geometry (see Figure 2.23)

$$\Delta_{st} = \theta_{des} \cdot (1 - \eta_{des} - \zeta) \cdot h_g \quad (2.72)$$

Select the debonded length for the mild steel reinforcement such that

$$l_{su} \geq \frac{\Delta_{st}}{\varepsilon_{st,max}} \quad (2.73)$$

Due to high cyclic strains, a growth in the debonded length of the mild steel reinforcement is expected. An overestimation of the debonded length results in smaller predicted strain in the mild steel reinforcement, which may cause premature bar fracture. An underestimation of the debonded length results in greater predicted strain in the mild steel reinforcement, delaying yielding of the bars. Placing more weight on the consequences of overestimating the growth length, the growth in the debonded length is assumed to be zero for design purposes.

STEP 17: Check confinement requirement for the compression region

The plane sections are not expected to remain plane as the beam deformation is concentrated in a single crack and the tendon is unbonded and prestressed. Thus, the concrete strain cannot be evaluated from the curvature within the plastic hinge length. Due to the lack of a completely rational method for evaluating the strain field in the concrete under these circumstances, the following average compression strain over the plastic hinge length is suggested:

$$\varepsilon_c = \frac{\theta_{des} \cdot (\eta_{des} \cdot h_g)}{l_p} = \frac{\theta_{des}}{k_p} \quad (2.74)$$

where k_p is the plastic hinge length factor. In the absence of experimental data, k_p is recommended to be taken as 1.0 based on the St Venant's Principle (St. Venant, 1855).

Spalling of concrete is expected when the compression strain exceeds the ultimate strain of the unconfined concrete. Under this condition, it is recommended that the compression region should be confined so that concrete can sustain high strains. If spalling of unconfined cover concrete is expected, a reduced beam section equal to the confined core dimensions should be used in the design calculations.

The steps described above for the design of hybrid frame systems as suggested in the PRESSS guidelines is summarized in a flowchart shown in Figure 2.24.

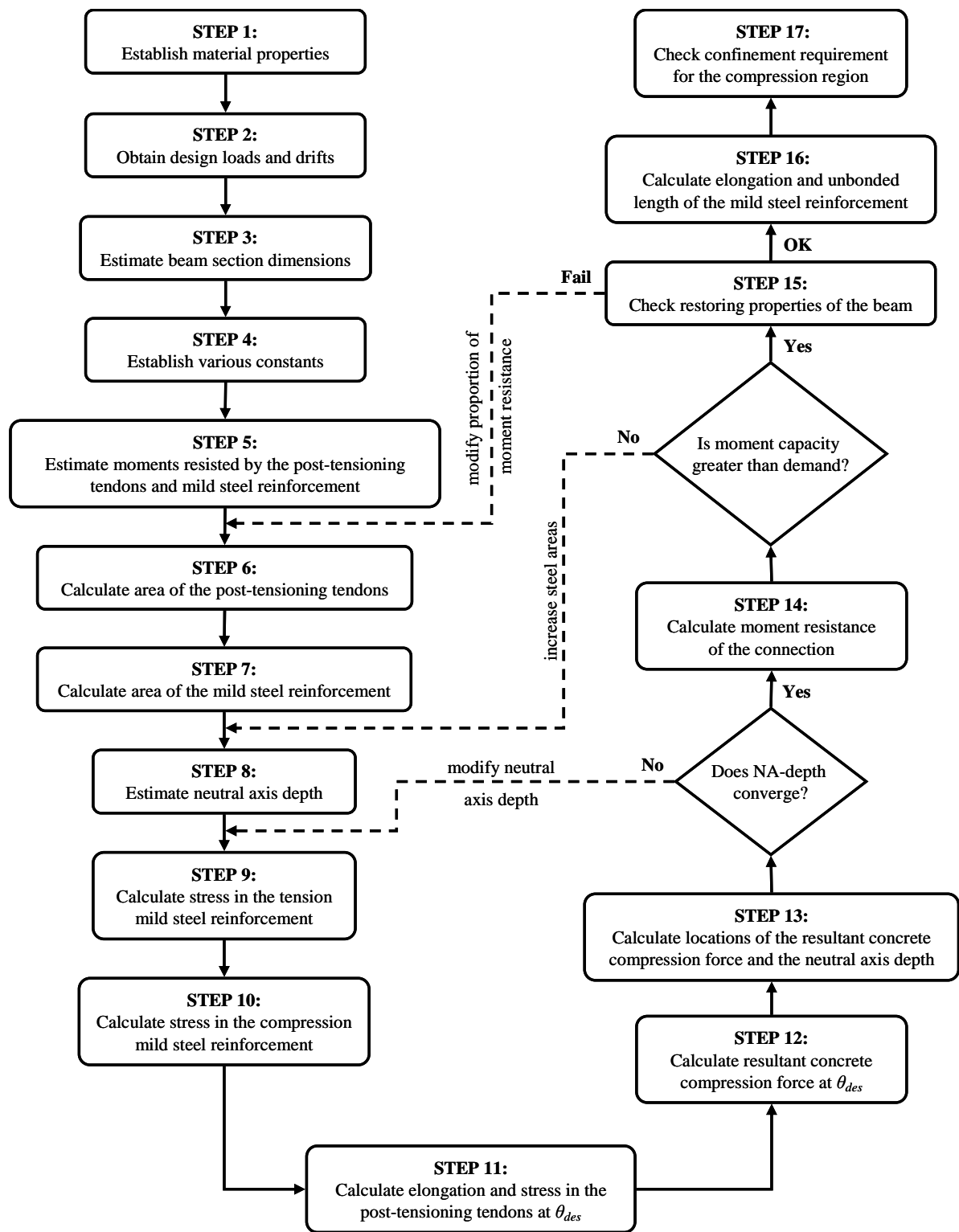


Figure 2.24 A flowchart representation of the PRESSS guidelines for designing hybrid frame connections.

2.4.3 ACI T1.2-03 (2003)

In the ACI T1.2-03 document [2.5], the ACI Innovative Task Group 1 and Collaborators have proposed a design procedure for hybrid moment frames composed of discretely jointed precast and post-tensioned concrete members. This design procedure, which is intended to provide hybrid connection details equivalent to monolithic frames in terms of strength and toughness, closely follows that recommended by Cheok et al. [2.3] (see Section 2.4.1) except for the changes noted below:

- In the probable strength calculation, the stress in the compression reinforcement is assumed to be $1.25 \cdot f_{sy}$. Hence,

$$f_{sc} = 1.25 \cdot f_{sy} \quad (2.75)$$

- The growth length in the debonded length of the mild steel reinforcement is limited to $5.5 \cdot d_b$, but not less than $2.0 \cdot d_b$. Consequently, Eq. 2.24 is expressed as:

$$\varepsilon_{st} = \frac{\Delta_{st}}{(l_{su} + \alpha_b \cdot d_b)} \quad (2.76)$$

where α_b is a coefficient quantifying the growth length in the debonded length of the mild steel reinforcement.

- Similar to Eq. 2.22 that is used for estimating A_s , the minimum prestressing force ($A_{pt} \cdot f_{se}$) is assumed using Eq. 2.77.

$$A_{pt} \cdot f_{se} \geq \frac{(1.4 \cdot V_D + 1.7 \cdot V_L)}{\phi \cdot \mu} \quad (2.77)$$

where f_{se} is the effective stress in the post-tensioning tendon, and μ is the coefficient of friction.

The nominal moment resistance calculation introduced by Cheok et al. [2.3] (see Section 2.4.1) is not defined in ACI T1.2-03. However, consistent with the ACI T1.2-03 assumptions and the procedure suggested by Cheok et al. [2.3], the nominal moment capacity is also calculated in this report (see Section 3.3 and Section 4.5).

2.5 References

- [2.1] Pampanin, S., Priestley, M. J. N., Sritharan, S., “Analytical Modeling of Seismic Behaviour of Precast Concrete Frames Designed with Ductile Connection,” *Journal of Earthquake Engineering*, Vol. 5, No. 3, 2001, pp. 329-367.
- [2.2] Vernu, S., “Connection and structural level analysis of precast hybrid frame systems,” *Master Thesis, Iowa State University, Ames, Iowa, 2003.*
- [2.3] Cheok, G. S., Stone, W. C., Nakaki, S. D., “Simplified Design Procedure for Hybrid Precast Concrete Connections,” National Institute of Standards and Technology, *SCTR 5765*, 1996.
- [2.4] Stanton, J. F. and Nakaki, S. D., “Design Guidelines For Precast Concrete Seismic Structural Systems,” *PRESSS Report No. 01/03-09, UW Report No. SM 02-02*, The University of Washington and The Nakaki Bashaw Group, Inc., 2002.
- [2.5] ACI Innovative Task Group 1 and Collaborators, *Special Hybrid Moment Frames Composed of Discretely Jointed Precast and Post-Tensioned Concrete Members (ACI T1.2-03) and Commentary (T1.2R-03)*, Michigan, 2003 (In Press).
- [2.6] Cheok, G. S., and Lew, H. S., “Performance of Precast Concrete Beam-to-Column Connections Subject to Cyclic Loading,” *PCI Journal*, Vol. 36, No. 3, 1991, pp. 56-67.
- [2.7] Cheok, G. S., and Lew, H. S., “Model Precast Concrete Beam-to-Column Connections Subject to Cyclic Loading,” *PCI Journal*, July-August, 1993, pp. 80-92.

- [2.8] Stone, W. C., Cheok, G. S., and Stanton, J. F., “Performance of Hybrid Moment Resisting Precast Beam-Column Concrete Connections Subject to Cyclic Loading,” *ACI Structural Journal*, Vol. 92, No. 2, 1995, pp. 229-249.
- [2.9] Stanton, J., Stone, W. C., Cheok, G. S., “A Hybrid Reinforced Precast Frame for Seismic Regions,” *PCI Journal*, Vol. 42, No. 2, 1997, pp. 20-32.
- [2.10] Priestley, M. J. N., and Tao, J., “Seismic Response of Precast Prestressed Concrete Frames With Partially Debonded Tendons,” *PCI Journal*, Vol. 38, No. 1, 1993, pp. 58-69.
- [2.11] Priestley, M. J. N., and Lew, H. S., “The Status of the U.S. Precast Seismic Structural Systems (PRESSS) Program,” *NIST SP 871*, September, 1994, pp. 365-368.
- [2.12] Priestley, M. J. N., “The PRESSS Program – Current Status and Proposed Plans for Phase III,” *PCI Journal*, Vol. 41, No. 2, 1996, pp. 22-40.
- [2.13] Sritharan, S., Igarashi, A., Priestley, M. J. N., Seible, F., “The Design of the PRESSS Five-Story Precast Test Building,” *SEAOC 1999 Convention*, pp. 255-261.
- [2.14] Priestley, M. J. N., Sritharan, S., Conley, J. R., Pampanin, S., “Preliminary Results and Conclusions From the PRESSS Five-Story Precast Concrete Test Building,” *PCI Journal*, Vol. 44, No. 6, 1999, pp. 42-67.
- [2.15] Englekirk, R. E., “An Analytical Approach to Establishing the Seismic Resistance Available in Precast Concrete Frame Structures,” *PCI Journal*, Vol. 34, No. 1, 1989, pp. 92-101.

- [2.16] El-Sheikh, M. T., Sause, R., Pessiki, S., Lu, L., “Seismic Behavior and Design of Unbonded Post-Tensioned Precast Concrete Frames,” *PCI Journal*, Vol. 44, No. 3, 1999, pp. 54-71.
- [2.17] Paulay, T., and Priestley M. J. N., “Seismic Design of Reinforced Concrete and Masonry Buildings,” *John Wiley and Sons, Inc.*, New York, 1992.
- [2.18] Sritharan, S., “Analysis of Concrete Bridge Joints subjected to Seismic Actions,” *PhD Dissertation, University of California, San Diego*, 1998.
- [2.19] Sritharan, S., and Vernu, S., “Analysis and Design of Precast Hybrid Frames,” *Proceedings of the Pacific Conference on Earthquake Engineering*, Paper No. 024, Christchurch, New Zealand, 2003.
- [2.20] Mattock, A. H., “Flexural Strength of Prestressed Concrete Sections by Programmable Calculator,” *PCI Journal*, Vol. 24, No. 1, 1979, pp. 26-37.
- [2.21] ACI Innovation Task Group 1 and Collaborators, *Acceptance Criteria for Moment Frames Based on Structural Testing (T1.1-01) and Commentary (T1.1R-01)*, Michigan, 2001.
- [2.22] International Conference of Building Officials, *Uniform Building Code*, Whittier, CA, 1977.
- [2.23] American Concrete Institute, *Building Code Requirements for Structural Concrete (ACI 318-99) and Commentary (ACI 318R-99)*, Michigan, 1999.

CHAPTER 3

FORMULATION OF VARIOUS ANALYSIS PROCEDURES

3.1 Introduction

The primary purpose of the study reported herein is to validate the PRESSSS guidelines [3.1] proposed for the design of precast hybrid frame connections and to make recommendations to improve the guidelines, where appropriate. In this chapter, an analysis procedure based on the PRESSSS design guidelines, summarized in Section 2.4.2, is first presented. The force equilibrium and strain compatibility conditions are commonly used in the classical reinforced concrete section analysis. However, the strain compatibility condition is applicable to a concrete section only if there exists perfect bond between concrete and steel reinforcement. In hybrid connections, the post-tensioning tendons and mild steel reinforcing bars are debonded at the critical section, thus the strain compatibility condition is violated. In the absence of this condition, the PRESSSS guidelines make a series of assumptions (see Eqs. 3.1 to 3.6) to establish the forces acting on the beam at the critical section and the moment resistance of the hybrid connection. These assumptions are used when formulating the

analysis procedure that will validate the PRESSS guidelines against experimental data. A computer program was developed in Mathcad 2001 Professional [3.2] (see Appendix A) to assist with this validation process.

Second, a modified PRESSS analysis method is presented. Based on the comparisons between the PRESSS analysis results, analytical results reported by Vernu [3.3] using the monolithic beam analogy concept, experimental data, and the outcome of the design validation study on jointed precast wall systems [3.4], several modifications to improve the PRESSS guidelines are reported in Section 3.2.2. The modified PRESSS analysis procedure uses all the recommended changes and a Mathcad program developed for this procedure is given in Appendix B.

Third, an analysis procedure utilizing the ACI T1.2-03 document [3.5] proposed for the design of hybrid moment frames composed of discretely jointed precast and post-tensioned concrete members (Section 3.3) is developed. Next, an alternative analysis method for hybrid frame connections based on the MBA concept is presented in Section 3.4. This concept uses the global displacement estimate and a plastic hinge length equivalent to that adopted for monolithic frame systems to perform analysis at the section. A computer program developed by Vernu [3.3] using the MBA concept was employed in this study.

Finally, a summary of relevant experimental results needed for the validation study is presented in this chapter in Section 3.5, which includes data from Specimens M-P-Z4 and

O-P-Z4 tested at NIST [3.6, 3.7] and the five-story, 60 percent scale precast concrete PRESSS building tested at the University of California, San Diego (UCSD) [3.8].

3.2 PRESSS Guidelines

3.2.1 PRESSS Analysis Procedure

The PRESSS design guidelines [3.1] proposed for unbonded post-tensioned frames with damping are reversed to establish a procedure for analyzing the hybrid frame connections. It is assumed in the proposed guidelines that the post-tensioning tendon is positioned at the mid-height of the beam section and that the connection has equal amounts of top and bottom mild steel reinforcing bars. For a given rotation at the beam-column connection interface, the analysis uses an iterative procedure to determine the corresponding neutral axis depth based on the following assumptions:

- the section dimensions (Figure 3.1) and material properties are known.
- the fiber grout pad experiences no strength degradation.
- stresses in the tension and compression mild steel reinforcing bars are known.

The last assumption stated above is essential to overcome the strain incompatibility condition at the connection interface. As detailed in Table 2.5, the PRESSS guidelines recommended appropriate stress values for the mild steel reinforcement at three states of the system response, which are termed as “first yield”, “design”, and “maximum credible”, respectively. At these three states, the guidelines also suggested anticipated strains in the reinforcement.

Assuming the drifts are 0.5% , 2.0% and 3.5% , respectively, for the three states as per References [3.1, 3.9], the validation of the PRESSS guidelines is performed only at these drifts.

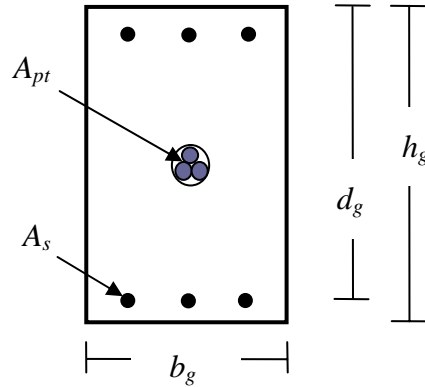


Figure 3.1: Dimensions of the beam section used in the hybrid frame analysis.

The steps involved in the section analysis of the hybrid connection using the PRESSS guidelines are summarized below for a given interface rotation. Incorporating the member flexibilities, the column story drift corresponding to the beam-column interface rotation may be computed as illustrated by Eq. 3.45.

STEP 1: Define reinforcement details, beam dimensions, and material properties

The following variables are defined in this step (see Figure 3.1):

Reinforcement Details

A_{pt} = area of the post-tensioning tendon,

A_s = area of the mild steel reinforcement, and

l_{pu} = unbonded length of the post-tensioning tendon.

Beam Dimensions

h_g = height of the grout pad at the interface,

b_g = width of the grout pad at the interface,

d_g = depth to the tension mild steel reinforcement from the extreme compression fiber in the grout pad, and

ζ = distance from the compression mild steel reinforcement to the extreme compression fiber in the effective section divided by h_g .

The pad dimensions instead of the beam dimensions are used in the analysis because grout pads with dimensions smaller than the beam dimensions may be used as suggested in the PRESSS guidelines [3.1], which reduce the contact area between the precast beam and column.

Material Properties

E_p = elastic modulus of the prestressing steel,

f_{py} = yield strength of the post-tensioning tendon,

f_{pi} = initial (jacking) stress in the post-tensioning tendon, after losses,

f_{sy} = yield strength of the mild steel reinforcement, and

f'_c = unconfined concrete compression strength.

STEP 2: Define stresses in the mild steel reinforcement at the beam-column interface for different system states

Stress in the tension steel (f_{st}):

$$f_{st} = \lambda_{st} \cdot f_{sy} \quad (3.1)$$

Stress in the compression steel (f_{sc}):

$$f_{sc} = \lambda_{sc} \cdot f_{sy} \quad (3.2)$$

The tension (λ_{st}) and compression (λ_{sc}) reinforcement over-strength factors are obtained from Table 2.5 for the selected state of the system.

STEP 3: Select interface rotation (θ)

Using the column drift corresponding to the system state, the interface rotation is obtained using appropriate stiffness for the beams and column. A value for θ may be θ_y , θ_{des} or

θ_{max} , where

θ_y = interface rotation at the beam-column connection at the first yield limit state,

θ_{des} = interface rotation at the beam-column connection at the design limit state, and

θ_{max} = interface rotation at the beam-column connection at the maximum credible limit state.

STEP 4: Estimate neutral axis depth at the selected θ and define η

Using an assumed neutral axis depth, compute

$$\eta = \frac{c}{h_g} \quad (3.3)$$

STEP 5: Calculate stress in the post-tensioning tendon

Using the neutral axis depth from Step 4, calculate the elongation in the tendon due to the imposed interface rotation θ from system geometry (see Figure 2.23) and the corresponding increase in stress.

$$\Delta_{pt} = \theta \cdot (0.5 - \eta) \cdot h_g \quad (3.4)$$

$$\Delta f_{pt} = \frac{\Delta_{pt}}{l_{pu}} \cdot E_p \quad (3.5)$$

The stress in the post-tensioning tendon (f_{pt}) at the selected θ is taken as

$$f_{pt} = (f_{pi} + \Delta f_{pt}) \not\geq f_{py} \quad (3.6)$$

STEP 6: Calculate forces

Using Eqs. 3.7 to 3.9, forces in the post-tensioning tendon, tension steel, and compression steel are calculated at the selected θ .

$$F_{pt} = A_{pt} \cdot f_{pt} \quad (3.7)$$

$$F_{st} = A_s \cdot f_{st} \quad (3.8)$$

$$F_{sc} = A_s \cdot f_{sc} \quad (3.9)$$

The concrete compression force acting on the beam at the interface is found from the equilibrium condition as follows:

$$F_c = F_{pt} + F_{st} - F_{sc} \quad (3.10)$$

STEP 7: Determine neutral axis depth using the Whitney's equivalent stress block

The depth of the equivalent rectangular compression stress block (a) corresponding to the compression force estimated in Eq. 3.10 is determined using

$$a = \frac{F_c}{0.85 \cdot f'_c \cdot b_g} \quad (3.11)$$

Therefore, the parameter (η) defining the neutral axis depth at the interface is obtained from Eq. 3.12.

$$\eta = \frac{a}{\beta_1 \cdot h_g} \quad (3.12)$$

As suggested in Article 10.2.7.3 of the ACI 318-99 Building Code [3.10], a value for β_1 in Eq. 3.12 is obtained from

$$\beta_1 = 0.85 - 0.05 \cdot (f'_c - 4) \quad (3.13)$$

where f'_c is expressed in ksi.

Steps 4 to 7 are repeated until the assumed and calculated neutral axis depth values converge to each other.

STEP 8: Compute moment resistance at the connection at selected θ

Using Eqs. 3.14 to 3.16, the moment resistance contributed by the post-tensioning tendon (M_{pt}), the tension mild steel reinforcement (M_{st}), and the compression mild steel reinforcement (M_{sc}) are determined with respect to the resultant concrete compression force (see Figure 3.2).

$$M_{pt} = F_{pt} \cdot (0.5 - \alpha) \cdot h_g \quad (3.14)$$

$$M_{st} = F_{st} \cdot (1 - \alpha - \zeta) \cdot h_g \quad (3.15)$$

$$M_{sc} = F_{sc} \cdot (\alpha - \zeta) \cdot h_g \quad (3.16)$$

where α is the distance from the resultant concrete compression force to the extreme concrete compression fiber divided by h_g .

Hence, the total moment capacity (M_{cap}) of the connection at the selected θ is

$$M_{cap} = M_{pt} + M_{st} + M_{sc} \quad (3.17)$$

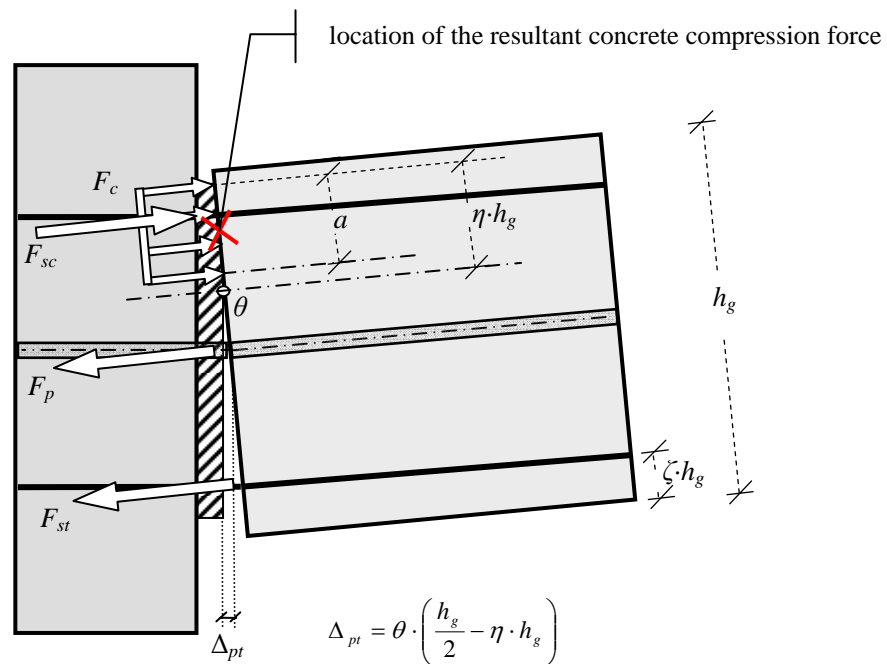


Figure 3.2: Forces acting on a precast concrete hybrid beam.

Repeat Steps 2 to 8 to determine the moment resistance at rotations corresponding to the other two states defined for the hybrid system in Table 2.5. A flowchart summarizing the analysis procedure described above is presented in Figure 3.3.

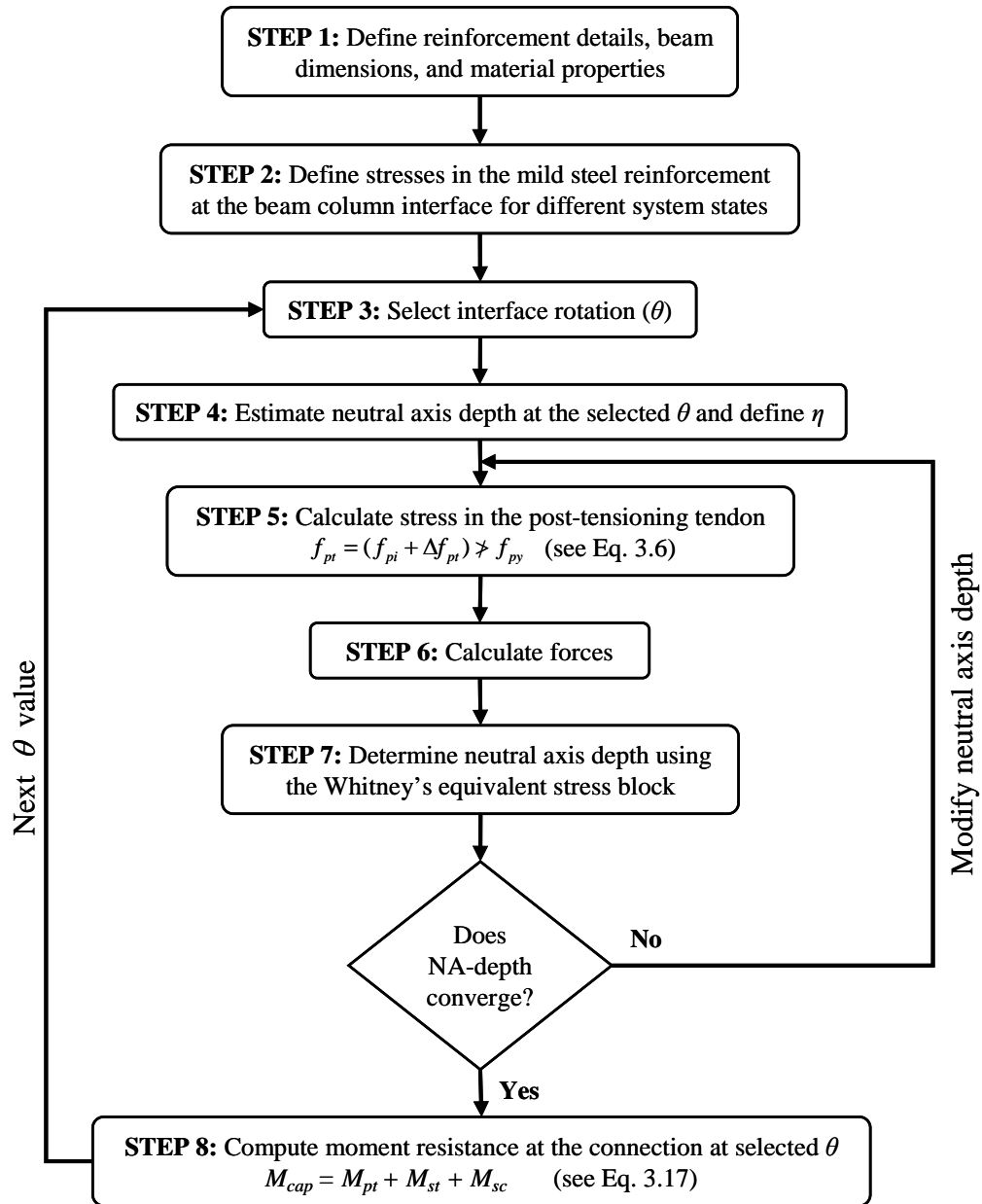


Figure 3.3: A flowchart summarizing the analysis procedure based on the PRESSS design guidelines.

In addition to the moment capacity calculation at the drifts corresponding to the three system states as described above, the following parameters are also examined as part of validating the PRESSS design guidelines proposed for the hybrid frames.

- (a) The final value for the depth of the Whitney's equivalent stress block from Step 7 is compared with that assumed for designing the steel areas. Although the final depth of the compression block is found from an iterative procedure, a depth of $0.1 \cdot h_g$ (i.e., $\alpha = 0.1$) is used for determining the steel areas in the PRESSS guidelines (see Section 2.4.2, Step 8).
- (b) According to the guidelines, the growth in the debonded length of the mild steel reinforcement may be taken as zero for design purposes. However, it is recognized that a growth length of up to 5.5 times the bar diameter (d_b) may be possible for #3 reinforcing bars (see Section 2.4.2, Step 16). Although experimental data are not available, this recommended growth length is compared with different values used in other analytical methods that predict the experimental results with good accuracy.
- (c) Although interface rotations are assumed for the three system states, rotations corresponding to the calculated moments in Eq. 3.17 may be computed from Eq. 3.18 using the section analysis results and the strain estimates given in Table 2.5.

$$\theta_{cal} = \frac{\varepsilon_{st} \cdot (l_{su} + \alpha_b \cdot d_b)}{d_g - \eta \cdot h_g} \quad (3.18)$$

where θ_{cal} is the calculated interface rotation, and α_b is a variable that defines the growth in the debonded length. It appears that α_b may be taken as 5.5 at the yield and maximum credible states for the system.

(d) To ensure adequate re-centering of the hybrid frame connection, the PRESSS guidelines suggest a check using different moment components (see Eq. 2.71). In this check, the top and bottom mild steel reinforcing bars are assumed to be subjected to compression forces at a stage during unloading. The corresponding stresses in both the tension and compression steel are approximated to f_{sy} with an over-strength factor of 1.0 as suggested for the compression steel in Table 2.5. The resisting moments provided by the post-tensioning tendon, and the tension and compression mild steel reinforcement at zero drift are calculated using Eqs. 2.63 to 2.70. If the moment resistance provided by the post-tensioning tendon is greater than that provided by the mild steel reinforcement (i.e., if $M_{pt,0} \geq M_{st,0} + M_{sc,0}$), no residual displacement is expected for the frame after subjected to a design-level earthquake (see Section 2.4.2, Step 15). In addition to providing this check, the observed residual drifts are reported for the test frame in Section 4.7.1.

(e) Although the maximum expected concrete strain is not used in the design calculation, the following average compression strain over the plastic hinge length is suggested by the PRESSS guidelines [3.1] to help quantify the confinement reinforcement in the beam end region adjacent to the connection interface (see Section 2.4.2, Step 17).

$$\varepsilon_c = \frac{\theta \cdot (\eta \cdot h_g)}{l_p} = \frac{\theta}{k_p} \quad (3.19)$$

Experimental data are not available for validating the variables in Eq. 3.19. However, the theoretical values suggested above are compared in Section 4.7.1 with those used for the MBA analysis.

3.2.2 Modified PRESSS Analysis Procedure

In an attempt to improve the connection level analysis presented in Section 3.2.1, and thus the proposed PRESSS design methodology described in Section 2.4.2, a modified procedure for analyzing the hybrid frame connections is presented in this section. The suggested modifications are based on the comparisons of results obtained from the PRESSS analysis procedure with (1) the experimental data provided by Stone et al. [3.6] and Stanton et al. [3.7] for two hybrid frame component tests, (2) the data from the five-story PRESSS building tested at UCSD [3.8], and (3) the analysis results from the monolithic beam analogy concept presented by Vernu [3.3]. Thomas [3.4] performed validation of the PRESSS guidelines proposed for the precast jointed wall systems. The outcomes of this study are also considered when establishing the modified analysis procedure, which emphasizes refining the depths of the equivalent stress block and neutral axis to improve the design of jointed connections. Descriptions of the different modifications suggested for the PRESSS analysis procedure are given below, while Mathcad programs for the analysis and design of hybrid connections based on the modified procedure are presented in Appendix B and Appendix C, respectively.

(a) Stress in Tension Mild Steel Reinforcement

The PRESSS guidelines do not provide an expression for estimating the stress in the tension mild steel reinforcement as a function of the beam-column interface rotation θ , which is required to perform validation of the design guidelines over a range of story drifts. The PRESSS guidelines are, therefore, examined only at three interface rotations as discussed in Section 3.2.1. In the modified analysis procedure, the stress in the tension mild steel reinforcement is assumed to be a function of θ as expressed in Eqs. 3.20a to 3.20c. These equations are based on the assumption that the interface rotations $\theta = 0.001$ rad. and 0.005 rad. are achieved, respectively, when the strain in the tension reinforcement reaches ε_{sy} and ε_{sh} . Eq. 3.20c is derived assuming a parabolic shape for the strain hardening portion of the steel and interface rotations of 0.5%, 2.0% and 3.5% at 1.0, 1.35 and 1.5 times the yield strength of the tension mild steel reinforcement, respectively, in accordance with Table 2.5. The critical values for θ required to derive Eq. 3.20c are based on the analytical results presented by Vernu [3.3] using the MBA concept and the recommended design drift levels in the ACI ITG 1.1 document [3.9].

$$f_{st} = (1000 \cdot \theta) \cdot f_{sy} \quad \text{for} \quad 0 \leq \theta < 0.001 \quad (3.20a)$$

$$f_{st} = f_{sy} \quad \text{for} \quad 0.001 \leq \theta < 0.005 \quad (3.20b)$$

$$f_{st} = (0.84 + 34.4 \cdot \theta - 444.4 \cdot \theta^2) \cdot f_{sy} \quad \text{for} \quad 0.005 \leq \theta \leq 0.035 \quad (3.20c)$$

The resulting relationship between f_{st} and θ from Eq. 3.20 is shown graphically in Figure 3.4.

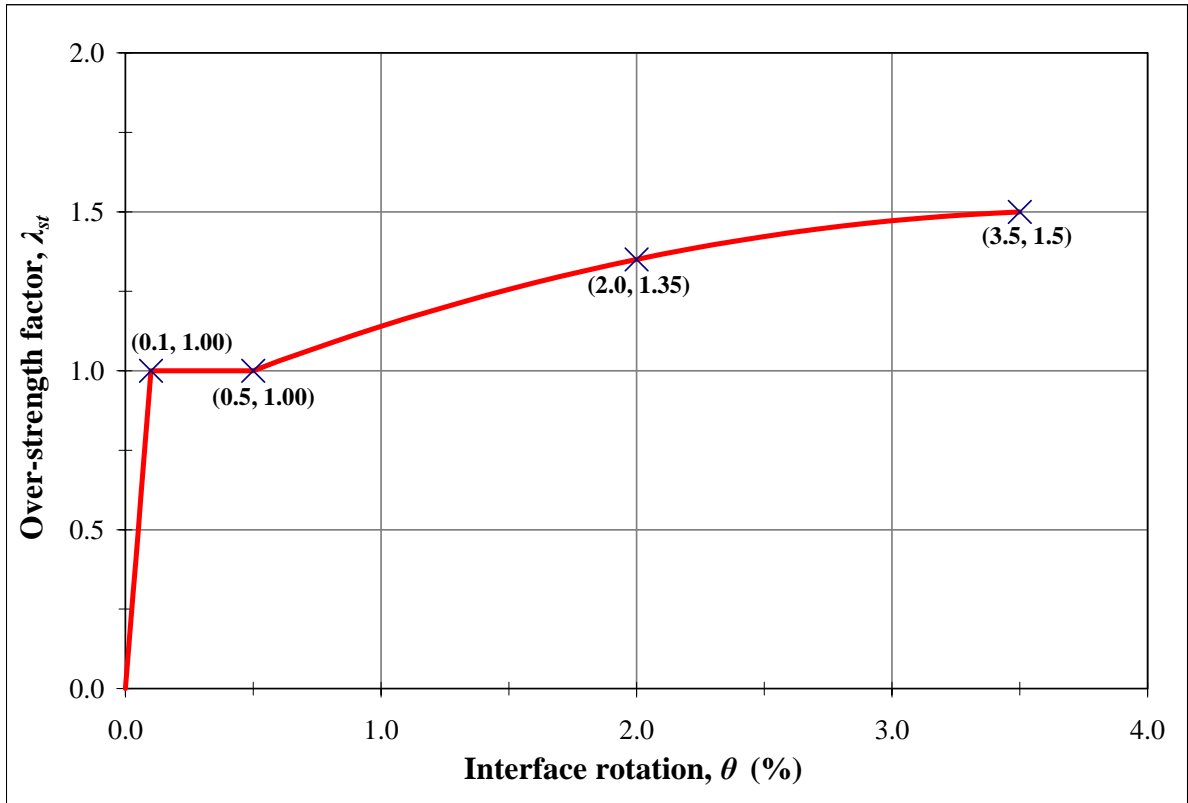


Figure 3.4: An assumed relationship between the over-strength factor and interface rotation for the tension mild steel reinforcement.

(b) Equivalent Rectangular (Whitney) Stress Block

In the PRESSS guidelines, the grout placed at the beam-column interface is assumed to be reinforced with fibers to avoid premature crushing and spalling out of the joint. The fibers also increase the grout strength. Since adequate models are not available to predict the inelastic behavior of the grout, including the confinement effects, it is suggested that the grout should be designed to have strength (f'_g) greater than the concrete strength (f'_c) of the adjoining precast members. Furthermore, accounting for the confinement effects, the

effective concrete compressive strength is taken as $1.6 \cdot f'_c$ at the design drift. Consequently, the depth of the equivalent rectangular stress block at this drift may be defined as:

$$a = \frac{F_c}{0.85 \cdot (1.6 \cdot f'_c) \cdot b_g} \quad (3.21)$$

The 1.6 factor for enhancing concrete strength is based on the results obtained from the MBA analysis results of the hybrid frame connections presented in this report. A similar factor was found to be appropriate in the design validation study conducted for the jointed wall systems [3.4]. Ideally, the analysis should consider two different concrete strengths for the confined and unconfined concrete. However, a single value of 1.6 is used for simplicity.

(c) Neutral Axis Depth

The experimental results of the five-story PRESSS test building and the analysis results of MBA reported for different hybrid frame connections [3.3] showed that the neutral axis depth does not significantly vary for rotations above 1 percent, as illustrated in Figure 3.5. Consistent with this observation, the neutral axis depth in the modified PRESSS analysis procedure is calculated at 2 percent beam-column interface rotation using the equivalent stress block concept and an average concrete compression strength of $1.6 \cdot f'_c$ as per Eq. 3.21. This neutral axis depth is then applied to the analysis of the hybrid connections at interface rotations from 0 to $\theta_{ultimate}$, where $\theta_{ultimate}$ is equal or greater than the beam-column interface rotation corresponding to the extreme drift expected at the system state termed “maximum credible”. Thomas [3.4] also showed that the same approach is applicable to precast jointed wall systems.

Although the neutral axis depth based on Eq. 3.21 is not satisfactory for $\theta < 1\%$ (see Figure 3.5), it is used for all θ values to simplify the analysis procedure and the results are found to be satisfactory. An improvement to this assumption is suggested in Section 4.7.1 for performing analysis at small interface rotations with an increased accuracy. However, such an improvement is not needed in the design procedure, as θ_{des} is likely to be greater than 1 percent.

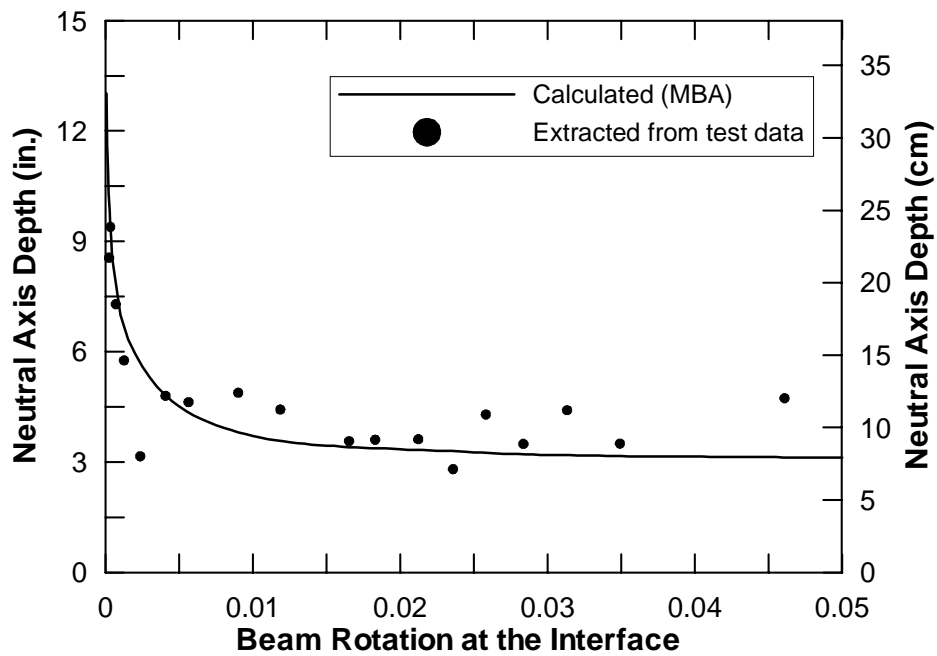
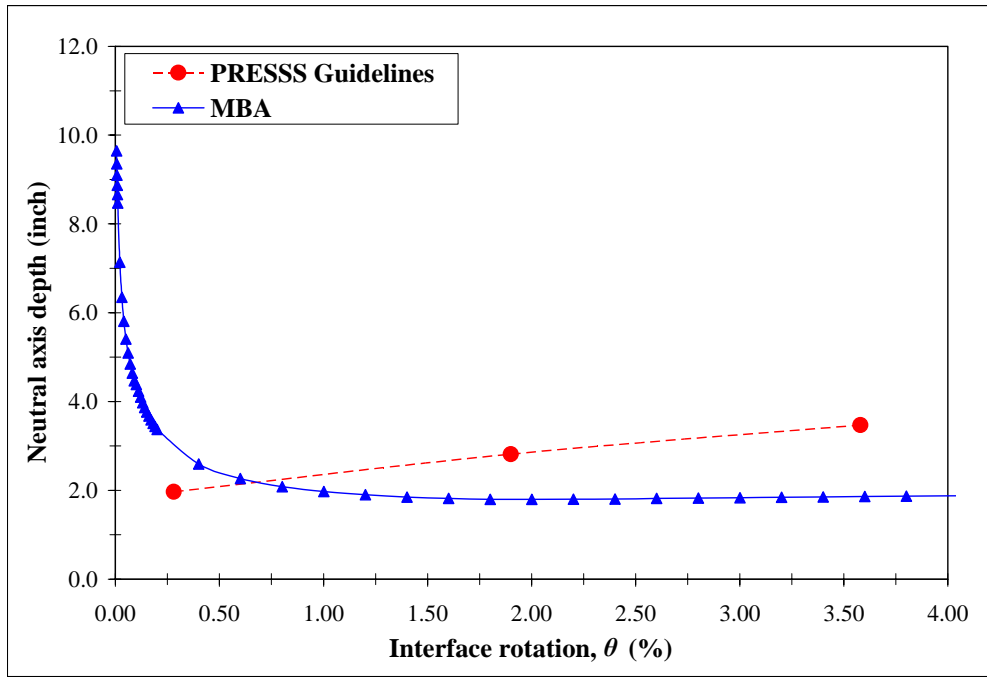


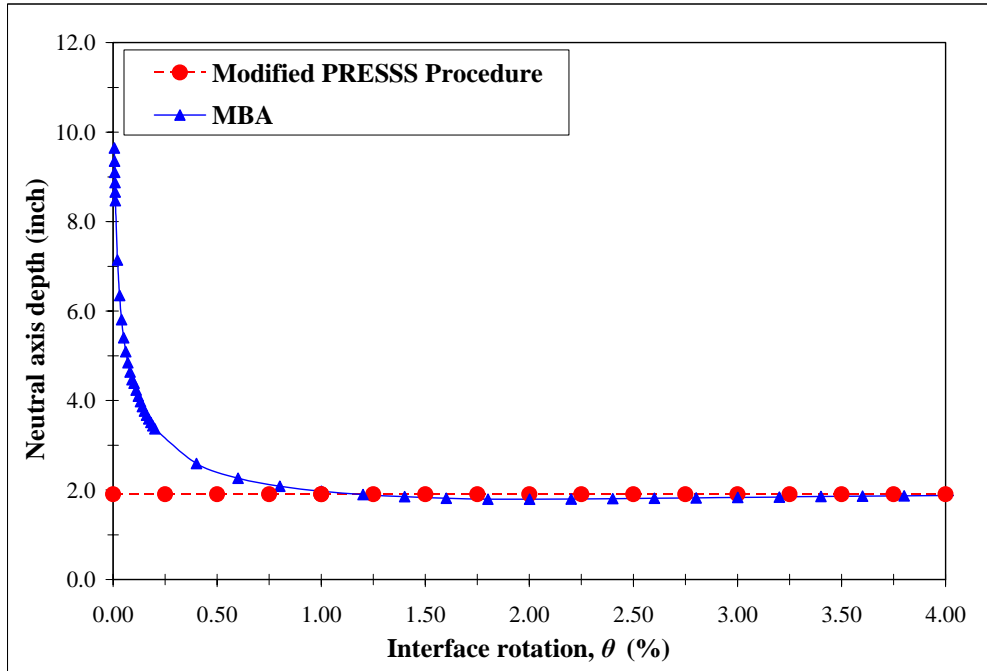
Figure 3.5: The neutral axis depth as a function of interface rotation for the PRESSSS first floor connection reported by Vernu [3.3].

The neutral axis depth calculated for Specimen M-P-Z4 using the PRESSSS guidelines (Section 3.2.1) and the modified PRESSSS analysis procedure (Section 3.2.2) are shown in Figures 3.6a and 3.6b, respectively. The neutral axis depth calculated using the MBA

analysis is also included in both figures to highlight the benefit of the proposed modification to the design guidelines. In addition to the poor correlation as seen in Figure 3.6a, the PRESSS guidelines fail to predict the expected trend in the variation of the neutral axis depth. As the interface rotation increases, the neutral axis depth should reduce or remain unchanged. The equivalent stress concept as used in the PRESSS guidelines (see Eq. 3.11) suggests an increase in the neutral axis depth as the interface rotation increases. The improved neutral axis depth prediction shown in Figure 3.6b closely matches with the MBA results starting at 1 percent interface rotation.



(a) PRESSSS Guidelines (Section 3.2.1)



(b) Suggested neutral axis depth

Figure 3.6: Neutral axis depth comparisons for the NIST test Specimen M-P-Z4.

As discussed earlier, the depth of compression block is assumed to be $0.1 \cdot h_g$ for designing the areas of the prestressing steel and mild steel reinforcement (see Section 2.4.2, Step 6).

The corresponding neutral axis depth is $0.1 \cdot \frac{h_g}{\beta_1}$. Although, this assumed neutral axis depth

differs from that calculated by the equivalent stress block, which is then used to calculate the moment resistance, the assumed value correlates well with the approach presented in the modified analysis as seen in Figure 3.7. Based on this comparison, it is believed that the neutral axis depth assumption used for calculating steel areas in the PRESSS guidelines is adequate.

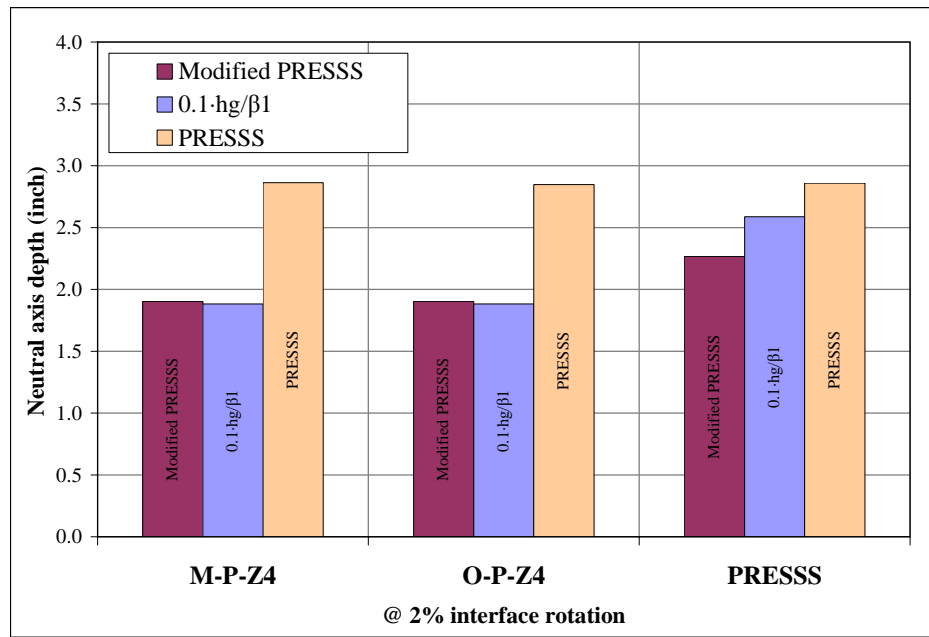


Figure 3.7: The neutral axis depth used for computing steel areas in the PRESSS guidelines with that calculated iteratively using the guidelines for computing moment resistance and that determined using Eq. 3.21 as part of the modified PRESSS analysis procedure at two percent interface rotation.

(d) Stress in Post-tensioning Tendons

For a given interface rotation, the strain in the post-tensioning tendons is calculated from system geometry as discussed in Section 2.3.4 and the corresponding stress is found from Eq. 3.22, which was recommended by Mattock [3.11] for Grade 270 prestressing strands. This modification is introduced to more accurately determine the prestressing stress when the frame is subjected to large drifts. Eq. 3.22 is graphically represented in Figure 3.8.

$$f_{pt} = \varepsilon_{pt} \cdot E_p \cdot \left[0.020 + \frac{0.98}{\left[1 + \left(\frac{\varepsilon_{pt} \cdot E_p}{1.04 \cdot f_{py}} \right)^{8.36} \right]^{\frac{1}{8.36}}} \right] \quad (3.22)$$

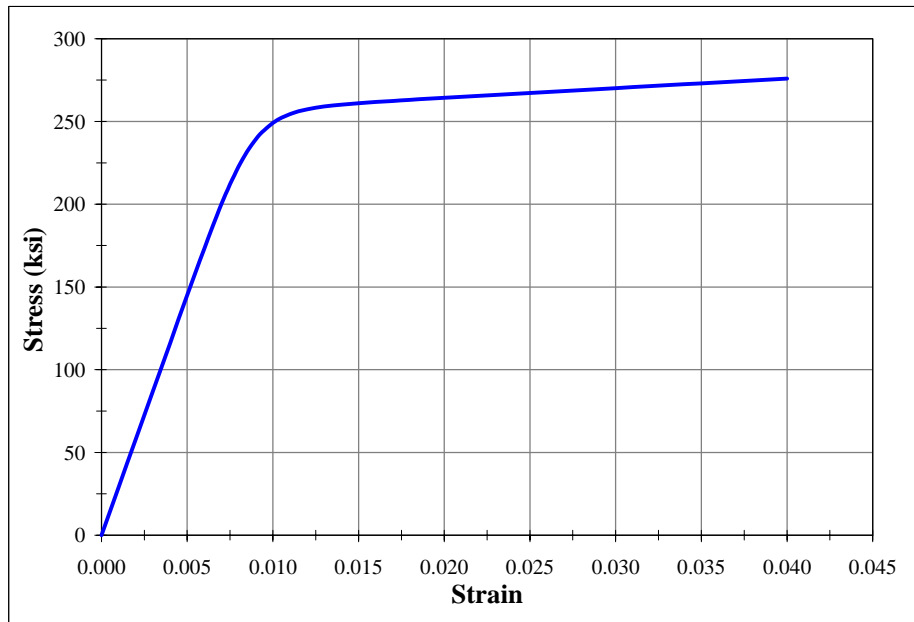


Figure 3.8: The theoretical stress-strain curve for Grade 270 prestressing strands proposed by Mattock [3.11].

(e) Decompression Point

In the modified PRESSS analysis procedure, the decompression point is also identified, which defines the beginning of a crack opening at the connection interface and corresponds to the condition when the stress in the extreme concrete compression fiber reaches zero at the beam end adjacent to the column face (see Figure 3.9). Accounting for the precompression introduced by the initial prestressing force (Figure 3.9a), and assuming a linear strain distribution at the critical section due to moment induced by decompression force F_{decomp} (Figure 3.9b), the following equations are used to determine the corresponding moment resistance and the beam end rotation at the free end. The decompression moment (M_{decomp}) is calculated from the elastic flexure formula $\sigma = \frac{M \cdot c}{I}$ and substituting the values for the neutral axis depth (c) and moment of inertia (I):

$$M_{decomp} = \frac{\sigma_i \cdot I}{c} \quad (3.23a)$$

where σ_i is the stress in the beam due to the initial prestressing and I is based on the gross section properties. Hence,

$$\sigma_i = \frac{F_{pi}}{b_g \cdot h_g} \quad (3.23b)$$

$$F_{pi} = f_{pi} \cdot A_{pr} \quad (3.23c)$$

$$I = \frac{1}{12} \cdot b_g \cdot h_g^3, \text{ and} \quad (3.23d)$$

$$c = \frac{h_g}{2} \text{ at this elastic state} \quad (3.23e)$$

where F_{pi} is the force in the tendon due to initial prestressing. At this stage the beam end rotation at the decompression point (γ_{decomp}) can be calculated by integrating the area of the elastic curvature along the member. Hence,

$$\gamma_{decomp} = \frac{1}{2} \cdot \phi_e \cdot l \quad (3.24a)$$

$$\phi_e = \frac{\varepsilon_i}{c}, \text{ and} \quad (3.24b)$$

$$\varepsilon_i = \frac{\sigma_i}{E_c} \quad (3.24c)$$

where ε_i is the strain in the beam due to initial prestressing, and E_c is the elastic modulus of concrete. The corresponding beam-to-column interface rotation is taken as zero.

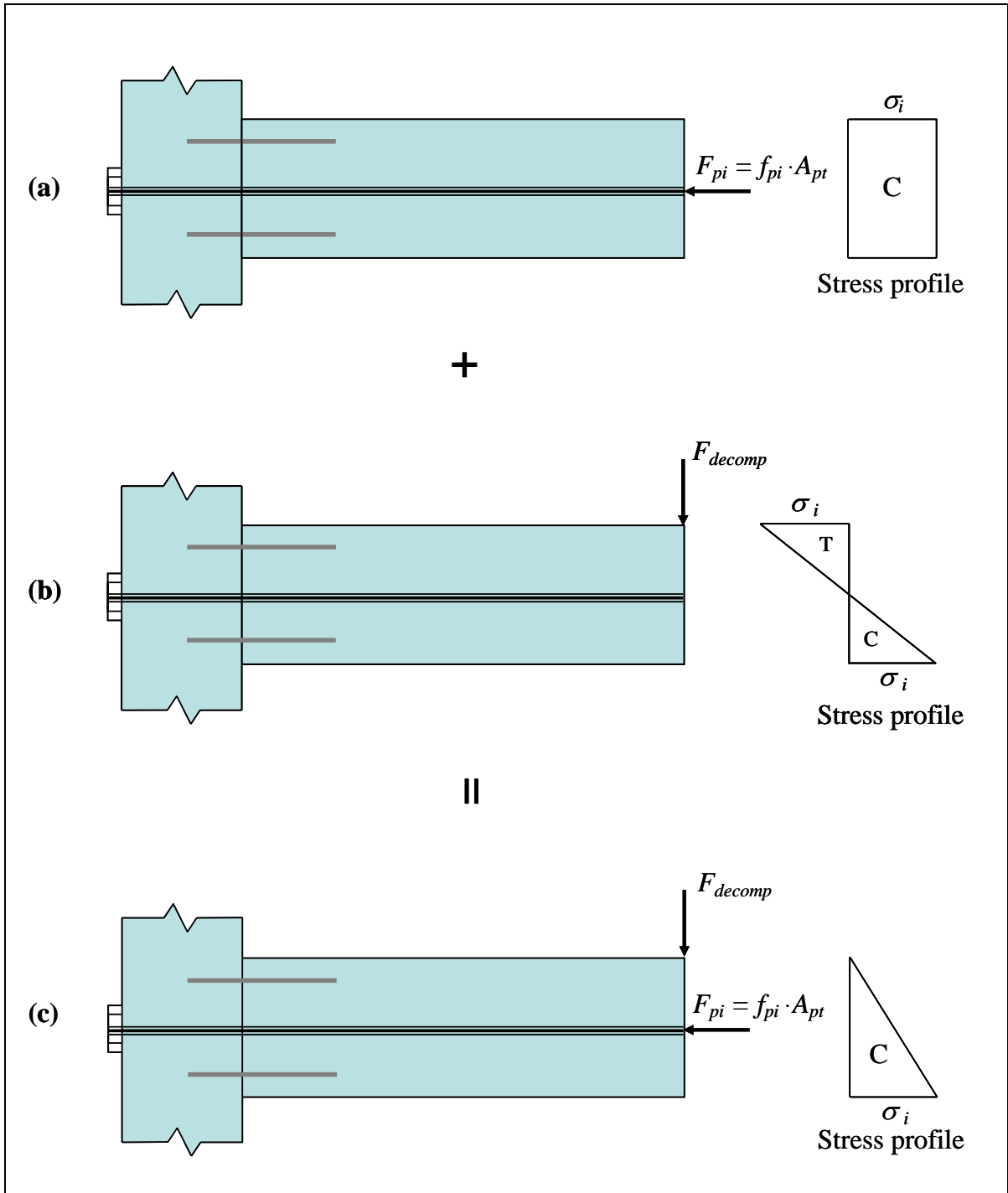


Figure 3.9: Stress profiles at the critical section caused by (a) prestressing force, (b) lateral decompression force F_{decomp} , (c) superposition of (a) and (b).

(f) Growth in Debonded Length of the Mild Steel Reinforcement

The purpose of debonding the mild steel reinforcement over a short length adjacent to the beam-column interface was previously discussed in Section 3.2.1. It was also noted that due to high cyclic strains at the interface, growth in the debonded length of these bars would occur. The magnitude of this growth depends on the confinement provided to the concrete surrounding the bar, bar strength, grout strength, and load history [3.1]. For bars grouted into a pre-formed hole in concrete as used in the NIST hybrid frame tests, Cheok and Stone [3.12] found the growth in the debonded length to be 5.5 times the bar diameter (d_b) for #3 bars, which is suggested as an upper bound value for the growth length in the PRESSSS design guidelines and in the ACI T1.2-03 document [3.5]. However, the MBA analysis uses a total growth length of $0.3 \cdot f_y \cdot d_b$, yielding a value of $18 \cdot d_b$ for G60 reinforcing bars. Although the growth length is not required when driving the moment-rotation behavior using the modified analysis procedure, a value of the debonded length may be calculated using the strain and interface rotation from an equation similar to Eq. 3.18. From Eq. 3.20, the stress in the mild steel is known at a selected θ . The corresponding strain that is needed in Eq. 3.18 is found from the stress-strain curve proposed for the mild steel reinforcement by Dodd and Restrepo-Posada [3.13]. The results are reported in Section 4.7.1.

Incorporating the modifications suggested above, the flowchart presented in Figure 3.3 for the PRESSSS guidelines may be altered as shown in Figure 3.10 to perform the hybrid frame connection analysis using the modified analysis procedure.

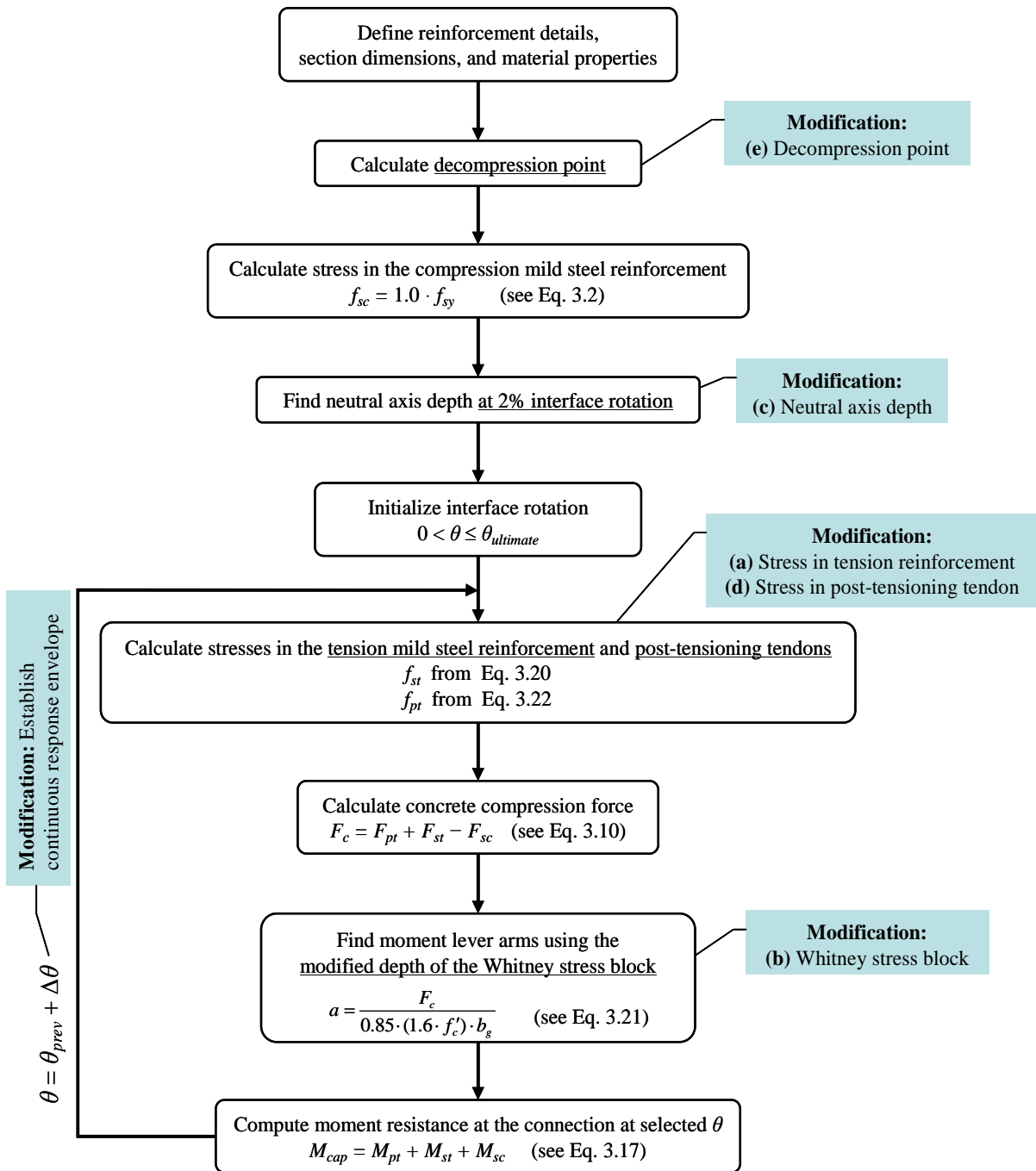


Figure 3.10: A flowchart summarizing the modified PRESSS analysis procedure.

3.3 ACI T1.2-03 Analysis Procedure

The design procedure suggested for hybrid moment frames composed of discretely jointed precast and post-tensioned concrete members in Section 2.4.3 is reversed to establish the ACI T1.2-03 analysis procedure. This procedure closely follows that presented in Section 3.2.1 for the PRESSS guidelines with the following changes:

- The moment calculations are performed at two drift levels. First, at the maximum drift of 3.5 percent, the moment resistance defines the probable moment strength of the hybrid frame connection. The second set of calculations establishes the nominal moment resistance at the onset of strain hardening in the tension reinforcement. The corresponding drift is taken as 0.5 percent as suggested in Figure 3.4. As discussed in Section 2.4.1, this moment definition is based on the design recommendations of Cheok et al. [3.14], which appear to be the basis for the ACI T1.2-03 document.
- The stress in the compression reinforcement is taken as $1.25 \cdot f_{sy}$ and $1.0 \cdot f_{sy}$ for the probable and nominal moment calculations, respectively.
- In the probable moment strength calculation, the tension reinforcement stress is approximated to f_{su} , where f_{su} is the ultimate tensile strength of the mild steel reinforcement.
- The nominal moment resistance of the hybrid connection is calculated using f_{sy} as the stress in the tension reinforcement. Approximating the nominal moment resistance to 70 percent of the probable moment capacity has also been suggested to

be acceptable [3.14]. However, in this report, the nominal moment is determined using f_{sy} in the tension reinforcement.

3.4 Monolithic Beam Analogy (MBA)

To overcome the strain incompatibility condition at the hybrid frame connection resulting from the use of unbonded reinforcement, an additional equation is introduced in the monolithic beam analogy [3.3, 3.15]. This is achieved by computing the global displacement at the beam end using a plastic hinge length similar to that adopted for monolithic frame systems. As shown below, MBA enables strains at the connection to be expressed as a function of rotation at the beam-to-column connection interface. Together with the force equilibrium condition and theoretical stress-strain relations for concrete, mild steel reinforcement, and post-tensioning tendon, the MBA concept can be used to establish a continuous moment-rotation response envelope for a hybrid frame system. Presented below are a summary of critical equations derived from the MBA concept, information on material models, and descriptions of various analysis steps.

STEP 1: Establish a relationship between concrete strain and neutral axis depth

Consistent with the MBA concept, the total beam end displacement of a hybrid frame is equated to that of a monolithically connected beam to establish a relationship between the compressive strain in the extreme concrete fiber and the neutral axis depth at the connection interface (see Figure 2.17).

$$\Delta_{precast} = \Delta_{monolithic} \quad (3.25)$$

For an equivalent monolithic beam, as shown in Figure 3.11, the total displacement at the beam end is given by the sum of an elastic and a plastic component:

$$\Delta_{monolithic} = \Delta_{elastic} + \Delta_{plastic} \quad (3.26)$$

The plastic curvature is assumed to be constant over an equivalent plastic hinge length, where l_p is defined as $0.08 \cdot l + 0.15 \cdot f_{sy} \cdot d_b \leq 0.3 \cdot f_{sy} \cdot d_b$, $0.15 \cdot f_{sy} \cdot d_b$ is the strain penetration length, and is identified as l_{sp} in Figure 3.11a. Therefore, the plastic rotation of the beam is given by

$$\theta_p = l_p \cdot \phi_p \quad (3.27)$$

where ϕ_p is the plastic curvature. The plastic displacement is the first moment of the plastic curvature area and hence,

$$\Delta_{plastic} = (l_p \cdot \phi_p) \cdot l \quad (3.28)$$

where $\phi_p = (\phi_u - \phi_e)$ (see Figure 3.11b). The elastic displacement includes the components due to the member elastic deformation and strain penetration:

$$\Delta_{elastic} = \left(\frac{1}{2} \cdot \phi_e \cdot l \right) \cdot \frac{2}{3} l + \left(\frac{2}{3} \cdot l_{sp} \cdot \phi_e \right) \cdot l \quad (3.29)$$

The first term on the right-hand side of Eq. 3.29 corresponds to the member elastic deformation (Δ'_e) which is the first moment of the elastic curvature area along the beam in Figure 3.11b. The second term accounts for the strain penetration and is based on a strain penetration length of $\frac{2}{3} \cdot l_{sp}$ as suggested for elastic response by Sritharan [3.16].

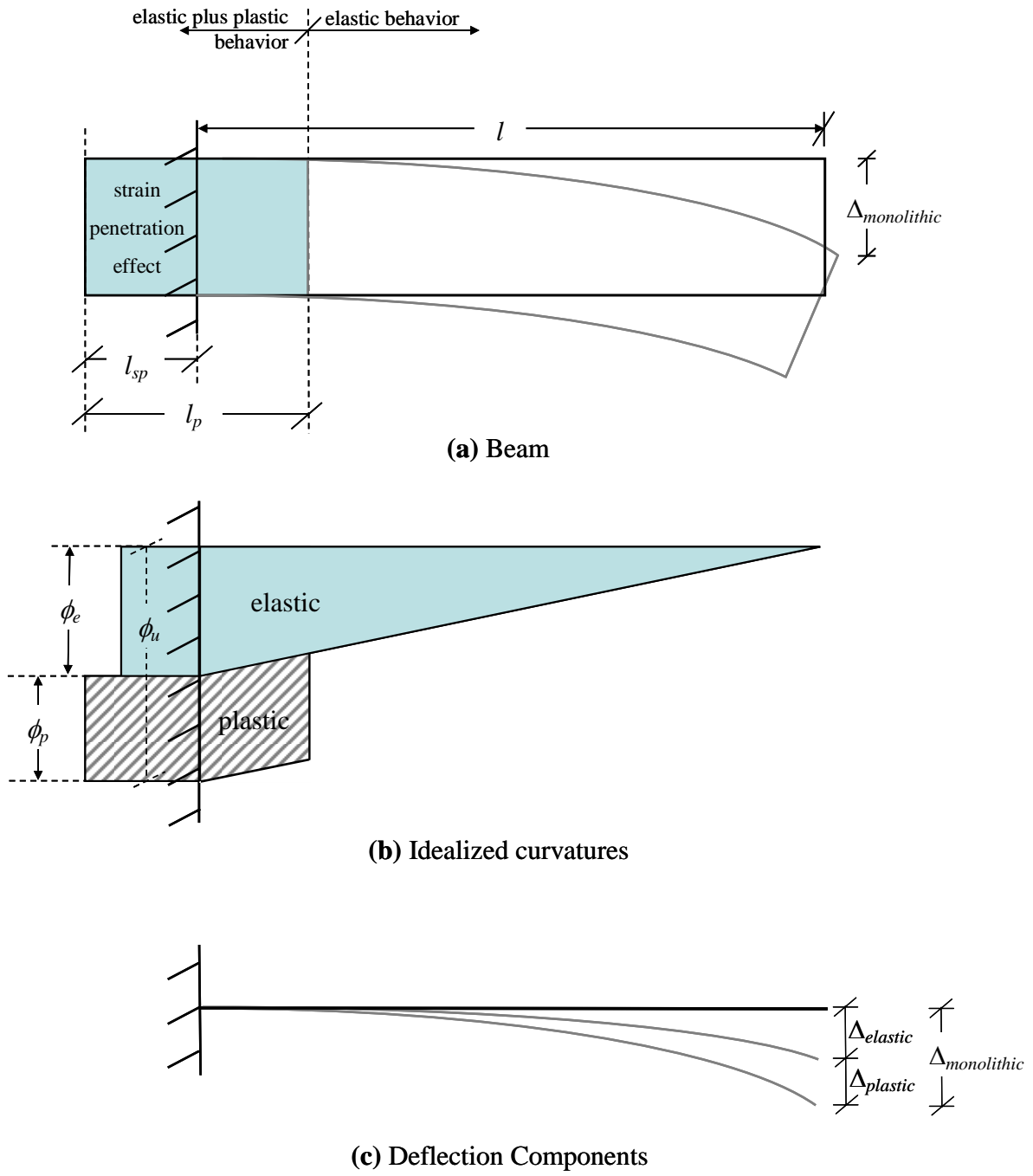


Figure 3.11 An idealization for the response of an equivalent monolithic beam.

For a beam connected with the hybrid concept, the total displacement at the beam end is due to the elastic curvature along the beam (Δ_e^*) and rotation at the beam-column interface as illustrated in Figure 3.12. Thus,

$$\Delta_{precast} = \Delta_e^* + \Delta_\theta \quad (3.30)$$

As a result of rotation θ at the interface

$$\Delta_\theta = \theta \cdot l \quad (3.31)$$

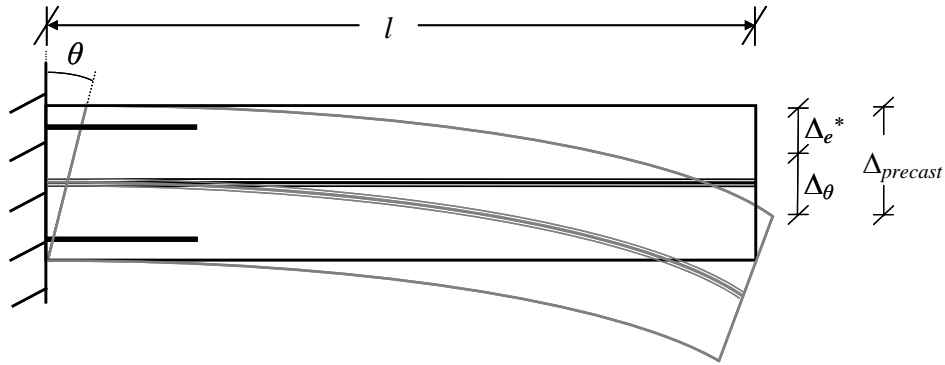


Figure 3.12: Deflection components at the end of a hybrid beam.

Approximating the difference in the elastic deformations along the beams in both cases to

$\left(\frac{2}{3} \cdot l_{sp} \cdot \phi_e\right) \cdot l$, Eqs. 3.25 to 3.31 are combined to establish the following relationship:

$$\theta \cdot l = \left(\frac{4}{3} \cdot l_{sp} \cdot \phi_e\right) \cdot l + [l_p \cdot (\phi_u - \phi_e)] \cdot l \quad (3.32)$$

For the monolithically connected beam, the ultimate curvature may be expressed as:

$$\phi_u = \frac{\epsilon_c}{c} \quad (3.33)$$

Note in References [3.3, 3.15], the elastic deformations of the two beams were taken as equal, which led to an equation similar to Eq. 3.32 with a $\frac{2}{3}$ factor instead of $\frac{4}{3}$. Substituting Eq. 3.33 in Eq. 3.32, the concrete strain is expressed as a function of rotation at the beam-column interface as follows:

$$\varepsilon_c = \left[\theta + \phi_e \cdot \left[l_p - \frac{4}{3} \cdot l_{sp} \right] \right] \cdot \frac{c}{l_p} \quad (3.34)$$

STEP 2: Calculate strains

Strain in Tension Mild Steel Reinforcement

Equation 2.16 suggested by Pampanin et al. [3.15] is used for defining the tension mild steel strain as a function of neutral axis depth. Note that the beam section may be defined using variables h_g and b_g as discussed in Section 3.2.1. Accordingly, these variables are used in Eqs. 3.35 to 3.37.

$$\varepsilon_{st} = \frac{(d_g - c) \cdot \theta + \frac{2}{3} \cdot l_{sp} \cdot \frac{f_{st}}{E_s}}{l_{su} + 2 \cdot l_{sp}} \quad (3.35)$$

Strain in Compression Mild Steel Reinforcement

In order to estimate the strain in the compression mild steel reinforcement, the following expression suggested by Vernu [3.3] is used.

$$\varepsilon_{sc} = \frac{1}{2} \cdot \left[\frac{(c - d'_g)}{c} \cdot \varepsilon_c + \varepsilon_{sy} \cdot \frac{M}{M_y} \right] \quad (3.36)$$

where d'_g is the distance from the compression mild steel reinforcement to the extreme compression fiber in the grout pad.

Strain in Post Tensioning Tendons

From geometry (see Figure 2.18), the relationship between the post-tensioning tendon strain and neutral axis depth is defined by Eq. 2.19 [3.3, 3.15]. Hence,

$$\varepsilon_{pt} = \frac{\left(\frac{h_g}{2} - c\right) \cdot \theta}{l_{pu}} + \varepsilon_{pi} \quad (3.37)$$

STEP 3: Determine stresses

Concrete Models

The stress-strain response of the confined and unconfined concrete are obtained from Eqs. 3.38a to 3.38h, as suggested by Mander et al. [3.17].

$$f'_c = \frac{f'_{cc} \cdot x \cdot r}{r - 1 + x'} \quad (3.38a)$$

$$f'_{cc} = f'_c \cdot \left(2.254 \cdot \sqrt{1 + \frac{7.94 \cdot f'_l}{f'_c}} - \frac{2 \cdot f'_l}{f'_c} - 1.254 \right) \quad (3.38b)$$

$$x = \frac{\varepsilon_c}{\varepsilon_{cc}} \quad (3.38c)$$

$$\varepsilon_{cc} = \varepsilon_{co} \cdot \left(1 + 5 \cdot \left[\frac{f'_{cc}}{f'_c} - 1 \right] \right) \quad (3.38d)$$

$$r = \frac{E_c}{E_c - E_{\text{sec}}} \quad (3.38e)$$

$$E_c = 4700 \cdot \sqrt{f'_c} \quad (3.38f)$$

$$E_{\text{sec}} = \frac{f'_{cc}}{\epsilon_{cc}} \quad (3.38g)$$

$$f'_l = K_e \cdot f_l \quad (3.38h)$$

where f'_c = unconfined concrete strength (ksi), ϵ_{co} = strain corresponding to f'_c ,
 f'_{cc} = confined concrete strength, E_c = elastic modulus of concrete,
 f'_l = effective lateral confinement pressure, E_{sec} = secant modulus of concrete at f'_{cc} ,
 ϵ_c = concrete strain, K_e = confinement effectiveness coefficient, and
 ϵ_{cc} = strain corresponding to f'_{cc} , f_l = maximum lateral confining pressure (zero for unconfined concrete).

Mild Steel Reinforcement

The following equations suggested by Dodd and Restrepo-Posada [3.13] are used to determine the stress corresponding to a strain in the mild steel reinforcement.

$$f_{st} = E_s \cdot \epsilon_{st} \quad \text{for} \quad \epsilon_{st} \leq \epsilon_{sy} \quad (3.39a)$$

$$f_{st} = f_{sy} \quad \text{for} \quad \epsilon_{sy} < \epsilon_{st} \leq \epsilon_{sh} \quad (3.39b)$$

$$f_{st} = f_{su} + (f_{sy} - f_{su}) \cdot \left(\frac{\epsilon_{su} - \epsilon_{st}}{\epsilon_{su} - \epsilon_{sh}} \right)^p \quad \text{for} \quad \epsilon_{sh} < \epsilon_{st} \leq \epsilon_{su} \quad (3.39c)$$

$$p = \frac{\log \left[\frac{f_{su} - f_x}{f_{su} - f_{sy}} \right]}{\log \left[\frac{\epsilon_{su} - \epsilon_x}{\epsilon_{su} - \epsilon_{sh}} \right]} \quad (3.39d)$$

where (ϵ_{st}, f_{st}) is a point on the stress-strain curve, (ϵ_{sy}, f_{sy}) is the yield point, (ϵ_{sh}, f_{sy}) is the point at the onset of strain hardening, (ϵ_{su}, f_{su}) defines the ultimate strength, and (ϵ_x, f_x) is an arbitrary point on the hardening portion of the curve. All of these variables are identified in Figure 3.13 that shows a typical stress-strain behavior of mild steel reinforcement up to the ultimate strength.

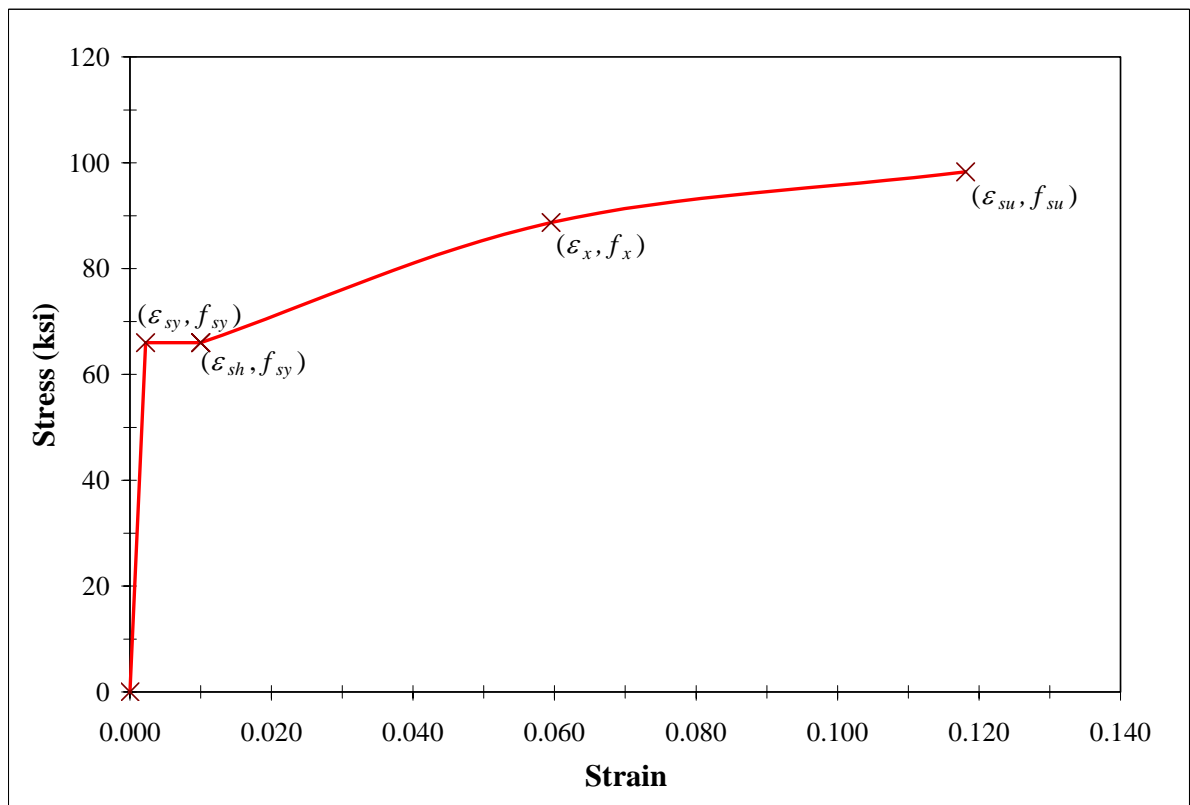


Figure 3.13: The data points required to define the stress-strain curve given by Eq. 3.39.

Post-tensioning Tendons

Eq. 3.22 recommended by Mattock [3.11] is used to define the stress-strain behavior of Grade 270 post-tensioning tendons.

STEP 4: Calculate forces

Using Steps 2 and 3 and an assumed neutral axis depth, the stresses in the post-tensioning tendons and mild steel reinforcement are estimated at a selected interface rotation θ . The corresponding forces in the post-tensioning tendons, and the tension and compression mild steel reinforcement are calculated by multiplying the stresses with the respective cross sectional areas as follows:

$$F_{pt} = A_{pt} \cdot f_{pt} \quad (3.40)$$

$$F_{st} = A_s \cdot f_{st} \quad (3.41)$$

$$F_{sc} = A_s \cdot f_{sc} \quad (3.42)$$

Similarly, a concrete stress profile is obtained from Mander's model [3.17] using the assumed neutral axis depth and the extreme fiber compression strain from Eq. 3.34. Dividing this stress profile into many rectangular regions, the resultant compression force and its location are obtained numerically using the Simpson's rule.

STEP 5: Check equilibrium

The resultant concrete compression force and forces in the steel reinforcement obtained in Step 4 are checked to see if the following equilibrium condition is satisfied.

$$F_c + F_{pt} + F_{st} + F_{sc} = 0 \quad (3.43)$$

If Eq. 3.43 is not satisfied, the neutral axis depth is increased and Steps 1 to 5 are repeated until a solution satisfying the equilibrium condition is obtained.

STEP 6: Calculate moment resistance

By taking the moments about the resultant concrete compression force (see Figure 3.2), moment contributions by the forces in the post-tensioning tendons, tension mild steel reinforcement, compression mild steel reinforcement, and the total moment resistance of the connection at θ are readily determined.

To establish a continuous moment rotation envelope for the hybrid connection, Steps 1 to 6 are repeated for θ values from 0 to $\theta_{ultimate}$. The procedure described above based on the MBA concept is summarized in a flowchart in Figure 3.14.

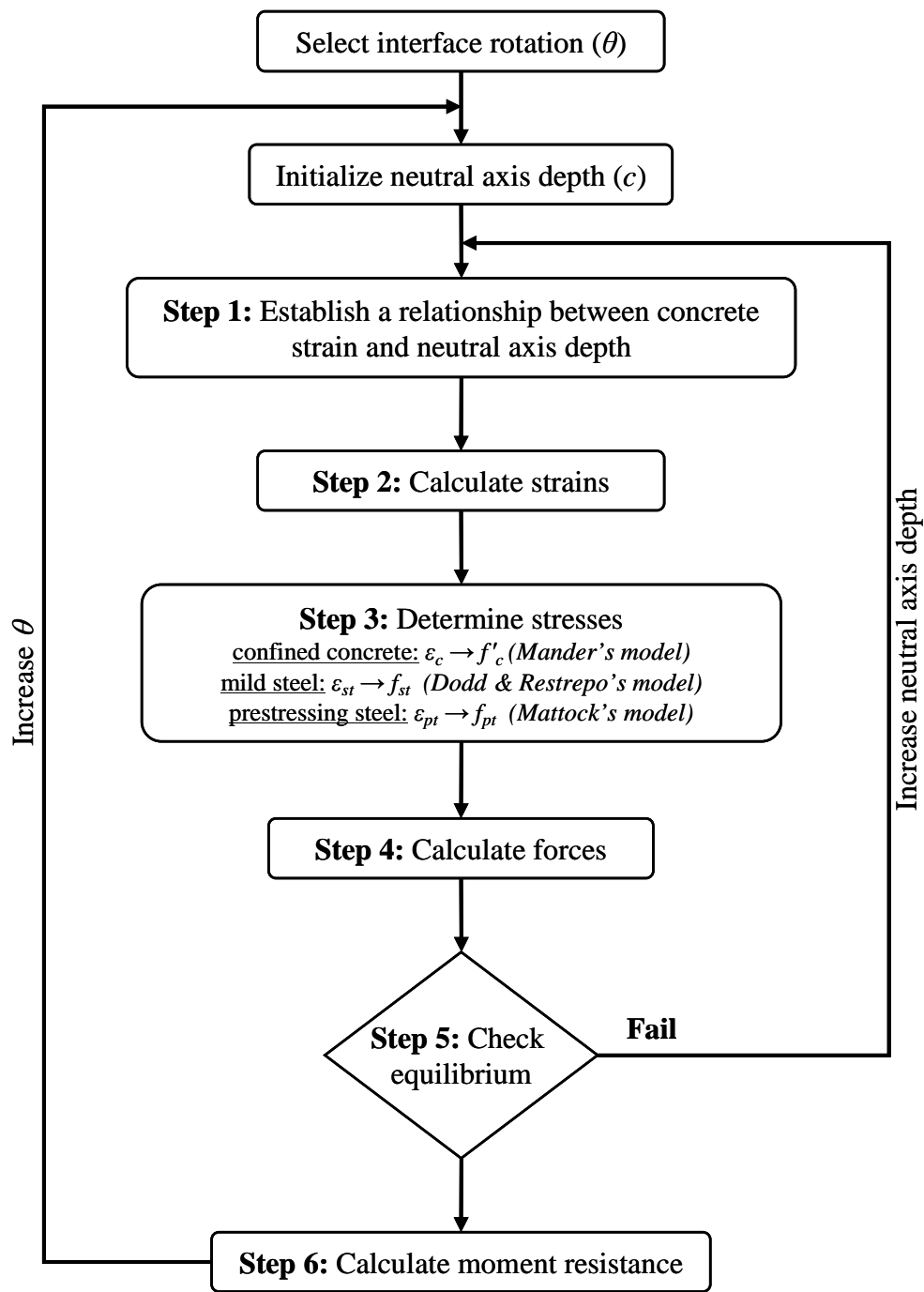


Figure 3.14 A flowchart summarizing the analysis based on the MBA concept.

3.5 Summary of Experimental Data

Several experimental studies on hybrid frame systems are briefly described in Section 2.2. This section summarizes the test data selected for validation of the design guidelines and other analysis methods described in this chapter.

Data from two specimens, namely M-P-Z4 and O-P-Z4, from Phase IV-B of the NIST test program and the PRESSSS five-story test building are mainly used for the validation study. The NIST test modeled an interior building frame, whereas the PRESSSS test building incorporated a three-story hybrid frame in one of two seismic frames. As shown in Table 3.1, the PRESSSS hybrid frame connection was based on equal moment contributions from the post-tensioning tendon and mild steel reinforcement. However, the NIST design was based on developing a larger percentage of moment resistance from the post-tensioning steel. More information on the test configuration, measured properties, and test results are provided below.

Table 3.1 Comparison of moment contributions and measured residual interface rotations (θ_{res}) after the frame is subjected to about 2% drift.

Test Unit	M_{pt}^* (kip-in)	M_{st}^* (kip-in)	θ_{res}^\dagger (%)
M-P-Z4	702 (73%)	260 (27%)	0.15
O-P-Z4	670 (58%)	484 (42%)	0.58
PRESSSS building	1576 (52%)	1540 (51%)	0.26

Note: * Target at design drift, † based on experimental data

3.5.1 Specimens M-P-Z4 and O-P-Z4

As detailed in Section 2.2.1, M-P-Z4 and O-P-Z4 tests were conducted at 1/3-scale in Phase IV-B of the NIST test program. Figure 2.1 provides overall dimensions and setup used for the component tests. The section details of these two specimens were the same except for the amount of mild steel reinforcement. Three No. 3 (0.375-in diameter) mild steel reinforcing bars in M-P-Z4 and two No. 3 reinforcing bars in O-P-Z4 were used at the top and bottom of the beam section in addition to the three 1/2-inch diameter, Grade 270 unbonded prestressing tendons at the mid-height of the beam. Mild steel bars were debonded in the beam end region over one-inch distance from each face of the column to avoid premature bar fracture.

Measured Properties

For satisfactory comparison of the analysis results with the test data, the measured material properties were used in the analysis wherever possible. Table 3.2 summarizes the measured properties obtained for Specimens M-P-Z4 and O-P-Z4. The post-tensioning tendons in these specimens were unbonded over 59.5 in. and bonded over 32 in. (see Figure 2.1). Accounting for the potential growth in the unbonded length of the tendons due to strain penetration, l_{pu} reported in Table 3.2 is taken as the effective unbonded length of tendons in both specimens. Using the development length equation (see Eq. 3.44), suggested in Article 12.9 of the ACI 318-99 Building Code [3.10], to model the force drop linearly in the bonded region, the effective length represents the tendon length over which f_{pt} may be assumed to be constant as shown in Figure 3.15. According to this figure, the stress in the bonded tendon

at the beam free end (i.e., point C) is not zero. In the test units, an anchorage device was placed at this location, which would have prevented the tendon from slipping.

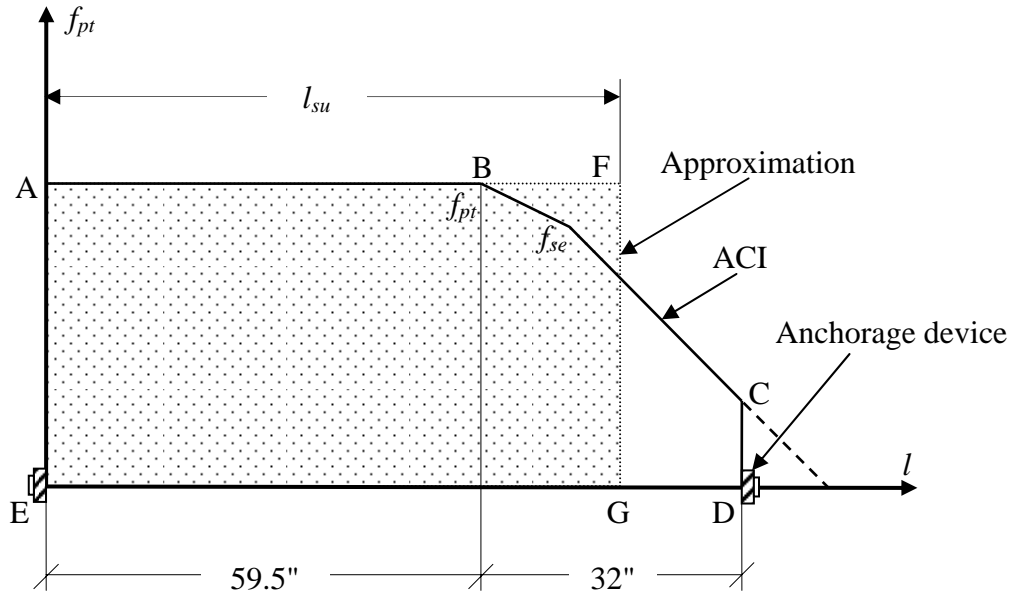


Figure 3.15 The post-tensioning tendon stress distribution assumed along the beam length for the NIST test units.

The ACI code equation for computing the development length is as follows:

$$l_d = \left(\frac{f_{se}}{3} \cdot d_{pt} \right) + (f_{pt} - f_{se}) \cdot d_{pt} \quad (3.44)$$

where l_d is the development length, f_{se} is the effective stress in the post-tensioning tendon, and d_{pt} is the diameter of the tendon bundle. The first term on the right-hand side of Eq. 3.44 represents the transfer length of the tendon. This is the bonded length of tendon required to develop the prestress f_{se} . The second term represents the additional length over which the tendon should be bonded so that the stress f_{pt} may develop in the tendon at the nominal

strength of the member. The value for l_{pu} was found by equating area ABCDE to area AFGE.

Table 3.2 Measured properties of Specimens M-P-Z4 and O-P-Z4.

Parameters	M-P-Z4	O-P-Z4
Beam dimensions: (see Figure 2.1)		
h , height of the beam (in); $h_g = h$	16	16
b , width of the beam (in); $b_g = b$	8	8
d , depth to the tension reinforcement from the extreme compression fiber (in)	15	15
d' , distance from the compression reinforcement to the extreme compression fiber (in)	1	1
l , length of the beam (in)	39.75	39.75
s , distance from the pin to the nearest member (in)	6	6
Reinforcement details:		
A_{pt} , area of the post-tensioning tendon (in ²)	0.459	0.459
A_s , area of the mild steel reinforcement (in ²)	0.22	0.33
d_b , diameter of the mild steel reinforcement (in)	0.375	0.375
l_{pu} , effective unbonded length of the post-tensioning tendon (in)	40.15	40.34
l_{su} , debonded length of the mild steel reinforcement at each interface (in)	2.0	2.0
Material Properties:		
E_p and E_s , elastic modulus of the prestressing and mild steel (ksi)	29000	29000
f_{py} , yield strength of the post-tensioning tendon (ksi)	247.95	247.95
f_{pi} , initial (jacking) stress in the post-tensioning tendon, after losses (ksi)	120.640	111.707
f_{sy} , yield strength of the mild steel reinforcement (ksi)	61.190	75.835
ϵ_{sy} , yield strain of the mild steel reinforcement	0.00211	0.00262
ϵ_{sh} , strain in the mild steel reinforcement at the onset of strain hardening	0.006	0.006
f_{su} , ultimate tensile strength of the mild steel reinforcement (ksi)	97.585	113.100
ϵ_{su} , ultimate strain of the mild steel reinforcement	0.088	0.078
f'_c , unconfined concrete compression strength (ksi)	6.815	6.815

Moment-Rotation Response

Using the actuator force applied to the column, the measured column drift, and the information on the test setup, the beam moment resistance at the connection interface was established as a function of interface rotation. The beam end moment was obtained assuming equal and opposite reactions at the pin-ends of the beams (see Figure 2.2). Using frame geometry and member flexibilities, the rotation at the hybrid connection was computed as a function of the column drift. In this calculation, the columns and beams were assumed to have effective moment of inertias of 40% and 60% of the gross moment of inertias, respectively. Accounting for the elastic deformation of the beams and columns at a given drift and ignoring the beam-to-column joint shear deformation, the following relationships were derived for the NIST test specimens and PRESSS test building, respectively:

$$\theta_{drift} = 0.85 \cdot \theta + 4.08 \cdot 10^{-6} \cdot M_{cap} \quad (3.45a)$$

$$\theta_{drift} = 0.91 \cdot \theta + 1.92 \cdot 10^{-6} \cdot M_{cap} \quad (3.45b)$$

where θ_{drift} is the column story drift in radians, θ is the rotation at the connection interface in radians, and M_{cap} is the beam moment resistance at the connection in kip-inches. Using Eq. 3.45a, the beam end moment is represented as a function of connection interface rotation for M-P-Z4 and O-P-Z4 in Figures 3.16 and 3.17, respectively.

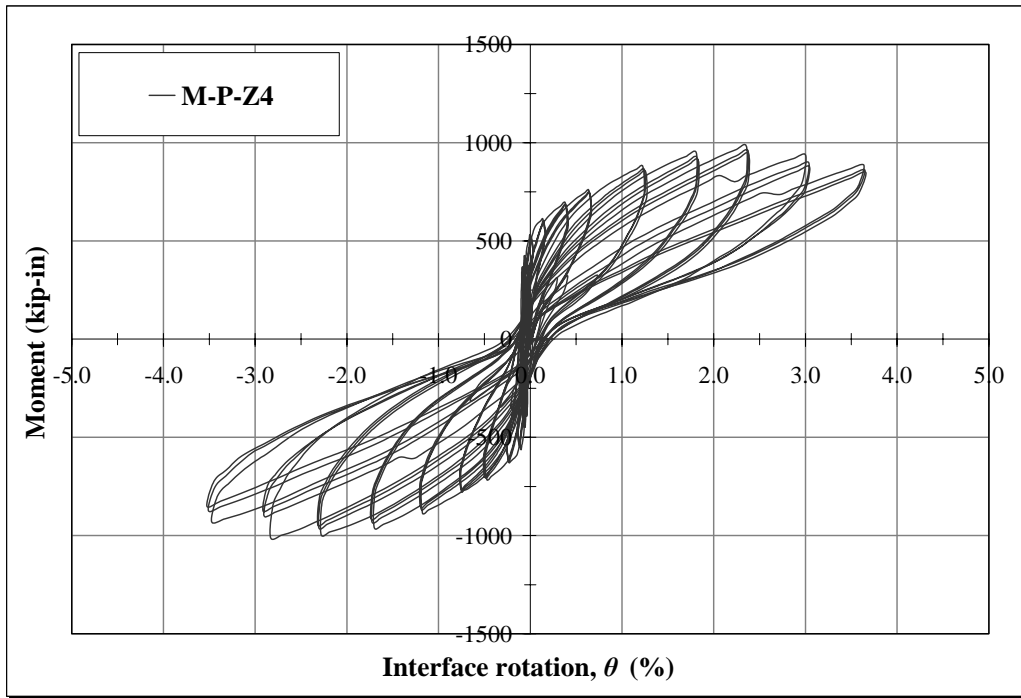


Figure 3.16: Beam moment resistance as a function of interface rotation for M-P-Z4.

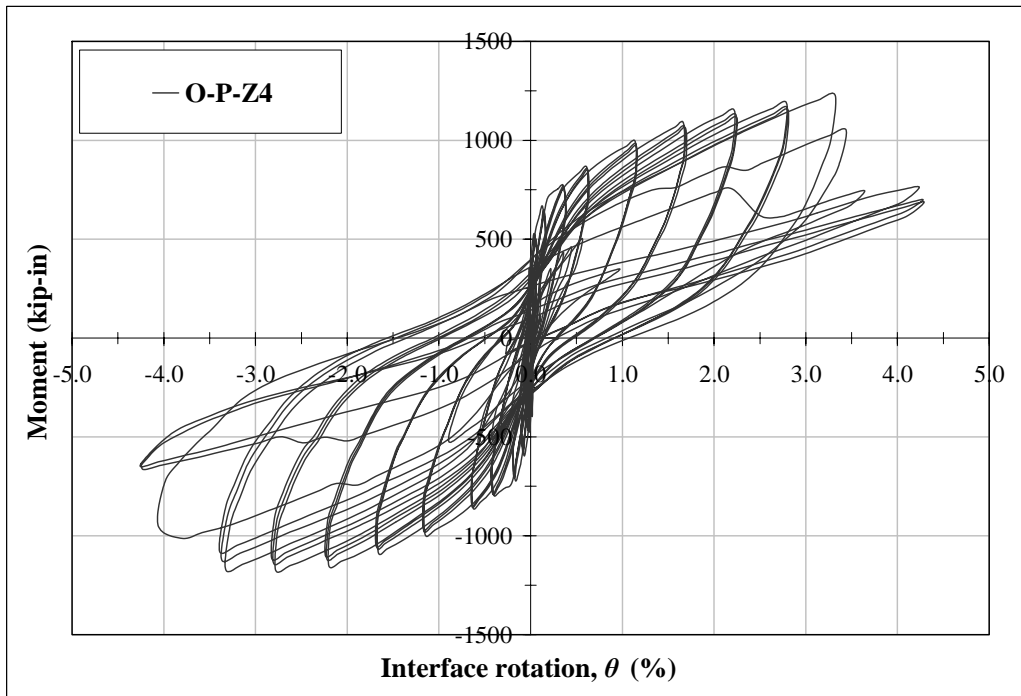


Figure 3.17: Beam moment resistance as a function of interface rotation for O-P-Z4.

Stress in Post-tensioning Tendons

As shown in Figure 2.3, the force in the post-tensioning tendon was continuously monitored during the M-P-Z4 and O-P-Z4 tests. Using the peak values obtained in the first-push and pull direction loading cycles at different drifts, the data shown in Figure 3.18 and 3.19 are established for evaluating the accuracy of the theoretical prediction for the increase in prestressing force as a function of column drift.

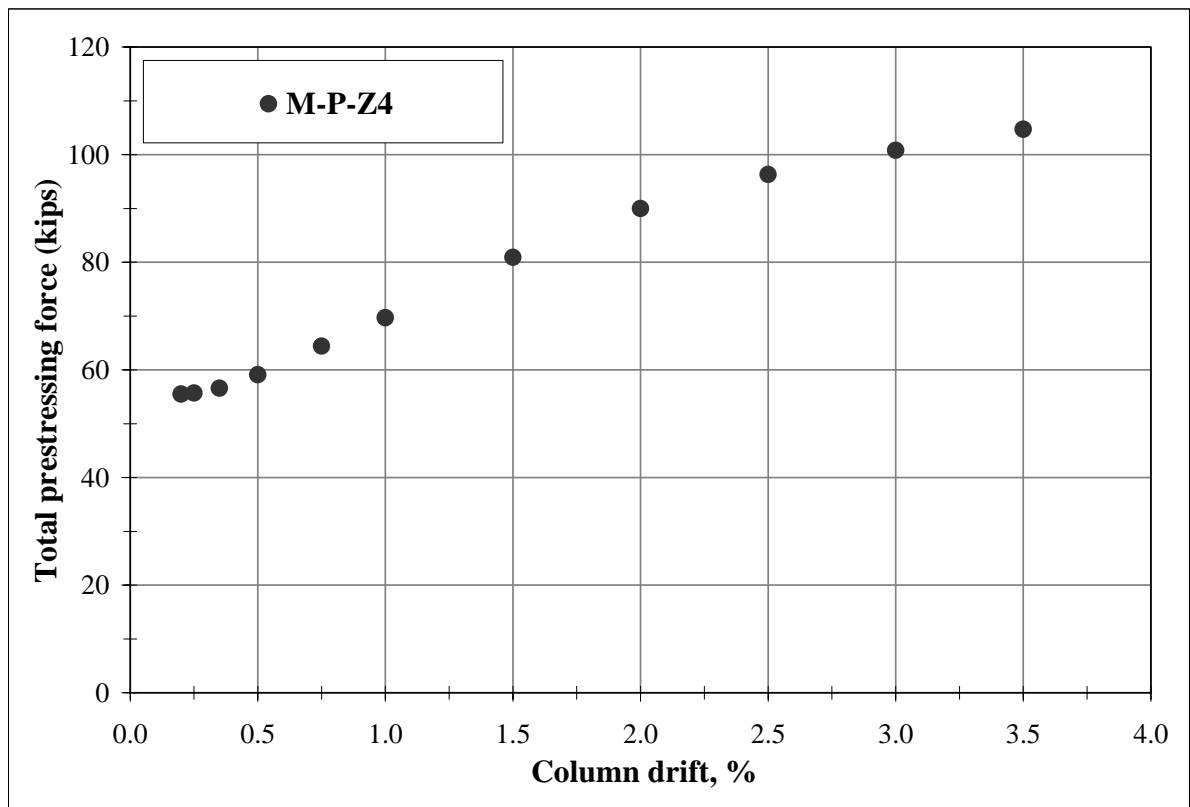


Figure 3.18: Total prestressing force as a function of story drift for Specimen M-P-Z4.

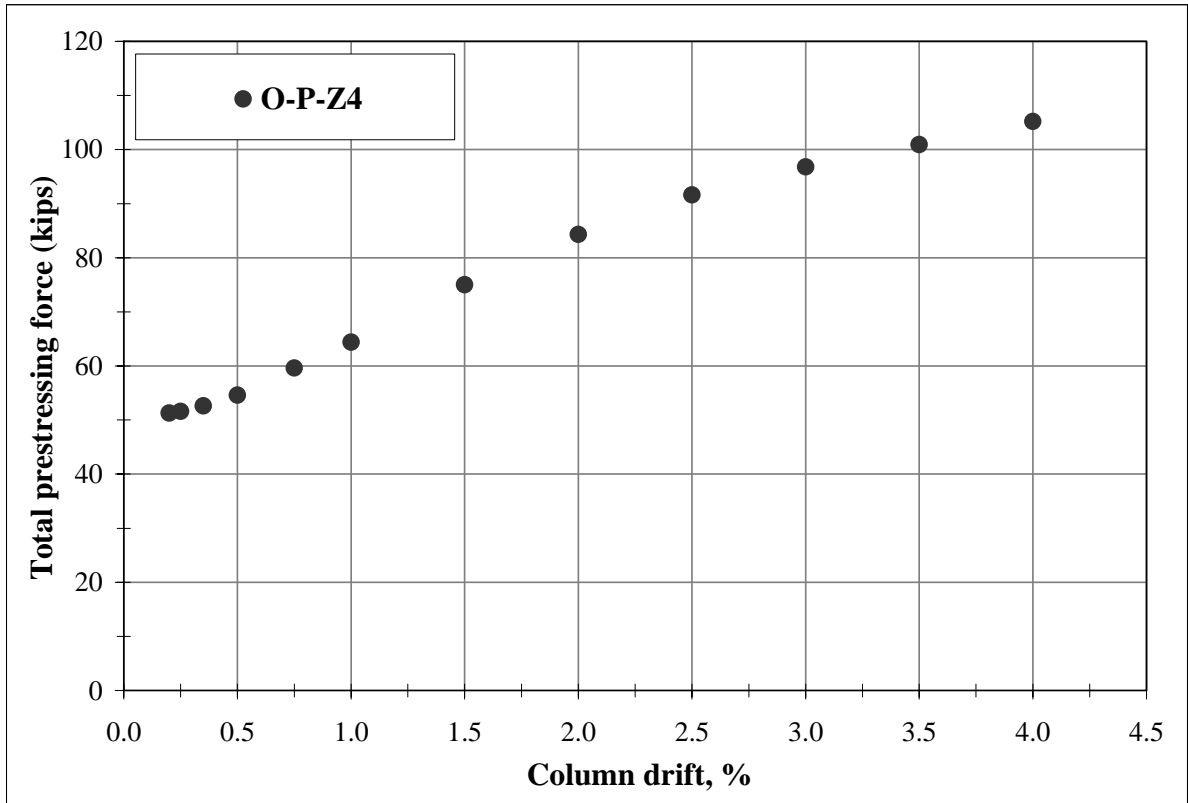


Figure 3.19: Total prestressing force as a function of story drift for Specimen O-P-Z4.

3.5.2 Hybrid Frame in the PRESSS Building

The measured properties and selected experimental results from the hybrid frame in the PRESSS building tested at UCSD [3.8] are summarized below.

Measured Properties

Table 3.3 summarizes the relevant properties for the hybrid frame in the PRESSS building, which is a two-bay, three-story frame. As shown in Figure 3.20, the beam section included chamfers at three corners, which were accounted for when determining the beam stiffness.

The contact area between the precast beam and column was reduced through the use of grout pads which had dimensions smaller than those of the beam section. Hence, the cross-sectional dimensions of the grout pads were used in the hybrid frame connection analysis.

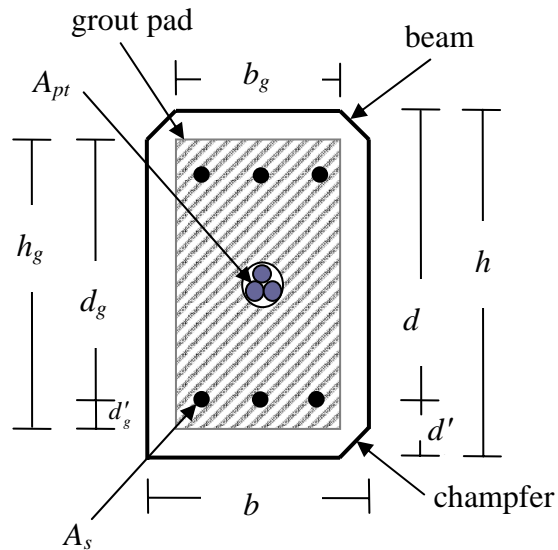


Figure 3.20 Variables defining the dimensions of the beam and grout pad as well as the connection details for the precast hybrid frame in the PRESSS test building.

Table 3.3 Parameters describing the hybrid frame in the PRESSS test building.

Parameters	Value
Frame dimensions:	
Bay length (in)	180
Story height (in)	90
Beam dimensions:	
ch , depth of the chamfer (in)	0.5
h , height of the beam (in)	23
h_g , height of the grout pad at the interface ($h_g=h-2ch$) (in)	22
b_g , width of the grout pad at the interface ($b_g=b-2ch$) (in)	13
d_g , depth to the tension reinforcement from the extreme compression fiber in the grout pad (in)	19.75
d' , distance from the compression reinforcement to the extreme compression fiber (in)	2.75
l , length of the beam (in)	81
Reinforcement details:	
A_{pt} , area of the post-tensioning tendon (in ²)	0.918
A_s , area of the mild steel reinforcement (in ²)	0.88
d_b , diameter of the mild steel reinforcement (in)	0.750
l_{pu} , unbonded length of the post-tensioning tendon corresponding to one hybrid connection (in)	106.5
l_{su} , debonded length of the mild steel reinforcement at the first floor (in)	4.0
Material properties for the connections at the first floor:	
E_p and E_s , elastic modulus of the prestressing and mild steel (ksi)	29000
f_{py} , yield strength of the post-tensioning tendon (ksi)	255.0
f_{pi} , initial (jacking) stress in the post-tensioning tendon, after losses (ksi)	118.95
f_{sy} , yield strength of the mild steel reinforcement (ksi)	68.026
ϵ_{sy} , yield strain of the mild steel reinforcement	0.00235
ϵ_{sh} , strain in the mild steel reinforcement at the onset of strain hardening	0.0138
ϵ_x , arbitrary strain in the mild steel reinforcement in the hardening region	0.0523
f_x , stress corresponding to ϵ_x (ksi)	91.601
f_{su} , ultimate tensile strength of the mild steel reinforcement (ksi)	97.873
ϵ_{su} , ultimate strain of the mild steel reinforcement	0.099
f'_c , unconfined concrete compression strength (ksi)	8.8

The stress-strain behavior of the mild steel reinforcement was established by subjecting steel coupons to uniaxial tension tests and data obtained from one such test is shown in Figure 3.21. The critical parameters identified in this figure are used in the analysis of the PRESSS building presented in this report.

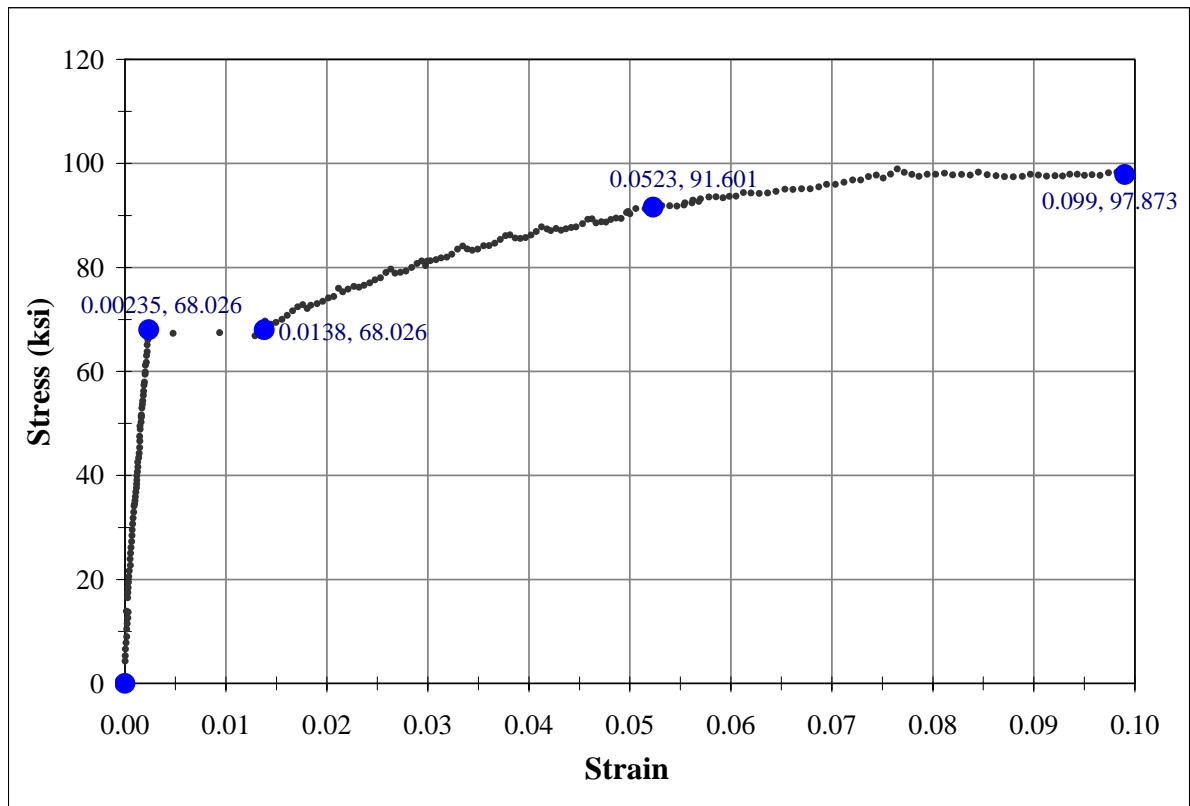
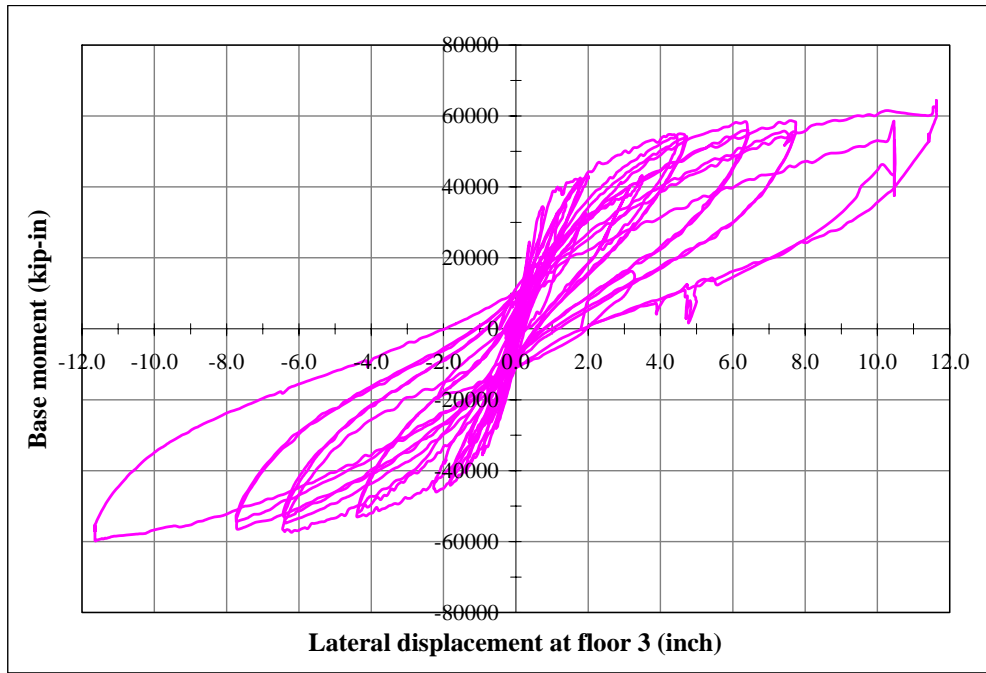


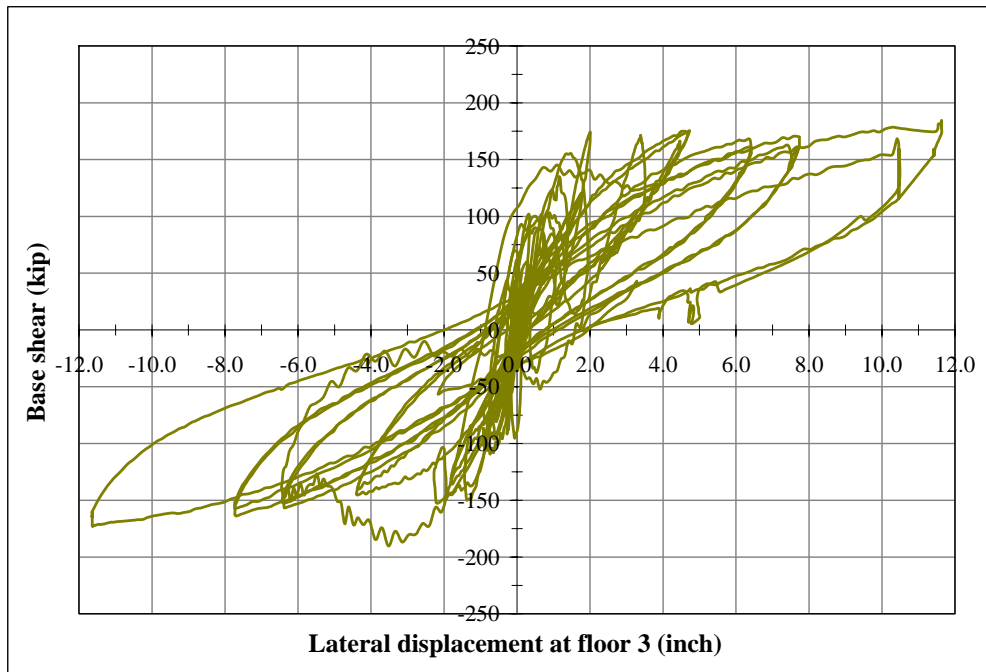
Figure 3.21: Stress-strain behavior of the mild steel reinforcement used in the PRESSS hybrid frame.

Frame Response

The observed base moment and base shear of the three-story hybrid frame as a function of the third floor lateral displacement are shown in Figures 3.22a and 3.22b, respectively. These reported results are based on all significant tests conducted in the frame direction of the building [3.18, 3.19]. The response envelope of the frame is analytically obtained in Section 4.7.2 using a pushover analysis.



(a) Base moment as a function of the third floor lateral displacement



(b) Base shear as a function of the third floor lateral displacement

Figure 3.22: Measured response of the hybrid frame in the PRESSS test building.

Neutral Axis Depth

Using three displacement transducers placed at each face of the interior column at the first floor of the hybrid frame, the neutral axis depth as a function of beam end rotation was investigated by Vernu [3.3]. Figure 3.23 presents the extracted data, in which EQ and IT represents the pseudo-dynamic and inverse triangular tests at different intensity levels [3.8].

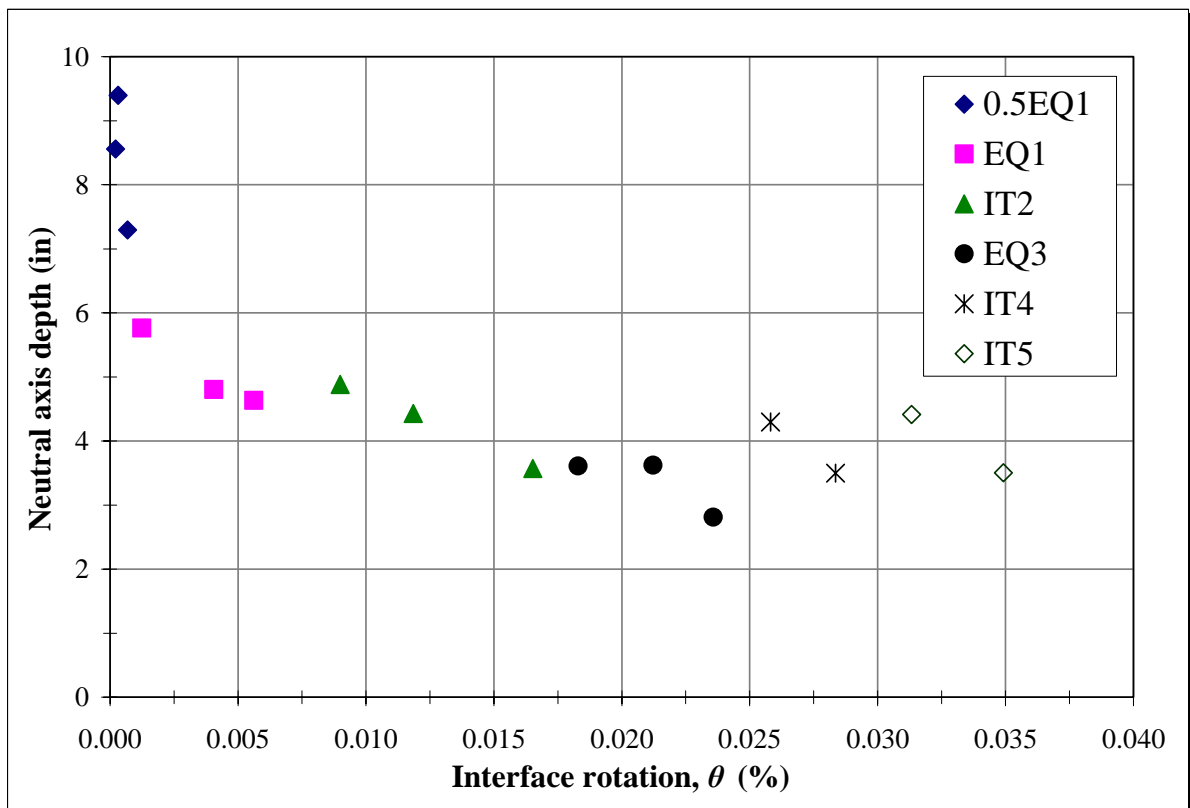


Figure 3.23: The neutral axis depth as a function of the interface rotation obtained at the first floor level for the hybrid frame of the PRESSS building.

Post-tensioning Tendon Elongation

The measured elongation of the post-tensioning tendon as a function of column drift is shown in Figure 3.24. The tendon elongation was directly measured whereas the drift was taken as the measured lateral displacement of the column divided by the column height [3.3].

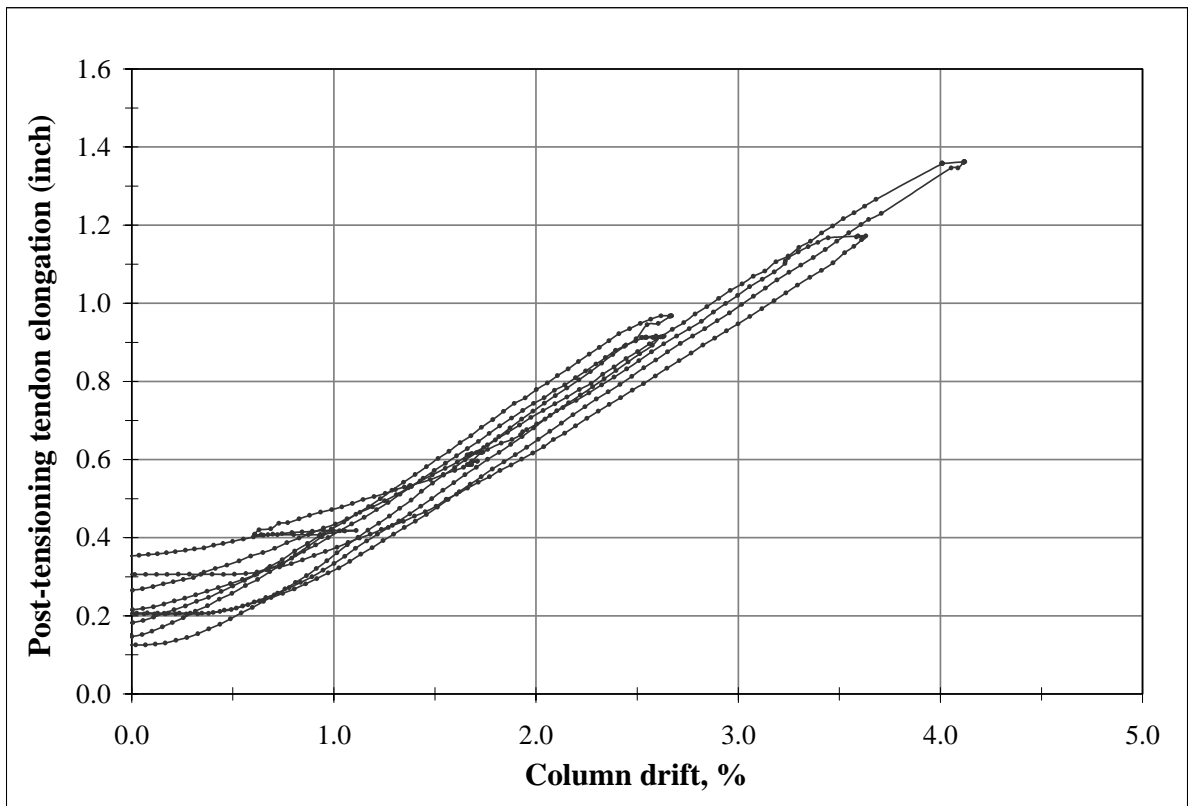


Figure 3.24: Post-tensioning tendon elongation as a function of column drift in the PRESSS test building.

3.6 References

- [3.1] Stanton, J. F. and Nakaki, S. D., “Design Guidelines For Precast Concrete Seismic Structural Systems,” *PRESSS Report No. 01/03-09, UW Report No. SM 02-02*, The University of Washington and The Nakaki Bashaw Group, Inc., 2002.
- [3.2] MathSoft Inc., Mathcad 2001 Professional.
- [3.3] Vernu, S., “Connection and structural level analysis of precast hybrid frame systems,” *Master Thesis, Iowa State University, Ames, Iowa, 2003*.
- [3.4] Thomas, D. J., “Analysis and Validation of a Seismic Design Method Proposed for Precast Jointed Wall Systems,” *Master Thesis, Iowa State University, Ames, Iowa, 2003*.
- [3.5] ACI Innovative Task Group 1 and Collaborators, *Special Hybrid Moment Frames Composed of Discretely Jointed Precast and Post-Tensioned Concrete Members (ACI T1.2-03) and Commentary (T1.2R-03)*, Michigan, 2003.
- [3.6] Stone, W. C., Cheok, G. S., and Stanton, J. F., “Performance of Hybrid Moment Resisting Precast Beam-Column Concrete Connections Subject to Cyclic Loading,” *ACI Structural Journal*, Vol. 92, No. 2, 1995, pp. 229-249.
- [3.7] Stanton, J., Stone, W. C., Cheok, G. S., “A Hybrid Reinforced Precast Frame for Seismic Regions,” *PCI Journal*, Vol. 42, No. 2, 1997, pp. 20-32.
- [3.8] Priestley, M. J. N., Sritharan, S., Conley, J. R., Pampanin, S., “Preliminary Results and Conclusions From the PRESSS Five-Story Precast Concrete Test Building,” *PCI Journal*, Vol. 44, No. 6, 1999, pp. 42-67.

- [3.9] ACI Innovation Task Group 1 and Collaborators, *Acceptance Criteria for Moment Frames Based on Structural Testing (T1.1-01) and Commentary (T1.1R-01)*, Michigan, 2001.
- [3.10] American Concrete Institute, *Building Code Requirements for Structural Concrete (ACI 318-99) and Commentary (ACI 318R-99)*, Michigan, 1999.
- [3.11] Mattock, A. H., “Flexural Strength of Prestressed Concrete Sections by Programmable Calculator,” *PCI Journal*, Vol. 24, No. 1, 1979, pp. 26-37.
- [3.12] Cheok, G. S., Stone, W. C., “Performance of 1/3-Scale Model Precast Concrete Beam-Column Connections Subjected to Cyclic Inelastic Loads – Report No: 4,” *NISTIR 5436*, NIST, Gaithersburg, June, 1994.
- [3.13] Dodd, L. L. and Restrepo-Posada, J. I., “Model for Predicting Cyclic Behavior of Reinforcing Steel,” *Journal of Structural Engineering, ASCE*, Vol. 121, No. 3, March, 1995, pp. 443-445.
- [3.14] Cheok, G. S., Stone, W. C., Nakaki, S. D., “Simplified Design Procedure for Hybrid Precast Concrete Connections,” National Institute of Standards and Technology, *SCTR 5765*, 1996.
- [3.15] Pampanin, S., Priestley, M. J. N., Sritharan, S., “Analytical Modeling of Seismic Behaviour of Precast Concrete Frames Designed with Ductile Connection,” *Journal of Earthquake Engineering*, Vol. 5, No. 3, 2001, pp. 329-367
- [3.16] Sritharan, S., “Analysis of Concrete Bridge Joints subjected to Seismic Actions,” *PhD Dissertation, University of California, San Diego*, 1998.

- [3.17] Mander, J. B., Priestley, M. J. N., and Park, R., "Theoretical Stress-Strain Model For Confined Concrete," *Journal of the Structural Division, ASCE*, Vol. 114, No. 8, August, 1988, pp. 1804-1826.
- [3.18] Sritharan, S., Pampanin, S., Conley, J. R., "Design Verification, Instrumentation, & Test Procedures," *PRESSS-3: The Five-Story Precast Test Building*, Vol. 3-3, Iowa State University, ISU-ERI-Ames Report ERI-03325, 2002.
- [3.19] Sritharan, S., "Performance of Four Jointed Precast Frame Systems under Simulated Seismic Loading," *In Proceedings of the Seventh U.S. National Conference on Earthquake Engineering*, Paper No. 480, Boston, Massachusetts, July, 2002.

CHAPTER 4

PRECAST HYBRID FRAME SYSTEMS: VALIDATION OF SEISMIC DESIGN GUIDELINES AND RECOMMENDATIONS

by

Onur Celik and Sri Sritharan

Department of Civil, Construction and Environmental Engineering

Iowa State University, Ames, IA 50011, USA

(With permission from PCMAC, this paper is intended for submission to the ACI Structural Journal.)

4.1 Abstract

The precast hybrid frame concept has been developed for seismic applications over the past decade, starting with the component tests at NIST (*National Institute of Standards and Technology*) through to the system level test in the PRESSS (*PREcast Seismic Structural*

Systems) test building. Along with these developments, guidelines for designing hybrid frame connections have been proposed. The main objective of the study reported in this paper is to validate the design guidelines proposed for hybrid frame systems by (1) Stanton and Nakaki as part of the PRESS program (2002) and (2) the ACI (*American Concrete Institute*) Innovation Task Group (2003), using experimental data from two NIST tests and the PRESS building test. By establishing analysis methods based on the proposed design steps and assumptions, and comparing the analysis results with the experimental results, the adequacy of the proposed guidelines is examined. The accuracy of the *Monolithic Beam Analogy* (MBA) concept in predicting the response of hybrid frame connections is also investigated as part of this study. Based on the comparisons between the experimental and various analytical results, recommendations are made to improve the design of precast hybrid frame connections.

Keywords: PRESS; unbonded; prestressing; post-tensioning; precast; concrete; hybrid frame; seismic; design

4.2 Introduction

Precast concrete can offer several advantages, including high quality, efficient use of materials, reduced construction time, and cost efficiency. In addition to these benefits, precast concrete allows architects and engineers to perform innovative building designs. Despite these benefits and unique properties of precast concrete, the application of precast concrete systems in high seismic regions of the United States has been limited due to the

restrictions imposed by the design codes and poor performance exhibited by precast concrete structures in past earthquakes [4.1, 4.2]. Over the past decade, a significant research effort has been made to promote the application of precast concrete in seismic regions, which includes the NIST experimental program [4.1, 4.3] and the PRESSS program [4.4]. As a result of this effort, guidelines for seismic design of precast concrete structures have been published in 2002 by Stanton and Nakaki [4.5], which address design of four different precast seismic frame systems and one precast seismic wall system. The study presented in this paper focuses on the validation of design guidelines proposed for the precast hybrid frame systems. The hybrid frame system, which is one of the frame systems addressed by Stanton and Nakaki [4.5], has been implemented in several buildings in high seismic regions, including the 39-story, 420-ft high, Paramount apartment building in San Francisco, California [4.7]. A seismic design procedure for the hybrid frame system has also been recently published by the ACI Innovation Task Group [4.6] which is also investigated in this paper.

The hybrid framing concept typically connects single bay precast concrete beams to multi-story precast columns utilizing unbonded post-tensioning steel and mild steel reinforcement (Figure 4.1). Unbonded post-tensioning steel, located at the mid-height of the beam, is designed to remain elastic when the hybrid frame is subjected to design-level earthquakes. On the other hand, the mild steel reinforcing bars, located at the top and bottom of the beam, contribute to moment resistance as well as energy dissipation by experiencing yielding in tension and compression in the beam end regions. As a result of the elastic response, the post-tensioning steel may be designed with sufficient restoring force to

minimize the residual displacements of the frame resulting from the development of inelastic strains in the mild steel reinforcement. Consequently, the hybrid frames can be designed to re-center after experiencing a horizontal direction earthquake motion.

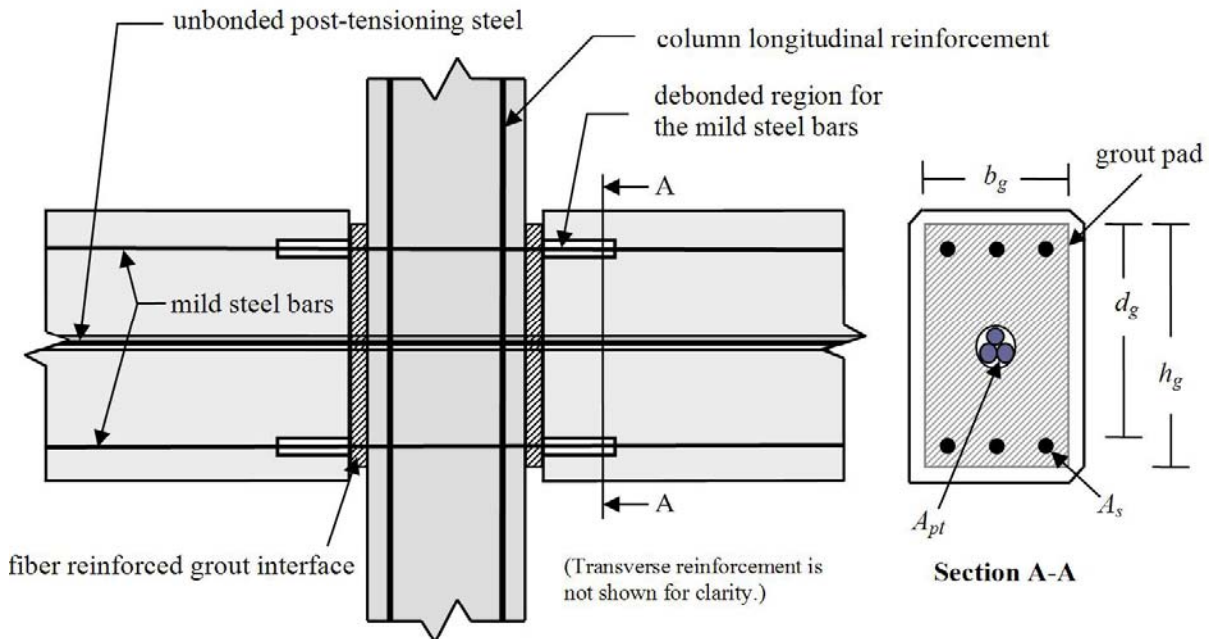


Figure 4.1 Typical hybrid frame connection details.

The re-centering potential of the hybrid frame systems depends on the ratio between the moment contributions by the post-tensioning steel and mild steel reinforcement, debonded length of the mild steel reinforcement, and the initial prestressing force [4.2]. The mild steel reinforcing bars are debonded over a short length at the beam ends to avoid premature fracture at the small to medium drift levels due to low cycle fatigue. A friction mechanism assisted by prestressing is relied upon to transfer shear from the beam to the column. A small

gap is left between the columns and beams and is filled with high strength fiber reinforced grout to ensure continuity between the precast members.

4.3 Research Significance

Restrictions imposed in design codes combined with the lack of confidence introduced by poor seismic performance of precast buildings in past earthquakes have led designers to generally limit concrete structures to cast-in-place systems in high seismic regions. The recent research studies, which have shown convincingly that precast systems are acceptable alternative building systems in seismic regions, have produced design guidelines to assist with seismic design of precast concrete systems. The objective of this study is to validate the design guidelines proposed for the hybrid frame systems and provide recommendations to improve the guidelines where appropriate. The presence of unbonded prestressing steel and debonded mild steel reinforcement at the hybrid connection interface introduces strain incompatibility between concrete and steel reinforcement. As a result, a section analysis cannot be performed at the precast connection as with the monolithic concrete frame design. To overcome the difficulties resulting from the strain incompatibility, the PRESSS guidelines [4.5] and the ACI design method [4.6] uses the equivalent stress block concept and assumed predetermined stresses in the mild steel reinforcement. This approach leads to an increase in the neutral axis depth as the interface rotation increases, which is opposite to the actual behavior expected at the precast connection. The experimental data are used to examine implications of this design approach.

4.4 Analysis Procedures

To validate the design guidelines against experimental data, suitable analysis procedures are first established using the assumptions and steps on which the guidelines are based on. The test units are then analyzed using these procedures, and results are compared against the relevant experimental data.

Several procedures for analyzing hybrid frame connections are presented below, which may be summarized as follows:

- An analysis procedure based on the PRESSSS design guidelines [4.5]
- A modified PRESSSS analysis procedure, which includes several improvements to the analysis procedure developed for the PRESSSS design guidelines
- Analysis procedure based on the ACI T1.2-03 document [4.6]
- Analysis procedure using the MBA concept [4.2]

4.4.1 PRESSSS Analysis Procedure

The PRESSSS design guidelines [4.5] proposed for unbonded post-tensioned frames with damping are reversed to establish a procedure for analyzing the hybrid frame connections. As detailed below, this procedure is only applicable at three interface rotations. Descriptions of the analysis steps are given below whereas a flowchart summarizing the analysis procedure is presented in Figure 4.2. (More details of the analysis steps may be found in Section 3.2.1).

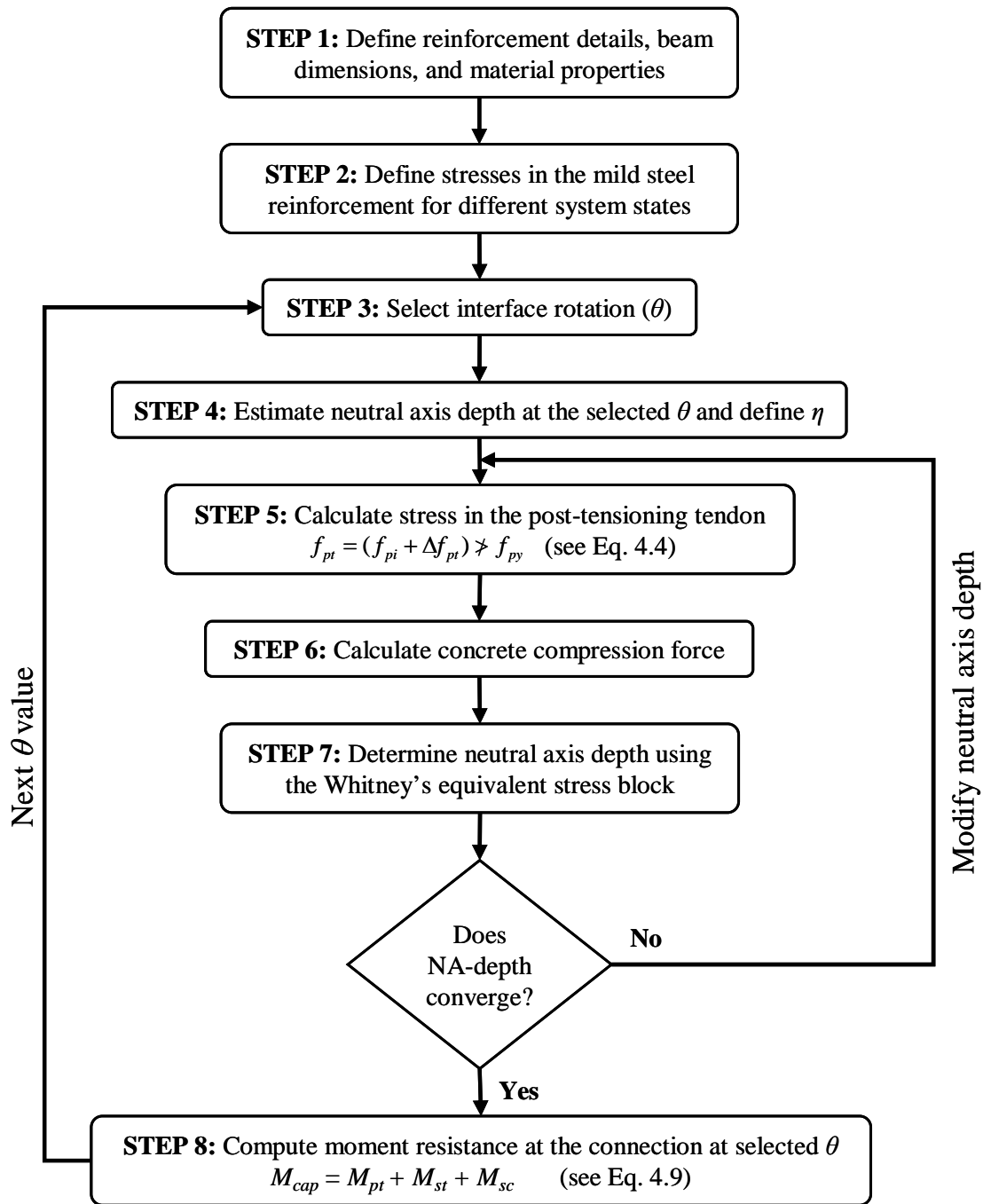


Figure 4.2: A flowchart summarizing the analysis procedure based on the PRESS design guidelines.

STEP 1: Define reinforcement details, beam dimensions, and material properties

The following variables are defined in this step (see Figure 4.1):

A_{pt} = area of the post-tensioning tendon,	E_p = elastic modulus of the prestressing steel,
A_s = area of the mild steel reinforcement,	f_{py} = yield strength of the post-tensioning tendon,
l_{pu} = unbonded length of the post-tensioning tendon,	f_{pi} = initial stress in the post-tensioning tendon,
h_g = height of the grout pad at the interface,	f_{sy} = yield strength of the mild steel reinforcement,
b_g = width of the grout pad at the interface,	f'_c = unconfined concrete compression strength,
d_g = depth to the tension mild steel reinforcement from the extreme compression fiber in the grout pad, and	
ζ = distance from the compression mild steel reinforcement to the extreme compression fiber in the effective section divided by h_g .	

Note that the grout pad reduces the contact area at the beam end as shown in Figure 4.1, and variables h_g and b_g define the effective beam gross section.

STEP 2: Define stresses in the mild steel reinforcement for different system states

For the selected state of the system, calculate the tension and compression mild steel stresses at the beam-column interface by multiplying the yield strength of the mild steel reinforcement by the corresponding over-strength factors listed in Table 4.1. Accordingly, the stresses are defined as:

$$f_{st} = \lambda_{st} \cdot f_{sy} \quad \text{in the tension reinforcement} \quad (4.1a)$$

$$f_{sc} = \lambda_{sc} \cdot f_{sy} \quad \text{in the compression reinforcement} \quad (4.1b)$$

where f_{st} and f_{sc} are, respectively, the stresses in the tension and compression reinforcement, and λ_{st} and λ_{sc} are, respectively, the over-strength factors for the tension and compression reinforcement. As seen in Table 4.1, λ_{st} and λ_{sc} are given at three drifts corresponding to the following system states: “first yield”, “design” and “maximum credible”. The interface rotations at the three states are defined with variables θ_y , θ_{des} , and θ_{max} , respectively. The θ_y , θ_{des} , and θ_{max} values are determined using column drifts of 0.5% , 2.0% and 3.5% as per PRESSS guidelines [4.5] and ACI ITG 1.1 [4.8] as well as appropriate stiffnesses for the columns and beams.

Table 4.1 Suggested reinforcement over-strength factors for ASTM 706 bars by Stanton and Nakaki [4.5].

Suggested System State	Strain	Interface Rotation, θ (%)	λ_{st}	λ_{sc}
First Yield	0.002	θ_y	1.0	1.0
Design	0.04	θ_{des}	1.35	1.0
Maximum Credible	0.08	θ_{max}	1.5	1.0

STEP 3: Select interface rotation (θ)

Select a beam-column interface rotation from Table 4.1 corresponding to one of the system states.

STEP 4: Estimate neutral axis depth (c) at the selected θ and define η

Using an assumed neutral axis depth, compute

$$\eta = \frac{c}{h_g} \quad (4.2)$$

STEP 5: Calculate stress in the post-tensioning tendon

Using the neutral axis depth from Step 4, calculate the elongation in the tendon (Δ_{pt}) due to the imposed interface rotation θ from system geometry (see Figure 4.3) and the corresponding increase in stress (Δf_{pt}).

$$\Delta f_{pt} = \frac{\Delta_{pt}}{l_{pu}} \cdot E_p \quad (4.3)$$

The stress in the post-tensioning tendon (f_{pt}) at the selected θ is taken as

$$f_{pt} = (f_{pi} + \Delta f_{pt}) \not\geq f_{py} \quad (4.4)$$

STEP 6: Calculate concrete compression force

By using the equilibrium condition and forces in the post-tensioning tendon (F_{pt}), tension steel (F_{st}), and compression steel (F_{sc}) at the selected θ , the resultant concrete compression force at the beam-column interface (F_c) is determined as follows (see Figure 4.3):

$$F_c = F_{pt} + F_{st} - F_{sc} \quad (4.5)$$

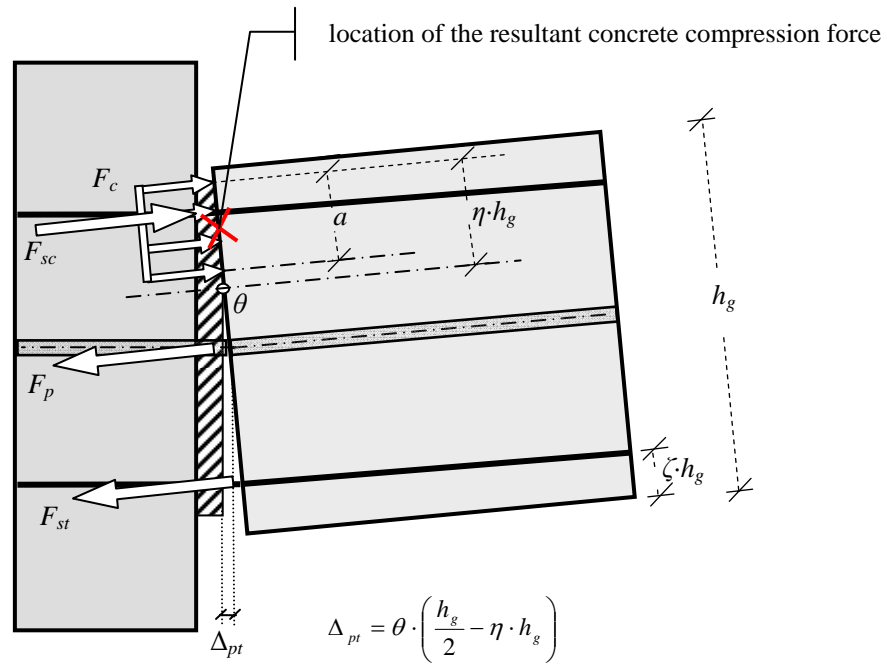


Figure 4.3: Forces acting on a precast concrete hybrid beam.

STEP 7: Determine neutral axis depth using the Whitney's equivalent stress block

The depth of the equivalent rectangular compression stress block (a) corresponding to the compression force estimated in Eq. 4.5 is determined using

$$a = \frac{F_c}{0.85 \cdot f'_c \cdot b_g} \quad (4.6)$$

Therefore, the parameter η defining the neutral axis depth at the interface is obtained from Eq. 4.7.

$$\eta = \frac{a}{\beta_1 \cdot h_g} \quad (4.7)$$

As suggested in Article 10.2.7.3 of the ACI 318-99 Building Code [4.9], a value for β_1 is taken as

$$\beta_1 = 0.85 - 0.05 \cdot (f'_c - 4) \quad (4.8)$$

where f'_c is expressed in ksi.

Steps 4 to 7 are repeated until the estimated and calculated neutral axis depth values converge to each other.

STEP 8: Compute moment resistance at the connection at selected θ

Moment capacity (M_{cap}) of the connection is calculated by adding the moments contributed by the post-tensioning tendon (M_{pt}), tension mild steel reinforcement (M_{st}), and compression mild steel reinforcement (M_{sc}) with respect to the resultant concrete compression force (see Figure 4.3).

$$M_{cap} = M_{pt} + M_{st} + M_{sc} \quad (4.9)$$

For validation of the design guidelines, Steps 2 to 8 are repeated at the three interface rotations identified in Table 4.1.

In addition to validating the key variables identified in the above analysis steps, other variables such as the growth in debonded length of the mild steel reinforcement, plastic hinge length and average compression strain as well as the re-centering check suggested in the

PRESSS guidelines are also examined in the current study. (See details in Sections 3.2.1 and 4.7.1).

4.4.2 Modified PRESSS Analysis Procedure

Considering several improvements to the PRESSS guidelines proposed for unbonded post-tensioned frames with damping [4.5], a modified procedure for analyzing the hybrid frame connections is presented in this section. The suggested modifications are based on the comparisons of results obtained from the PRESSS analysis procedure with (1) the experimental data provided by Stone et al. [4.1] and Stanton et al. [4.3] for two hybrid frame component tests, (2) the data from the five-story PRESSS building tested at UCSD [4.10], and (3) the analysis results from the monolithic beam analogy concept presented by Vernu [4.2]. Thomas [4.11] performed validation of the PRESSS guidelines proposed for the precast jointed wall systems. The outcomes of this study are also considered when establishing the modified analysis procedure, which emphasizes improving the depths of the equivalent stress block and neutral axis to improve the design of jointed connections. Descriptions of the different modifications suggested for the PRESSS analysis procedure are given below with a flowchart summarizing the modified PRESSS analysis procedure in Figure 4.4. (More detailed information on the suggested changes may be found in Section 3.2.2).

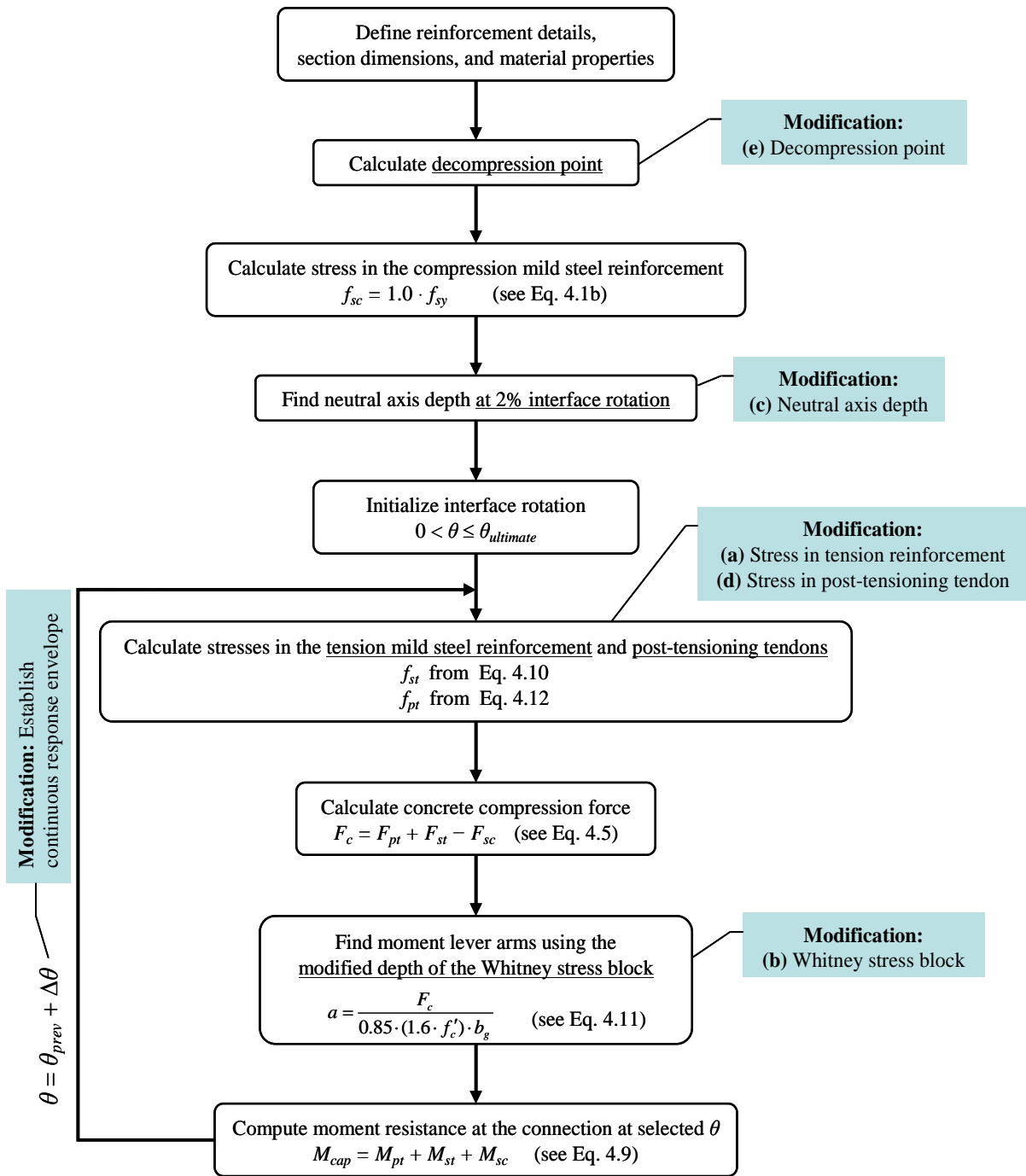


Figure 4.4: A flowchart summarizing the modified PRESSS analysis procedure.

(a) Stress in Tension Mild Steel Reinforcement

The PRESSS guidelines do not provide an expression for estimating the stress in the tension mild steel reinforcement as a function of the beam-column interface rotation θ , which is required to perform validation of the design guidelines over a range of story drifts. The PRESSS guidelines are, therefore, examined only at three interface rotations as discussed in Section 4.4.1. In the modified analysis procedure, the stress in the tension mild steel reinforcement is assumed to be a function of θ as expressed in Eqs. 4.10a to 4.10c. These equations are based on the assumption that the interface rotations $\theta = 0.001$ rad. and 0.005 rad. are achieved, respectively, when the strain in the tension reinforcement reaches ε_{sy} and ε_{sh} , where ε_{sy} is the yield strain of the reinforcing bar and ε_{sh} is the strain at the onset of strain hardening. Eq. 4.10c is derived assuming a parabolic shape for the strain hardening portion of the steel and interface rotations of 0.5%, 2.0% and 3.5% at 1.0, 1.35 and 1.5 times the yield strength of the tension mild steel reinforcement, respectively, in accordance with Table 4.1. The critical values for θ required to derive Eq. 4.10c are based on the analytical results presented by Vernu [4.2] using the MBA concept and the recommended design drift levels in the ACI ITG 1.1 document [4.8].

$$f_{st} = (1000 \cdot \theta) \cdot f_{sy} \quad \text{for} \quad 0 \leq \theta < 0.001 \quad (4.10a)$$

$$f_{st} = f_{sy} \quad \text{for} \quad 0.001 \leq \theta < 0.005 \quad (4.10b)$$

$$f_{st} = (0.84 + 34.4 \cdot \theta - 444.4 \cdot \theta^2) \cdot f_{sy} \quad \text{for} \quad 0.005 \leq \theta \leq 0.035 \quad (4.10c)$$

The resulting relationship between f_{st} and θ from Eq. 4.10 is represented graphically in Figure 4.5.

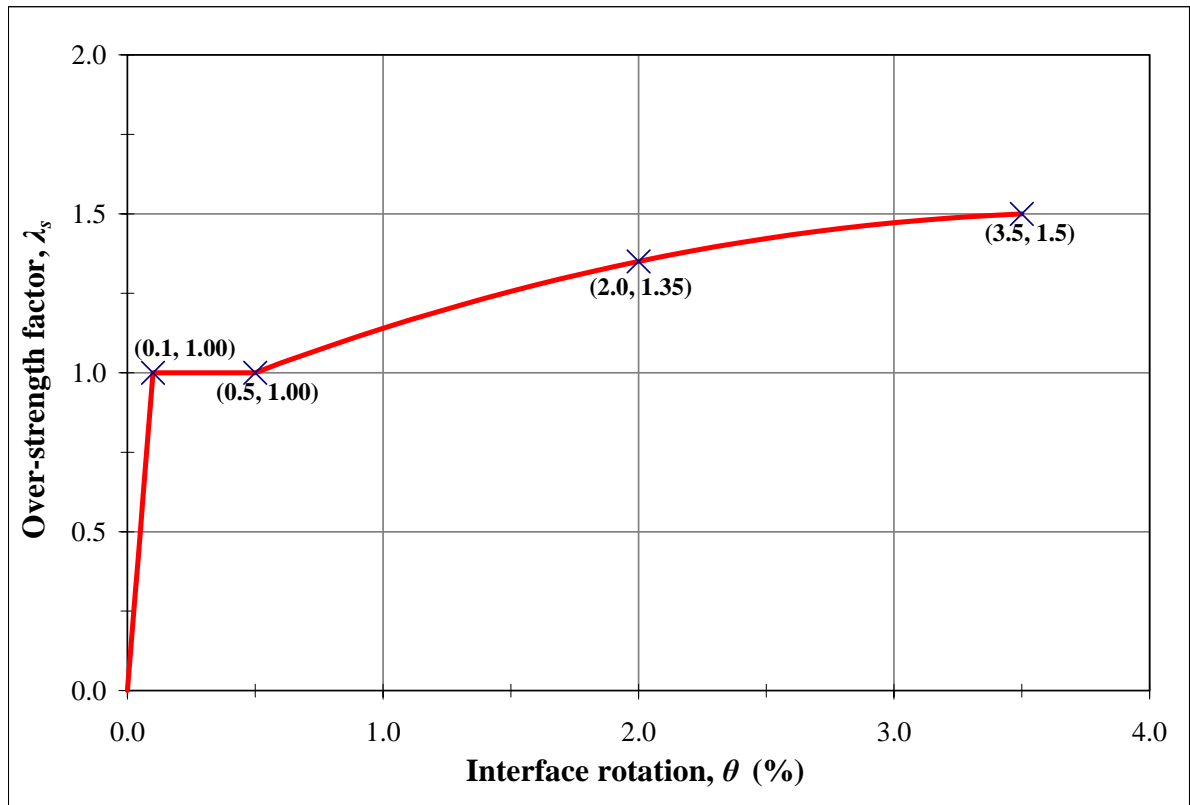


Figure 4.5: An assumed relationship between the over-strength factor and interface rotation for the tension mild steel reinforcement.

(b) Equivalent Rectangular (Whitney) Stress Block

In the PRESSS guidelines, the grout placed at the beam-column interface is assumed to be reinforced with fibers to avoid premature crushing and spalling out of the joint. The fibers also increase the grout strength. Since adequate models are not available to predict the inelastic behavior of the grout, including the confinement effects, it is suggested that the grout should be designed to have strength (f'_g) greater than the concrete strength of the adjoining precast members. Furthermore, accounting for the confinement effects, the

effective concrete compressive strength is taken as $1.6 \cdot f'_c$ at the design drift. Consequently, the depth of the equivalent rectangular stress block at this drift may be defined as:

$$a = \frac{F_c}{0.85 \cdot (1.6 \cdot f'_c) \cdot b_g} \quad (4.11)$$

The 1.6 factor for enhancing concrete strength is based on the results obtained from the MBA analysis results of the hybrid frame connections presented in this report. A similar factor was found to be appropriate in the design validation study conducted for the jointed wall systems [4.11]. Ideally, the analysis should consider two different concrete strengths for the confined and unconfined concrete. However, a single value of 1.6 is used for simplicity.

(c) Neutral Axis Depth

The experimental results of the five-story PRESSSS test building and the analysis results of MBA reported for different hybrid frame connections [4.2] showed that the neutral axis depth does not significantly vary for interface rotations above 1 percent, as illustrated in Figure 4.6. Consistent with this observation, the neutral axis depth in the modified PRESSSS analysis procedure is calculated at 2 percent beam-column interface rotation using the equivalent stress block concept and an average concrete compression strength of $1.6 \cdot f'_c$ as per Eq. 4.11. This neutral axis depth is then applied to the analysis of the hybrid connections at interface rotations from 0 to $\theta_{ultimate}$, where $\theta_{ultimate}$ is equal or greater than the beam-column interface rotation corresponding to the extreme drift expected at the system state termed “maximum credible”. The PRESSSS guidelines, presented in Section 4.4.1, fail to predict the expected trend in the variation of the neutral axis depth (see Figure 4.7). As the interface rotation

increases, the neutral axis depth should reduce or remain unchanged. The equivalent stress block concept as used in the PRESSSS guidelines (see Eq. 4.11) suggests an increase in the neutral axis depth as the interface rotation increases. However, the modification proposed in this study alleviates the theoretical incorrectness in the PRESSSS guidelines to estimate the neutral axis depth and leads to a simplified design procedure. Thomas [4.11] also showed that the same approach is applicable to precast jointed wall systems. Although the neutral axis depth based on Eq. 4.11 is not satisfactory for $\theta < 1\%$, it is used for all θ values to simplify the analysis procedure and the results are found to be satisfactory. An improvement to this assumption is suggested in Section 4.7.1 for performing analysis at small interface rotations with an increased accuracy. However, such an improvement is not needed in the design procedure as θ_{des} is likely to be greater than 1 percent.

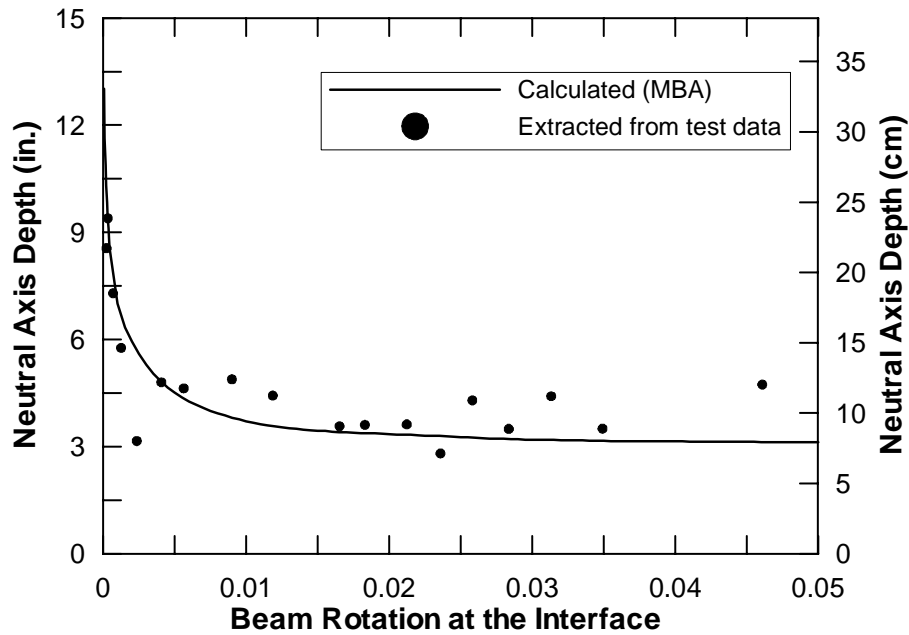


Figure 4.6: The neutral axis depth as a function of the interface rotation reported for the PRESSSS first floor hybrid connection by Vernu [4.2].

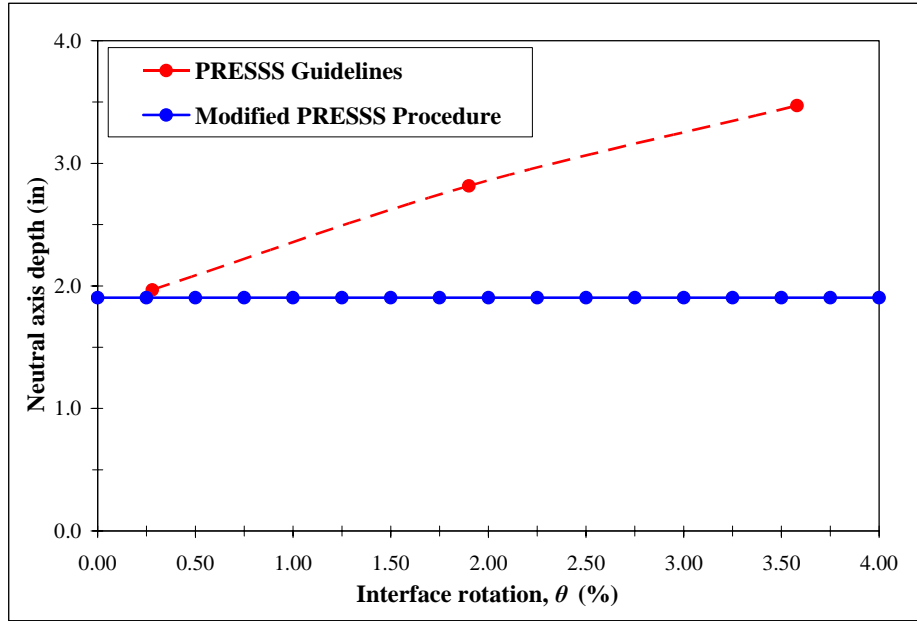


Figure 4.7: Comparison of neutral axis depths calculated from the PRESSSS guidelines [4.5] and the modified PRESSSS procedure for the NIST test Specimen M-P-Z4.

(d) Stress in Post-Tensioning Tendons

From system geometry (see Figure 4.3), the strain in the post-tensioning tendon is calculated and the corresponding stress is found from Eq. 4.12, which was recommended by Mattock [4.12] for Grade 270 prestressing strands. This modification is introduced to more accurately determine the prestressing stress at large interface rotations. Eq. 4.12 is graphically represented in Figure 4.8.

$$f_{pt} = \varepsilon_{pt} \cdot E_p \cdot \left[0.020 + \frac{0.98}{\left[1 + \left(\frac{\varepsilon_{pt} \cdot E_p}{1.04 \cdot f_{py}} \right)^{8.36} \right]^{\frac{1}{8.36}}} \right] \quad (4.12)$$

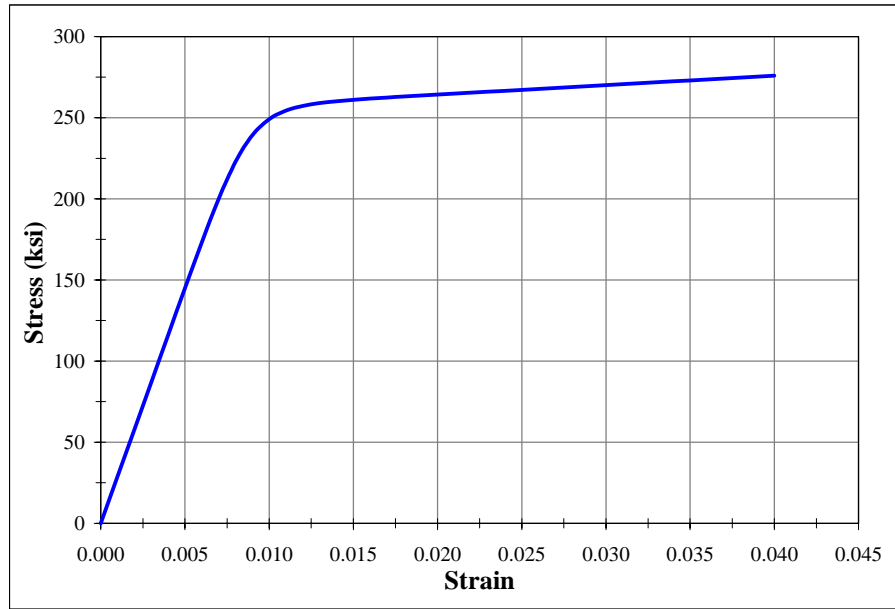


Figure 4.8: A theoretical stress-strain curve proposed for Grade 270 prestressing strands by Mattock [4.12].

(e) Decompression Point

In the modified PRESSS analysis procedure, the decompression point is also identified, which defines the beginning of a crack opening at the connection interface and corresponds to the condition when the stress in the extreme concrete compression fiber reaches zero at the beam end adjacent to the column. Accounting for the precompression introduced by the initial prestressing force, and assuming a linear strain distribution at the critical section, the following equations are used to determine the moment resistance (M_{decomp}) and the corresponding beam end rotation (γ_{decomp}) at the decompression point.

$$M_{decomp} = \frac{\sigma_i \cdot I}{c} \tag{4.13}$$

where σ_i is the stress in the beam due to initial prestressing, I is the moment of inertia of the beam section based on the gross section properties, and c is the neutral axis depth and is equal to $\frac{h_g}{2}$.

$$\gamma_{decomp} = \frac{1}{2} \cdot \phi_e \cdot l \quad (4.14)$$

where ϕ_e is the elastic curvature along the member, and l is the length of the beam.

4.5 ACI T1.2-03 Analysis Procedure

The design procedure suggested for hybrid moment frames composed of discretely jointed precast and post-tensioned concrete members in the ACI T1.2-03 document [4.6] is reversed to establish an alternative analysis procedure. This procedure closely follows that presented in Section 4.4.1 for the PRESSS guidelines with the following changes:

- The moment calculations are performed at two drift levels. First, at the maximum drift of 3.5 percent, the moment resistance defines the probable moment strength of the hybrid frame connection. Although not specially defined in this document, the second set of calculations establishes the nominal moment resistance at the onset of strain hardening in the tension reinforcement. The drift corresponding to the nominal moment is taken as 0.5 percent as suggested in Figure 4.5. This moment definition is based on the recommendations of Cheok et al. [4.13], which appears to be the basis for the ACI T1.2-03 document.

- The stress in the compression reinforcement is taken as $1.25 \cdot f_{sy}$ for both moment calculations.
- In the probable strength calculation, the tension reinforcement stress is approximated to f_{su} , where f_{su} is the ultimate tensile strength of the mild steel reinforcement.
- The nominal moment resistance of the hybrid connection is calculated using f_{sy} as the stress in the tension reinforcement. Approximating the nominal moment resistance to 70 percent of the probable moment capacity has also been suggested to be acceptable [4.13]. However, in this document, the nominal moment is determined using f_{sy} in the tension reinforcement.

4.6 Monolithic Beam Analogy (MBA)

To overcome the strain incompatibility condition at the hybrid frame connection resulting from the use of unbonded reinforcement, an additional equation is introduced in the monolithic beam analogy [4.2, 4.14]. This is achieved by computing the global displacement at the beam end using a plastic hinge length similar to that adopted for monolithic frame systems. As shown below, MBA enables strains at the connection to be expressed as a function of rotation at the beam-to-column connection interface. Together with the force equilibrium condition and theoretical stress-strain relations for concrete, mild steel reinforcement, and post-tensioning tendon, the MBA concept can be used to establish a continuous moment-rotation response envelope for a hybrid frame system. Presented below are a summary of critical equations derived from the MBA concept, information on material

models, and descriptions of various analysis steps. A flowchart summarizing the MBA analysis procedure is given in Figure 4.9. (More details on the analysis of hybrid frame connections based on MBA may be found in Section 3.4).

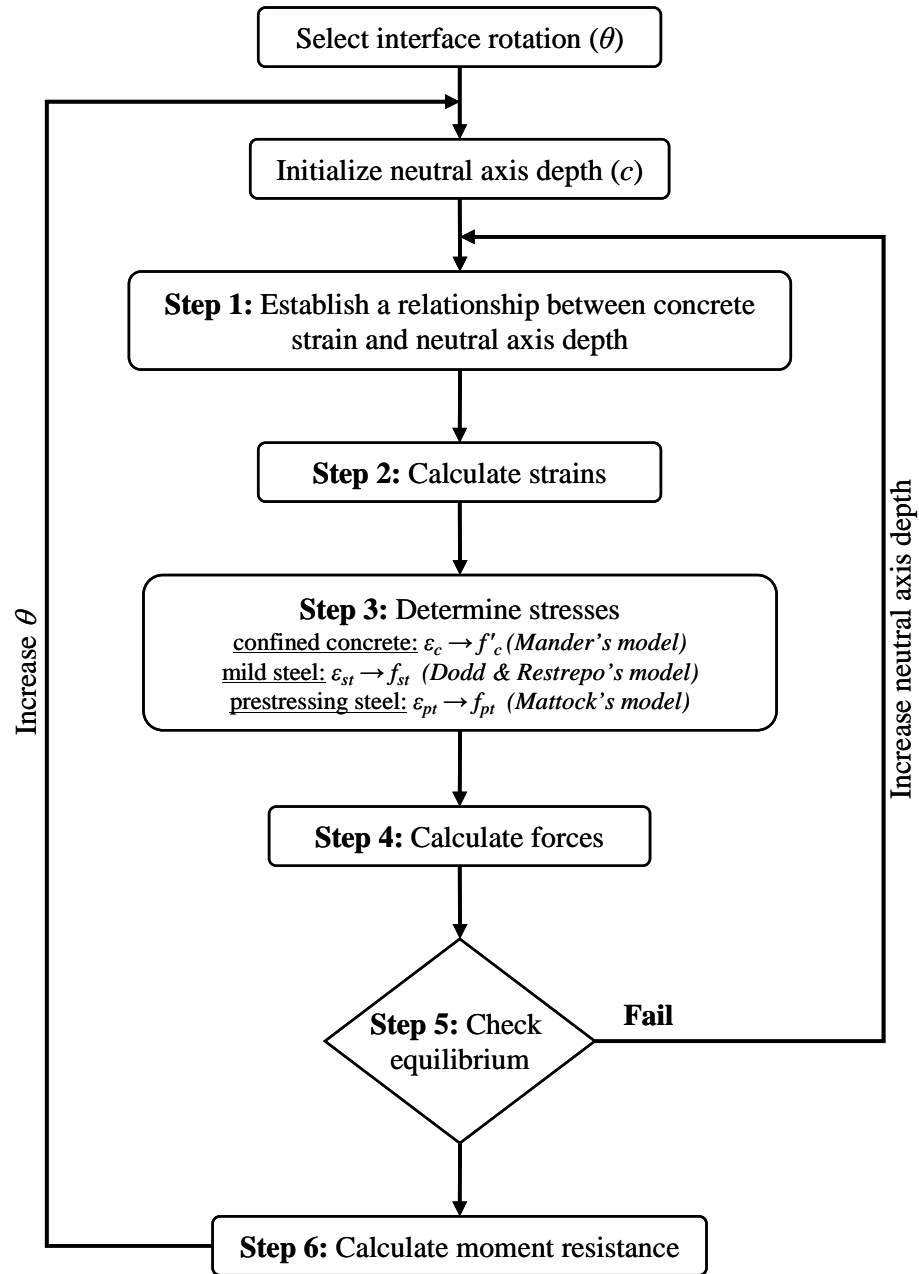


Figure 4.9 A flowchart describing the MBA analysis procedure [4.14].

STEP 1: Establish a relationship between concrete strain and neutral axis depth

Assuming that the total member end displacements are equal for both the precast hybrid beam ($\Delta_{precast}$) and an equivalent monolithic beam ($\Delta_{monolithic}$), as shown in Figure 4.10, the strain in the extreme compression fiber (ε_c) of the hybrid frame connection is related to an assumed neutral axis depth (c) at a given interface rotation θ using Eq. 4.15 (see Section 3.4).

$$\varepsilon_c = \left[\theta + \phi_e \cdot \left(l_p - \frac{4}{3} \cdot l_{sp} \right) \right] \cdot \frac{c}{l_p} \quad (4.15)$$

where l_p is the plastic hinge length, and l_{sp} is the strain penetration length.

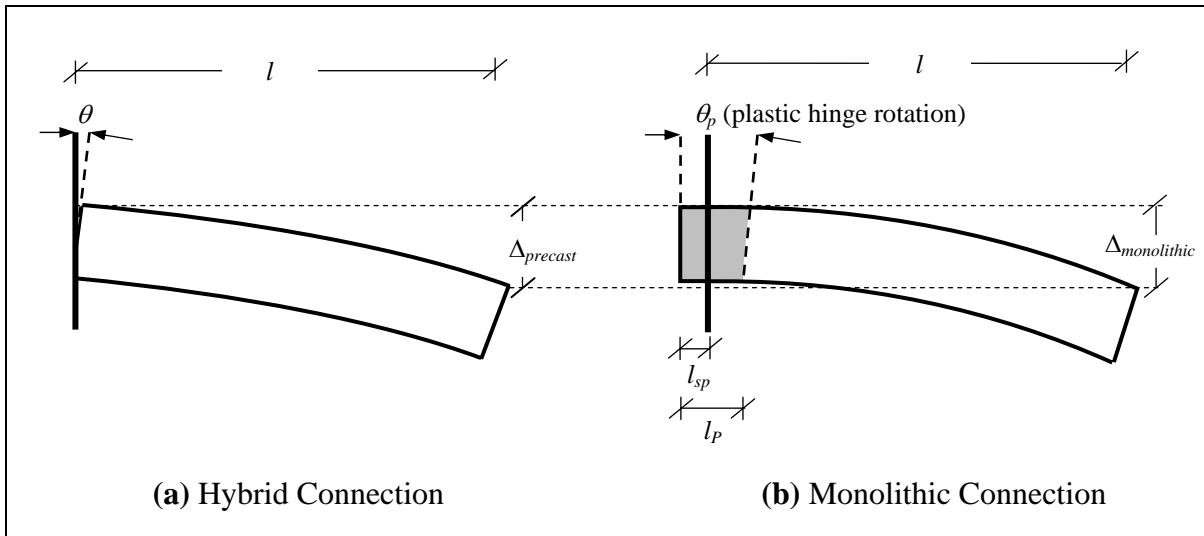


Figure 4.10 The concept of the Monolithic Beam Analogy ($\Delta_{precast} = \Delta_{monolithic}$).

STEP 2: Calculate strains

For the assumed neutral axis depth at θ , the following equations are used to define the strains in the post-tensioning tendon, tension mild steel reinforcement, and compression mild steel reinforcement (ε_{sc})[4.2, 4.14]:

$$\varepsilon_{pt} = \frac{\left(\frac{h_g}{2} - c\right) \cdot \theta}{l_{pu}} + \varepsilon_{pi} \quad (4.16)$$

$$\varepsilon_{st} = \frac{(d_g - c) \cdot \theta + \frac{2}{3} \cdot l_{sp} \cdot \frac{f_{st}}{E_s}}{l_{su} + 2 \cdot l_{sp}} \quad (4.17)$$

$$\varepsilon_{sc} = \frac{1}{2} \cdot \left[\frac{(c - d'_g)}{c} \cdot \varepsilon_c + \varepsilon_{sy} \cdot \frac{M}{M_y} \right] \quad (4.18)$$

where ε_{pi} is the strain in the tendon due to initial prestressing, E_s is the elastic modulus of the mild steel reinforcement, d'_g is the distance from the compression mild steel reinforcement to the extreme compression fiber in the effective section, M is the moment resistance in the previous step of the iteration procedure, and M_y is the yield moment defined when tension reinforcement reaches ε_{sy} .

STEP 3: Determine stresses

For strains calculated in Steps 1 and 2, stresses are estimated using appropriate constitutive models. The models proposed by Mander et al. [4.15], Dodd and Restrepo-Posada [4.16], and

Mattock [4.12] are used, respectively, for determining stresses in concrete, mild steel reinforcement and prestressing tendons.

STEP 4: Calculate forces

Using stresses computed in Step 3, the forces acting on the beam section are calculated by multiplying the stresses with the respective areas.

STEP 5: Check equilibrium

The equilibrium condition at the critical section is examined using forces obtained in Step 4.

If the equilibrium condition is not satisfied, the neutral axis depth is modified and Steps 1 to 5 are repeated until the desired condition is achieved.

STEP 6: Calculate moment resistance

By taking the moments about the resultant concrete compression force (see Figure 4.3), moment contributions by the forces in the post-tensioning tendons, tension and compression steel, and the total moment resistance of the connection at θ are readily determined.

To establish a continuous moment rotation envelope for the hybrid connection, Steps 1 to 6 are repeated for θ values from 0 to $\theta_{ultimate}$.

4.7 Comparison with Experimental Results

To validate the design guidelines proposed for the hybrid frame connections, the results based on the analysis procedures described above are compared with selected experimental results in this section. For this purpose, the test data from the five-story, 60 percent scale PRESSSS building [4.10] and one-third scale Specimens M-P-Z4 and O-P-Z4 from the NIST component tests [4.1, 4.3] are used. First, the validation is performed at the connection level using the moment-rotation response envelope, neutral axis depth, and change of force in the post-tensioning tendons. Also, compared is the theoretical stress-strain behavior of mild steel reinforcement assumed in different analysis procedures with that obtained from a steel coupon testing. Next, a system level validation is performed by comparing the measured response of the three-story hybrid frame incorporated into the PRESSSS building with the pushover analysis results obtained from a 2D model of the frame. The moment-rotation behavior of various hybrid connections in the 2D model is defined using the modified PRESSSS analysis procedure described in Section 4.4.2. A finite element computer program, RUAUMOKO [4.17], is used to perform the pushover analyses.

4.7.1 Connection Level Validation

(a) Moment-rotation response

The measured responses of Specimen M-P-Z4 and O-P-Z4 are compared with the different analysis results. The overall dimensions, connection details, and test setup of these test units

are illustrated in Figure 4.11. The connection details of the two specimens were the same except for the amount of mild steel reinforcement. In addition to the three 1/2-inch diameter, Grade 270 unbonded prestressing tendons at the mid-height of the beam section, three No. 3 (0.375-in diameter) mild steel reinforcing bars in M-P-Z4 and two No. 3 reinforcing bars in O-P-Z4 were used as the top and bottom beam reinforcement in the connection region. Mild steel bars were debonded in the beam over a one-inch distance from the column face to avoid premature bar fracture. The unbonded length of the prestressing tendons was 59.5 inches. Accounting for the growth in the unbonded length due to partial debonding of the tendons in the grouted region, the total effective unbonded length in the frame was taken as about 80 inches in the analysis. (See more details in Section 3.5.1).

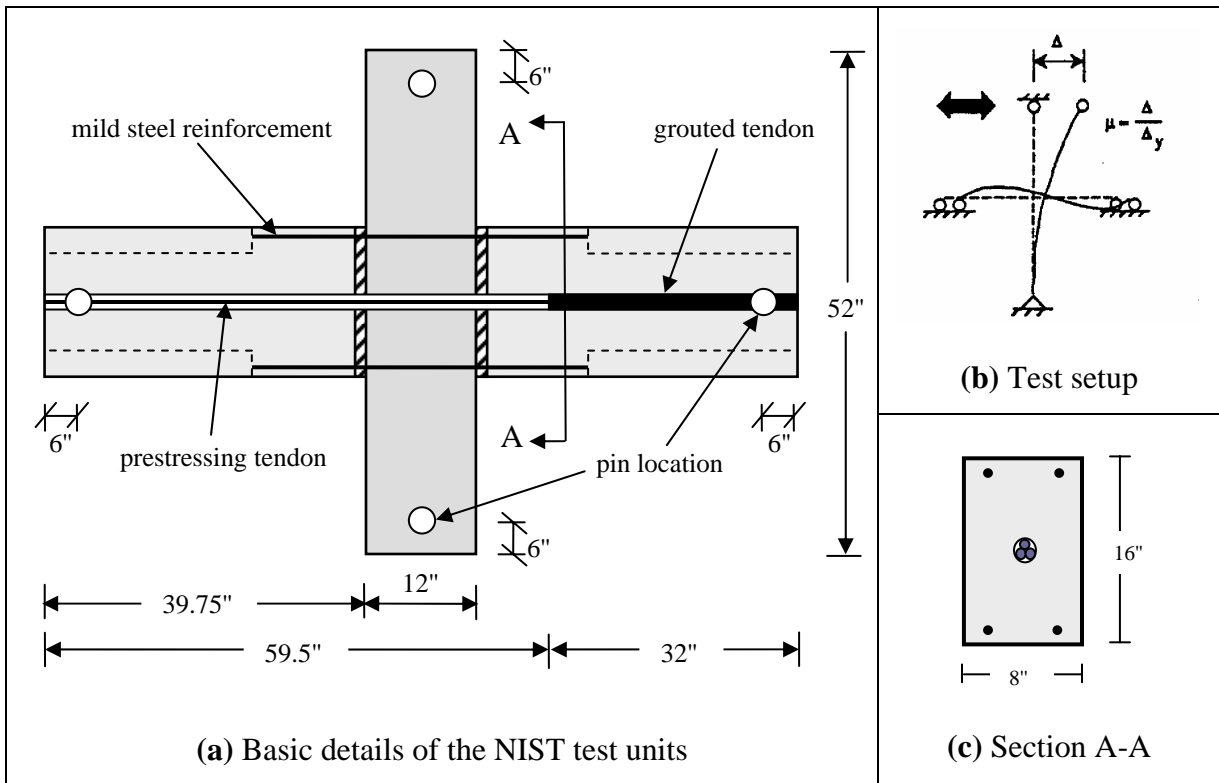


Figure 4.11 Details of the frame tests conducted in Phase VI-B by Stone et al. [4.3].

To simulate the seismic effects, a reverse cyclic loading as shown in Figure 4.12 was imposed on the test units. Each specimen was tested until a significant drop in the lateral strength was experienced.

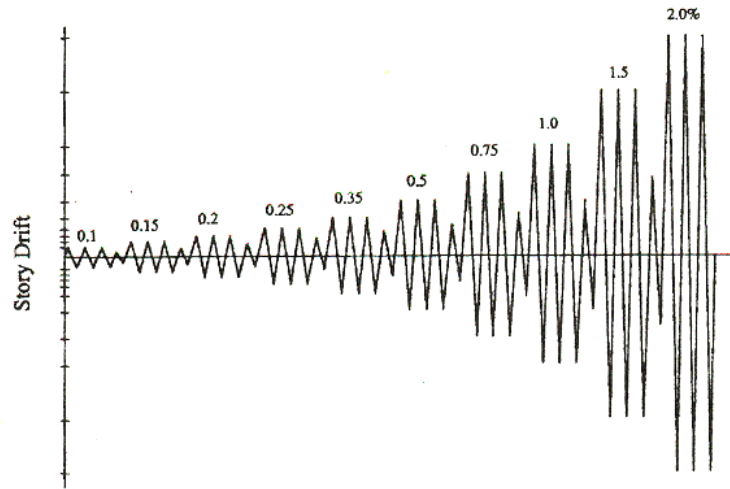


Figure 4.12 Lateral cyclic load sequence used for testing NIST Specimens [4.1].

The moment-rotation envelopes predicted by the PRESSS, modified PRESSS, ACI T1.2-03, and MBA analysis procedures are compared with the experimental responses in Figure 4.13 and 4.14 for test Specimens M-P-Z4 and O-P-Z4, respectively. The following observations are made:

- All analysis procedures satisfactorily predict the measured moment resistance.
- The MBA analysis, which uses accurate constitutive models for the material behavior, provided the best prediction of the overall response including the elastic stiffness.
- Despite using simplifications, the modified PRESSS analysis procedure provides satisfactory response envelopes. The elastic stiffness predicted by this procedure is somewhat greater because the calculation is based on a neutral axis depth, which is smaller than that expected in the elastic range.

- Because of the similarities, the ACI and PRESSS analysis procedures provided comparable strengths at the maximum drift of 3.5 percent.
- The test units experienced strength degradation at large interface rotations. Capabilities for capturing such strength degradation were not included in the analysis procedures. Consequently, large discrepancies between analysis results and experimental results are seen at the maximum interface rotations.

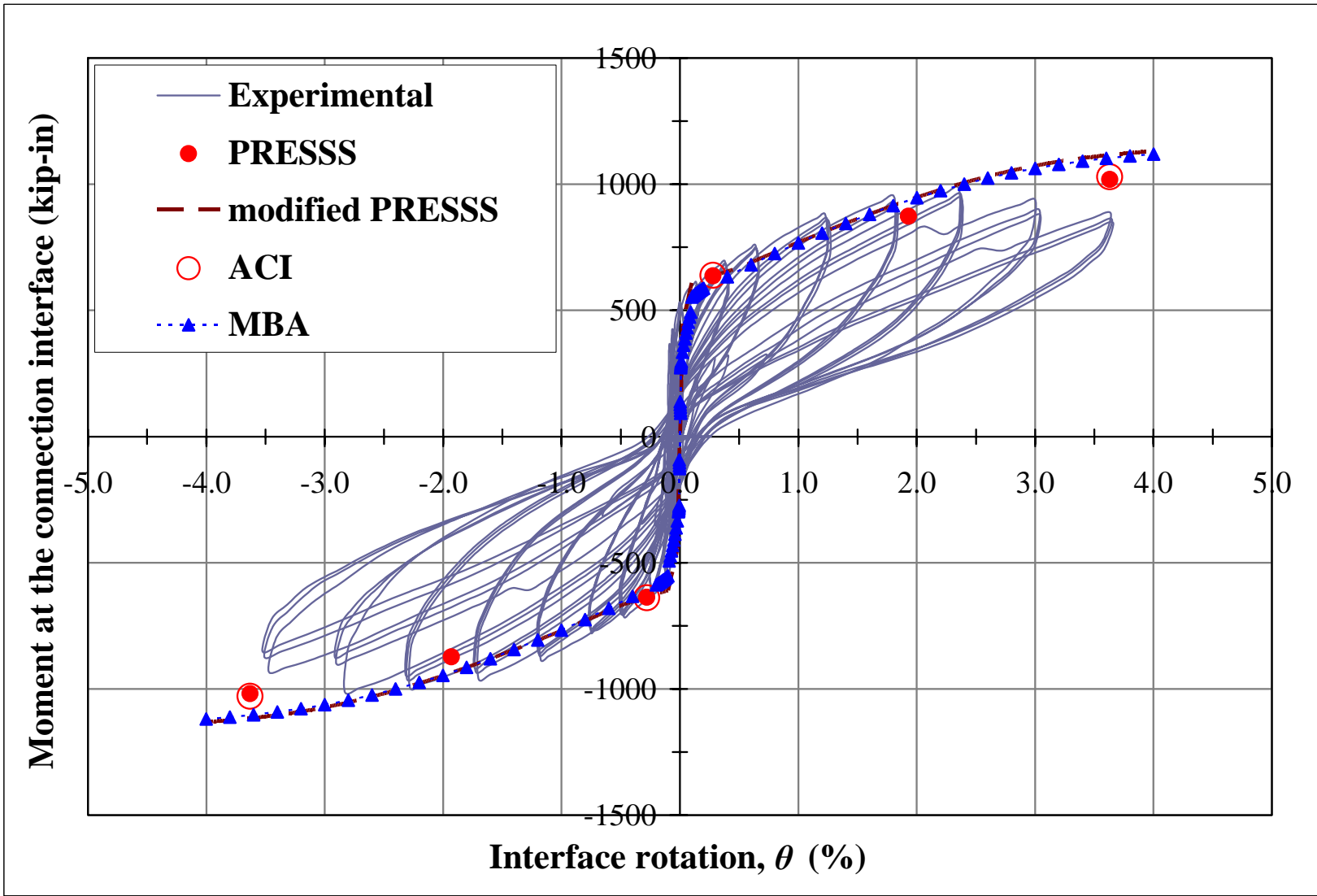


Figure 4.13 Response of NIST Specimen M-P-Z4.

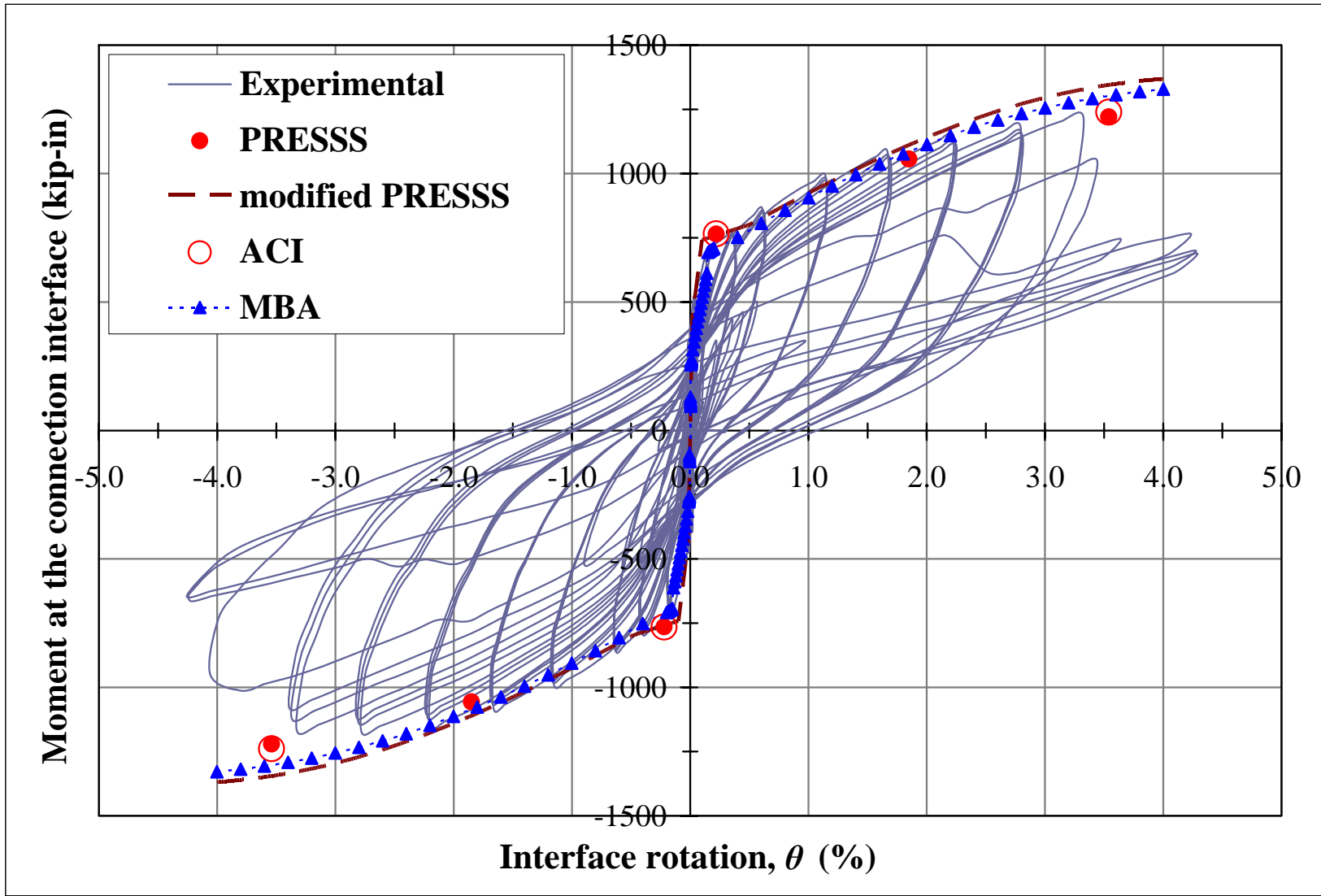


Figure 4.14 Response of NIST Specimen O-P-Z4.

To improve the calculation of the elastic stiffness in the modified analysis procedure a trilinear idealization is suggested for the neutral axis depth as a function of interface rotation. This is demonstrated in Figure 4.15, where point 1 corresponds to the beam height at 0 percent interface rotation, and points 2 and 3 are defined at interface rotations of 0.1 percent and 1.0 percent, respectively. The neutral axis depth (c) at point 3 is found from Eq. 4.11 as suggested in Section 4.4.2, whereas the neutral axis depth corresponding to point 2 is approximated to $2c$.

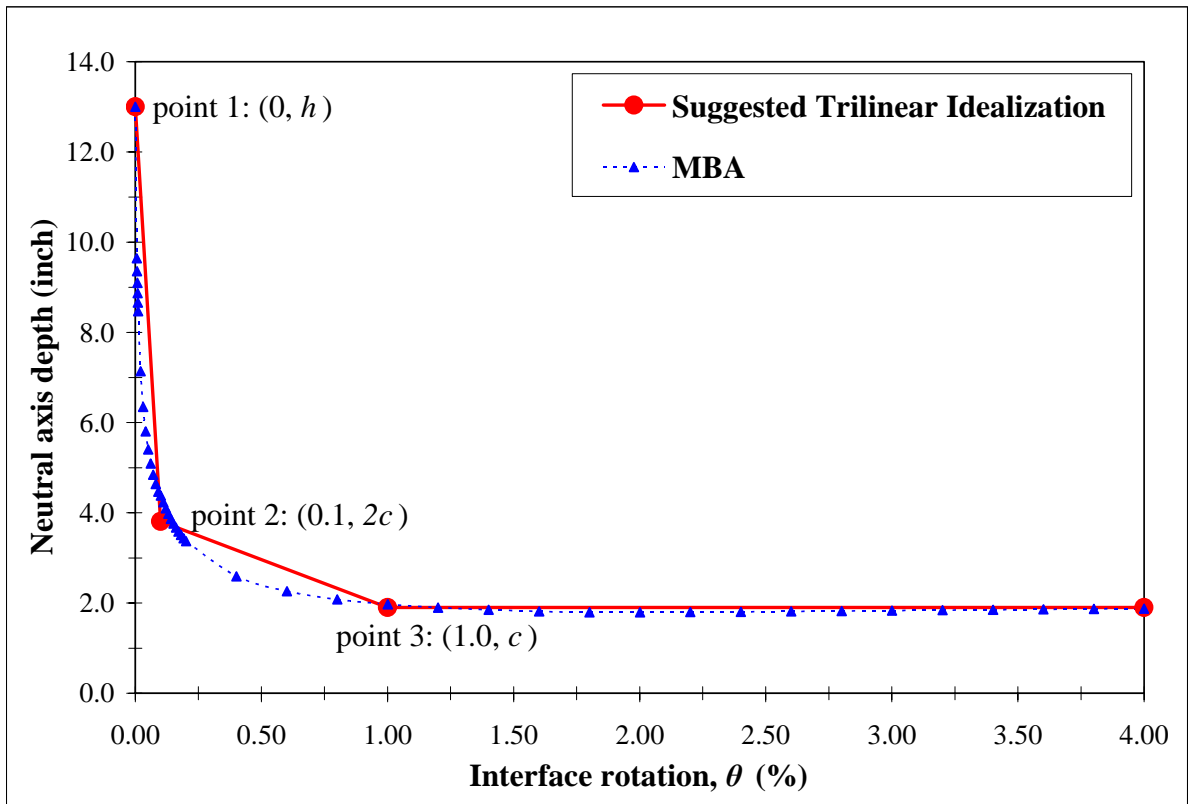


Figure 4.15 Suggested trilinear idealization to improve the neutral axis depth representation in the modified PRESSSS analysis procedure.

In Figures 4.13 and 4.14, the PRESSS analysis results were plotted against the target rotations assumed at the different system states. Using the calculated neutral axis depth and the assumed strains for different system states (see Table 4.2) for this analysis procedure, an interface rotation may be computed as follows:

$$\theta_{cal} = \frac{\varepsilon_{st} \cdot (l_{su} + \alpha_b \cdot d_b)}{d_g - c} \quad (4.19)$$

where θ_{cal} is the calculated interface rotation corresponding to the moment estimated from Eq. 4.9 and α_b is a variable that defines the growth in the debonded length of the mild steel reinforcing bars. Assuming two values for α_b (i.e., $\alpha_b = 0$ and 5.5 that were suggested as the lower and upper bond values for α_b in References [4.5 and 4.13]), Figure 4.16 compares the assumed interface rotations with those calculated from Eq. 4.19 at all three states, which shows consistently that the calculated rotations are significantly lower than the assumed rotations (also see Table 4.2). The implications of the comparisons presented in Figure 4.16 and Table 4.2 are that: (1) the strains suggested for the selected λ_{st} values in the PRESSS guidelines are not compatible as confirmed later in Figure 4.22, and (2) the assumed growth for the debonded length of the mild steel tension reinforcement may not be satisfactory. Also included in Table 4.2 are the λ_{st} values obtained from Eq. 4.19 corresponding to the calculated rotations. When these lower λ_{st} values were used, the moment resistance of the hybrid connections was reduced by about 5–10 percent of those reported for the PRESSS analysis procedure in Figures 4.13 and 4.14.

Table 4.2 Comparison of assumed and calculated interface rotations for Specimen M-P-Z4.
(Similar comparisons were also observed for O-P-Z4).

Suggested System State	Strain	Assumed			Calculated		
		Drift (%)	Rotation (%)	λ_{st}	Drift (%)	Rotation (%)*	λ_{st}
First Yield	0.002	0.5	0.28	1.0	0.27	0.03	0.30
Design	0.04	2.0	1.93	1.35	1.45	1.30	1.21
Max. Credible	0.08	3.5	3.63	1.5	2.74	2.76	1.45

* α_b was taken as 5.5; rotations and drifts are related by Eq. 3.45a.

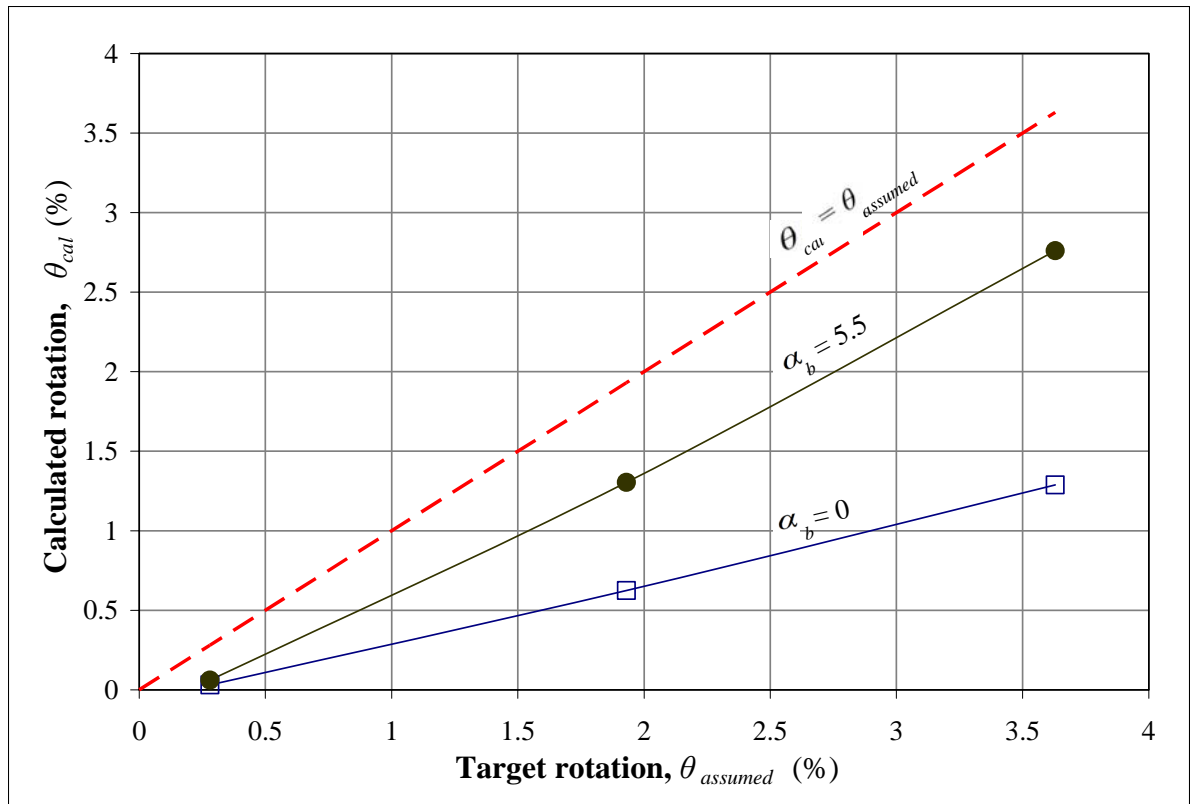


Figure 4.16 Comparison of the assumed interface rotations with the calculated interface rotations for Specimen M-P-Z4.

(b) Neutral axis depth

The neutral axis depth as a function of interface rotation was established using three displacement transducers mounted to each face of the interior column at the first floor of the PRESSSS test building. As shown in Figure 4.17, the neutral axis depth and interface rotation were determined using variables 'a' and 'b' when the top part of the interface experienced a crack opening.

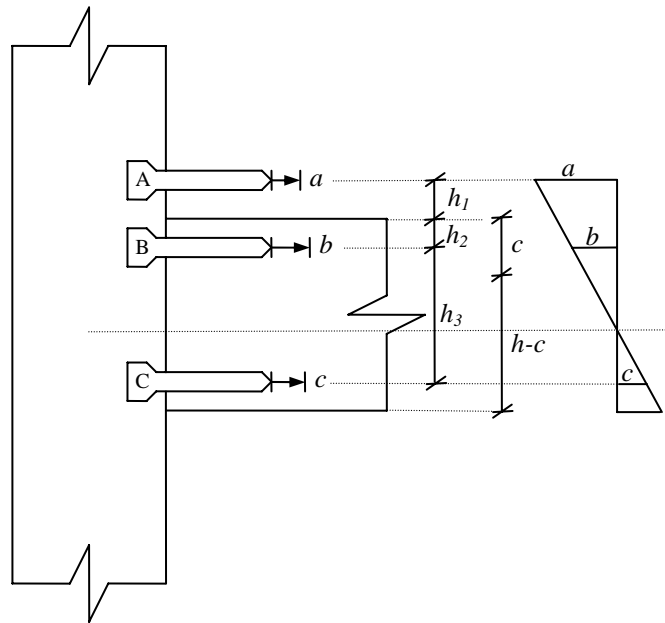


Figure 4.17 An illustration showing displacement transducers mounted to the face of the column at first floor of the hybrid frame in the PRESSSS test building.

In Figure 4.18, the reduced experimental data are compared with various analysis results. The MBA prediction satisfactorily captures the envelope of the data points while the procedure adopted in the modified PRESSSS analysis appears satisfactory for interface rotations from 1.0 to 4.0 percent. A trilinear approximation suggested above for the modified analysis will

significantly improve the comparisons at interface rotations below 1 percent. An increase in the neutral axis depth as θ increases in Figure 4.18 for the PRESSS and ACI T1.2-03 procedures contradicts the actual test observations. Although these procedures appear to show good correlations with experimental data at $\theta_{\max} = 3.15$ percent rotation, it is important to note that a small increase in the neutral axis depth indicated by the test data at higher rotations was primarily due to damage that occurred to the beam corners and grout pads. Such damage was not modeled by the analysis procedures.

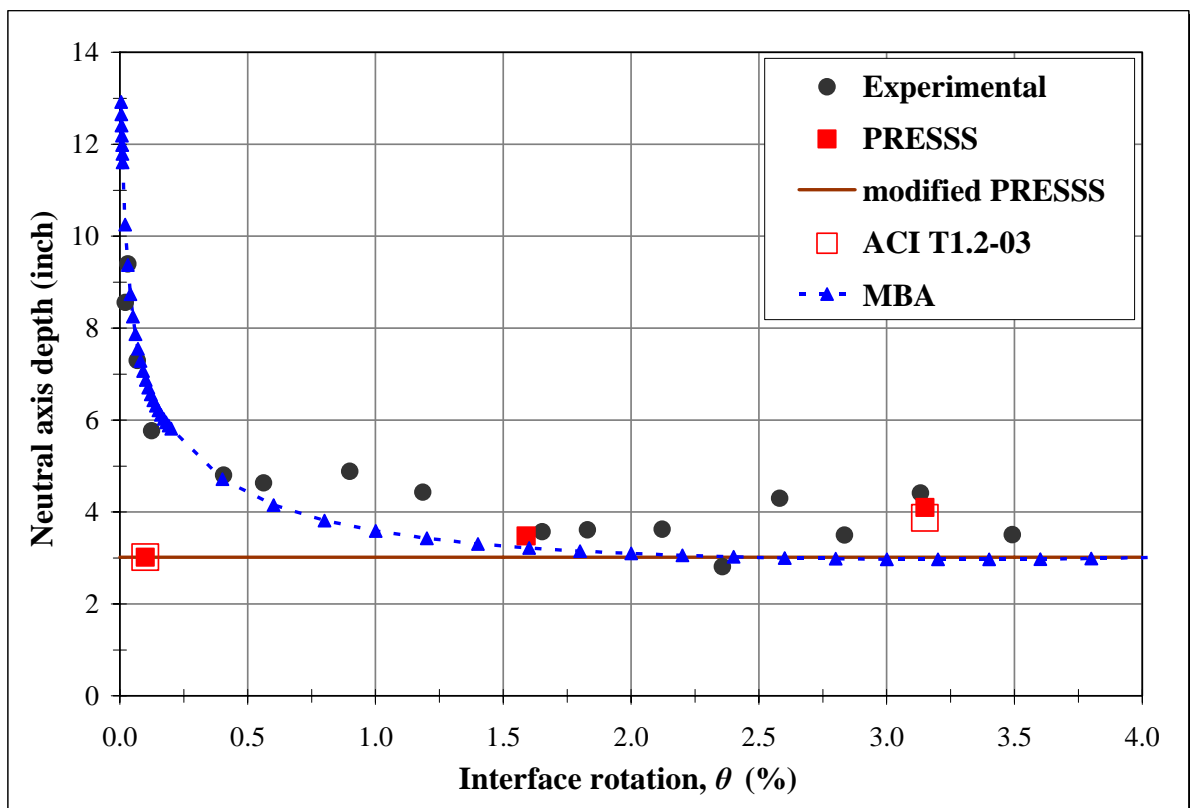


Figure 4.18: The neutral axis depth variation in the hybrid frame connection at the first floor of the PRESSS test building.

(c) Post-tensioning tendon elongation

As the interface rotation increases, the elongation of the post-tensioning steel and the stress in the tendon are expected to increase, both of which depend on the height of the beam and neutral axis depth (see Figure 4.3 and Eq. 4.20).

$$\Delta_{pt} = \theta \cdot \left(\frac{h_g}{2} - c \right) \quad (4.20)$$

A comparison between the analytical predictions and measured elongations is shown in Figure 4.19 using the PRESSS test data, which confirms analytical procedures satisfactorily predict the experimentally obtained elongation vs. interface rotation envelope. Given the damage that occurred to the beam corners and grout pads at large drifts, the MBA analysis is again relatively more accurate than the other analytical methods, and provides a reliable prediction of the elongation as a function of interface rotation. Despite the error in the neutral axis depth calculation, the PRESSS and ACI analysis procedures show satisfactory comparisons at all three system states. This is because the distance between the tendon location and the neutral axis depth is relatively small and that the width to depth ratio of the beam section is sufficiently large. For wall systems, the section dimension ratio is considerably small and the distance to the tendon location from the neutral axis depth is relatively large. As a result, Thomas [4.11] found the PRESSS analysis based on the equivalent stress concept underestimated the tendon elongation by up to 26 percent.

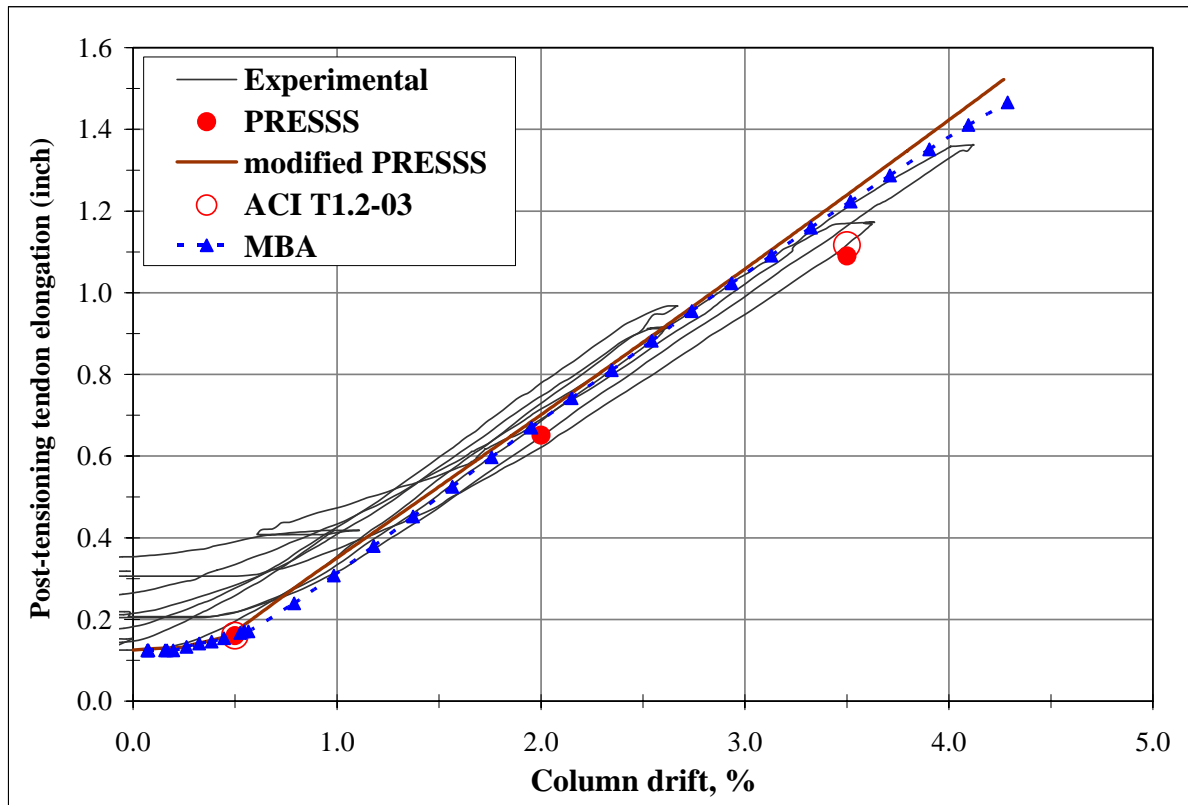


Figure 4.19: Prestressing tendon elongation vs. column drift at the first floor of the PRESSS test building.

In the NIST tests, the change in the prestressing force due to the tendon elongation was directly measured. Figures 4.20 and 4.21 compare the experimentally measured total tendon force as a function of column drift with that predicted by various analysis procedures for M-P-Z4 and O-P-Z4, respectively. All the analytical methods show satisfactory predictions of the experimental values. It is seen that the MBA method marginally overpredicts the prestressing force at drifts greater than 2.5 percent. As evidence in Figures 4.13 and 4.14, some damage to the NIST test specimens occurred at these drifts, which was not modeled in the MBA or in any other analysis methods. Thus, for comparison purposes, it may be

appropriate to examine the results of other analysis methods with the MBA results. As seen in Figures 4.20 and 4.21, the modified PRESSS analysis prediction exactly matches the MBA prediction while the PRESSS and ACI T1.2-03 analysis results give slightly lower values at the maximum credible state.

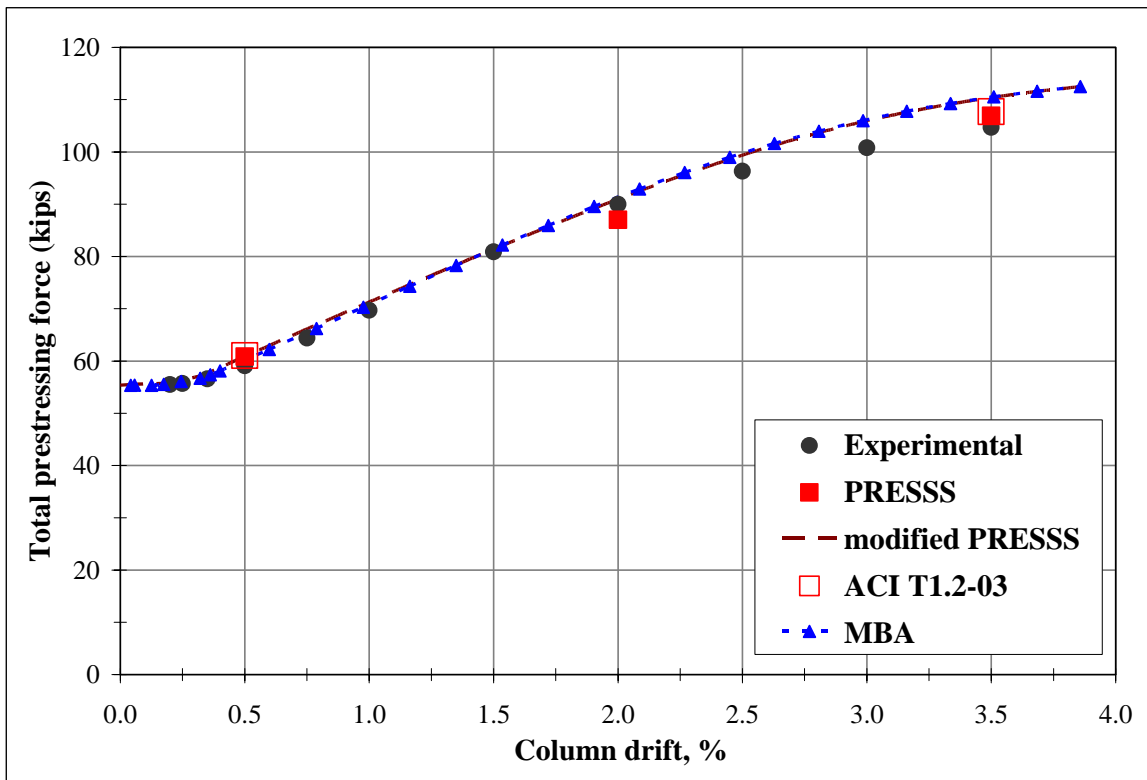


Figure 4.20 The total prestressing force as a function of column drift for Specimen M-P-Z4.

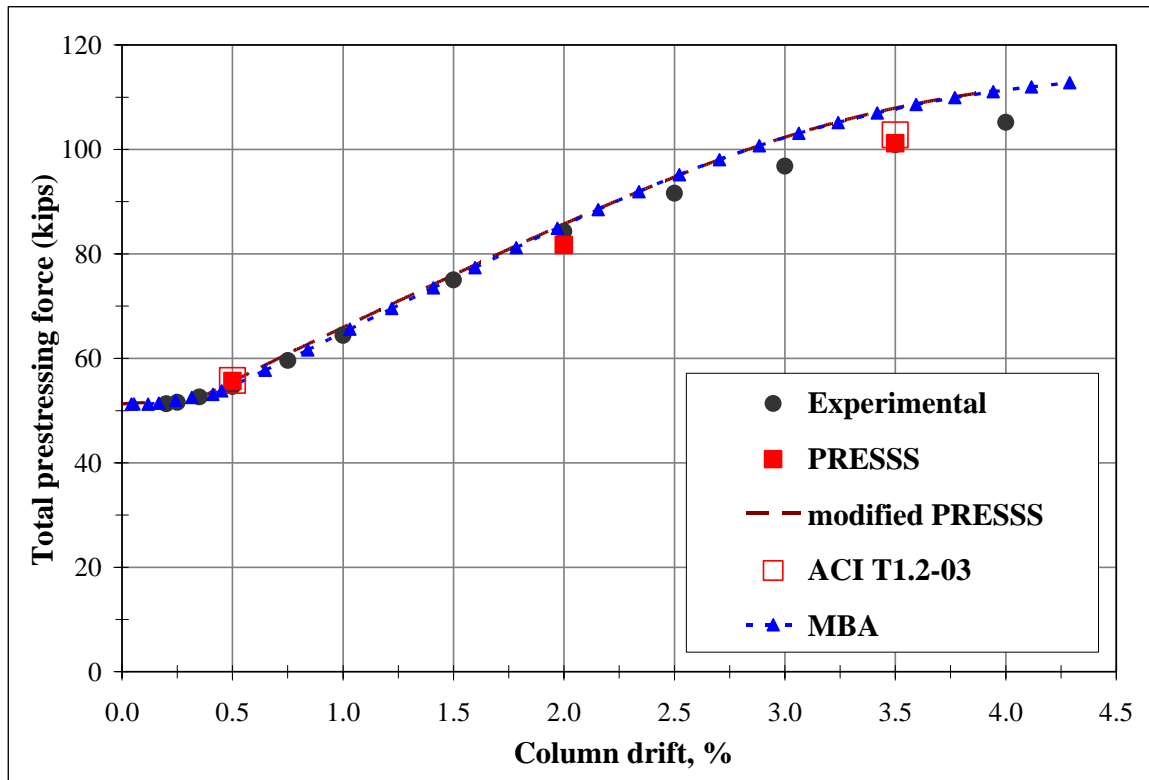


Figure 4.21 The Total prestressing force as a function of column drift for Specimen O-P-Z4.

(d) Stress-strain behavior of mild steel reinforcement

To examine how the stress-strain behavior of the tension reinforcement is modeled in various analysis procedures, the measured response of an A-706 steel coupon obtained as part of the PRESSS test is compared to different approaches in Figure 4.22. As seen, the Dodd and Restrepo-Posada Model [4.16] used in the MBA method provides a good correlation with experimental data. The suggested stress-strain values in the PRESSS guidelines somewhat overestimate the stresses at strains chosen for the design and maximum credible states, which would lead to an increase in the prediction of the moment resistance at the precast connections. In the modified PRESSS analysis, an assumed relationship between the steel

stress and interface rotation was used (see Figure 4.5 and Eq. 4.10). Strains corresponding to the rotations in Eq. 4.10 may be found using Eq. 4.19 if an appropriate growth for the debonded length of the mild steel reinforcement is known. In the PRESSSS guidelines, it is suggested that the growth length may be taken as $5.5 \cdot d_b$ whereas the MBA analysis assumed a growth length of $20.5 \cdot d_b$. To fit the experimental data in Figure 4.22, it was found from a trial and error procedure that the modified PRESSSS analysis suggests a growth of $13.5 \cdot d_b$ in the debonded length of the mild steel reinforcement. The significant discrepancies seen in the growth of the unbonded length suggests that a further investigation on this subject matter is required.

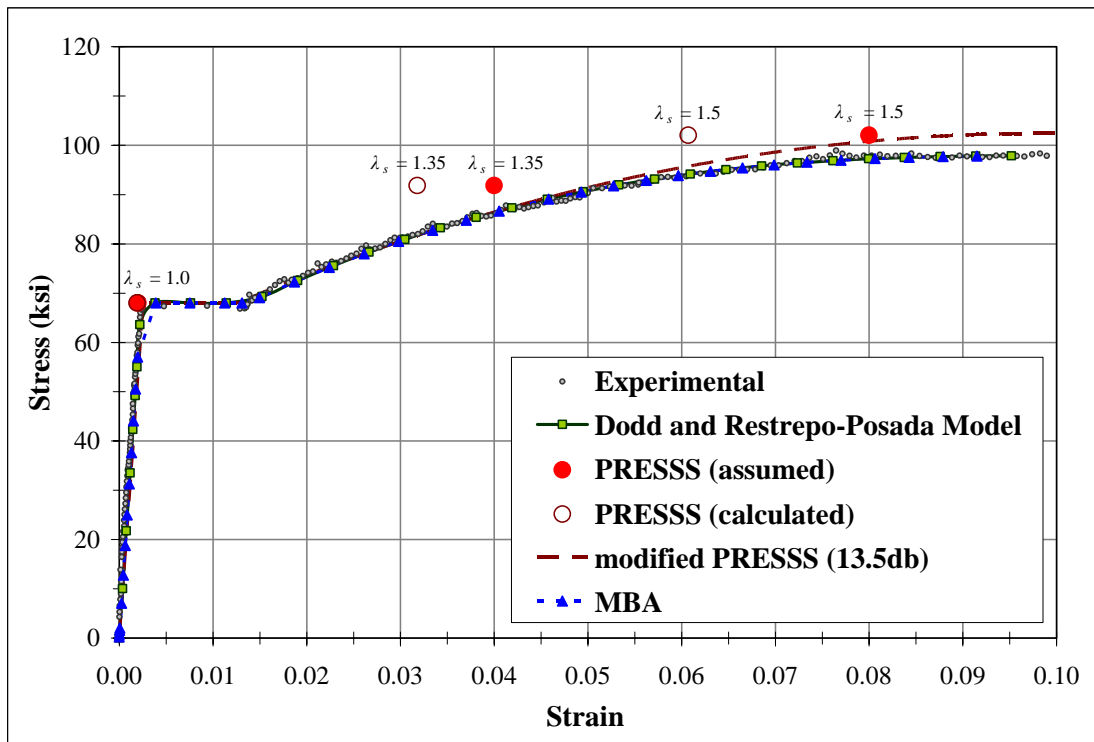


Figure 4.22: Stress-strain response of the tension mild steel reinforcement used in the first floor of the PRESSSS building.

(e) Re-centering check

As discussed in Section 3.2.1, the re-centering check suggested in the PRESSSS guidelines is examined in Table 4.3 using the experimental data. Despite satisfying the suggested condition, it is seen that experimental results indicate that the hybrid frames examined in this study did not produce complete re-centering at the design and maximum credible states. In Table 4.3, the reported residual drifts are those found from the experimental data after the test units were subjected to drifts at or close to the drifts assumed for the system states. Even when subjected to the design level drift, O-P-Z4 and the PRESSSS building produced a significant residual drift. Hence, a further investigation is recommended for improving the re-centering check in the design procedure.

Table 4.3 Re-centering check as suggested by the PRESSSS guidelines at the design and maximum system states.

Test Unit	$M_{pt,0}$	$M_{st,0}$	$M_{sc,0}$	$M_{pt,0} > M_{st,0} + M_{sc,0} ?$	Residual Drift (%)
Design system state (Drift = 2%)					
M-P-Z4	628	189	0	Yes	0.14
O-P-Z4	599	353	-2	Yes	0.41
PRESSSS	1471	1138	-91	Yes	0.25
Maximum credible system state (Drift = 3.5%)					
M-P-Z4	755	186	3	Yes	0.18
O-P-Z4	731	347	4	Yes	0.91
PRESSSS	1749	1129	-81	Yes	0.48

Note: * Interpolated from experimental data where necessary

(f) Plastic hinge length and compression strain

The PRESSS guidelines also suggested an approximate plastic hinge length and an average compressive strain ($\varepsilon_{c,av}$) over the suggested hinge length (see Section 3.2.1). Table 4.4 compares the PRESSS suggested values with the plastic hinge length used in the MBA analysis and the maximum concrete compressive strain ($\varepsilon_{c,max}$) computed in the MBA analysis. Significantly different values seen for the plastic hinge length and concrete compressive strains warrant further investigation into these parameters. However, it is noted that the l_p and $\varepsilon_{c,av}$ values are not used in the PRESSS guidelines and are only required for detailing the confinement reinforcement, which is currently achieved based on the ACI building standard [4.9].

Table 4.4 Comparisons of the plastic hinge length and concrete compressive strain suggested by the PRESSS guidelines with those used in the MBA analysis at the design system state.

Test Unit	θ_{des}	MBA		PRESSS	
		l_p	$\varepsilon_{c,max}$	l_p	$\varepsilon_{c,av}$
M-P-Z4	0.0193	6.62	0.00518	2.83	0.0193
O-P-Z4	0.0185	7.44	0.00440	2.78	0.0185
PRESSS	0.0159	14.85	0.00272	3.48	0.0159

4.7.2 System Level Validation

Since the modified PRESSSS analysis procedure can produce a continuous moment-rotation response for hybrid connections, a system level verification is performed on a five-story building using a pushover analysis and an inverted triangular load pattern. The building dimensions are identical to the PRESSSS building, which consisted of two seismic frames (see Section 2.2.2). For the system level analysis, both seismic frames were assumed to be identical to the prestressed frame in the PRESSSS building with hybrid connections at all five levels (see Figure 4.23). In the PRESSSS building, hybrid connections were used in the lower three floors with pretensioned connections in the upper two floors. These upper floor connections were redesigned to with hybrid connections, and all connection details are summarized in Table 4.5.

Each of the frame connections was analyzed using the modified PRESSSS analysis procedure, and the resulting moment-rotation response envelopes were represented in the frame model using spring elements as illustrated in Figure 4.24. The springs modeled the moment resistance contributed by the post-tensioning tendons and mild steel reinforcement as a function of interface rotation. Figure 4.25 shows the comparison of moment-rotation behaviors of these spring elements obtained by the modified PRESSSS analysis procedure with hybrid connection behavior obtained from the analytical model using the computer program RUAUMOKO [4.17]. The frame model, which was originally developed by Vernu [4.2] using RUAUMOKO, was subjected to a gradually increasing inverted lateral load until a displacement of 12 inches was reached at the third floor level. In this model, the columns

and beams were assumed to have effective moment of inertias of 60% and 50% of the gross moment of inertias, respectively.

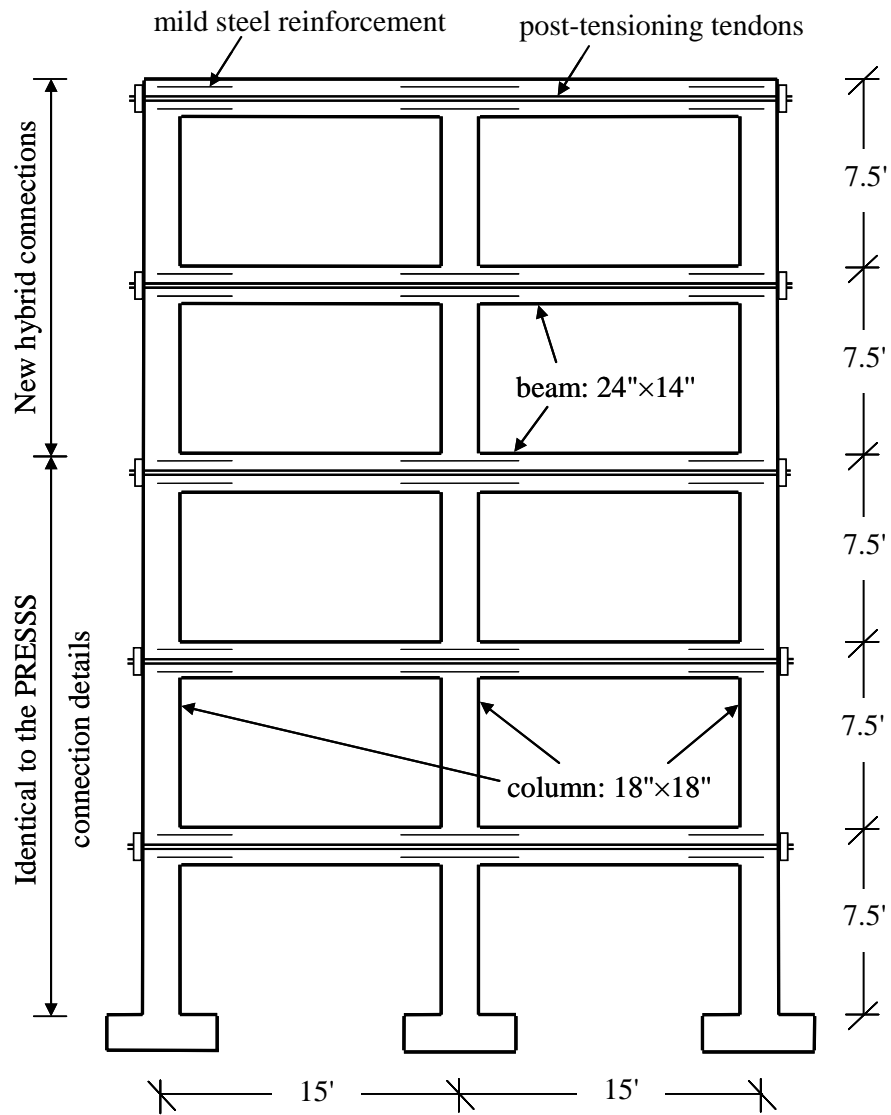


Figure 4.23 Details of the five-story hybrid frame.

Table 4.5 Hybrid connection details used for the building frame in Figure 4.23.

Floor	A_s (in ²)	A_{pt} (in ²)	f_{pi} (ksi)
1	0.88 (2 #6)	0.918 (6 strands)	118.95
2	0.62 (2 #5)	0.765 (5 strands)	118.95
3	0.62 (2 #5)	0.765 (5 strands)	118.95
4	0.465	0.635	118.95
5	0.420	0.310	118.95

Note: At floors 4 and 5, the required post-tensioning tendon and mild steel reinforcement were determined using the modified PRESSS design procedure (see Appendix C).

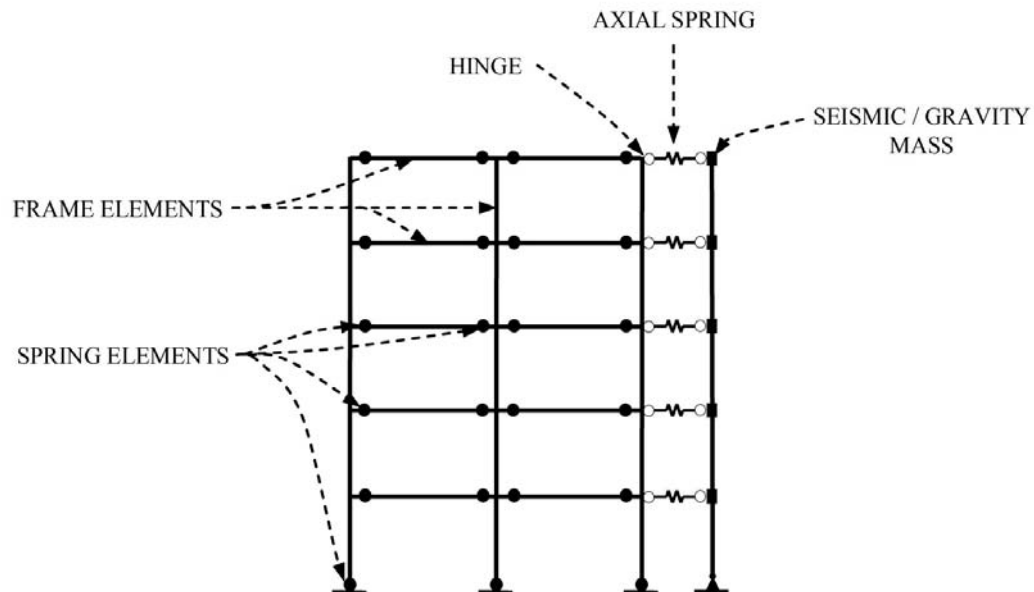
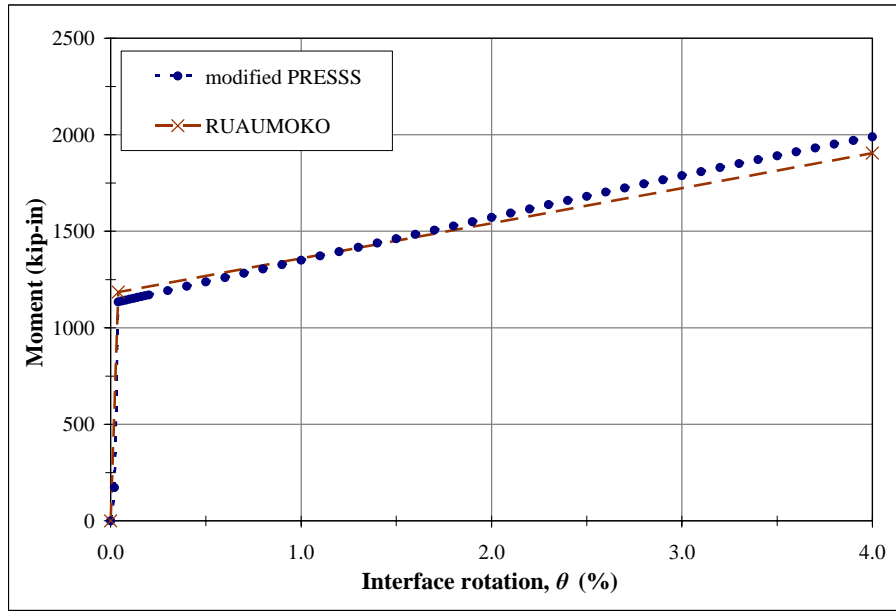
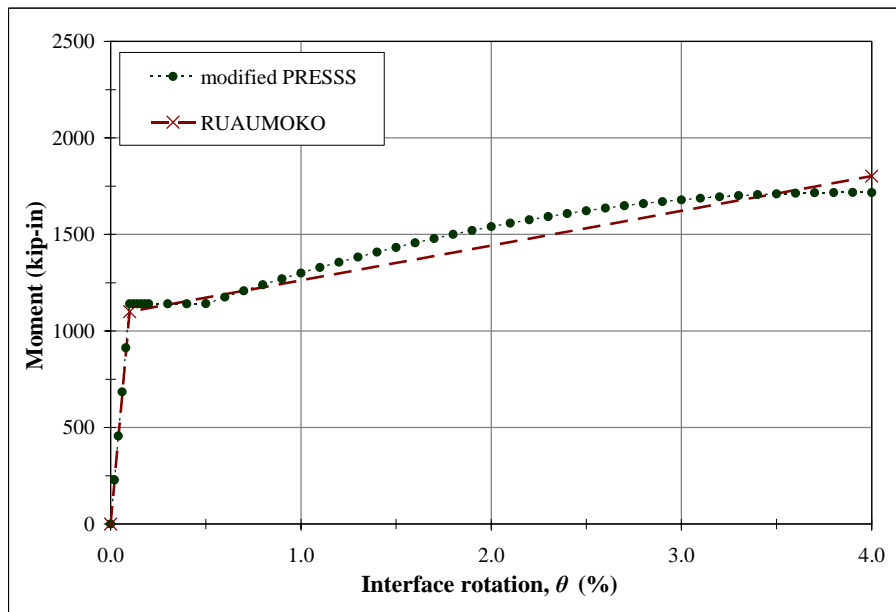


Figure 4.24 Finite element model of the frame [4.2]



(a) Moment contribution by the post-tensioning tendons



(b) Moment contribution by the mild steel reinforcement

Figure 4.25 Comparison of hybrid connection behavior obtained by the modified PRESSS analysis procedure and analytical model using RUAUMOKO.

A comparison between the analytical prediction and experimentally measured base moment vs. lateral displacement at the third floor of the building is shown in Figure 4.26; a similar figure using the base shear as the main variable is produced in Figure 4.27. The modified PRESSS analysis procedure appears to be satisfactory for predicting the hybrid frame response at the system level. As previously noted, some damage occurred to the connection regions at large displacements, which led to some discrepancies between the analytical and experimental values in this displacement range. A similar investigation using the MBA analysis procedure was conducted by Vernu [4.2], who also found satisfactory comparisons between the experimental and analytical results.

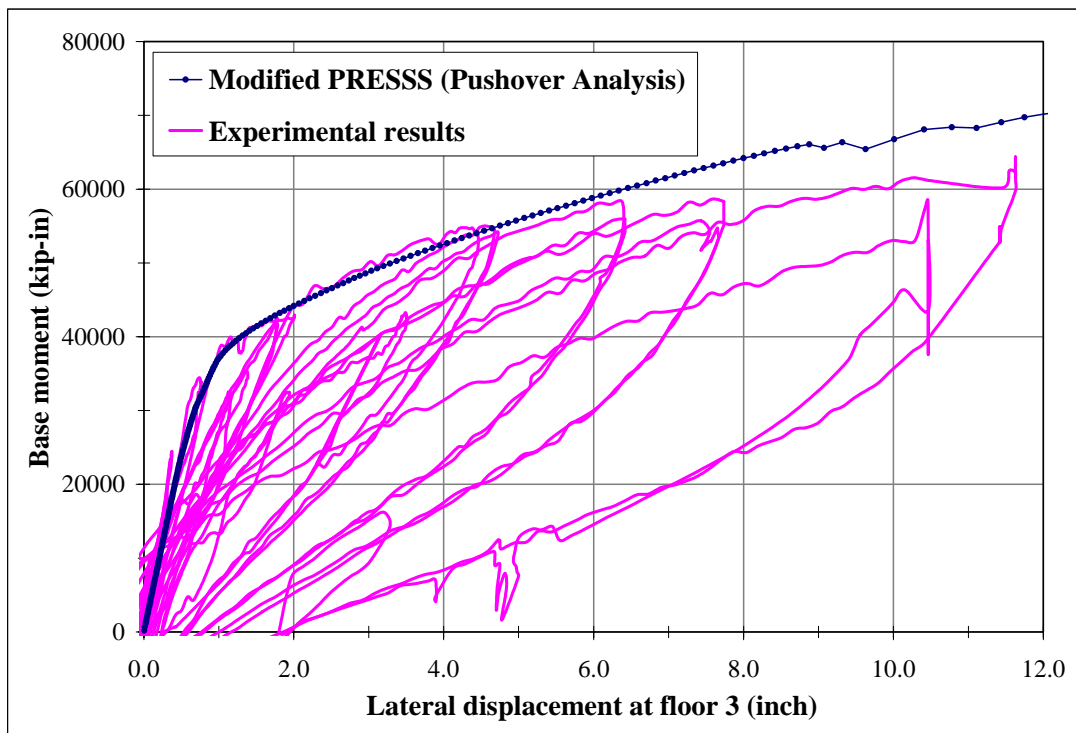


Figure 4.26: Comparison of the base moment resistance of the hybrid building as a function of lateral displacement at the third floor.

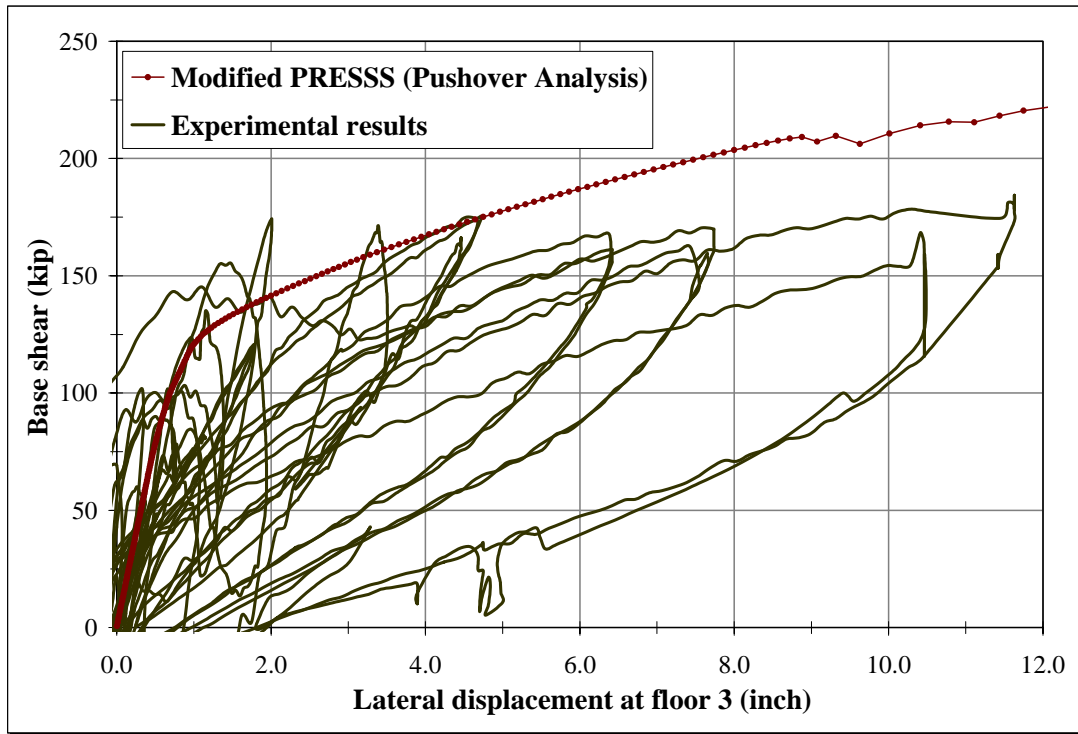


Figure 4.27: Comparison of the base shear resistance of the hybrid building as a function of lateral displacement at the third floor.

4.8 Conclusions

Based on the investigation conducted in this report, the following conclusions have been drawn:

- 1) The analysis methods based on the PRESSS design guidelines and ACI T1.2-03 document adequately predicted the moment resistance of the two hybrid frame systems (M-P-Z4 and O-P-Z4) when they were compared against experimental data at the suggested drifts in the design procedures. However, the assumed drifts for the

- different system states differed significantly from those calculated based on the suggested strains for the tension mild steel reinforcement in the design procedures.
- 2) Although the elongation in the post-tensioning steel appeared to have been satisfactorily predicted by the PRESSS and ACI T1.2-03 analysis procedures, it is anticipated that these methods will underestimate the elongation of the post-tensioning steel in the hybrid frames at large drifts. This is because the test units used in this study experienced some strength degradation at large drifts, which helped the experimental data to move closer to the analytical predictions. The percentage of error will depend on the width to depth ratio of the section. As the ratio reduces, the error is expected to increase.
 - 3) By using the equivalent stress concept to compute the neutral axis depth at a given drift, the PRESSS guidelines and the ACI T1.2-03 document suggest an increase in neutral axis depth as the interface rotation increases. This is in direct contrast to the expected behavior, which has been confirmed by the test data. This incorrect modeling of the neutral axis trend contributes to underestimation of the tendon elongation, requiring a larger amount of prestressing steel at a given design drift.
 - 4) For the maximum drift of 3.5 percent, the ACI T1.2-03 document recommends an over-strength factor of 1.25 for the compression mild steel reinforcement at the connection, whereas a factor of 1.0 is suggested in the PRESSS guidelines. The difference in the over-strength factors provided no significant change to the moment resistance of the hybrid connection due to the close proximity of the compression steel location with respect to the neutral axis.

- 5) The analysis based on the monolithic beam analogy concept, which employed satisfactory constitutive models for the behavior of concrete, mild steel reinforcement, and prestressing steel, provided accurate prediction of the moment-rotation responses of the hybrid connections. This analysis procedure also provided good estimates for the neutral axis depths and elongations in the post-tensioning tendons.
- 6) The modified PRESSSS analysis procedure provided good predictions for the moment-rotation responses, elongations in the post-tensioning steel, and neutral axis depths. Despite the simplifications used in the analysis, the results are very close to those predicted by the MBA analysis. In addition to having the capability to predict moment resistance of a hybrid connection as a function of interface rotation, the modified analysis simplifies the design procedure suggested by Stanton and Nakaki [4.5] and the ACI Innovation Task group [4.6].
- 7) With a system level response verification, it has been shown that the results from the modified PRESSSS analysis procedure can be used to perform satisfactory pushover analyses on hybrid frame buildings.
- 8) The investigation found that the research information available to date is not sufficient to recommend the use of grout material that is weaker in strength than the concrete of the precast members. More research is also required to satisfactorily quantify the growth in the debonded length of the mild steel reinforcement and the extreme fiber concrete strain, and to improve the check on the re-centering capability of the hybrid frame in the design procedures. While the concrete strains obtained

from different methods varied significantly, the re-centering check suggested in the PRESSS guidelines was found to be inadequate.

4.9 Recommendations

Based on the design validation investigation conducted in this report, the PRESSS design guidelines suggested for the design of hybrid frames may be improved by the following recommendations:

- 1) The grout in the precast connection interface should be designed to have compressive strength greater than the compressive strength of concrete of the adjoining precast column and beams. The design of the hybrid connection should be based on the concrete strength of the beam located adjacent to the grout pad.
- 2) The beam concrete strength (f'_c) should be approximated to $1.6 \cdot f'_c$ to account for concrete confinement effects when the confinement reinforcement is based on seismic provisions of the ACI Building Code [4.9] or a similar document.
- 3) The tensile steel stress should be presented as a function of beam to column interface rotation as suggested in Eq. 4.10.
- 4) The neutral axis depth should be calculated at a design drift of 2 percent or at 2 percent interface rotation at the connection, and this neutral axis depth may be used for design calculations at all other interface rotations that are greater than 1 percent. This approach will also simplify the design of hybrid connections.

- 5) At the design drift, the stress in the post-tensioning tendons should be accurately estimated. Eq. 4.12 may be used for this purpose when Grade 270 prestressing strands are used.

Most of the above recommendations were incorporated in the modified PRESSS analysis procedure investigated in this paper, which provided good predictions of the experimental results at the connection as well as at the system level.

4.10 References

- [4.1] Stone, W. C., Cheok, G. S., and Stanton, J. F., “Performance of Hybrid Moment-Resisting Precast Beam-Column Concrete Connections Subjected to Cyclic Loading,” *ACI Structural Journal*, Vol. 92, No. 2, 1995, pp. 229-249.
- [4.2] Vernu, S., “Connection and structural level analysis of precast hybrid frame systems,” *Master Thesis, Iowa State University, Ames, Iowa, 2003.*
- [4.3] Stanton, J., Stone, W. C., Cheok, G. S., “A Hybrid Reinforced Precast Frame for Seismic Regions,” *PCI Journal*, Vol. 42, No. 2, 1997, pp. 20-32.
- [4.4] Priestley, M. J. N., “The PRESSS Program – Current Status and Proposed Plans for Phase III,” *PCI Journal*, Vol. 41, No. 2, 1996, pp. 22-40.
- [4.5] Stanton, J. F. and Nakaki, S. D., “Design Guidelines For Precast Concrete Seismic Structural Systems,” *PRESSS Report No. 01/03-09, UW Report No. SM 02-02*, The University of Washington and The Nakaki Bashaw Group, Inc., 2002.
- [4.6] ACI Innovative Task Group 1 and Collaborators, *Special Hybrid Moment Frames Composed of Discretely Jointed Precast and Post-Tensioned Concrete Members (ACI T1.2-03) and Commentary (T1.2R-03)*, Michigan, 2003.
- [4.7] Englekirk, R. E., “Design-Construction of The Paramount – A 39-Story Precast Concrete Apartment Building,” *PCI Journal*, July-August, 2002, pp. 56-69.
- [4.8] ACI Innovation Task Group 1 and Collaborators, *Acceptance Criteria for Moment Frames Based on Structural Testing (T1.1-01) and Commentary (T1.1R-01)*, Michigan, 2001.

- [4.9] American Concrete Institute, *Building Code Requirements for Structural Concrete (ACI 318-99) and Commentary (ACI 318R-99)*, Michigan, 1999.
- [4.10] Priestley, M. J. N., Sritharan, S., Conley, J. R., Pampanin, S., "Preliminary Results and Conclusions From the PRESSS Five-Story Precast Concrete Test Building," *PCI Journal*, Vol. 44, No. 6, 1999, pp. 42-67.
- [4.11] Thomas, D. J., "Analysis and Validation of a Seismic Design Method Proposed for Precast Jointed Wall Systems," *Master Thesis, Iowa State University, Ames, Iowa*, 2003.
- [4.12] Mattock, A. H., "Flexural Strength of Prestressed Concrete Sections by Programmable Calculator," *PCI Journal*, Vol. 24, No. 1, 1979, pp. 26-37.
- [4.13] Cheok, G. S., Stone, W. C., Nakaki, S. D., "Simplified Design Procedure for Hybrid Precast Concrete Connections," National Institute of Standards and Technology, *SCTR 5765*, 1996.
- [4.14] Celik, O., "Analysis and Validation of a Seismic Design Method Proposed for Precast Hybrid Systems," *Master Thesis, Iowa State University, Ames, Iowa*, 2004.
- [4.15] Mander, J. B., Priestley, M. J. N., and Park, R., "Theoretical Stress-Strain Model For Confined Concrete," *Journal of the Structural Division, ASCE*, Vol. 114, No. 8, August, 1988, pp. 1804-1826.
- [4.16] Dodd, L. L. and Restrepo-Posada, J. I., "Model for Predicting Cyclic Behavior of Reinforcing Steel," *Journal of Structural Engineering, ASCE*, Vol. 121, No. 3, March, 1995, pp. 443-445.
- [4.17] Carr, A. J., "Ruaumoko, Computer Program Library," University of Canterbury, Christ Church, New Zealand, Version 2.0, 1999.

4.11 Acknowledgements

The design validation study on hybrid precast frames reported in this paper was funded by the *Precast/Prestressed Concrete Manufacturers Association of California (PCMAC)*, which is gratefully acknowledged. The authors also thank Gerry Cheok and Sivakkolundu Vernu for their assistance with interpretation of the NIST test data and MBA analysis of the hybrid connections, respectively.

APPENDIX A

PRESSS ANALYSIS PROCEDURE

PRESSS Analysis v.6.1

This appendix presents the Mathcad program developed for analyzing hybrid frame connections based on the PRESSS guidelines proposed by Stanton and Nakaki [4.5].

INPUT: (Section & Material Properties (e.g., M-P-Z4))

Section Properties:

$$\begin{aligned}h &:= 16 \\b &:= 8 \\d' &:= 1 \\A_{pt} &:= 0.459 \\A_s &:= 0.22 \\I_{pu} &:= 40.15\end{aligned}$$

Material Properties:

$$\begin{aligned}E_p &:= 29000 \\f_{py} &:= 247.95 \\f_{sy} &:= 61.19 \\f_{c'} &:= 6.815 \\f_{pi} &:= 120.640\end{aligned}$$

Others:

$$\begin{aligned}\lambda_{sc} &:= 1.0 \\ \lambda_{st}(\theta) &:= \begin{cases} \lambda_{st} \leftarrow 1.0 & \text{if } \theta = 0.0028 \\ \lambda_{st} \leftarrow 1.35 & \text{if } \theta = 0.0193 \\ \lambda_{st} \leftarrow 1.5 & \text{if } \theta = 0.0363 \end{cases} \\ \beta_1 &:= 0.85 - 0.05 \cdot (f_{c'} - 4) \\ \beta_1 &= 0.709 \\ \zeta &:= \frac{d'}{h} \\ \zeta &= 0.0625\end{aligned}$$

ANALYSIS:

ORIGIN := 1

Neutral axis depth:

$$\begin{aligned} \text{NA}(\theta, A_{pt}, A_s) := & \left. \begin{aligned} & f_{sc} \leftarrow \lambda_{sc} \cdot f_{sy} \\ & f_{st} \leftarrow \lambda_{st}(\theta) \cdot f_{sy} \\ & \eta \leftarrow 0 \\ & \eta_{\text{check}} \leftarrow 1 \\ & \text{while } \eta_{\text{check}} - \eta > 0.001 \\ & \quad \left| \begin{aligned} & \eta \leftarrow \eta + 0.001 \\ & \Delta_{pt} \leftarrow \theta \cdot (0.5 - \eta) \cdot h \\ & \Delta f_{pt} \leftarrow \frac{\Delta_{pt}}{l_{pu}} \cdot E_p \\ & f_{p0} \leftarrow f_{py} - \Delta f_{pt} \\ & \text{if } f_{p0} > f_{pi} \\ & \quad \left| \begin{aligned} & f_{p0} \leftarrow f_{pi} \\ & f_{pt} \leftarrow f_{p0} + \Delta f_{pt} \end{aligned} \right. \\ & f_{pt} \leftarrow f_{py} \text{ otherwise} \\ & F_{pt} \leftarrow A_{pt} \cdot f_{pt} \\ & F_{st} \leftarrow A_s \cdot f_{st} \\ & F_{sc} \leftarrow A_s \cdot f_{sc} \\ & F_c \leftarrow F_{pt} + F_{st} - F_{sc} \text{ if } \eta > \zeta \\ & F_c \leftarrow F_{pt} + F_{st} + F_{sc} \text{ otherwise} \\ & a \leftarrow \frac{F_c}{0.85 \cdot f_c' \cdot b} \\ & \eta_{\text{check}} \leftarrow \frac{a}{\beta_1 \cdot h} \end{aligned} \right. \\ & \eta \cdot h \end{aligned} \end{aligned}$$

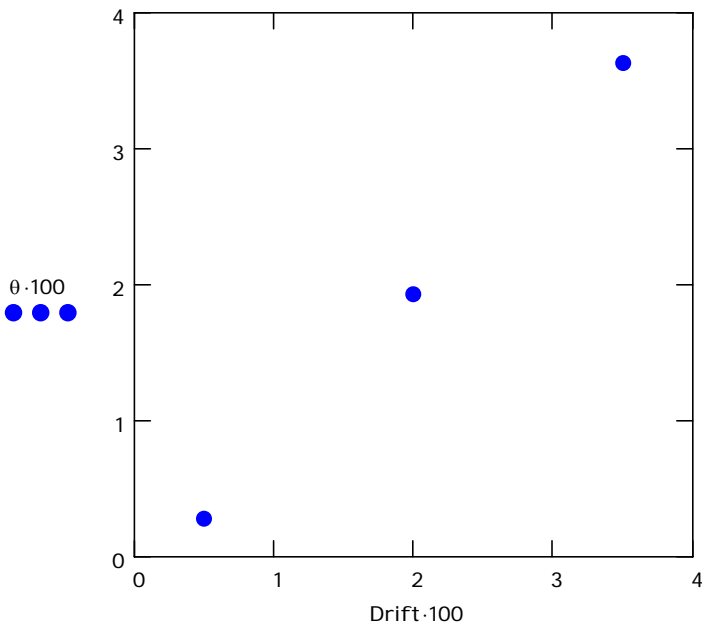
Hybrid Connection Analysis: (valid at 3 system states: "first yield", "design", and "max. credible")

$$\begin{aligned}
 \text{Hybrid}(\theta, A_{pt}, A_s) := & \left\{ \begin{array}{l}
 f_{sc} \leftarrow \lambda_{sc} \cdot f_{sy} \\
 f_{st} \leftarrow \lambda_{st}(\theta) \cdot f_{sy} \\
 \eta \leftarrow \frac{NA(\theta, A_{pt}, A_s)}{h} \\
 \Delta_{pt} \leftarrow \theta \cdot (0.5 - \eta) \cdot h \\
 \Delta f_{pt} \leftarrow \frac{\Delta_{pt}}{l_{pu}} \cdot E_p \\
 f_{p0} \leftarrow f_{py} - \Delta f_{pt} \\
 \text{if } f_{p0} > f_{pi} \\
 \quad \left\{ \begin{array}{l}
 f_{p0} \leftarrow f_{pi} \\
 f_{pt} \leftarrow f_{p0} + \Delta f_{pt}
 \end{array} \right. \\
 f_{pt} \leftarrow f_{py} \text{ otherwise} \\
 F_{pt} \leftarrow A_{pt} \cdot f_{pt} \\
 F_{st} \leftarrow A_s \cdot f_{st} \\
 F_{sc} \leftarrow A_s \cdot f_{sc} \\
 F_c \leftarrow F_{pt} + F_{st} - F_{sc} \text{ if } \eta > \zeta \\
 F_c \leftarrow F_{pt} + F_{st} + F_{sc} \text{ otherwise} \\
 a \leftarrow \frac{F_c}{0.85 \cdot f_c \cdot b} \\
 \alpha \leftarrow \frac{a}{2 \cdot h} \\
 M_{pt} \leftarrow F_{pt} \cdot (0.5 - \alpha) \cdot h \\
 M_{st} \leftarrow F_{st} \cdot (1.0 - \zeta - \alpha) \cdot h \\
 M_{sc} \leftarrow F_{sc} \cdot (\alpha - \zeta) \cdot h \\
 M_{cap} \leftarrow M_{pt} + M_{st} + M_{sc} \\
 \left(\begin{array}{l}
 \Delta_{pt} \\
 f_{st} \\
 F_{pt} \\
 M_{pt} \\
 M_{st} \\
 M_{sc} \\
 M_{cap}
 \end{array} \right)
 \end{array} \right. \\
 \Delta_{pt}(\theta) := & \text{Hybrid}(\theta, A_{pt}, A_s)1 \\
 f_{st}(\theta) := & \text{Hybrid}(\theta, A_{pt}, A_s)2 \\
 F_{pt}(\theta) := & \text{Hybrid}(\theta, A_{pt}, A_s)3 \\
 M_{pt}(\theta) := & \text{Hybrid}(\theta, A_{pt}, A_s)4 \\
 M_{st}(\theta) := & \text{Hybrid}(\theta, A_{pt}, A_s)5 \\
 M_{sc}(\theta) := & \text{Hybrid}(\theta, A_{pt}, A_s)6 \\
 M_{cap}(\theta) := & \text{Hybrid}(\theta, A_{pt}, A_s)7 \\
 \text{Drift}(\theta) := & 0.85 \cdot \theta + 4.08 \cdot 10^{-6} \cdot M_{cap}(\theta)
 \end{aligned}$$

OUTPUT:

$$\theta := \begin{pmatrix} 0.0028 \\ 0.0193 \\ 0.0363 \end{pmatrix} \quad \varepsilon_{st} := \begin{pmatrix} 0.002 \\ 0.04 \\ 0.08 \end{pmatrix} \quad \text{Drift} := \begin{pmatrix} \text{Drift}(\theta_1) \\ \text{Drift}(\theta_2) \\ \text{Drift}(\theta_3) \end{pmatrix}$$

Drift-rotation relationship

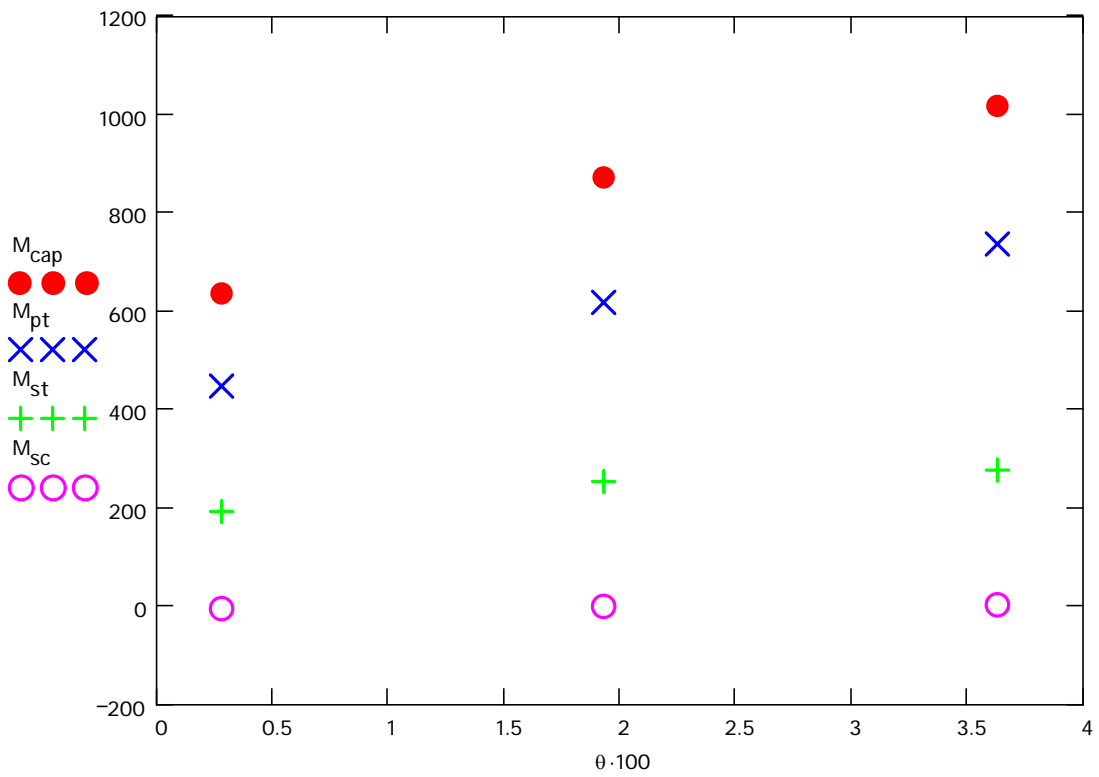


$$\Delta_{pt} := \begin{pmatrix} \Delta_{pt}(\theta_1) \\ \Delta_{pt}(\theta_2) \\ \Delta_{pt}(\theta_3) \end{pmatrix} \quad \text{NA} := \begin{pmatrix} \text{NA}(\theta_1, A_{pt}, A_s) \\ \text{NA}(\theta_2, A_{pt}, A_s) \\ \text{NA}(\theta_3, A_{pt}, A_s) \end{pmatrix}$$

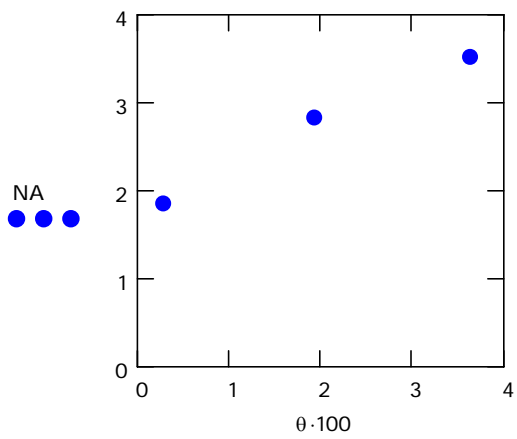
$$f_{st} := \begin{pmatrix} f_{st}(\theta_1) \\ f_{st}(\theta_2) \\ f_{st}(\theta_3) \end{pmatrix} \quad F_{pt} := \begin{pmatrix} F_{pt}(\theta_1) \\ F_{pt}(\theta_2) \\ F_{pt}(\theta_3) \end{pmatrix}$$

$$M_{pt} := \begin{pmatrix} M_{pt}(\theta_1) \\ M_{pt}(\theta_2) \\ M_{pt}(\theta_3) \end{pmatrix} \quad M_{st} := \begin{pmatrix} M_{st}(\theta_1) \\ M_{st}(\theta_2) \\ M_{st}(\theta_3) \end{pmatrix} \quad M_{sc} := \begin{pmatrix} M_{sc}(\theta_1) \\ M_{sc}(\theta_2) \\ M_{sc}(\theta_3) \end{pmatrix} \quad M_{cap} := \begin{pmatrix} M_{cap}(\theta_1) \\ M_{cap}(\theta_2) \\ M_{cap}(\theta_3) \end{pmatrix}$$

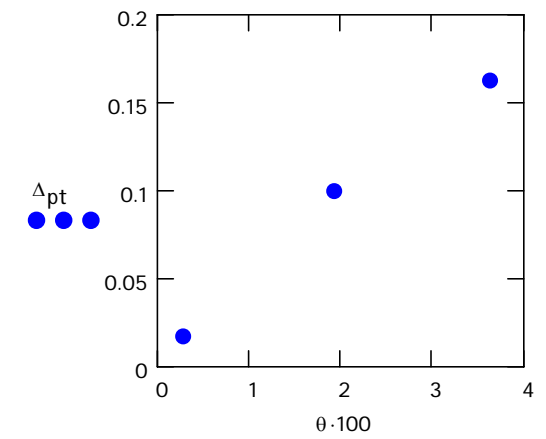
Moment-rotation response



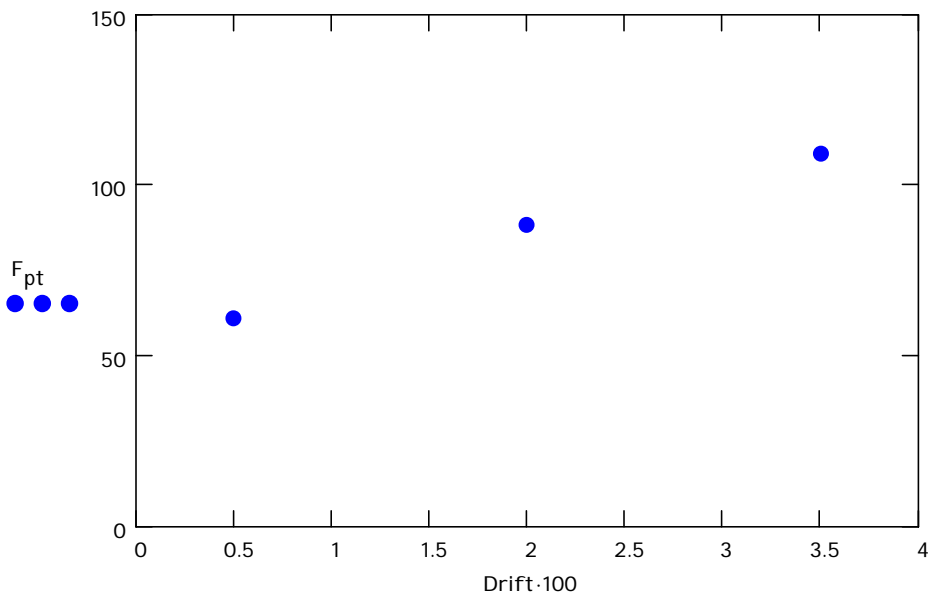
Neutral axis depth variation



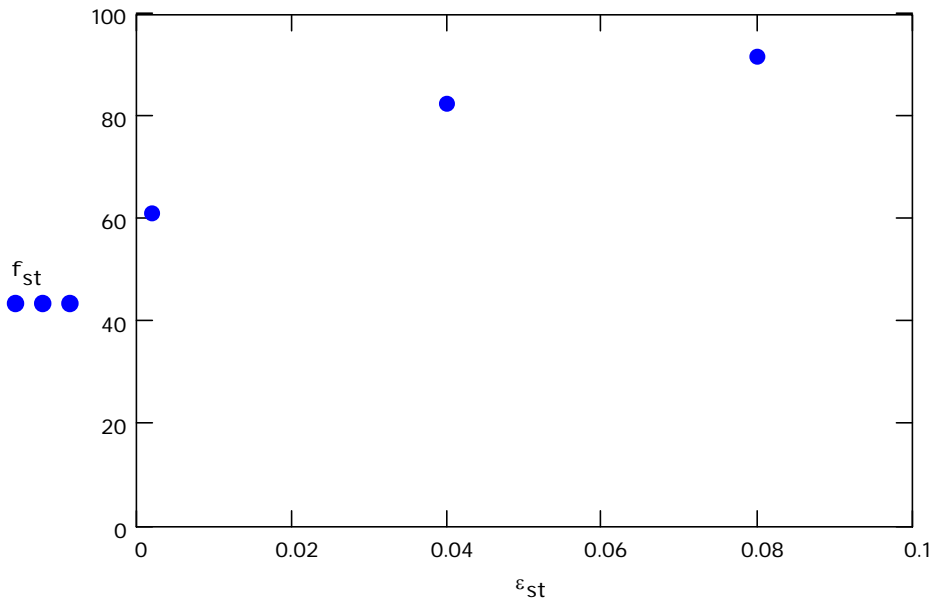
Elongation of post-tensioning tendon



Total force in post-tensioning tendon



Stress-strain behavior assumed for the mild steel reinforcement



APPENDIX B

MODIFIED PRESSS ANALYSIS PROCEDURE

Modified PRESSS Analysis v.6.1

This appendix presents the Mathcad program developed for analyzing hybrid frame connections using the modified PRESSS analysis procedure described in Section 3.2.2.

INPUT: (Section & Material Properties (e.g., M-P-Z4))

Section Properties: Material Properties: Others:

$$h := 16$$

$$E_p := 29000$$

$$\lambda_{sc} := 1.0$$

$$b := 8$$

$$f_{py} := 247.95$$

$$\lambda_{st}(\theta) := \left. \begin{array}{l} \lambda_{st} \leftarrow 1000 \cdot \theta \quad \text{if } 0 \leq \theta < 0.001 \\ \lambda_{st} \leftarrow 1 \quad \text{if } 0.001 \leq \theta < 0.005 \\ \lambda_{st} \leftarrow 0.84 + 34.4 \cdot \theta - 444.4 \cdot \theta^2 \quad \text{if } 0.005 \leq \theta \leq 0.04 \end{array} \right\}$$

$$d' := 1$$

$$f_{sy} := 61.19$$

$$A_{pt} := 0.459$$

$$f_{c'} := 6.815$$

$$A_s := 0.22$$

$$f_{pi} := 106.5$$

$$\beta_1 := 0.85 - 0.05 \cdot (f_{c'} - 4)$$

$$I_{pu} := 40.15$$

$$\beta_1 = 0.709$$

$$\zeta := \frac{d'}{h}$$

ANALYSIS:

ORIGIN := 1

Neutral axis depth: (obtain at 2 percent interface rotation)

$$\begin{aligned}
 \text{NA}(\theta, A_{pt}, A_s) := & \left. \begin{aligned}
 & f_{sc} \leftarrow \lambda_{sc} \cdot f_{sy} \\
 & f_{st} \leftarrow \lambda_{st}(\theta) \cdot f_{sy} \\
 & \eta \leftarrow 0 \\
 & \eta_{\text{check}} \leftarrow 1 \\
 & \text{while } \eta_{\text{check}} - \eta > 0.001 \\
 & \quad \left. \begin{aligned}
 & \eta \leftarrow \eta + 0.001 \\
 & \Delta_{pt} \leftarrow \theta \cdot (0.5 - \eta) \cdot h \\
 & \varepsilon_{pt} \leftarrow \frac{\Delta_{pt}}{l_{pu}} + \frac{f_{pi}}{E_p} \\
 & f_{pt} \leftarrow \varepsilon_{pt} \cdot E_p \cdot \left[0.02 + \frac{0.98}{1 + \left(\frac{\varepsilon_{pt} \cdot E_p}{1.04 \cdot f_{py}} \right)^{8.36}} \right] \\
 & F_{pt} \leftarrow A_{pt} \cdot f_{pt} \\
 & F_{st} \leftarrow A_s \cdot f_{st} \\
 & F_{sc} \leftarrow A_s \cdot f_{sc} \\
 & F_c \leftarrow F_{pt} + F_{st} - F_{sc} \quad \text{if } \eta > \zeta \\
 & F_c \leftarrow F_{pt} + F_{st} + F_{sc} \quad \text{otherwise} \\
 & a \leftarrow \frac{F_c}{0.85 \cdot (1.6 \cdot f_c') \cdot b} \\
 & \eta_{\text{check}} \leftarrow \frac{a}{\beta_1 \cdot h}
 \end{aligned} \right\} \\
 & \eta \cdot h
 \end{aligned}
 \right.
 \end{aligned}$$

$$c := \text{NA}(0.02, A_{pt}, A_s)$$

Hybrid Connection Analysis:

$$\begin{aligned}
 \text{Hybrid}(\theta, A_{pt}, A_s) := & \left[\begin{array}{l}
 f_{sc} \leftarrow \lambda_{sc} \cdot f_{sy} \\
 f_{st} \leftarrow \lambda_{st}(\theta) \cdot f_{sy} \\
 \eta \leftarrow \frac{c}{h} \\
 \Delta_{pt} \leftarrow \theta \cdot (0.5 - \eta) \cdot h \\
 \varepsilon_{pt} \leftarrow \frac{\Delta_{pt}}{l_{pu}} + \frac{f_{pi}}{E_p} \\
 f_{pt} \leftarrow \varepsilon_{pt} \cdot E_p \cdot \left[0.02 + \frac{0.98}{\left[1 + \left(\frac{\varepsilon_{pt} \cdot E_p}{1.04 \cdot f_{py}} \right)^{8.36} \right]^{\frac{1}{8.36}}} \right] \\
 F_{pt} \leftarrow A_{pt} \cdot f_{pt} \\
 F_{st} \leftarrow A_s \cdot f_{st} \\
 F_{sc} \leftarrow A_s \cdot f_{sc} \\
 F_c \leftarrow F_{pt} + F_{st} - F_{sc} \quad \text{if } \eta > \zeta \\
 F_c \leftarrow F_{pt} + F_{st} + F_{sc} \quad \text{otherwise} \\
 a \leftarrow c \cdot \beta_1 \\
 \alpha \leftarrow \frac{a}{2 \cdot h} \\
 M_{pt} \leftarrow F_{pt} \cdot (0.5 - \alpha) \cdot h \\
 M_{st} \leftarrow F_{st} \cdot (1.0 - \zeta - \alpha) \cdot h \\
 M_{sc} \leftarrow F_{sc} \cdot (\alpha - \zeta) \cdot h \\
 M_{cap} \leftarrow M_{pt} + M_{st} + M_{sc} \\
 \left(\begin{array}{l}
 \Delta_{pt} \\
 f_{st} \\
 F_{pt} \\
 M_{pt} \\
 M_{st} \\
 M_{sc} \\
 M_{cap}
 \end{array} \right)
 \end{array} \right.
 \end{aligned}$$

Continuous Response Envelope:

```

Analysis := for i ∈ 0, 1.. 400
  |
  | θi+1 ← 0.0001·i
  | Δpti+1 ← Hybrid(θi+1, Apt, As)1
  | fsti+1 ← Hybrid(θi+1, Apt, As)2
  | Fpti+1 ← Hybrid(θi+1, Apt, As)3
  | Mpti+1 ← Hybrid(θi+1, Apt, As)4
  | Msti+1 ← Hybrid(θi+1, Apt, As)5
  | Msci+1 ← Hybrid(θi+1, Apt, As)6
  | Mcapi+1 ← Hybrid(θi+1, Apt, As)7
  |
  | Mcap1 ← 0
  |
  | 
$$M_{cap_2} \leftarrow \frac{\left( \frac{f_{pt} \cdot A_{pt}}{b \cdot h} \right) \cdot \left( \frac{1}{12} \cdot b \cdot h^3 \right)}{\left( \frac{h}{2} \right)}$$

  |
  | ( θ )
  | ( Δpt )
  | ( fst )
  | ( Fpt )
  | ( Mpt )
  | ( Mst )
  | ( Msc )
  | ( Mcap )

```

θ := Analysis₁ M_{pt} := Analysis₅

Δ_{pt} := Analysis₂ M_{st} := Analysis₆

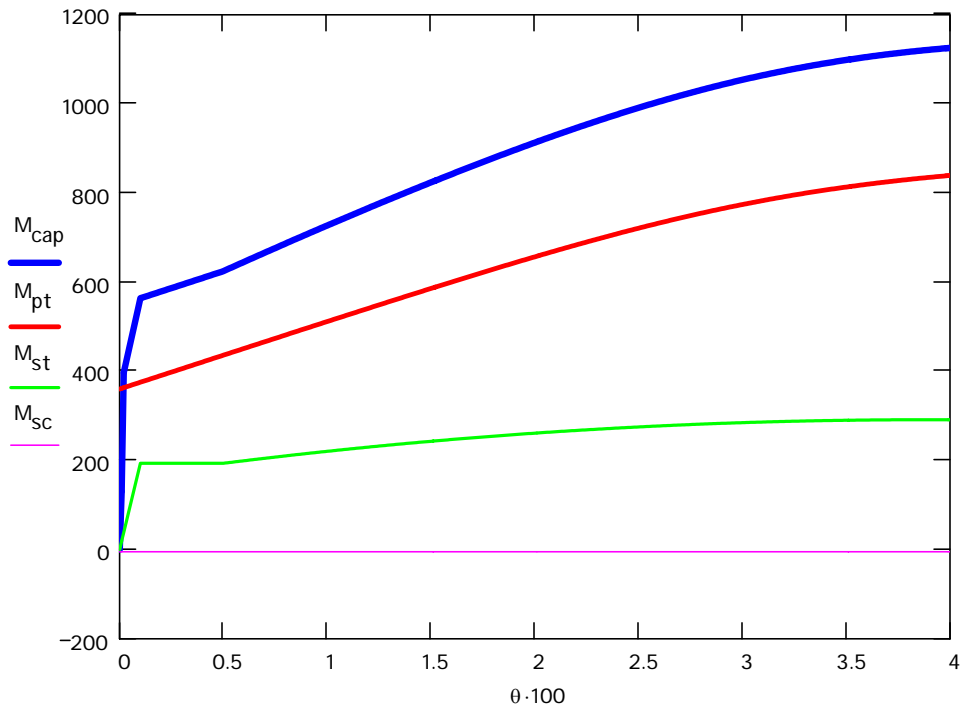
f_{st} := Analysis₃ M_{sc} := Analysis₇

F_{pt} := Analysis₄ M_{cap} := Analysis₈

Drift := 0.85·θ + 4.08·10⁻⁶·M_{cap}

OUTPUT:

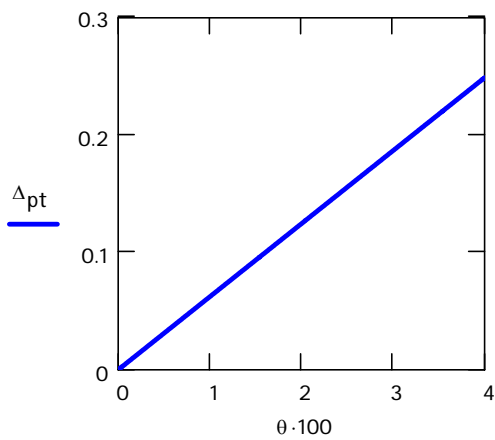
Moment-rotation response



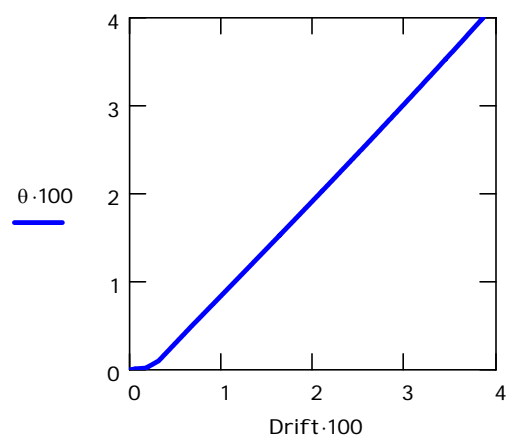
Neutral axis depth variation

$c = 1.776$

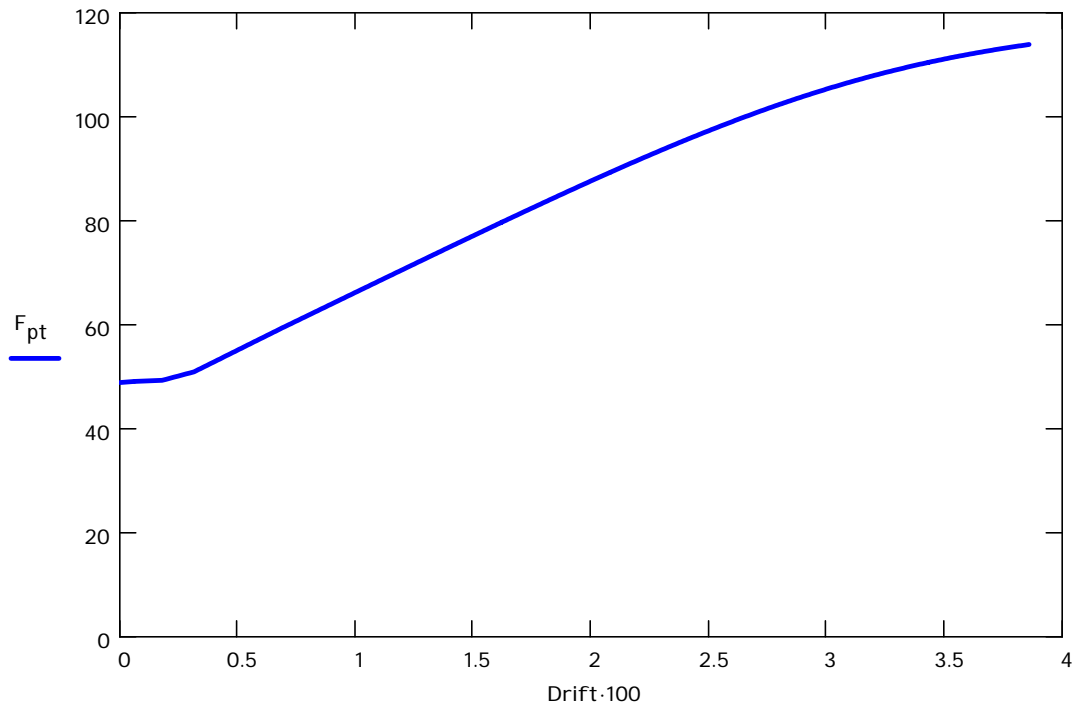
Elongation of post-tensioning tendon



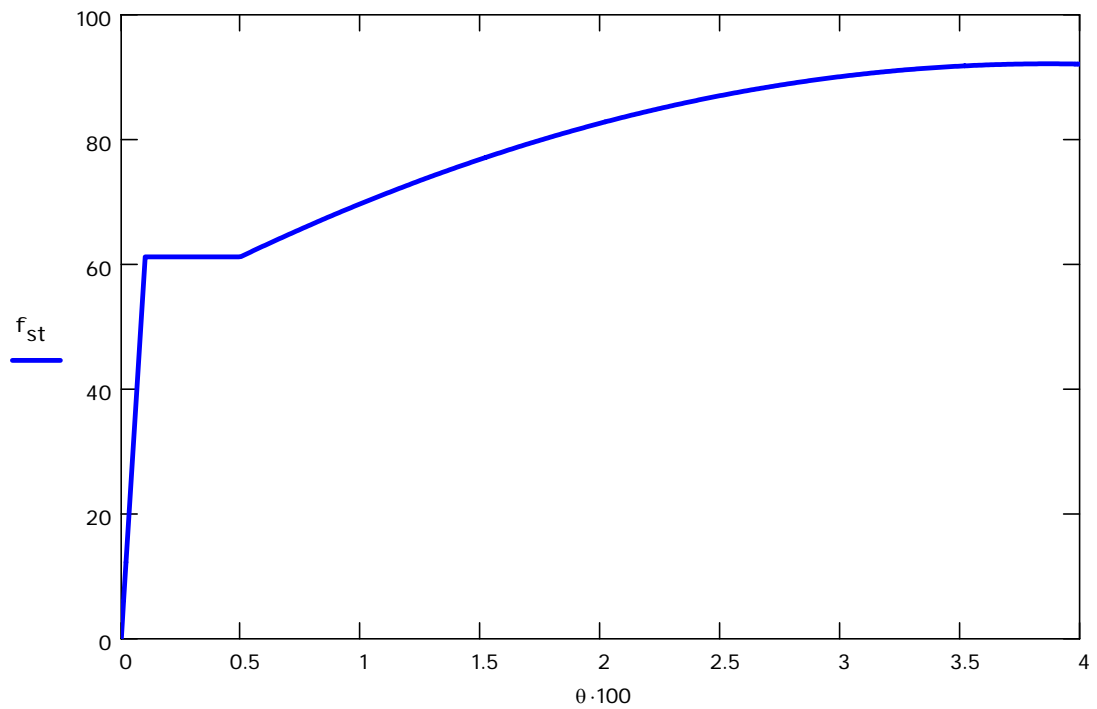
Drift-rotation relationship



Total force in post-tensioning tendon



Stress-rotation behavior of mild steel reinforcement



APPENDIX C

MODIFIED PRESSS DESIGN PROCEDURE

Modified PRESSS Design v.6.1

This appendix presents the Mathcad program developed for designing hybrid frame connections using the modified PRESSS analysis procedure.

INPUT: (Design Requirements, Section Properties, and Material Properties (e.g., PRESSS 1st Floor))

Design Requirements:

$$M_{des} := 2518$$

$$\theta_{des} := 0.02$$

$$\phi_{des} := 0.55 \text{ (initial guess)}$$

Section Properties:

$$h := 23$$

$$b := 14$$

$$d' := 2.25$$

$$ch := 0.5$$

$$I_{pu} := 106.5$$

Material Properties:

$$E_p := 29000$$

$$f_{py} := 255$$

$$f_{sy} := 68.026$$

$$f_{g'} := 8.8$$

$$f_{pi} := 118.95$$

Others: (This part is calculated automatically)

$$h_g := h - 2 \cdot ch$$

$$b_g := b - 2 \cdot ch$$

$$\zeta := \frac{d'}{h_g}$$

$$\beta_1 := 0.85 - 0.05 \cdot (f_{g'} - 4)$$

$$\lambda_{sc_des} := 1$$

$$\lambda_{st_des}(\theta) := \begin{cases} \lambda_{st} \leftarrow 1000 \cdot \theta & \text{if } 0 \leq \theta < 0.001 \\ \lambda_{st} \leftarrow 1 & \text{if } 0.001 \leq \theta < 0.005 \\ \lambda_{st} \leftarrow 0.84 + 34.4 \cdot \theta - 444.4 \cdot \theta^2 & \text{if } 0.005 \leq \theta \leq 0.04 \end{cases}$$

$$\lambda_{st_des}(\theta_{des}) = 1.35$$

+

DESIGN:

ORIGIN := 1

$$f_{st_des} := \lambda_{st_des}(\theta_{des}) \cdot f_{sy}$$

$$f_{sc_des} := \lambda_{sc_des} \cdot f_{sy}$$

Neutral axis depth:

$$\begin{aligned} \text{NA}(\theta_{des}, A_{pt}, A_s) := & \left. \begin{aligned} & \eta_{des} \leftarrow 0 \\ & \eta_{check} \leftarrow 1 \\ & \text{while } \eta_{check} - \eta_{des} > 0.0001 \\ & \quad \eta_{des} \leftarrow \eta_{des} + 0.0001 \\ & \quad \Delta_{pt} \leftarrow \theta_{des} \cdot (0.5 - \eta_{des}) \cdot h_g \\ & \quad \epsilon_{pt} \leftarrow \frac{\Delta_{pt}}{I_{pu}} + \frac{f_{pi}}{E_p} \\ & \quad f_{pt_des} \leftarrow \epsilon_{pt} \cdot E_p \cdot \left[0.02 + \frac{0.98}{\left[1 + \left(\frac{\epsilon_{pt} \cdot E_p}{1.04 \cdot f_{py}} \right)^{8.36} \right]^{8.36}} \right] \\ & \quad F_{pt_des} \leftarrow A_{pt} \cdot f_{pt_des} \\ & \quad F_{st_des} \leftarrow A_s \cdot f_{st_des} \\ & \quad F_{sc_des} \leftarrow A_s \cdot f_{sc_des} \\ & \quad F_{c_des} \leftarrow F_{pt_des} + F_{st_des} - F_{sc_des} \quad \text{if } \eta_{des} > \zeta \\ & \quad F_{c_des} \leftarrow F_{pt_des} + F_{st_des} + F_{sc_des} \quad \text{otherwise} \\ & \quad a_{des} \leftarrow \frac{F_{c_des}}{0.85 \cdot (1.6 \cdot f'_g) \cdot b_g} \\ & \quad \eta_{check} \leftarrow \frac{a_{des}}{\beta_1 \cdot h_g} \\ & \quad \eta_{des} \cdot h_g \end{aligned} \right\} \end{aligned}$$

Hybrid Connection Analysis:

$$\text{Hybrid}(\phi_{des}, \theta_{des}) := \begin{cases} M_{pt_des} \leftarrow \phi_{des} \cdot M_{des} \\ A_{pt} \leftarrow \frac{M_{pt_des}}{(0.45 \cdot h_g) \cdot f_{py}} \\ A_s \leftarrow \frac{M_{des} - M_{pt_des}}{(0.95 - \zeta) \cdot h_g \cdot f_{st_des}} \\ \eta_{des} \leftarrow \frac{NA(0.02, A_{pt}, A_s)}{h_g} \\ \Delta_{pt} \leftarrow \theta_{des} \cdot (0.5 - \eta_{des}) \cdot h_g \\ \varepsilon_{pt} \leftarrow \frac{\Delta_{pt}}{l_{pu}} + \frac{f_{pi}}{E_p} \\ f_{pt_des} \leftarrow \varepsilon_{pt} \cdot E_p \cdot \left[0.02 + \frac{0.98}{\left[1 + \left(\frac{\varepsilon_{pt} \cdot E_p}{1.04 \cdot f_{py}} \right)^{8.36} \right]^{8.36}} \right] \\ F_{pt_des} \leftarrow A_{pt} \cdot f_{pt_des} \\ F_{st_des} \leftarrow A_s \cdot f_{st_des} \\ F_{sc_des} \leftarrow A_s \cdot f_{sc_des} \\ F_{c_des} \leftarrow F_{pt_des} + F_{st_des} - F_{sc_des} \quad \text{if } \eta_{des} > \zeta \\ F_{c_des} \leftarrow F_{pt_des} + F_{st_des} + F_{sc_des} \quad \text{otherwise} \\ a_{des} \leftarrow (\eta_{des} \cdot h_g) \cdot \beta_1 \\ \alpha_{des} \leftarrow \frac{a_{des}}{2 \cdot h_g} \\ M_{pt_des} \leftarrow F_{pt_des} \cdot (0.5 - \alpha_{des}) \cdot h_g \\ M_{st_des} \leftarrow F_{st_des} \cdot (1.0 - \alpha_{des} - \zeta) \cdot h_g \\ M_{sc_des} \leftarrow F_{sc_des} \cdot (\alpha_{des} - \zeta) \cdot h_g \\ M_{cap} \leftarrow M_{pt_des} + M_{st_des} + M_{sc_des} \end{cases}$$

$$\text{Hybrid}(\phi_{des}, \theta_{des}) = \begin{pmatrix} 0.55 \\ 0.66 \\ 167.12 \\ 950.32 \\ 2039.02 \end{pmatrix}$$

Moment Capacity Check:

$$\begin{aligned}
 \text{Check}_1(\phi_{\text{des}}, \theta_{\text{des}}) := & \left\{ \begin{array}{l}
 A_{\text{pt}} \leftarrow \text{Hybrid}(\phi_{\text{des}}, \theta_{\text{des}})1 \\
 A_s \leftarrow \text{Hybrid}(\phi_{\text{des}}, \theta_{\text{des}})2 \\
 f_{\text{pt_des}} \leftarrow \text{Hybrid}(\phi_{\text{des}}, \theta_{\text{des}})3 \\
 M_{\text{pt_des}} \leftarrow \text{Hybrid}(\phi_{\text{des}}, \theta_{\text{des}})4 \\
 M_{\text{cap}} \leftarrow \text{Hybrid}(\phi_{\text{des}}, \theta_{\text{des}})5 \\
 \text{while } M_{\text{cap}} < M_{\text{des}} \\
 \quad \left\{ \begin{array}{l}
 A_{\text{pt}} \leftarrow A_{\text{pt}} + 0.001 \text{ if } M_{\text{pt_des}} < \phi_{\text{des}} \cdot M_{\text{cap}} \\
 A_s \leftarrow A_s + 0.001 \text{ otherwise} \\
 F_{\text{pt_des}} \leftarrow A_{\text{pt}} \cdot f_{\text{pt_des}} \\
 F_{\text{st_des}} \leftarrow A_s \cdot f_{\text{st_des}} \\
 F_{\text{sc_des}} \leftarrow A_s \cdot f_{\text{sc_des}} \\
 \eta_{\text{des}} \leftarrow \frac{\text{NA}(0.02, A_{\text{pt}}, A_s)}{h} \\
 a_{\text{des}} \leftarrow (\eta_{\text{des}} \cdot h_g) \cdot \beta_1 \\
 \alpha_{\text{des}} \leftarrow \frac{a_{\text{des}}}{2 \cdot h_g} \\
 M_{\text{pt_des}} \leftarrow F_{\text{pt_des}} \cdot (0.5 - \alpha_{\text{des}}) \cdot h_g \\
 M_{\text{st_des}} \leftarrow F_{\text{st_des}} \cdot (1.0 - \alpha_{\text{des}} - \zeta) \cdot h_g \\
 M_{\text{sc_des}} \leftarrow F_{\text{sc_des}} \cdot (\alpha_{\text{des}} - \zeta) \cdot h_g \\
 M_{\text{cap}} \leftarrow M_{\text{pt_des}} + M_{\text{st_des}} + M_{\text{sc_des}} \\
 \phi_{\text{des}} \leftarrow \frac{M_{\text{pt_des}}}{M_{\text{cap}}}
 \end{array} \right. \\
 \left(\begin{array}{c}
 A_{\text{pt}} \\
 A_s \\
 M_{\text{pt_des}} \\
 M_{\text{st_des}} \\
 M_{\text{sc_des}} \\
 M_{\text{cap}} \\
 \phi_{\text{des}}
 \end{array} \right)
 \end{array} \right.
 \end{aligned}$$

$$\text{Check}_1(\phi_{\text{des}}, \theta_{\text{des}}) = \left(\begin{array}{c}
 0.8 \\
 0.69 \\
 1385.58 \\
 1207.39 \\
 -74.62 \\
 2518.35 \\
 0.55
 \end{array} \right)$$

Restoring Capacity Check:

$$\text{Check}_2(\phi_{\text{des}}, \theta_{\text{des}}) := \left\{ \begin{array}{l} M_{\text{pt}_0} \leftarrow 0 \\ M_{\text{st}_0} \leftarrow 1 \\ M_{\text{sc}_0} \leftarrow 1 \\ \text{while } (M_{\text{pt}_0} < M_{\text{st}_0} + M_{\text{sc}_0}) \wedge (\phi_{\text{des}} < 1) \\ \quad \left\{ \begin{array}{l} A_{\text{pt}} \leftarrow \text{Check}_1(\phi_{\text{des}}, \theta_{\text{des}})_1 \\ A_{\text{S}} \leftarrow \text{Check}_1(\phi_{\text{des}}, \theta_{\text{des}})_2 \\ f_{\text{pt_des}} \leftarrow \text{Hybrid}(\phi_{\text{des}}, \theta_{\text{des}})_4 \\ F_{\text{pt}_0} \leftarrow A_{\text{pt}} \cdot f_{\text{pt_des}} \\ F_{\text{st}_0} \leftarrow A_{\text{S}} \cdot f_{\text{sc_des}} \\ F_{\text{sc}_0} \leftarrow A_{\text{S}} \cdot f_{\text{sc_des}} \\ F_{\text{c}_0} \leftarrow F_{\text{pt}_0} - F_{\text{st}_0} - F_{\text{sc}_0} \\ a_0 \leftarrow \frac{F_{\text{c}_0}}{0.85 \cdot (1.6 \cdot f_g) \cdot b_g} \\ \alpha_0 \leftarrow \frac{a_0}{2 \cdot h_g} \\ M_{\text{pt}_0} \leftarrow F_{\text{pt}_0} \cdot (0.5 - \alpha_0) \cdot h_g \\ M_{\text{st}_0} \leftarrow F_{\text{st}_0} \cdot (1.0 - \zeta - \alpha_0) \cdot h_g \\ M_{\text{sc}_0} \leftarrow F_{\text{sc}_0} \cdot (\alpha_0 - \zeta) \cdot h_g \\ \phi_{\text{des}} \leftarrow \phi_{\text{des}} + 0.01 \text{ if } M_{\text{pt}_0} < M_{\text{st}_0} + M_{\text{sc}_0} \end{array} \right. \\ M_{\text{cap}} \leftarrow \text{Check}_1(\phi_{\text{des}}, \theta_{\text{des}})_6 \\ \left(\begin{array}{c} \phi_{\text{des}} \\ A_{\text{pt}} \\ A_{\text{S}} \\ M_{\text{cap}} \end{array} \right) \end{array} \right.$$

$$\text{Check}_2(\phi_{\text{des}}, \theta_{\text{des}}) = \left(\begin{array}{c} 0.55 \\ 0.8 \\ 0.69 \\ 2518.35 \end{array} \right)$$

OUTPUT:

$$\phi := \text{Check}_2(\phi_{\text{des}}, \theta_{\text{des}})1$$

$$\phi = 0.55$$

Moment capacity:

$$M_{\text{cap}} := \text{Check}_2(\phi_{\text{des}}, \theta_{\text{des}})4$$

$$M_{\text{cap}} = 2518.35$$

Area of post-tensioning tendon

$$A_{\text{pt}} := \text{Check}_2(\phi_{\text{des}}, \theta_{\text{des}})2$$

$$A_{\text{pt}} = 0.802$$

$$n_{\text{pt}} := \frac{A_{\text{pt}}}{0.153}$$

$$n_{\text{pt}} = 5.239$$

$$\text{ceil}(n_{\text{pt}}) = 6 \quad \text{strands}$$

Area of mild steel reinforcement

$$A_s := \text{Check}_2(\phi_{\text{des}}, \theta_{\text{des}})3$$

$$A_s = 0.688$$

$$n_s := \frac{A_s}{0.44}$$

$$n_s = 1.565$$

$$\text{ceil}(n_s) = 2 \quad \#6$$